

# **A Systematic Experimental Approach to Cavitation Noise Prediction of Marine Propellers**



**Batuhan Aktas**

School of Marine Science and Technology  
Newcastle University

This dissertation is submitted for the degree of

*Doctor of Philosophy*

August 2016



Dedicated to my Parents

# **Declaration**

I hereby declare that except where specific reference is made to the work of others, the contents of this dissertation are original and have not been submitted in whole or in part for consideration for any other degree or qualification in this, or any other university. This dissertation is my own work and contains nothing which is the outcome of work done in collaboration with others, except as specified in the text and Acknowledgements.





# Acknowledgements

This thesis represents not only my work in front of a computer; It is a milestone in my life, produced during more than half a decade of work at Newcastle University. Especially the time I have spent within the Emerson Cavitation Tunnel has enhanced my engineering understanding and taught me a lot through a steep learning curve following my B.Eng. degree.

First and foremost, I would like to thank my supervisor, Prof. Mehmet Atlar, director of Emerson Cavitation Tunnel. I owe my deepest gratitude to Mehmet as he has been supportive since my undergraduate days. We first worked together on my final year project. Ever since he provided guidance, encouragement and advice when needed. I hope to pursue further work with him while searching for the perfect slow cooked brisket as we did during SMP'2015 conference in Austin, Texas.

I am deeply grateful to Mr. Patrick Fitzsimmons. Patrick has not only lectured, guided, supported all along my studies but also shared his vast and invaluable experience without hesitation.

I also would like to express my gratitude to Dr. Noriyuki Sasaki for not only providing the funding through Newcastle University but also for sharing his immense knowledge on marine hydrodynamics.

I also would like to say a huge thank you to Dr. Roderick Sampson. Since the commencement of my studies, I have learned a tremendous amount from him. Moreover, although he was across the pond over in the USA, he has always been there to help me out.

I am also indebted to Prof. Emin Korkut. He has guided me through my first cavitation tunnel experiments and helped me writing my first tunnel report. It was not only a pleasure to work with him but also an enjoyable experience throughout.

My thanks extend to Mr. George Mitchell, whom provided the wisdom when in need. He has been the first point of contact to talk about the tunnel, telling us about all the previous experiences and predecessors.

Members of the Emerson Cavitation Tunnel group have contributed immensely to my personal and professional time at Newcastle University. The group has been a source of friendships as well as good advice and collaboration. Therefore, I am grateful to Dr. Kwang-Cheol Seo, Mr. George Politis, Dr. Serkan Turkmen, Mr. Weichao Shi, Miss Irma Yeginbayeva, Mr. Alessandro Carchen, Mr. Chang Li, Dr. Musa Bashir and Miss Rosalynna Rosli.

I am indebted to Dr. Paula Kellett whom supported the proofreading, Dr. Antonis Mantouvalos and Dr. Francesca Tagliaferri for artificial neural network content and Mr. Jeff Neasham for the acoustic characterization of Emerson Cavitation Tunnel part of this thesis.

This Ph.D. study would not have been possible without the cooperation and support of the technical team of the Hydrodynamic facilities and the crew of “The Princess Royal”. They have not only contributed with their professional experience but also have been extremely helpful; throughout my studies. Thus, my deepest appreciation goes to: Mr. Peter Bowes, Mr. Robert Hindhaugh, Mr. Ian Paterson, Mr. Phil Letouze, Mr. Ian Howard-Row, Mr. Liam Rogerson, Mr. Kieron Fallows, Mr. Neil Armstrong and Mr. Barry Pearson.

Last but not least, I would like to thank my family for all their encouragement and support.

Batuhan Aktas, March 2016



# Abstract

Minimization of propeller cavitation noise is best achieved through accurate and reliable predictions at an early design stage. The effect of cavitation and particularly the dynamics of cavitation on URN is rather complex to understand and the current state of the art does not offer a plausible cavitation noise prediction method which can be implemented within the propeller design spiral. Within this framework, the aim of the present thesis is to enhance the understanding of the propeller cavitation noise by conducting detailed systematic cavitation tunnel tests to investigate the main propeller design parameters and operating conditions and to scrutinize their impact on propeller Radiated Noise Levels (RNL). The resulting experimental data are also utilized to compile a database that enables engineering a novel noise prediction method to be developed and used at preliminary design stage, using standard series approach.

A holistic approach to cavitation noise has been adopted through experimental investigations into oblique flow effects on propeller noise and by conducting full scale and model scale noise experiments of a research vessel. These have been used to evaluate the capabilities of the adopted standard series based experimental prediction methodology.

The accumulated knowledge based on prior experiments has been utilized to design standard series propeller test campaign. Experiments using members of Meridian standard propeller series were tested both in an open water condition and also behind systematically varied wake inflows. Initially, a small subset of the Meridian standard propeller series was chosen, with loading conditions derived from in-service, ocean-going vessels. The resulting measured noise data were extrapolated to full-scale based on the powering information of these vessels to compare with average shipping noise data. Finally, a larger subset of the propeller series was tested systematically to compile a database of propeller cavitation noise and for the development of noise prediction software.

# Contents

Declaration .....	iv
Acknowledgements .....	vi
Abstract .....	ix
Contents .....	x
List of Figures .....	xv
List of Tables .....	xxiii
Nomenclature .....	xxv
Chapter 1    Introduction .....	1
1.1    Introduction .....	1
1.2    Motivation .....	1
1.3    Aims and Objectives .....	8
1.4    Layout of the Thesis .....	11
1.5    Summary .....	12
Chapter 2    Literature Review .....	13
2.1    Introduction .....	13
2.2    History of underwater sound .....	13
2.3    Background .....	15
2.4    Fundamental acoustics .....	15
2.4.1    Underwater sound propagation .....	18
2.4.2    Ambient noise sources .....	19
2.5    Shipping noise .....	20
2.6    Propeller design and URN .....	23
2.6.1    Hull shape and wake inflow .....	23
2.6.2    Propeller geometry .....	25
2.7    Cavitation .....	30
2.7.1    Types of cavitation experienced by propellers .....	33
2.7.2    Consequences of cavitation .....	38
2.8    Propeller noise prediction methods .....	39
2.8.1    Computational propeller noise prediction methods .....	43
2.8.2    Experimental propeller noise prediction .....	44
2.9    Experimental propeller noise test cases .....	48
2.9.1    Inclined shaft effect on propellers .....	51

2.9.2	ANN for data management & post processing of systematic experimental data	53
2.10	Conclusions.....	54
Chapter 3	Experimental Facilities, Equipment & Data Analysis.....	56
3.1	Introduction.....	56
3.2	Emerson Cavitation Tunnel .....	56
3.3	Research Vessel “The Princess Royal” .....	58
3.4	The Equipment inventory .....	60
3.4.1	Flow measurement.....	60
3.4.2	Water quality .....	67
3.4.3	Dynamometers.....	70
3.4.4	Cavitation observations .....	74
3.4.5	Pressure sensors and data acquisition.....	80
3.4.6	Noise measurement equipment and analysing methodology .....	84
3.5	Conclusions.....	90
Chapter 4	Systematic Cavitation Tunnel Tests of a Propeller in Uniform and Inclined Flow Conditions .....	92
4.1	Introduction.....	92
4.2	Experimental setup & test conditions .....	92
4.2.1	Propeller design and model propeller.....	94
4.3	Open water performance tests.....	95
4.4	Cavitation observations.....	96
4.4.1	Cavitation inception.....	97
4.5	Noise measurements .....	101
4.5.1	Analysis and presentation of the noise results.....	102
4.6	Discussion.....	109
4.6.1	Open water efficiency performance .....	109
4.6.2	Cavitation observations .....	111
4.6.3	Noise measurements .....	113
4.7	Conclusions.....	115
Chapter 5	Underwater Radiated Noise Investigations of Cavitating Propellers Using a Medium Size Cavitation Tunnel and Full-Scale Trials .....	117
5.1	Introduction.....	117
5.2	Further details of experimental facilities and setup .....	117
5.2.1	Main particulars of “The Princess Royal” and propeller.....	118
5.2.2	Wake simulations .....	120
5.3	Cavitation test conditions.....	123
5.4	Cavitation observations.....	126

5.5	Pressure pulse measurements .....	129
5.5.1	Presentation of results .....	129
5.6	Noise measurements.....	134
5.6.1	Presentation of results .....	135
5.7	Discussion .....	140
5.8	Conclusions .....	146
Chapter 6	Propeller Cavitation Noise Prediction Using a Standard Propeller-Series Approach .....	147
6.1	Introduction .....	147
6.2	Philosophy of standard series approach to URN prediction of a propeller .....	148
6.3	Adopted experimental approach.....	150
6.3.1	Selection of standard propeller series .....	151
6.3.2	Development of systematic variation of wake inflow .....	153
6.3.3	Experimental setup.....	157
6.4	URN data with commercially representative small subset of Meridian propeller series .....	163
6.4.1	Test matrix and adopted approach for tests .....	164
6.4.2	Noise measurement results.....	167
6.4.3	Remarks on test results with small subset of propeller series .....	170
6.5	URN data with extended subset of Meridian propeller series.....	171
6.5.1	Presentation of results and advance analysis of cavitation induced noise data using JTFA technique.....	175
6.6	Development of an ANN tool for cavitation noise prediction .....	197
6.6.1	ANN for total noise level prediction.....	201
6.6.2	ANN for background noise level prediction .....	204
6.6.3	Standalone executable tool development.....	207
6.7	Validation of the developed RNL prediction method .....	211
6.7.1	Case Study 1: Training Ship “Sein-Maru”.....	211
6.7.2	Case Study 2: “Merchant Tanker (M/T) Olympus” .....	218
6.7.3	Further remarks on validation case studies .....	224
6.8	Conclusions .....	226
Chapter 7	Conclusions and Recommendations .....	228
7.1	Introduction .....	228
7.2	Philosophical review of the thesis .....	228
7.3	Main conclusions.....	233
7.4	Recommendation for future work .....	237
References	.....	241



Appendix A	– “The Princess Royal” Propeller and Hull Wake Details.....	A-1
A.1	Introduction.....	A-1
A.2	Detailed propeller and wake data.....	A-1
Appendix B	– Drawings and Other Details of Meridian Standard Propeller Series .....	B-1
B.1	Introduction.....	B-1
B.2	Propeller blade sections and details .....	B-1
Appendix C	- Background Noise Measurements for Standard Series Propeller Tests ....	C-1
C.1	Introduction.....	C-1
C.2	Background noise measurements.....	C-1
Appendix D	- Fundamentals of Artificial Neural Network & Associated Prediction Software .....	D-1
D.1	Introduction.....	D-1
D.2	Fundamentals of ANN .....	D-1
D.3	MATLAB code for the determination of optimum number of hidden neurons .....	D-4
D.4	MATLAB code for the noise prediction tool.....	D-8



# List of Figures

Figure 1-1 Historical ambient noise levels in 25-50 Hz indicating the increasing trend of shipping contribution (Reproduced from Frisk, 2012).....	2
Figure 1-2 Impact of Anthropogenic noise on marine mammals (Reproduced from National Geographic Magazine, 2011). ....	3
Figure 2-1 The sketches for the experiments to prove sound propagation through water (Reproduced from (Bjørnø & Bjørnø, 1999)). ....	14
Figure 2-2 Sample Ambient noise spectra (reproduced from Wenz, 1972).....	19
Figure 2-3 Numbers of vessels (dashed line) and gross tonnage of vessels (continuous line) in the world's fleet by Lloyd's Register of shipping for self-propelled, merchant vessels over 100 gross tonnes (Reproduced from (Hildebrand, 2009))......	21
Figure 2-4 Propeller cavitation tests with Parsons' world's first cavitation tunnel (Courtesy of M. Atlar). ....	31
Figure 2-5 Representation of the most common types of cavitation (ITTC, 2002a).....	34
Figure 2-6 ITTC approved schematic patterns used for hand sketches and cavitation tunnel cavitation images for bubble cavitation (Courtesy of Emerson Cavitation Tunnel Archives). ....	35
Figure 2-7 ITTC approved schematic patterns used for hand sketches and cavitation tunnel cavitation images for bubble cavitation (Courtesy of Emerson Cavitation Tunnel Archives). ....	36
Figure 2-8 ITTC approved schematic patterns used for hand sketches and cavitation tunnel cavitation images for bubble cavitation (Courtesy of Emerson Cavitation Tunnel Archives). ....	37
Figure 2-9 ITTC approved schematic patterns used for hand sketches and cavitation tunnel cavitation images for bubble cavitation (Courtesy of Emerson Cavitation Tunnel Archives). ....	38
Figure 2-10 Flow chart for the computational prediction of cavitation noise (Reproduced from (van Wijngaarden, 2011)).....	44
Figure 2-11 Wake non-uniformities (left) and propeller pitch distributions (right) of Konno et al., (2002). ....	50
Figure 2-12 Inclined Flow Effect (Carlton, 2012).....	51
Figure 3-1 Sketch of Emerson Cavitation Tunnel. ....	57
Figure 3-2 Panoramic view of Emerson Cavitation Tunnel and test set-up. ....	57
Figure 3-3 Views of Newcastle University's new research vessel, "The Princess Royal". ....	59
Figure 3-4 Setup of Stereoscopic PIV for measurement of Dummy Hull wake. ....	62
Figure 3-5 Calibration target installed on the dummy-hull model .....	63

Figure 3-6 Calibration result (left image for the forward camera and right image for backward camera).....	63
Figure 3-7 An example of PIV Images .....	64
Figure 3-8 Normalised cross-correlation map .....	64
Figure 3-9 BSA Flow software user interface. ....	66
Figure 3-10 Grid of measurement points used for the wake screen development (reproduced from (Korkut, 1999)).....	66
Figure 3-11 Hydrolab mini sonde MS5. ....	68
Figure 3-12 YSI 550A Handheld DO <sub>2</sub> Meter. ....	68
Figure 3-13 Bubble Injection cylinders of the ECT.....	69
Figure 3-14 Degassing process of the ECT by application of millimetre bubbles under vacuum condition.....	70
Figure 3-15 Kempf & Remmers H33 dynamometer attached to the bevel gearbox (Left) and during calibration (right). ....	71
Figure 3-16 Kempf & Remmers R45 dynamometer attached to the bevel gearbox (Left) and during calibration (right). ....	71
Figure 3-17 National Instruments hardware and software. ....	72
Figure 3-18 Full-scale borescope cavitation observation arrangement. ....	76
Figure 3-19 Borescope observation technique parts. ....	77
Figure 3-20 Full-scale high-speed camera cavitation observation setup through observation windows. ....	78
Figure 3-21 Full-scale DSLR Camera sample image. ....	78
Figure 3-22 Cavitation observation using stroboscopic lighting. ....	79
Figure 3-23 Model scale continuous light cavitation observation set-up at ECT.....	80
Figure 3-24 Pressure and vibration Data Acquisition Hardware including NI CDAQ Chassis with Modules and pressure sensors.....	81
Figure 3-25 Appearance of typical simultaneous pressure Pulse Acquisition (left) and FFT analysis (right) in the Labview software domain. ....	82
Figure 3-26 B&K Type 8103 Hydrophone (on the right) and its streamlined foil support to fit inside the tunnel test section (on the left). ....	85
Figure 3-27 Calibration configuration of the Hydrophone (Top). The connection diagram of the hydrophone (Middle). Typical Receiving Frequency Characteristics of B&K 8103 (Bottom). ....	86
Figure 3-28 Pulse Labshop DAQ window. ....	87
Figure 4-1 Angle convention for the conducted shaft inclination tests at ECT.....	93
Figure 4-2 Axial speed profile of the Emerson Cavitation Tunnel for 4m/s inflow velocity measured at the propeller plane where the origin is the shaft centreline. ....	94

Figure 4-3 Scale comparison of the full-scale (port) and model-scale (starboard) propellers .	95
Figure 4-4 Open water performance of model propeller, for various inclination angles under high vacuum condition. ....	96
Figure 4-5 Cavitation developments at $-9^\circ$ inclination angle under high vacuum condition. ..	97
Figure 4-6 Images of the cavitation inception and desinence points for propeller model at $0^\circ$ inclination angle under high vacuum condition. ....	98
Figure 4-7 Variation of cavitation inception J number (Advance Coefficient) with respect to inclination angles. ....	100
Figure 4-8 A view of hydrophone glued on the side window (top); An overall view of the dynamometer with inclined shaft arrangement in test section of the tunnel (bottom). ....	101
Figure 4-9 Comparison of noise levels at varying inclination angles at advance coefficient of $J=0.60$ under high vacuum condition. ....	102
Figure 4-10 Background noise level spectrum (at Atmospheric condition) and SPL for $6^\circ$ inclination at $J 0.4$ (at various cavitation condition). ....	103
Figure 4-11 Comparison of noise levels for varying shaft inclination angles on advance coefficients under different cavitation conditions at 630 Hz. ....	105
Figure 4-12 Cavitation observation for varying shaft inclination angles on advance coefficients under different cavitation conditions. ....	106
Figure 4-13 Comparison of noise levels for varying advance coefficients on shaft inclination angles under different cavitation conditions at 630 Hz. ....	107
Figure 4-14 Comparison of noise levels for varying advance coefficients on shaft inclination angles under different cavitation conditions at 6.3 kHz. ....	108
Figure 4-15 Tip vortex breakdown due to interaction with the sheet cavitation extension at $J=0.4$ . ....	109
Figure 4-16 The Non-Dimensional Performance Coefficients at $J=0.4$ for different vacuum conditions. ....	110
Figure 4-17 Cavitation patterns at $0^\circ$ inclination angle under Atmospheric condition. ....	112
Figure 4-18 Cavitation patterns at $6^\circ$ inclination angle under medium vacuum condition. ....	112
Figure 4-19 Cavitation patterns at $-6^\circ$ inclination angle under high vacuum condition. ....	113
Figure 5-1 : Dummy-hull model fitted in Emerson Cavitation Tunnel. ....	121
Figure 5-2 : Contour plots of target wake (left) and simulated wake (right) together with the vector plot of the radial and tangential components of the target wake (bottom). ....	122
Figure 5-3 : Comparative plots of axial wake velocities at $r/R=0.827$ . ....	122
Figure 5-4 : Comparative plots of axial wake velocities at $r/R=1.013$ . ....	123
Figure 5-5 Cavitation observations from tunnel tests for Condition 1; $\sigma_n = 1.20$ , $K_Q=0.378$ . ....	126
Figure 5-6 Cavitation observations from full scale trials for Condition 1; $\sigma_n = 1.20$ , $K_Q=0.378$ . ....	126

Figure 5-7 Cavitation observations from tunnel tests trials for Condition 2; $\sigma_n=0.54$ , $K_Q=0.336$ .	127
Figure 5-8 Cavitation observations from full scale trials for Condition 2; $\sigma_n=0.54$ , $K_Q=0.336$ .	127
Figure 5-9 Cavitation observations from tunnel tests for Condition 3 Condition 3; $\sigma_n=0.3$ , $K_Q=0.318$ .	127
Figure 5-10 Cavitation observations from full scale trials for Condition 3 Condition 3; $\sigma_n=0.3$ , $K_Q=0.318$ .	128
Figure 5-11 Cavitation observations from tunnel tests for Condition 4; $\sigma_n=0.11$ , $K_Q=0.318$ .	128
Figure 5-12 Cavitation observations from full scale trials for Condition 4; $\sigma_n=0.11$ , $K_Q=0.318$ .	128
Figure 5-13 Starboard side pressure sensor (indicated by SP*) and borescope hole (indicated by SB*) arrangement of “The Princess Royal”.	129
Figure 5-14 Comparative full-scale pressure peaks based on the extrapolation from model tests for Condition 1; $\sigma_n=1.20$ , $K_Q=0.378$ .	130
Figure 5-15 Comparative full-scale pressure peaks based on the extrapolation from model tests for Condition 2; $\sigma_n=0.54$ , $K_Q=0.336$ .	130
Figure 5-16 Comparative full-scale pressure peaks based on the extrapolation from model tests for Condition 3; $\sigma_n=0.3$ , $K_Q=0.318$ .	131
Figure 5-17 Comparative full-scale pressure peaks based on the extrapolation from model tests for Condition 4; $\sigma_n=0.11$ , $K_Q=0.318$ .	131
Figure 5-18 Comparison of the full scale and extrapolated model scale measurements for P2 position Condition 1; $\sigma_n=1.20$ , $K_Q=0.378$ .	132
Figure 5-19 Comparison of the full scale and extrapolated model scale measurements for P2 position for Condition 2; $\sigma_n=0.54$ , $K_Q=0.336$ .	132
Figure 5-20 Comparison of the full scale and extrapolated model scale measurements for P2 position for Condition 3; $\sigma_n=0.3$ , $K_Q=0.318$ .	133
Figure 5-21 Comparison of the full scale and extrapolated model scale measurements for P2 position for Condition 4; $\sigma_n=0.11$ , $K_Q=0.318$ .	133
Figure 5-22 Condition 1 - Comparison of total RNL from full-scale trials and tunnel test measurements based extrapolations at $\sigma_n=1.20$ , $K_Q=0.378$ .	136
Figure 5-23 Condition 2 - Comparison of total RNL from full-scale trials and tunnel test measurements based extrapolations at ; $\sigma_n=0.54$ , $K_Q=0.336$ .	136
Figure 5-24 : Condition 3 - Comparison of total RNL from full-scale trials and tunnel test measurements based extrapolations at $\sigma_n=0.3$ , $K_Q=0.318$ .	137
Figure 5-25 Condition 4 - Comparison of total RNL from full-scale trials and tunnel test measurements based extrapolations at $\sigma_n=0.11$ , $K_Q=0.318$ .	137

Figure 5-26 Condition 1 - Comparison of net RNL from full-Scale trials and tunnel test measurement based on extrapolations at $\sigma_n=1.20$ , $K_Q=0.378$ .	138
Figure 5-27 Condition 2 - Comparison of net RNL from full-scale trials and tunnel test measurement based on extrapolations at $\sigma_n=0.54$ , $K_Q=0.336$ .	139
Figure 5-28 Condition 3 - Comparison of RNL from full-Scale trials and tunnel test measurement based on extrapolations at $\sigma_n=0.3$ , $K_Q=0.318$ .	139
Figure 5-29 Condition 4 - Comparison of net RNL from full-scale trials and tunnel test measurement based on extrapolations at $\sigma_n=0.11$ , $K_Q=0.318$ .	140
Figure 5-30 Model scale total noise measurements overview.	144
Figure 5-31 Full-scale net noise measurements overview.	145
Figure 6-1 Philosophy behind the experimental approach for URN prediction.	148
Figure 6-2 Representation of wake depth ( $\Delta W$ ) and half wake width for three representative wake distributions at $r/R=0.7$ .	155
Figure 6-3 Comparison of target (theoretical) and simulated wakes (ECT) at $r/R=0.7$ .	155
Figure 6-4 Constructed wake screens.	156
Figure 6-5 Contour plots of axial velocity distributions of the simulated 3 representative wakes.	157
Figure 6-6 Testing set-up of model propeller behind wake ECT2 at a distance of 1.5 propeller diameter.	158
Figure 6-7 Locations of two B&K hydrophones relative to model propeller inside ECT.	159
Figure 6-8 CAD model of the experimental setup in ECT test section.	159
Figure 6-9 - Setup of the known noise source for the determination of the acoustical transfer functions	160
Figure 6-10 - Agilent arbitrary waveform generator	161
Figure 6-11 Channel impulse response in time domain for 5-20 kHz sweep signal over 0.5 second.	161
Figure 6-12 Narrowband frequency response of the tunnel with the calibrated noise source response.	162
Figure 6-13 Narrowband frequency domain transfer function of the ECT.	163
Figure 6-14 Main propeller parameters from the 3-member Meridian Series subset (on the Left). Subset images: KCD 129 (top left), KCD 193 (Top right), KCD 191 (bottom).	164
Figure 6-15 Measurement matrix given together with the operating conditions of the target vessels. (Operating conditions are denoted by circles while operating regions are denoted by dashed lines for each vessel type).	165
Figure 6-16 Handy Bulk carrier dimensions used for extrapolation of the KCD 191 noise data.	167
Figure 6-17 PANAMAX Bulk carrier dimensions for extrapolation of the KCD 129 noise data.	168

Figure 6-18 Container ship dimensions for extrapolation of the KCD 193 noise data.....	168
Figure 6-19 Extrapolated noise levels of KCD 129 in open water condition and .....	169
Figure 6-20 Extrapolated noise levels of KCD 193 in open water condition and .....	169
Figure 6-21 Comparison of predicted noise levels with average shipping noise data.....	170
Figure 6-22 Extended subset of Meridian propellers and wake screens used for tests.....	173
Figure 6-23 Layout of an advanced analysis tool for cavitation induced URN.....	176
Figure 6-24 The comparison of the KCD193 propeller behind ECT 1 wake at propeller speed of 600 RPM and 1750 RPM.....	177
Figure 6-25 Noise comparison of the KCD193 propeller behind ECT 1 and in open water condition at propeller speed of 1750 RPM. ....	178
Figure 6-26 Noise comparison of KCD 129 and KCD 65 propellers behind ECT 2 wake at propeller speed of 2000 RPM. ....	179
Figure 6-27 The comparison of the KCD 74 and KCD 65 propellers behind ECT 1 wake at propeller speed of 2000 RPM. ....	180
Figure 6-28 The comparison of the KCD 193 and KCD 191 propellers behind ECT 1 wake at propeller speed of 1750 RPM. ....	181
Figure 6-29 Synchronous time domain pressure signals and cavitation observations under atmospheric pressure for KCD 193 behind ECT1 for 1750 RPM (left) and 600 RPM (right). ....	183
Figure 6-30 Synchronous time domain pressure signals and cavitation observations under atmospheric pressure for KCD 193 at 1750 RPM behind ECT1 (left) and open water condition (right). ....	184
Figure 6-31 Synchronous time domain pressure signals and cavitation observations under 150 mmHg vacuum behind ECT2 at 2000 RPM for KCD 65 (left) and KCD 129 (right).....	185
Figure 6-32 Synchronous time domain pressure signals and cavitation observations under 150 mmHg vacuum behind ECT1 at 2000 RPM for KCD 74 (left) and KCD 65 (right).....	186
Figure 6-33 Synchronous time domain pressure signals and cavitation observations under atmospheric pressure behind ECT1 at 17500 RPM for KCD 193 (Left) and KCD 191 (Right). ....	187
Figure 6-34 Joint-time frequency analysis of KCD 193 propeller behind ECT1 under atmospheric condition at 1750 RPM.....	188
Figure 6-35 Joint-time frequency analysis of KCD 193 propeller behind ECT1 under atmospheric condition at 600 RPM.....	189
Figure 6-36 Joint-time frequency analysis of KCD 193 propeller in open water condition under atmospheric condition at 1750 RPM.....	190
Figure 6-37 Joint-time frequency analysis of KCD 129 propeller behind ECT2 under 150 mmHg vacuum at 2000 RPM (5 blades).....	191
Figure 6-38 Joint-time frequency analysis of KCD 65 propeller behind ECT2 under 150 mmHg vacuum at 2000 RPM.....	192



Figure 6-39 Joint-time frequency analysis of KCD 74 propeller behind ECT1 under 150 mmHg vacuum at 2000 RPM. ....	193
Figure 6-40 Joint-time frequency analysis of KCD 65 propeller behind ECT1 under 150 mmHg vacuum at 2000 RPM. ....	194
Figure 6-41 Joint-time frequency analysis of KCD 191 propeller behind ECT1 under atmospheric condition at 1750 RPM. ....	195
Figure 6-42 Representative sketch of a three layer feedforward ANN (reproduced from (Basheer & Hajmeer, 2000)). ....	197
Figure 6-43 Defined model scale total noise prediction parameters for the ANN. ....	199
Figure 6-44 Flow chart of the prediction tool using ANN. ....	201
Figure 6-45 The MSE surface plot of the two hidden layer ANN for total noise levels. ....	202
Figure 6-46 MSE plot of the one hidden layer ANN for total noise levels. ....	202
Figure 6-47. Artificial Neural Network training window of the MATLAB toolbox - Neural Network fitting with 46 hidden layer neurons for noise prediction. ....	203
Figure 6-48 The statistical justification of the trained ANN for the prediction of total noise levels. ....	204
Figure 6-49 The MSE surface plot of the two hidden layer ANN for background noise levels. ....	205
Figure 6-50 MSE plot of the one hidden layer ANN for background noise levels. ....	206
Figure 6-51 The statistical justification of the trained ANN for background noise level prediction. ....	207
Figure 6-52 Propeller cavitation noise prediction method user interface. ....	208
Figure 6-53 Executable cavitation noise prediction tool properties. ....	209
Figure 6-54 The noise prediction based on the given input data. ....	210
Figure 6-55 Original (left) and digitised (right) axial wake data of “Sein-Mar”. ....	212
Figure 6-56 Full-scale measurements of the “Sein-Mar” HSPII and CP propeller at 163 RPM. ....	215
Figure 6-57 Full-scale cavitation sketches of the “Sein-Mar” HSPII and CP propeller at 163 RPM. ....	216
Figure 6-58 Comparison of the Full-scale and ECT_CAV_NOISE predictions of the “Sein-Mar” HSPII at 163 RPM. ....	217
Figure 6-59 Comparison of the Full-scale and ECT_CAV_NOISE predictions of the “Sein-Mar” CP propeller at 163 RPM. ....	218
Figure 6-60 Original and digitized wake data of “M/T Olympus” ....	219
Figure 6-61 Full-scale cavitation observations from model test of the “M/T Olympus” for trial condition LC1 and LC5. ....	222

Figure 6-62 Comparison of full-scale RNLs with the predictions from ECT\_CAV\_NOISE cavitation noise prediction tool for “M/T Olympus” for trial condition LC1 (design pitch setting)..... 223

Figure 6-63 Comparison of full-scale RNLs with the predictions from ECT\_CAV\_NOISE cavitation noise prediction tool for “M/T Olympus” for trial condition LC5 (off-design pitch setting)..... 224

# List of Tables

Table 2-1 Frequency limits for octave bands and 1/3-Octave bands. ....	17
Table 2-2 Underwater noise sources for ships (Reproduced from (ITTC, 2014))......	22
Table 3-1 Emerson Cavitation Tunnel specifications.....	58
Table 3-2 Main particulars of “The Princess Royal” as built.....	59
Table 3-3 Propeller, engine and gearbox particulars of “The Princess Royal”.....	59
Table 3-4 Details about the Stereoscopic PIV.....	61
Table 3-5 Technical details of the LDA system. ....	65
Table 3-6: Camera Specifications.....	75
Table 3-7 Components of DAQ System.....	81
Table 3-8 Full-scale Pressure sensors specification. ....	83
Table 3-9 Model-scale Measurement Specialities model Pressure sensors specification. ....	83
Table 3-10 Model-scale Kulite Pressure sensors specification. ....	83
Table 4-1 A summary of test conditions. ....	93
Table 4-2 Cavitation inception and desinence points of propeller model at varying inclination angles and cavitation numbers.....	99
Table 5-1 Full-scale vessel and dummy-hull model particulars.....	119
Table 5-2: Full-scale propeller and model propeller particulars .....	120
Table 5-3 : Selected full-scale test conditions and relevant data for “The Princess Royal”. .	124
Table 5-4 : A summary of cavitation tunnel test conditions.....	125
Table 5-5 Offset of hydrophone location in the tunnel. ....	134
Table 6-1 Fixed pitch, non-ducted propeller series (Reproduced from (Carlton, 2012))......	151
Table 6-2 Significant wake parameters for wake distributions selected. ....	156
Table 6-3 Offset of hydrophone location used during tests in ECT.....	158
Table 6-4 Commercially representative small subset test matrix.....	166
Table 6-5 Propeller design parameters of the chosen standard series subset. ....	172
Table 6-6 Extended subset of Meridian series test matrix.....	174
Table 6-7 Main particulars and an image of “Sein-Maru”. ....	212
Table 6-8 Main particulars of Sein-Maru’s conventional and highly skewed propeller. ....	213
Table 6-9 The input table for ECT_CAV_NOISE cavitation noise prediction tool for “Sein-Maru”.....	214
Table 6-10 Main particulars and an image of “M/T Olympus”. ....	219
Table 6-11 “M/T Olympus” Propeller details. ....	220
Table 6-12 Input table for ECT_CAV_NOISE for “M/T Olympus”. ....	221



# Nomenclature

<u>Item</u>	<u>Description</u>	<u>Units</u>
$L_{oa}$	<i>Length overall</i>	<i>m</i>
$L_{wl}$	<i>Waterline Length</i>	<i>m</i>
$B$	<i>Breadth</i>	<i>m</i>
$B_{wl}$	<i>Waterline Breadth</i>	<i>m</i>
$V$	<i>Speed</i>	<i>knots or m/s</i>
$\Delta$	<i>Displacement</i>	<i>t</i>
$T$	<i>Draft</i>	<i>m</i>
$\rho$	<i>Water density</i>	<i>kg/m<sup>3</sup></i>
$g$	<i>Gravitational acceleration</i>	<i>m/s<sup>2</sup></i>
$h$	<i>Water Depth</i>	<i>m</i>
$V$	<i>Speed</i>	<i>m/s</i>
$V_r$	<i>Water velocity relative to propeller's blade</i>	<i>m/s</i>
$V_a$	<i>Advance velocity</i>	<i>m/s</i>
$r$	<i>Distance between two points</i>	<i>m</i>
$n$	<i>Propeller revolution speed</i>	<i>rps</i>
$D$	<i>Propeller Diameter</i>	<i>m</i>
$P_{atm}$	<i>Atmospheric Pressure</i>	<i>Pa</i>
$P_v$	<i>Vapour Pressure</i>	<i>Pa</i>
$\sigma$	<i>Cavitation Number</i>	<i>non-dimensional</i>
$J$	<i>Advance Coefficient</i>	<i>non-dimensional</i>
$\lambda$	<i>scale factor</i>	<i>non-dimensional</i>
$CPA$	<i>The closest point of approach</i>	<i>m</i>
$SPL$	<i>Sound Pressure Level</i>	<i>dB</i>
$t$	<i>Temperature</i>	<i>°C</i>
$c$	<i>Speed of sound</i>	<i>m/s</i>
$f$	<i>Wave frequency</i>	<i>Hz</i>
$dB$	<i>Decibel</i>	<i>non-dimensional</i>
$P_0$	<i>underwater reference pressure</i>	<i>1 μPa</i>
$P$	<i>Pressure</i>	<i>Pa</i>
$C_p$	<i>Pressure coefficient</i>	<i>non-dimensional</i>
$C_{pmin}$	<i>Minimum value of pressure coefficient</i>	<i>non-dimensional</i>
$P_{st}$	<i>Static pressure at a reference point on propeller blade</i>	<i>Pa</i>
$P_M$	<i>local pressure</i>	<i>Pa</i>

$\sigma_i$	<i>cavitation inception number</i>	<i>non-dimensional</i>
$P_{min}$	<i>minimum pressure</i>	<i>Pa</i>
$Re$	<i>Reynolds Number</i>	<i>non-dimensional</i>
$L$	<i>Length</i>	<i>m</i>
$B$	<i>Breadth</i>	<i>m</i>
$H$	<i>Height</i>	<i>m</i>
$Q$	<i>Torque</i>	<i>Nm</i>
$Q_m$	<i>Measured torque</i>	<i>Nm</i>
$q_0$	<i>Idle torque</i>	<i>Nm</i>
$K_Q$	<i>Torque Coefficient</i>	<i>non-dimensional</i>
$T_S$	<i>Thrust due to static pressure head</i>	<i>N</i>
$H_{ST}$	<i>Static Head</i>	<i>m</i>
$T_D$	<i>Thrust due to boss drag</i>	<i>N</i>
$T_{Cor}$	<i>Corrected Thrust</i>	<i>N</i>
$K_T$	<i>Thrust coefficient</i>	<i>non-dimensional</i>
$T$	<i>Thrust</i>	<i>N</i>
$C_{0.7R}$	<i>0.7 Radius Chord Length</i>	<i>m</i>
$\nu$	<i>Kinematic Viscosity</i>	<i>m<sup>2</sup>/s</i>
$\sigma_V$	<i>Free Stream Cavitation Number</i>	<i>non-dimensional</i>
$h_s$	<i>Propeller Shaft depth</i>	<i>m</i>
$\sigma_n$	<i>Rotational Cavitation Number</i>	<i>non-dimensional</i>
$\sigma_{vr}$	<i>Resultant Cavitation Number</i>	<i>non-dimensional</i>
$SPL$	<i>Sound Pressure Level</i>	<i>dB</i>
$\eta_0$	<i>Propeller efficiency</i>	<i>non-dimensional</i>
$W_{Max}$	<i>Maximum wake fraction</i>	<i>non-dimensional</i>
$W_\Delta$	<i>BSRA Wake Criteria (Wake non-uniformity parameter)</i>	<i>non-dimensional</i>
$\overline{W}$	<i>Mean wake</i>	<i>non-dimensional</i>
$W_{Min}$	<i>Minimum wake fraction</i>	<i>non-dimensional</i>
$K_p$	<i>Pressure Coefficient</i>	<i>non-dimensional</i>

### Abbreviations

<i>AMT</i>	<i>Advanced Measurement Technologies</i>	<i>JTFA</i>	<i>Joint Time-Frequency Analysis</i>
<i>ANN</i>	<i>Artificial Neural Network</i>	<i>ITTC</i>	<i>International Towing Tank Conference</i>
<i>ANSI</i>	<i>American National Standards Institute</i>	<i>ITU</i>	<i>Istanbul Technical University</i>
<i>B&amp;K</i>	<i>Brüel &amp; Kjaer</i>	<i>K&amp;R</i>	<i>Kempf &amp; Remmers</i>
<i>BAR</i>	<i>Blade Area Ratio</i>	<i>LAN</i>	<i>Local Area Network</i>

<i>BC</i>	<i>Before Christ</i>	<i>LDA</i>	<i>Laser Doppler Anemometry</i>
<i>BEM</i>	<i>Boundary Element Method</i>	<i>LES</i>	<i>Large Eddy Simulations</i>
<i>BMT</i>	<i>British Maritime Technology</i>	<i>MAST</i>	<i>School of Marine Science and Technology</i>
<i>BNC</i>	<i>Bayonet Neill–Concelman</i>	<i>MEPC</i>	<i>Marine Environment Protection Committee</i>
<i>BPF</i>	<i>Blade Passage Frequency</i>	<i>MSE</i>	<i>Mean Squared Error</i>
<i>BRF</i>	<i>Blade Rate Frequency</i>	<i>MSFD</i>	<i>Marine Strategy Framework Directive</i>
<i>BSRA</i>	<i>British Ship Research Association</i>	<i>NI</i>	<i>National Instruments</i>
<i>CAD</i>	<i>Computer Aided Design</i>	<i>NoE</i>	<i>Network of Excellence</i>
<i>CFD</i>	<i>Computational Fluid Dynamics</i>	<i>NWG</i>	<i>Noise Working Group</i>
<i>CoP</i>	<i>Community of Practice</i>	<i>P/D</i>	<i>Pitch to Diameter ratio</i>
<i>CPB</i>	<i>Constant Percentage Bandwidth</i>	<i>PDA</i>	<i>Phase Doppler Anemometry</i>
<i>CRS</i>	<i>Cooperative Research Ships</i>	<i>PIV</i>	<i>Particle Image Velocimetry</i>
<i>DAQ</i>	<i>Data Acquisition</i>	<i>PSD</i>	<i>Power Spectral Density</i>
<i>DNV</i>	<i>Det Norske Veritas</i>	<i>R&amp;D</i>	<i>Research and Development</i>
<i>DSLR</i>	<i>digital single-lens reflex camera</i>	<i>RANS</i>	<i>Reynolds Averaged Navier Stokes</i>
<i>EAR</i>	<i>Expanded Area Ratio</i>	<i>RNL</i>	<i>Radiated Noise Levels</i>
<i>ECT</i>	<i>Emerson Cavitation Tunnel</i>	<i>RPM</i>	<i>Round Per Minute</i>
<i>EU</i>	<i>European Union</i>	<i>rps</i>	<i>Revolution per second</i>
<i>FFT</i>	<i>Fast Fourier Transform</i>	<i>RV</i>	<i>Research Vessel</i>
<i>FP</i>	<i>Framework Programme</i>	<i>SMP</i>	<i>Stone Marine Propulsion</i>
<i>fps</i>	<i>frame per second</i>	<i>SONAR</i>	<i>SOund Navigation And Ranging</i>
<i>FW-H</i>	<i>Ffowcs Williams-Hawkings</i>	<i>SONIC</i>	<i>Suppression Of Noise Induced by Cavitation</i>
<i>Gb</i>	<i>Gigabyte</i>	<i>SPIV</i>	<i>Stereoscopic PIV</i>
<i>Gige</i>	<i>Gigabit Ethernet</i>	<i>SPL</i>	<i>Sound Pressure Level</i>
<i>HMS</i>	<i>Her Majesty's Ship</i>	<i>TTL</i>	<i>Transistor-Transistor Logic</i>
<i>HTA</i>	<i>Hydro Testing Alliance</i>	<i>TVC</i>	<i>Tip Vortex Cavitation</i>
<i>HTF</i>	<i>Hydro Testing Forum</i>	<i>TVI</i>	<i>Tip Vortex Index</i>
<i>ICES</i>	<i>International Council for the Exploration of the Sea</i>	<i>UNEW</i>	<i>Newcastle University</i>
<i>IEPE</i>	<i>Integrated Electronic Piezoelectric</i>	<i>URN</i>	<i>Underwater Radiated Noise</i>
<i>IMO</i>	<i>International Maritime Organisation</i>	<i>USB</i>	<i>Universal Serial Bus</i>
<i>IR</i>	<i>Infrared</i>	<i>WWI</i>	<i>World War I</i>
<i>ISO</i>	<i>International Standard Organization</i>	<i>WWII</i>	<i>World War II</i>
<i>JRP</i>	<i>Joint Research Project</i>		





# Chapter 1 Introduction

## 1.1 Introduction

*Chapter 1 is dedicated to setting the scene for this thesis and to provide an introduction. The chapter initially states the motivations to conduct research on prediction of propeller cavitation noise. Then, aims of this research are revealed together with the necessary objectives that need to be measured in order to achieve the stated aim. Following this, a general layout of the thesis is provided together with a summary of the chapter.*

## 1.2 Motivation

Over the past half century, the volume of commercial shipping has experienced an increasing trend due to increasing ship size, service speed and number of ships operating (Hildebrand, 2009). This trend has resulted in significant elevation of various emissions by the seagoing vessels. In order to ensure sustainable shipping, various anthropogenic impacts have been targeted by the rising environmental awareness. Whilst initial focus of international organizations was on greenhouse gas output of the maritime transportation, recently underwater noise created by commercial ships has been targeted due to its potential impact on the marine fauna. Although there is no solid evidence on how commercial shipping imposes a threat to marine fauna, ambient noise measurements indicate a potentially dangerous tendency (Frisk, 2012). The consequences of this trend within the world fleet have been observed to affect the low frequency range of ambient noise levels (10-500 Hz) which has been identified by Wenz, (1962) as the dominant frequency range of shipping noise sources. Measurements made in the Pacific Ocean indicate a 3 dB increase per decade (or 10 dB per half century) in terms of measured background noise levels as summarized in Figure 1-1 by Frisk based on the compiled historical ambient noise data (Chapman & Price, 2011; McDonald et al., 2008; Hildebrand, 2005).

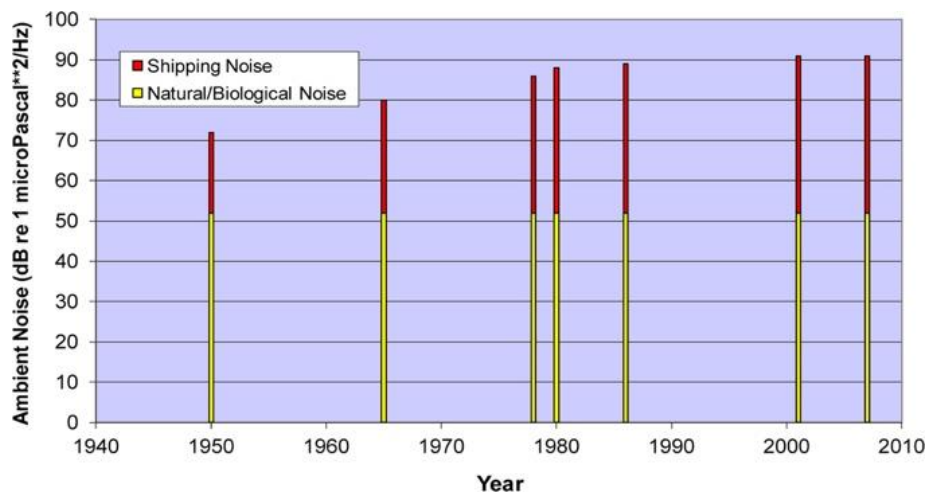


Figure 1-1 Historical ambient noise levels in 25-50 Hz indicating the increasing trend of shipping contribution (Reproduced from Frisk, 2012).

Notwithstanding this fact alone the low frequency region of the ambient noise levels inherently has a low absorption rate due to the medium through which they propagate (Fisher & Simmons, 1977). This consequently means that a single vessel may pollute large masses of water with underwater noise in the low frequency range.

Thus, combination of the aforementioned two properties of Underwater Radiated Noise (URN), namely low attenuation and increasing ambient noise levels at low frequency, does impose a potential threat to marine fauna when it is also borne in mind that the low frequency region is utilized by marine mammals for various fundamental living activities. Hence, it may be concluded that underwater noise pollution in the low frequency range may shadow the survivability of marine mammals by affecting their behaviours or causing distress (White & Pace, 2010; Richardson et al., 2013). The potential threat to marine species can be better understood if it is considered that naturally occurring ambient noise levels are thought to have remained the same for tens of centuries. Nevertheless, total ambient noise is now starting to see a significant rise within time periods of decades. Thus, it may be concluded that it is nearly impossible for such living organisms to adapt to such a violent change in their environment with a swift response. Therefore, if no regulatory precaution is taken to limit shipping noise, exposing them to such an abrupt change in the ambient noise levels may disorient marine mammals or disrupt their communication, leading to behavioural changes of these mammals or local extinction (Figure 1-2).

## 1.2 Motivation

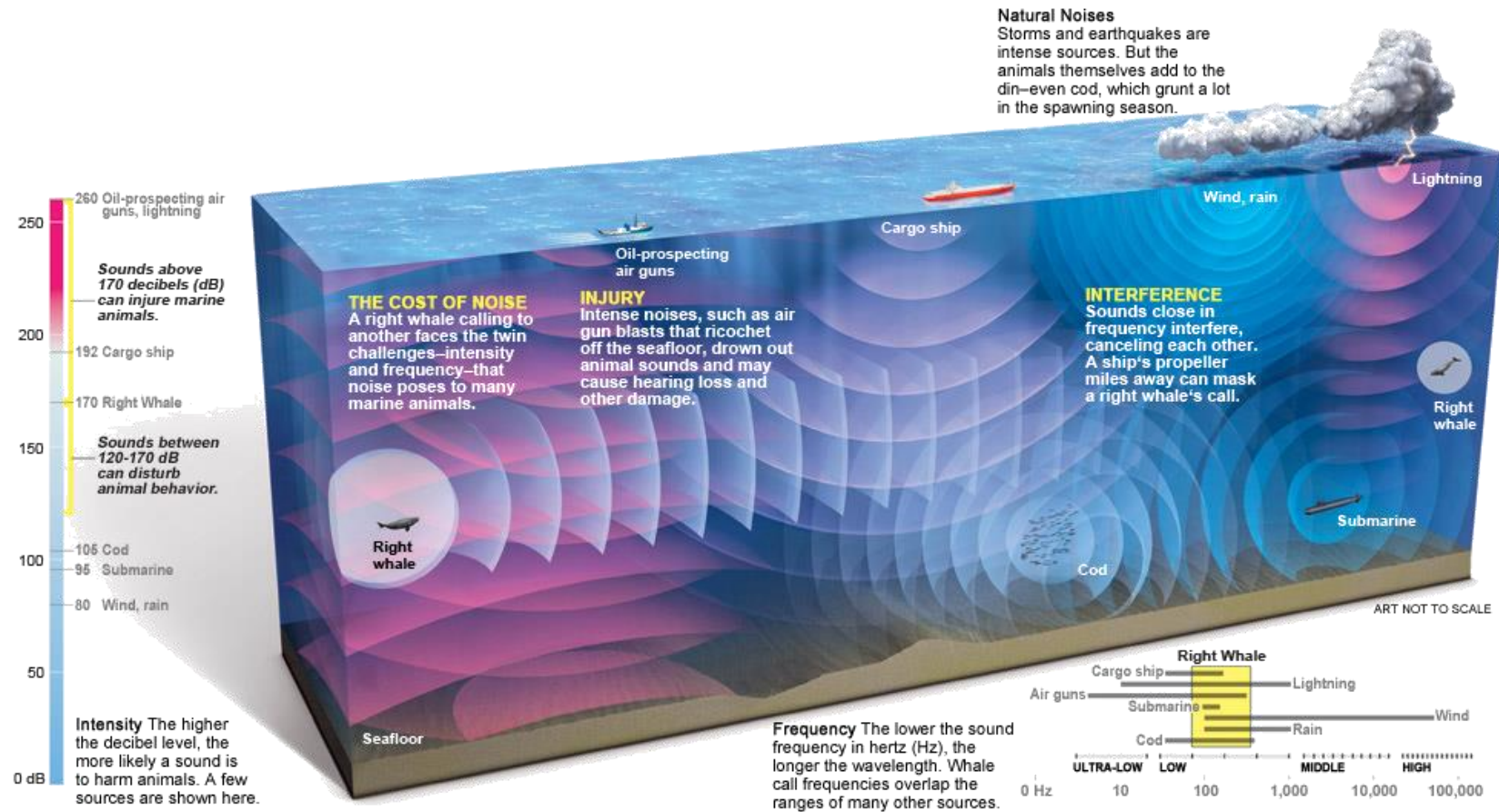


Figure 1-2 Impact of Anthropogenic noise on marine mammals (Reproduced from National Geographic Magazine, 2011).

Originating from these concerns international organizations and committees, such as the International Maritime Organization (IMO) and the Marine Environmental Protection Committee (MEPC) (IMO, 2011, 2013) have made calls and initiated activities to study the URN from commercial shipping to help in the development of potential guidelines and regulations. Moreover, the EU has established the Marine Strategy Framework Directive (MSFD) to investigate and implement programmes of measures which are designed to achieve or maintain ‘Good Environmental Status’ in the marine environment (Van der Graaf et al., 2012).

In complementing the European R&D activities on the subject of URN from commercial shipping, several collaborative European R&D projects were completed recently (e.g. SILENV, AQUO, SONIC) under the 7<sup>th</sup> Framework Programme (FP) of EU. Amongst them, SONIC (Suppression Of Noise Induced by Cavitation) has brought together 12 world-leading hydrodynamic institutes, noise experts, propeller designers, universities, European shipyards and marine biologists to develop guidelines to assist in regulating the underwater noise emitted by shipping (SONIC, 2012). In complementing the above activities Joint Research Programme (JRP)10, which was called “Noise Measurements”, was established within the Hydro Testing Alliance-Network of Excellence (HTA-NoE) and which successfully completed its mission in 2011 (AMT 2011). The members of JRP10 decided to form a working group to investigate underwater radiated noise issues further. This working group, which was initially named “Noise Working Group” (NWG), later has become “Noise Community of Practice (Noise CoP)” of Hydro Testing Forum (HTF) as a longer continuation of the HTA-NoE, which was phased out by then (AMT 2013).

Shipping noise originates from various sources on board a vessel. At low ship speeds, on-board machinery noise is dominant until propeller cavitation occurs, which then dominates the overall radiated noise spectrum (Ross, 1976). Above inception, well-developed cavitation may occur on the propeller, contributing a significant increase in noise levels that may occur across the entire frequency band of the URN spectrum (Arveson & Vendittis, 2000; Abrahamsen, 2012); such cavitation noise tends to overshadow the other contributing sources and dominates the overall URN spectra (Fischer & Brown, 2005). Whilst it is not possible to avoid cavitation at

service speed conditions for efficient commercial ships, various full-scale URN measurements have shown room for improvement. Among the same type of vessels, full-scale measurements have shown up to 20 dB difference in the measured noise levels (McKenna et. Al., 2012; MCR, 2011; Wales & Heitmeyer, 2002). This may suggest that current practices in ship design can be further scrutinized in terms of the URN characteristics of the ships and hence may lead to minimizing the impact on ever-increasing ambient noise levels in the world's oceans (Renilson, 2009; Chekab et al., 2013).

In order to address the above concerns, a reliable and accurate prediction of URN at an early design stage of ships is essential. The current state of the art methods for the URN predictions utilize experimental methods based mainly on cavitation tunnels; semi-empirical methods based on statistical databases; and Computational Fluid Dynamics (CFD) methods with significant simplifications. Although computational power has been increasing at an exponential pace, URN prediction using the CFD method is in its infancy and requires coupling of as many as five different codes as reported e.g. in (van Wijngaarden, 2005). Currently, CFD based noise predictions are made using incompressible Reynolds Averaged Navier Stokes (RANS) equations coupled with the Ffowcs Williams-Hawkings (FW-H) equation. These have made physics-based URN predictions possible, however, further developments are necessary in order to improve the accuracy of the predictions as well as the cost of the computational resources (Bertschneider et al., 2014). Semi-empirical methods are based on a number of different approaches; some being developed based on data from the World War II period, others constructed upon the theoretical acoustic pressure of a single cavitation bubble collapse multiplication for statistically determined cavitation events. These early methods over-predict the measured URN levels of present-day commercial ships (Okamura & Asano, 1988) due to developments in the field of propeller design (Ross, 1976; Brown, 1976) and testing. More recently-introduced semi-empirical methods are commercially confidential, being based on simple models for which various coefficients have been derived from large databases of full-scale noise measurements (e.g. Raestad, 1996). By considering the additional complexities associated with the numerical modelling of the propeller cavitation, perhaps, the most reliable current prediction method may be that based on experimental methods (Bertschneider et al., 2014) by which much of the essential physics of the cavitation phenomena are well represented.

Despite the relative success of the experimental techniques, outside the research vessel and naval communities, which are inherently confidential research, publicly available information is scarce for both full-scale URN levels and cavitation tunnel based predictions. Furthermore, such data, which are publicly available, are either unsatisfactory due to lack of information on the main particulars of the subject vessels and their operating conditions and/or measurement techniques and methods used to collect the data (Bark, 1985). Allied with this unfavourable status the complementary information, which can enhance the understanding of the noise emitting mechanisms such as cavitation observations, pressure pulse measurements, is even more scarce thus creating a significant gap in the current state of the art.

Moreover, modern propeller design is conducted in stages and includes both in-house databases and sophisticated computational tools. The latter design stages make use of computational methods (e.g. lifting line, lifting surface (Oosterveld & Van Oossanen, 1975; Lee, 1979)). In the initial stage, selection of the main design parameters (e.g. optimum diameter, pitch, blade area ratio) for propulsive efficiency, is still made using systematic propeller series databases due to their reliability (e.g. Wageningen B-Series, Meridian Series etc. (Burrill & Emerson, 1962; Emerson & Sinclair, 1978; Troost, 1938)). Such propeller series data mainly present the basic propeller performance coefficients (i.e.  $K_T$ ,  $K_Q$  and hence  $\eta_o$ ). This information has been complemented further by experiment based cavitation diagrams (e.g. Burrill's chart and the SSPA erosion criterion) to give a preliminary indication for the risk of thrust breakdown and cavitation erosion as well as the extent of particular types of cavitation over the blades in a systematic manner. Also in the 1980's, empirical methods were derived from full-scale data for predicting hull pressures at blade and twice blade passing frequency (Sontvedt & Frivold, 1976), based on simple descriptions of blade designs and wake characteristics. Within the same initial design framework, however, noise predictions are largely limited to empirical methods such as Brown (1976) and Raestad (1996). There seems to be no information or at least any attempt to complement systematic propeller series databases with the noise characteristics of any standard propeller series. Such a tool could be useful in preliminary design or as a control parameter in addressing the increasing concerns for increased levels of URN.

Whilst standard series of propellers are traditionally tested in uniform flow conditions due to the insignificant effect of wake inflow in terms of the efficiency coefficients, the main noise producing mechanism during the operation of a marine propeller is cavitation volume variation

caused by the presence of the hull in front. Thus, implementation of a novel systematic variation of wake inflow is not attempted by any study, which can provide an attractive design information to propeller designer for URN prediction in early design stage for practical investigation purposes.

Within the above framework, there has been a recent surge of worldwide interest to the subject of URN. As a natural response to this surge, Newcastle University has been in the forefront of the collaborative R&D activities (e.g. through FP7 SONIC Project, HTF Noise CoP) by taking advantage of their complementary experimental facilities (i.e. the Emerson Cavitation Tunnel, RV “The Princess Royal”) and accumulated knowledge in the field. These have provided the essential thrust to motivate the Author to set the aim of his research involving the subject of URN as a graduate of Newcastle University. This would also complement the Author’s personal curiosity on the subject as a young naval cadet trained on a mine sweeper with optimised noise signature qualities which always intrigued him.

### **1.3 Aims and Objectives**

Various national authorities worldwide have concluded that cavitation noise may impose a threat to the marine fauna if the current trend of the commercial shipping is not regulated. Yet, current state of the art is not able to address the knowledge gap due to the limited, non-proprietary data and research available in the URN field that would enable a better understanding of the ship and propeller design phenomena leading to quiet, efficient ships.

Thus, the main aim of the present research is to enhance the understanding of the propeller cavitation noise by conducting detailed systematic cavitation tunnel tests in order to investigate the main propeller design parameters and operating conditions and to scrutinize their impact on propeller Radiated Noise Levels (RNL). The resulting experimental data are also utilized to

compile a database that enables engineering noise prediction methods to be developed and used at a preliminary design stage, together with a standard series approach.

The above aim is achieved through a systematic series of experiments. The first experimental study considered the effect of shaft inclination on cavitation noise by conducting systematic cavitation tunnel tests. These tests also served to reveal potential areas where noise measurement accuracy could be improved as well as providing training for cavitation tunnel operation. Following this, full-scale trials were conducted on-board the Newcastle research vessel to enhance understanding of cavitation phenomena at ship scale. Cavitation observations were made and hull pressures were measured. Differences between ship and model results were also studied through cavitation tunnel tests using scaled models of the hull and propeller to evaluate and confirm the cavitation noise prediction capabilities of the experimental approach adopted in this thesis.

Furthermore, a small, but commercially representative, subset of the Meridian standard series of propeller models were tested in the Emerson Cavitation Tunnel (ECT) behind different severities of axial wake created using two-dimensional wake screens. Based on the measured noise data the results were extrapolated to full-scale using an available in-house database for some real commercial vessels with the similar main particulars to the standard series of propellers. The extrapolated data was compared with the average commercial shipping noise data (Wales & Heitmeyer, 2002) to make a rough validation of the generated noise data in order to address any uncertainty due to the small scale factor of the research vessel, tunnel experiments and utilization of the wake screen.

Finally, a larger subset of the Meridian propeller series were chosen to cover a significant range of propeller design parameters from the noise radiation point of view; including pitch to diameter ratio, blade area ratio, number of blades and operating conditions. This subset was tested using a similar approach to the commercially representative propeller subset experiments but



using more members of the series in a systematic manner. The approach enabled compilation of a quantitative database supported by an artificial neural network tool to predict URN. The produced systematic data also provided further insight into the noise-creating mechanisms of cavitation dynamics by analysis of the synchronised cavitation observations and pressure pulse measurements.

The aforementioned research study, which leads to the achievement of the aim of the thesis, has been conducted to meet the following specific and measurable objectives of the research study presented in this thesis:

1. To make a critical review of the state of the art on propeller cavitation noise to identify the gaps, especially seeking to make a contribution in cavitation noise prediction at early stage of propeller design.
2. To design and conduct systematic cavitation tunnel tests with a special focus on the effect of the shaft inclination on the RNL of a model propeller as well as cavitation inception. Also, to obtain a better understanding of the nature of systematic cavitation tests and tunnel operation training.
3. To conduct full-scale trials on-board a research vessel to provide URN data and to enhance the understanding of the phenomena by making cavitation observations and measuring pressure pulses as well as relating these data to the measured URN from the same vessel. The full-scale trials are further complemented by the simulation of the trial conditions in cavitation tunnel by use of a scaled-model.
4. To provide dedicated propeller cavitation noise data in model and full-scale to be able to scrutinise experimental methods to predict full-scale noise data using medium-size cavitation tunnels.
5. To investigate the feasibility of a systematic series approach to predict the cavitation induced URN of commercial vessels. To demonstrate and validate the approach by conducting preliminary systematic cavitation tunnel tests using a small but commercially representative subset of a standard propeller series with loadings based on in-service vessels and operating in different grades of wake non-uniformity.

6. To conduct systematic cavitation tunnel tests with a larger subset of standard series to establish the standard series approach and associated tool to predict the cavitation induced URN and to validate the capability of the developed tool.
7. To implement an advanced data analysis tool by making use of the synchronized pressure pulses, cavitation images and URN data. Using this tool and the systematic data produced with the series members investigate the effects of some major propeller design and operational parameters on the URN as well as the effect of cavitation dynamics.

## 1.4 Layout of the Thesis

The thesis is presented in seven chapters. Chapter 1 specifies the motivations for conducting research into far-field propeller noise and in setting the aims and objectives of the study as well as describing the layout of the thesis.

In Chapter 2, a critical review of the literature is made, and gaps in the state of the art are given in order to justify the study. Background information is provided for URN mainly in terms of the fundamental acoustics. Due to the multi-disciplinary nature of the study, this chapter covers both acoustical and hydrodynamic aspects. It looks into the acoustic analogy of the hydrodynamic phenomena, with a specific focus on the current state of underwater noise prediction methods and systematically designed experimental propeller tests focussing on propeller cavitation noise.

Chapter 3 presents the experimental facilities and equipment utilized within the framework of this study. An overview of the full-scale research vessel and model scale facility is initially given. This is followed by the various key pieces of equipment used during the experiments. The analysing methodology and the set-up information are provided within the section for the equipment inventory.

Chapter 4 presents the systematic cavitation tunnel tests looking into the effect of oblique flow on the propeller and discusses the cavitation observations, cavitation inception, noise and propeller performance parameters to reveal the impact of the inclined shaft effect.

Chapter 5 compares the measurements made on the full-scale research vessel with data from the corresponding dummy model tests in the Emerson Cavitation Tunnel which can be categorized as a medium size cavitation tunnel, to validate the prediction methods for the cavitation extent, noise and induced pressures.

Chapter 6 has two parts. The first part investigates the feasibility of establishing a cavitation induced URN prediction methodology based on a standard series approach by using a commercially representative small subset of the Meridian standard propeller series. Having demonstrated its viability the second part presents the further establishment of the methodology by conducting systematic cavitation tunnel tests with the extended subset Meridian standard series. An artificial neural network based URN predictor is developed and tested on two full-scale case studies. In the same chapter, an advanced data analysis tool is implemented by making use of the synchronized time-series pressure pulses, cavitation images and the frequency domain URN data. Using this tool and the systematic data produced with the series members the effects of some major propeller design parameters and operational conditions on the URN are investigated as well as the effect of cavitation dynamics.

Finally, chapter 7 presents conclusions drawn from the thesis together with the recommendations for the future work.

## **1.5 Summary**

Chapter 1 provided an introduction to the thesis by first setting the scene with the motivations for the research conducted in the thesis. Following this, the aims for conducting such a research is given together with the necessary objectives that lead to the accomplishment of the set aim. Finally, a layout of the thesis is provided to guide readers through the thesis.

## Chapter 2 Literature Review

### 2.1 Introduction

*Chapter 2 contains a critical review of the state of the art related to URN. The literature review is used to explain and justify the experimental approach adopted in this work. Emphasis is placed on the prediction methods for induced noise from propeller cavitation, to create a better understanding of their nature and how they have been developed. Initially, the scene is set with the history and fundamentals of underwater acoustics. Then, the impact of shipping noise is presented together with various other anthropogenic sources. Following this, various methods employed in cavitation noise prediction are reviewed. These include developed cavitation noise predictions methods, those based on computational fluid dynamics and experimental propeller noise prediction methods. Then, systematic propeller tests that are conducted to tests major operational propeller parameters are visited. Moreover, the simplest variation of a propeller operation is investigated by looking into the aspects of shaft inclination together with a review of Artificial Neural Network as a tool for systematic database management. The ultimate aim of the chapter is to rationalize the adopted experimental approach by critically reviewing the state of the art of prediction methods as well as to locate gaps in the current state of the knowledge.*

### 2.2 History of underwater sound

Aristotle (384–322 BC) was one of the first to note that sound can be heard in water as well as in air. It was nearly 2000 years later when Leonardo da Vinci (1452-1519) mentioned underwater sound in his notes (1490), indicating a potential use of this phenomenon.

*“If you cause your ship to stop and place the head of a long tube in the water and place the outer extremity to your ear, you will hear ships at a distance from you.”*

It was another 200 years, during which numerous breakthroughs occurred (such as the laws of vibrating strings by Marin Mersenne and Galileo in 1620's and Sir Isaac Newton's mathematical theory (1687) on how sound travels), before the first underwater sound experiment became possible. Abbé J. A. Nollet, in 1743 conducted a number of experiments to prove the propagation of sound underwater with an experimental setup as shown in Figure 2-1 (Bjørnø & Bjørnø, 1999).

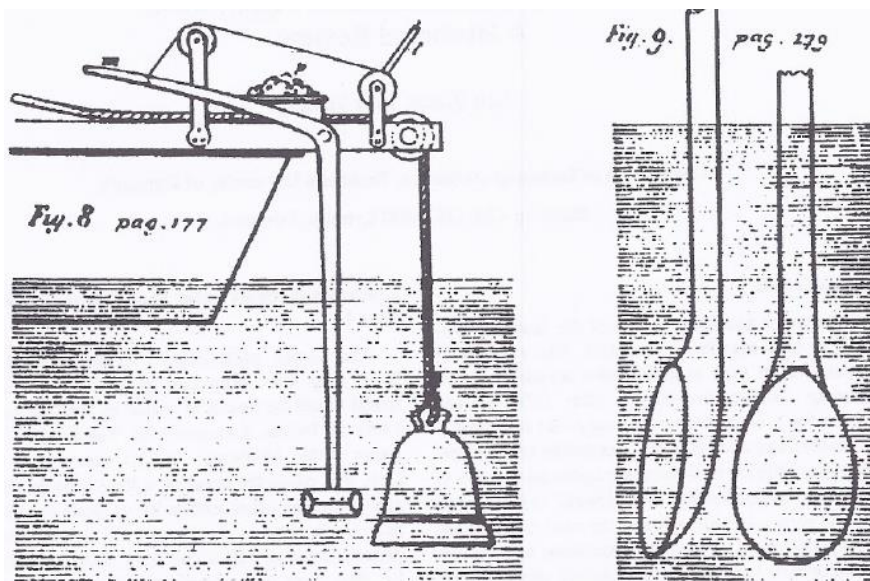


Figure 2-1 The sketches for the experiments to prove sound propagation through water (Reproduced from (Bjørnø & Bjørnø, 1999)).

Following the proof that sound travels through water, the potential to detect enemy presence from miles away using underwater acoustic devices, as previously quoted by Leonardo da Vinci, resulted in a surge of interest in underwater noise during WWI. This significantly affected naval warfare and was thus studied extensively by naval research offices. Unfortunately, due to the inherent nature of naval warfare, such research was not available to the civil community. Following this interest in underwater noise from marine vehicles increased again due to the usage of acoustic devices for various research purposes such as seismic survey and fisheries research vessels. This time, the interest focused on reducing vessel noise with the aim of minimizing the disturbance to the measurement device, to increase the accuracy of results. However, it was not until recently that rising environmental awareness focused on underwater radiated shipping noise due to its adverse impacts on marine life (IMO, 2011, 2007).

## 2.3 Background

The emphasis on underwater acoustics necessitated knowledge of the fundamentals of the subject. The multi-disciplinary nature of the subject requires both advanced knowledge in the fields of acoustics as well as marine hydrodynamics in order to enable interpretation of the hydrodynamic phenomena and to link these to the acoustic response.

Within this framework, the following sections are structured to initially review and provide necessary fundamental knowledge on underwater acoustics. Following the fundamental acoustics, the anthropogenic noise sources, that are present, are reviewed and their relative impact on marine fauna is evaluated. As one of the major noise sources, propellers and propeller design is further scrutinized. Propeller design methodologies are first presented, followed by the cavitation as the dominant noise source during the operation of a propeller. As cavitation is unavoidable during the normal service conditions of an efficient commercial vessel, various kinds of cavitation and their noise signatures are discussed. Finally, various propeller noise prediction methods are critically reviewed in chronological order, together with more recent computational and experimental approaches, in order to evaluate the best possible and practical approach to be adopted for the execution of the experimental approach intended for this research.

## 2.4 Fundamental acoustics

The term noise is generally referred to as the unwanted sound that is produced during the operation of a system that interferes with the normal functioning of it. Although noise is defined as unwanted, it is unavoidable at the same time as no mechanical process can take place without any losses. The losses occur during the motion induced by the process, producing various by-products that reduce the system efficiency, such as heat, vibration, friction, etc. (Ross, 1976). It, however, constitutes a relatively smaller amount of power in comparison with the total mechanical power produced with even lower levels for underwater systems. Nevertheless, acoustical properties in water are significantly different than in air, and hence, result in various consequences such as higher speed within the medium and lower absorption rate, which will be discussed in detail in the following subsection.

Acoustic measurements are expressed using the unit of “decibel”, which is a description of a logarithmic ratio of an actual measurement and a predefined reference value (Hildebrand, 2009). The origin of the use of the decibel is from the electrical industry and is named after the inventor of the telephone, Alexander Graham Bell. In order to avoid fractional values, the unit bell is defined as ten times the bell and named as the decibel with the abbreviation of ‘dB’. The use of the decibel unit simplifies the understanding of the large variations experienced in the measurements. The use of the decibel scale, since then, has widened from its original application to become a basis for the measurement of different quantities with dynamic range. In the context of assessing noise, the sound pressure level (SPL) is the fundamental measure of sound pressure and its definition is based on pressure ratios as given by the International Standard Organization (ISO) (ISO, 2015):

$$SPL = 20\log_{10}(P/P_0)dB \quad \text{Equation 1}$$

where;  $P_0$  is a reference pressure normally set to  $1 \mu Pa$  for water and  $P$  is the measured pressure at the point of interest.

The use of the decibel unit dictates a scaling to the measured levels. Due to the inherent properties of the logarithmic operator, a 6 dB difference between two measurements means the higher pressure measurement is two times, the lower pressure measurement. Likewise, a 12 dB difference corresponds to the higher measurement being four times, the lower measurement.

Another important aspect of acoustical measurements is the spectral domain. As the time signals of the noise measurements are rather complex for interpretation, various signal manipulation methods are employed to be able to convert the time signal to a frequency or spectral domain. For this purpose, Fast Fourier Transform (FFT) methods or wavelet methods are employed. The application of the post-processing approach to the measured time signal transforms the measurement to the spectral domain where results are displayed as a function of frequency. In the spectral domain, the noise may be either presented as a level in a 1Hz band, for which all bands are equally 1 Hz wide, or it can be split into a series of adjacent frequency bands based on a constant ratio of upper and lower frequency. For the proportional bandwidths, the power spectral density of the spectrum is averaged from the upper to the lower band edge frequency to calculate the spectral level at the centre frequency for the chosen bandwidth. The most common underwater acoustic constant bandwidth frequency band is the octave band.

The octave bands are defined as the ratio of the upper and lower frequency band based on the power of 2. Therefore, an “octave” band means the upper frequency is twice the lower frequency, whereas a “1/3<sup>rd</sup>-octave” band further subdivides each octave band into three parts as shown in Table 2-1. Thus, octave filters do not have an absolute constant bandwidth but do have a constant relative bandwidth that increases logarithmically with the increasing frequency.

Table 2-1 Frequency limits for octave bands and 1/3-Octave bands.

Frequency (Hz)					
Octave Bands			1/3 Octave Bands		
Lower Band Limit	Centre Frequency	Upper Band Limit	Lower Band Limit	Centre Frequency	Upper Band Limit
11	16	22	14.1	16	17.8
			17.8	20	22.4
			22.4	25	28.2
22	31.5	44	28.2	31.5	35.5
			35.5	40	44.7
			44.7	50	56.2
44	63	88	56.2	63	70.8
			70.8	80	89.1
			89.1	100	112
88	125	177	112	125	141
			141	160	178
			178	200	224
177	250	355	224	250	282
			282	315	355
			355	400	447
355	500	710	447	500	562
			562	630	708
			708	800	891
710	1000	1420	891	1000	1122
			1122	1250	1413
			1413	1600	1778
1420	2000	2840	1778	2000	2239
			2239	2500	2818
			2818	3150	3548
2840	4000	5680	3548	4000	4467
			4467	5000	5623
			5623	6300	7079



Narrow-band analysis results are used for the close-up investigation of spectral levels to locate and confirm noise producing events at discrete frequencies. On the other hand octave and third-octave band levels are used for interpretation of the general trend of the spectral levels. The use of such bands are clearly demonstrated by McKenna et al. (2012).

### 2.4.1 Underwater sound propagation

The attenuation properties of sound underwater also carry great importance with regards to the significance of the subject. Not only does sound travel approximately 4.4 times faster underwater (Lovett, 1978), but also the associated propagation losses are significantly lower mainly due to the well-known wavelength equation. A higher propagation speed results in a greater acoustic wavelength, as by definition, wavelength is given by Equation 2:

$$\lambda = \frac{c}{f} \quad \text{Equation 2}$$

where  $\lambda$  is wavelength in m,  $c$  is speed of sound in m/s and  $f$  is the wave frequency in Hz.

Furthermore, since the wavelength is a function of the frequency, the lower frequencies inherently have a longer wavelength. Since the physics enable higher attenuation efficiency of the sound with longer wavelength, this results in significantly lower absorption rate for the low frequency sound enabling it to travel hundreds of miles (Urlick, 1983). A very detailed study has been carried out by Fisher and Simmons looking at the mechanisms of sound absorption (Fisher & Simmons, 1977; Francois & Garrison, 1982).

Due to the changing nature of sound absorption with frequency, the sound spectrum may be divided into 3 frequency bands: 10 to 500 Hz for low frequency, 500 to 2500 Hz for medium frequency and values higher than 2.5 kHz for high frequency. It can be concluded that a low frequency underwater noise may pollute large masses of world seas due to the inherent low absorption properties, whereas medium frequency noises are generally associated with rather regional sources and for high frequency the source may be in close proximity (Hildebrand, 2009).

There are other factors affecting the sound absorption such as the depth of the sea, the reflection from the sea surface also known as the Lloyd's Mirror effect and seabed type (Bell, 2008; Wittekind, 2014; Simmonds et al., 1997). These also significantly influence the attenuation properties and requires necessary attention for the acoustic measurements.

### 2.4.2 Ambient noise sources

In order to be able to process the underwater noise measurement data for vessels, detailed knowledge about the various other sources present within the underwater environment is vital. The information on the possible contributors to the raw noise measurements enables the accurate interpretation of the sound of interest. Ambient noise level spectra of the world seas are dominated by a number of factors that each applies to a particular frequency region (Gotz et al., 2009). Amongst them are turbulent pressure fluctuations, wind-dependent noise from bubble, spray and resulting surface agitation and shipping noise (Wenz, 1962; Cato, 2008). Whilst there are other intermittent and instantaneous sources also present, the main components can be confined to these three components in the context of ambient noise; they are illustrated in the frequency domain as shown in Figure 2-2 (Wenz, 1972).

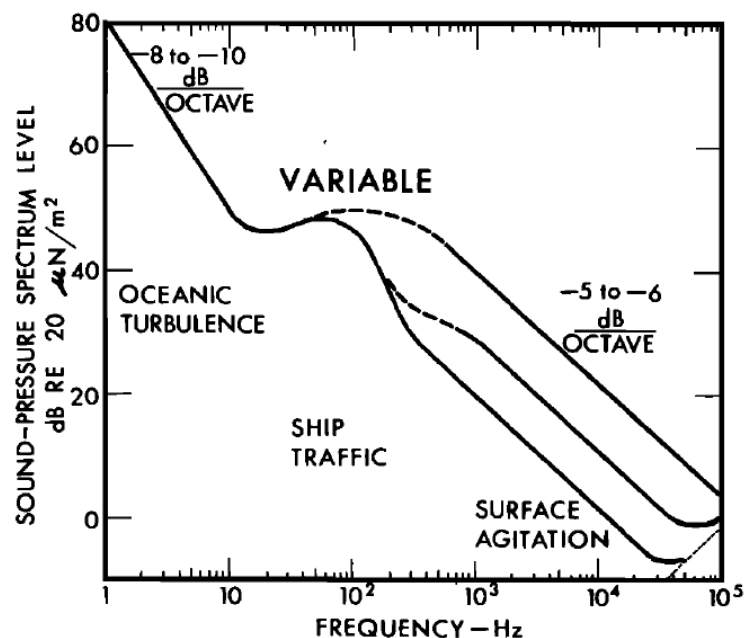


Figure 2-2 Sample Ambient noise spectra (reproduced from Wenz, 1972)

The overall ambient noise spectrum is therefore dominated by large-scale oceanic turbulence up to 20 Hz with small contributions from storms at a remote location and seismic events. The frequency region of 500 Hz to 25 kHz shows a trend of 5 to 6 dB decrease per octave and is mainly related to sea state and associated causes such as the wind, rain and wave. The third band of 10 to 500 Hz region is dominated by distant shipping noise (Wenz, 1972) related to various on- and off-board noise sources (Ross, 2005).

## **2.5 Shipping noise**

The anthropogenic activities with the world seas are many and varying, ranging from seismic surveys to piling, sonar exploration and commercial shipping. Except for shipping, however, these sources are rather intermittent and instantaneous (Hildebrand, 2005). Hence, the impact of such activities are not recognizable through ambient noise measurements (Mueller-Blenke et al., 2010; Richards et al., 2007).

The technological advancements that have taken place in the last decades have resulted in significant developments within the maritime industry. This has manifested itself in the commercial shipping sector as an increasing trend in ship and engine size, number of ships in service and the operating speed. The transportation of goods has thus become relatively cheaper and easier as the concept of globalization has developed. Such trends experienced by commercial shipping, however, have resulted in significant increases in various emissions produced by the ocean-going vessels. One of the most adverse by-products has been underwater noise (McKenna et al., 2013).

Figure 2-3, shows that while the world gross tonnage has increased as much as 6 times over the course of 60 years, the number of vessels sailing the world's seas has nearly tripled. The impact of such an extraordinary expansion of the world fleet has resulted in a 3 dB increase per decade in ambient noise level based on measurements (Hildebrand, 2009) as shown in Figure 1-1 and as discussed by Chapman & Price (2011).

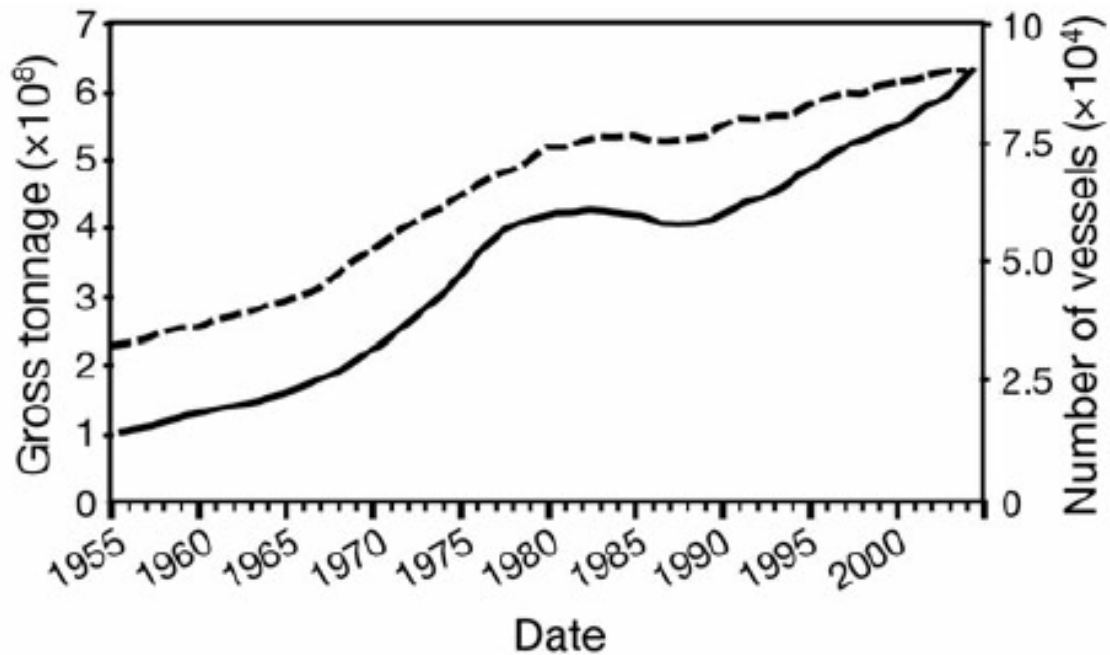


Figure 2-3 Numbers of vessels (dashed line) and gross tonnage of vessels (continuous line) in the world's fleet by Lloyd's Register of shipping for self-propelled, merchant vessels over 100 gross tonnes (Reproduced from (Hildebrand, 2009)).

Thus, the expansion of the world's fleet has exposed marine fauna to higher levels of background noise (Mitson, 1995). The marine organisms and especially marine mammals use acoustic vocalizations for finding food, mates and various activities regarding their survivability (Simmonds et al., 1997). Hence, exposing them to such an abrupt change in the ambient noise levels within a short period of time, considering their evolution period, they may not adequately adapt and evolve (Weilgart, 2008, 2005).

This consequently shows that, the main anthropogenic cause for the rising ambient noise levels of the world seas is commercial shipping; hence various on- and off-board noise sources of a vessel are worthwhile to be reviewed. Table 2-2, lists such noise producing systems on a vessel together with their impacts both for the ship and for the environment as outlined by ITTC (Bertschneider et al., 2014).

Table 2-2 Underwater noise sources for ships (Reproduced from (ITTC, 2014))

Noise source	Frequency range	Impact on environment	Impact on ship
Propeller noise non-cavitating tonal components	Blade Passage Frequencies (BPFs)	Low/ medium	Depend on ship
Singing propeller	100 Hz – 2 kHz	high	high
Propeller non-cavitating broadband	1 Hz – 20 kHz	low	low
Propeller cavitating tonal	BPFs	high	high
Propeller cavitating broadband	10Hz - 20kHz	high	high
Propeller-hull interaction	BPFs and structural NF	low	high
Cavitation on appendages	100 Hz – 20 kHz	medium	medium
Wave breaking	100 Hz – 10 kHz	low	low
Slamming	1 Hz – 100 Hz	low	low
Sea water cooling systems	100 Hz – 10 kHz	medium	medium
Main engines	1 Hz – 500Hz	medium	high
Driving systems	10 Hz – 1 kHz	low	medium
Auxiliary engines and systems	10 Hz – 2 kHz	low	medium
Active sonar military	100 Hz – 50 kHz	high	Medium
Active sonar echo-sounder	10 Hz – 30 kHz	low	low
Active sonar navigation	10 Hz – 100 kHz	low	low
Airguns	1 Hz – 100 Hz	high	low

A review of these sources indicates that whilst there are numerous noise sources on a vessel, the propeller is generally the dominant source due to its high impact both on in-board noise and to the underwater environment. Furthermore, the impact is even more significant once cavitation inception is reached (Norwood, 2002). In addition, underwater acoustical sources can be characterized depending on their dominant acoustic radiation mechanism. In this respect, cavitation acts as a monopole source while various non-cavitating noise sources associated with vortex shedding, fluctuating loads, turbulent trailing edge noise, flow induced vibrations act as dipole sources. Turbulent fluid motions are related to quadrupole sources. The significance of the acoustical sources essentially lies in the radiation efficiency associated with each. Therefore, when considering far field noise due to the presence of a monopole source (i.e. cavitation), dipole components may be negligible i.e. non-cavitating components (van Wijngaarden, 2000). In conclusion, a combination of the factors discussed identifies cavitation as the primary source of shipping noise contributing to ambient noise levels (Wittekind, 2009).

## **2.6 Propeller design and URN**

The propeller is a vessel's thrust-producing mechanism which drives it through the seas. During the production of such a large force, the propeller is forced to operate in extremes. Therefore, it is the duty of a propeller designer to ensure that the propeller does not fail while satisfying the requirements set out. The propeller design, however, is a skill that requires numerous engineering decisions to be made to achieve a design with high efficiency, low vibration, cost-effective, silent and durable performance. Since it is impossible to design a propeller that attains all these merits at the same time, the propeller designer compromises (trades-off) some aspects in order to achieve a propeller balanced design for satisfactory operation through ship's life cycle (Carlton, 2012).

The most fundamental aspects of propeller noise in the marine environment are related to the cavitation. In this respect, various environmental, operational and design parameters have an impact on the RNL's. Thus, it is utmost profitable to conduct a review regarding the main propeller design parameters in order to aid the decision-making process for the systematic experiments. The review is structured in two parts: hull shape and wake inflow, and propeller geometry.

### **2.6.1 Hull shape and wake inflow**

The propeller operates behind the hull and hence its inflow is affected by the hull wake caused by the potential and viscous components of the flow over the hull. The propeller is located at the stern of the ship to recoup some of the energy in the hull boundary layer, as well as for improved manoeuvrability properties and protection against damage. Due to the presence of the hull in front and its proximity to the rudder which is behind, the flow in which the propeller operates (the wake) is not uniform. This non-uniformity results in variations in the angle of attack of the propeller inflow and chordwise extent of cavitation experienced by the propeller and consequently results in higher RNLs.

The hull shape, especially the underwater stern shape, has a significant influence on the wake properties. Based on initial criteria proposed by Huse (1974), the stern shape can be categorized to be ‘U’ shape, ‘V’ shape or ‘Bulbous’ shaped (Carlton, 2012). The bulbous stern generally has higher naked resistance properties since it tends to consume energy in creating vortical flows within the wake. However, the wake properties can be significantly improved as a result of the flow that is channelled up to the propeller wake shadow area by vortices formed in the concave shape of the stern. A ‘U’ shape stern is used for bulk carriers as it enables larger cargo area for this heavy commodity. The wake of the ‘U’ shape stern tends to have a very low axial speed wake peak. Since it is a relatively full shape, the recovery from the low axial velocity region is also slow resulting in higher excitation levels being experienced as well as the higher RNL’s due to subsequent cavitation volumes experienced by the propeller. The ‘V’ shape with conventional apertures tends to generate high wake peaks at the top dead centre position in front of the propeller. However, the extent of the low axial velocity regions is smaller in comparison to the ‘U’ shaped stern. This results in rapid variations of the angle of attack of the propeller section causing violent growth and collapse of the cavitation formed in the wake shadow area.

Another important aspect regarding the ship stern is the propeller hull clearance. Whilst it is of utmost importance for propeller-excitation forces impacting on the adjacent hull, it also carries importance for RNL as the hull also acts as a hard reflector in close proximity to cavitation sources (Fitzsimmons & Odabasi, 1977). Forced excitation effects of cavitation dynamics have caused various problems including stress cracks, noise and vibration. This has resulted in regulations and guidelines to be announced by various classification societies that ensure sufficient clearance between propeller and ship’s hull (Lloyd’s Register, 2014).

The non-uniformity of the wake must be investigated to enable a better understanding of the forces which a propeller may generate. In this context the following simple descriptors have been used; axial wake, tangential wake, depth and width of wake peak.

First of all, the axial wake non-uniformity in the outer radii of the propeller is the most important parameter for propeller cavitation dynamics and should be carefully considered during the afterbody design of a new ship. The severity of the wake is generally expressed in terms of its depth and width. These affect the cavitation volume developed and the violence of its collapse both on and off the blade surface. Konno et al. (2002) have investigated the importance of the wake using four different severities of wake by altering the velocity gradient of the axial variation of inflow speed at constant radii. The most severe wake had the most rapid change of speed whilst the least severe one has a rather gradual change. The corresponding measurements have shown significant acoustic pressure elevations for the wakes with higher velocity gradients, thus demonstrating the importance of the axial wake factor for acoustic tests of the marine propellers; in particular when pursuing a standard series approach as presented in this thesis.

The tangential component of the wake is generated by the 3-dimensional shape of the hull and may be due to the streamline directions of the hull flow or due to an embedded bilge vortex flow. These components change from “with” the blade rotation to “against” the rotation across the 12 o’clock position and hence also alter the angle of attack to the propeller blade. In combination with the axial wake gradient they can cause the cavitation volume to change more rapidly due to the added variation in the section angle of attack. Whilst, they have a greater importance for twin screw vessels, the systematic representation of the tangential wake for cavitation tunnel tests is cumbersome and practically very expensive.

### **2.6.2 Propeller geometry**

The propeller design has various parameters that are significant both in terms of their effect on the efficiency of the propeller as well as on the development of cavitation and consequently, noise. The major parameters are reviewed below with remarks made to the design requirements. Particular emphasis is placed on their influence on RNL.



**Diameter:** The propeller design process encourages the propeller designer to select the largest possible diameter and lowest RPM within permissible limits. The maximum diameter is determined by both the vessel's immersed stern geometry at the ballast aft draft and the adopted proper clearance following rules and regulations as proposed by the classification societies (Lloyd's Register, 2010, 2014). A larger propeller diameter both reduces the load/unit area and also reduces the tip speed, which influences the amount of tip vortex cavitation. An empirical prediction method (Ross, 1976) was given for ship source level noise based on propeller tip speed utilizing the WWII noise measurements. The importance of the tip speed is also taken into account the by tip vortex index (TVI) method (Raestad, 1996) where a term for a calculated circulation strength at propeller tip is included. The diameter is thus a significant parameter that needs to be carefully treated in terms of radiated noise.

**Number of blades:** The number of propeller blades is vital in terms of reducing the specific loading on each blade and hence the pressure experienced by structures in close proximity to the propeller as well as noise radiated in the far field. Fewer blades lead to a higher specific loading which consequently results in worse cavitation performance or utilization of a larger diameter. Thus, the number of blades is a major factor affecting the loading around the blade tip. Hence, the tip vortex strength and consequent RNL can be lowered for propellers with higher numbers of blades and unloaded tips. However, various compromises that should be made in terms of propulsive efficiency and various other related aspects should be borne in mind. It is generally preferred to choose number of blades and blade rate harmonics to not to coincide with the main engine cylinder frequencies to avoid resonance due to overlapping shaft force and moments. In addition, the frequency of the excitation forces depends on the number of blades (Blade Rate Frequency) and the number of blades is hence selected not to coincide with natural frequencies of a part of hull such as the superstructure (Gomez & Gonzalez-Adalid, 1998).

**Blade area ratio:** Blade area ratio is a function of chord length, which is mainly dominated by the hydrodynamic requirements from a propeller. The larger blade area results in lower specific loading (thrust density) hence making it less susceptible to cavitation. However with the increase of the area of the blade, the hydrodynamic drag also increases and hence a loss in efficiency of the propeller occurs. Thus, while cavitation performance may be improved with a larger blade area ratio, it conflicts directly with the highest propulsive efficiency. As a preliminary guidance, the blade area ratio to minimise the cavitation risk can be selected by using e.g. Burrill's diagram as a function of the thrust loading and cavitation number (Burrill, 1944; Burrill & Emerson, 1962). Thus, it may be deduced that while providing better cavitation performance with the increasing blade area, the section drag properties experience a loss, and these need to be carefully balanced. The resulting cavitation performance consequently relates to the URN induced by a propeller.

**Rake:** Rake is a parameter utilized especially to ensure sufficient clearance between propeller and ship hull. The introduction of rake locally on the propeller blades, especially in the tip region, has been used to achieve better operating conditions for the propeller. The local variation around the tip region and with the propeller being at a location further away from the hull results in relatively better inflow conditions and can be expected to have a good impact on cavitation performance, and hence a reduction in URN.

**Chord Distribution:** The chord distribution of a propeller is optimized from the aspect of propeller efficiency which strongly depends on spanwise circulation distributions. To obtain the optimum circulation distribution, the tip of the propeller has a narrower chord. A narrow tip is also effective in minimizing the cavity extent in this region if the thickness is not excessive. Where a low noise signature is at a premium for certain types of vessels such as warships, narrow tip chords can be utilized whilst compromising the efficiency. However, for commercial shipping, the chord should be chosen based on the limitations defined by the minimum lift to chord ratio.

**Skew distribution:** Skew is a parameter used to reduce the severity of cavity dynamics (i.e. impact of sudden entrance of the whole propeller blade into the wake shadow area in which the direction of the flow and incidence angle vary dramatically). Thus, incorporation of skew results in a reduction of the second derivative of cavitation volume variation (acceleration of the cavity volume) which is proportional to radiated hydro-acoustic pressure (Fitzsimmons, 1988). As acceleration of the cavitation volume has been known to be the dominating parameter for the noise radiation, the introduction of skew can be expected to reduce the noise signature of a vessel. However, utilization of skew needs attention due to the structural problems that might arise from the stress concentrations around inflection point which appear in the tip regions for extremely large skew (more than 60 degree) and in the trailing edge at the mid-span for medium skew.

**Pitch distribution:** Pitch distribution of the propeller blade is determined to give the optimum spanwise thrust distributions with adequate attack angle and in conjunction with the camber distribution. The required load is then distributed along the blade mainly for the optimum propeller efficiency although other design priorities may dominate depending on the design objectives (e.g. cavitation, noise, etc.). However, local alterations to the pitch can also be utilized to optimize the propeller in certain areas in terms of cavitation performance. A common method is to off-load the propeller around the tip with a view to suppress the tip vortex cavitation. However, off-loading should be applied with care to avoid the occurrence of any face cavitation for higher inflow speed areas. Cavitation bucket diagrams can be utilized to implement suitable pitch distribution in order avoid such phenomena being experienced.

## **Propeller blade section**

Through history, various types of blade sections have been utilized for marine propulsion. These have included various early stage and very inefficient designs from aerofoils, as given by Abbott and Doenhoff (1959). However due to the difference between the application and the fluid, in which they are operating, none has been found to be sufficiently effective. The development of various different section shapes both symmetric (thickness) and non-symmetric (camber) has been extensively studied by Eppler & Shen (1979; 1981). Furthermore, previous

studies were also complemented by the famous sections of the time such as the Gawn-Burrill and Wageningen sections (Gawn & Burrill, 1957; Oosterveld & Van Oossanen, 1975). However, further development of the sections and the increasing requirements expected by the propellers inherently resulted in definitions such as the camber and thickness distribution to be utilized for the section design. This was due to the fact that earlier propellers contained only one type of section for the whole propeller. However, it became apparent that depending on the radial location of the section, the requirements differ significantly. For example, whilst structural integrity is more important for the sections in the root region, cavitation performance is the priority for a section at the tip region. Therefore, camber and thickness distribution are important definitions that are used to define a section shape and they are reviewed below.

**Camber distribution:** Propeller design procedure inherently adopts a camber distribution that provides the necessary loading hence thrust. Earlier propeller designs adopted excessive usage of camber in the mid-chord region, which resulted in propellers to experience bubble cavitation. Model scale experience with such propeller designs and bubble cavitation proved to be noisy and highly erosive. Thus, more contemporary propeller designs avoided bubble cavitation by using less camber and higher angle of attack to exhibit sheet cavitation (Kuiper, 1998). The same principles regarding local alteration can apply to the reduction of the cavitation extent experienced around the tip region if utilized carefully. The lift of the blade section can be achieved by using both propeller pitch and camber. The designer has to decide how much will come from each, taking the two types of cavitation which will occur into account. The first one is excessive sheet or face cavitation due to leading edge separation which will be introduced by improper pitch angle. The second cavitation type is bubble cavitation on the mid-chord of the blade section which will be brought by excessive camber as mentioned previously.

**Thickness distribution:** The thickness distribution is mainly a parameter to ensure structural integrity of the propeller. The induced forces produced by the torque and thrust should be adequately handled by the structural properties of a propeller. However, in addition to that, thickness is also critical in terms of the cavitation performance, especially in the leading edge region. For example, whilst the most desirable thickness distribution for the optimum cavitation

performance is elliptic distribution, its drag properties are not that much superior. Excessive thickness may also affect the inflow direction to the blade section and hence angle of attack.

**Hub Shape:** The propeller hub is often observed to experience a stable vortex cavitation arising from the flow through the root sections of the blades accumulating towards the hub. The rotation of the propeller introduces a circulation movement to the flow. The circulating flow experiences a pressure drop due to increased rotational velocity as it travels in the slipstream and leaves the hub resulting in the propeller hub vortex cavitation phenomena. Various different hub designs have been investigated to avoid the cavitation experienced by the propeller hub or to extract back the energy that is used by this kind of cavitation structure (Hansen, 2011; Atlar & Patience, 1998).

With the above review of the various propeller design parameters in perspective, one may conclude on a number of outcomes. While a number of variants have been discussed above, only some of them can be used as parameters for standard series of propeller tests. These are limited to Blade Area Ratio (BAR), pitch to diameter (P/D) ratio and blade number, in conjunction with selected wake flow variations.

Also, no matter how well the propeller is designed, cavitation is unavoidable for an efficient commercial vessel at service speed. Thus, it is in one respect crucial to have an understanding of the propeller design parameters, yet their influence on the type of cavitation and the severity of the cavitation bubble dynamics is of greater importance.

## 2.7 Cavitation

Cavitation is defined as the rupture experienced in a liquid medium due to a local static pressure drop. Although it was first mentioned in the history of science by Euler (1754) in his work on the theory of water wheels, it took another 150 years, with the advent of steam turbines and high-powered screw propellers, for the phenomenon to become the focus of research.

The term cavitation is credited to R.E. Froude, when it was first observed by Thornycroft & Barnaby (1895). During the trials of the “HMS Daring”, a high-speed torpedo-boat designed

for the Admiralty, it was deduced that the propeller started to cause ruptures and voids in the water above a certain speed due to the thrust loading density. It was however not until the trials made with “Turbinia” in 1896, that cavitation research experienced its breakthrough when Sir Charles Parsons devised the world’s first cavitation tunnel (Burrill, 1963). This tunnel, (Figure 2-4), contained almost all of the same components as a modern cavitation tunnel, except for an impeller for water circulation. A turning mirror was used for stroboscopic photographs of the 2-inch propeller, while an arc lamp was used to achieve cavitation simulation by heating the water instead of applying a vacuum as in today’s cavitation tunnels.

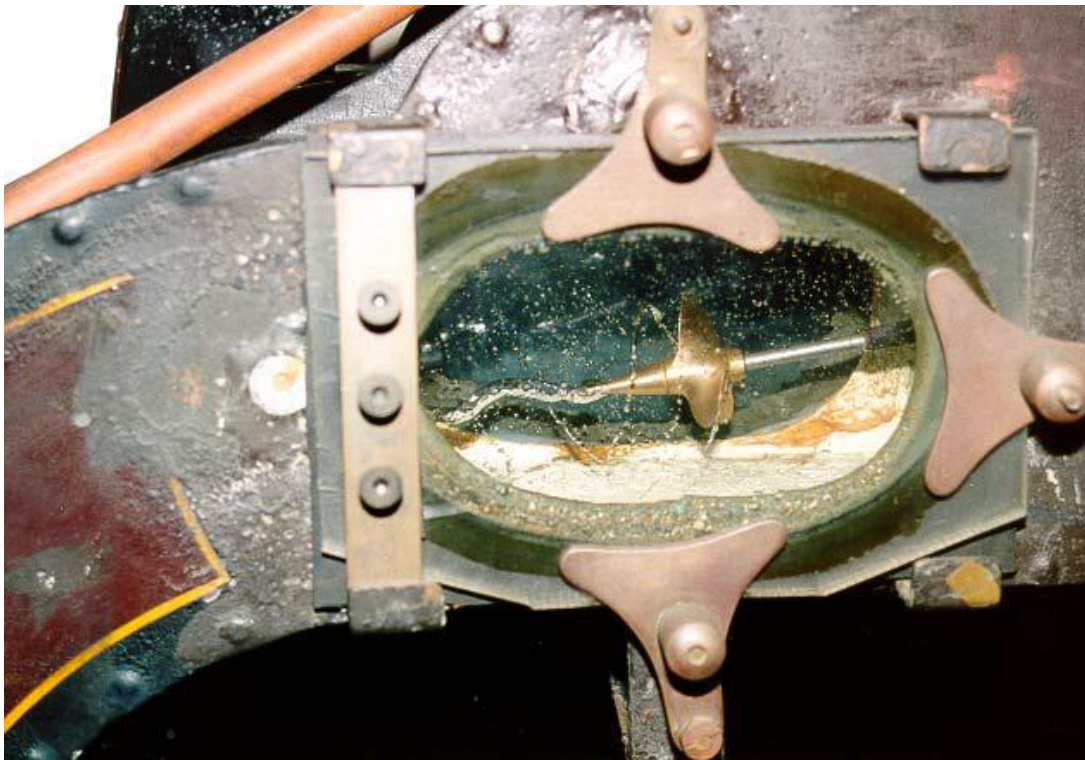


Figure 2-4 Propeller cavitation tests with Parsons’ world’s first cavitation tunnel (Courtesy of M. Atlar).

Cavitation is a general fluid mechanics phenomenon which takes place in flowing liquids, such as found in channels, valves, pumps, propellers and other hydrodynamic machinery where there is a drop in the pressure. The phenomenon is caused by fluid velocity variations resulting in pressure fluctuations within a fluid (Knapp, 1970). The physical process which generally governs the cavitation phenomenon can be found as an extension of the situation where water will boil at a lower temperature when taken to the top of a high mountain, where the pressure is lower from that at sea level.

Cavitation occurs due to the presence of the very small gas/vapour filled bubbles of 1-100 micron meter diameter. These bubbles serve as the impurities within the fluid causing ruptures to occur at a much lower pressure, whilst a pure liquid may sustain very high tensions without experiencing cavitation. These impurities within the water are recognized as the seeds of the cavitation and referred to as nuclei. As the nuclei pass through a region with strongly reduced pressure (below the critical vapour pressure) a rapid vaporization process occurs (Chahine, 2004).

Although there are a number of non-dimensional parameters in existence to characterize the flow and forces in a hydrodynamic system, the two parameters given by Equation 3 and Equation 4 are of utmost importance in terms of defining the inception point of cavitation. The pressure coefficient “ $C_p$ ” characterizes the forces acting on a body in water and enables calculation of the pressure field around it. The pressure field map allows the determination of the points vulnerable to cavitation. Following the same approach, Cavitation Number “ $\sigma$ ” given by the Equation 4, was created to map the tendency of a flow to cavitate.

$$C_p = \frac{P_M - P_{st}}{\frac{1}{2}\rho V_R^2} \quad \text{Equation 3}$$

$$\sigma = \frac{P_{st} - P_V}{\frac{1}{2}\rho V_R^2} = \frac{\text{static pressure head}}{\text{dynamic pressure head}} \quad \text{Equation 4}$$

where  $C_p$  is the pressure coefficient,  $P_M$  is the local pressure,  $P_{st}$  is the static pressure at a reference point,  $V_R$  is the propeller resultant velocity,  $\rho$  is the fluid density,  $\sigma$  is the cavitation number and  $P_V$  is the vapour pressure.

Theoretically as long as the sum of cavitation number and pressure coefficient is positive no cavitation will occur: cavitation should start when their sum is zero and remain for negative values. In practice, this is not quite accurate, but the above implies that the higher the cavitation number, the lesser the chance is for cavitation to occur.

The “cavitation inception number”  $\sigma_i$  derived from Equation 3 and Equation 4, is defined in Equation 5. To simplify the inherently complex phenomena, the minimum pressure at which cavitation inception occurs is assumed to be the vapour pressure as in Equation 6.

$$\sigma_i = -C_{pmin} \quad \text{Equation 5}$$

$$P_{min} = P_V \quad \text{Equation 6}$$

Beyond the point of cavitation inception and with decreasing cavitation number, the extent of the cavitation enlarges up until the point when the pressure inside the bubble is the same as or larger than that outside. At this point, due to the pressure recovery experienced, the cavitation bubble will cease growing, reverse the procedure and collapse, potentially resulting in the production of shock waves. The resulting acoustic pressure emits noise as well as causing a micro-jet to be formed leading to the erosion on a nearby solid interface (Choi & Ceccio, 2007).

### **2.7.1 Types of cavitation experienced by propellers**

Due to the inception of cavitation with decreasing cavitation number, the extent of cavitation enlarges and takes the form of developed cavitation. The cavitation can be categorized based on its location on the propeller blade and its physical appearance. Since the noise signature of cavitation is more attributed to its physical appearance, the following four main cavitation types will be reviewed with particular attention to their implication in terms of the emitted noise levels together with the main reason behind the formation of each (Bark & Berlekom, 1978). Namely, these are sheet, vortex, cloud and bubble cavitation. Photographic examples of each type are also provided within the review together with the ITTC approved cavitation schematic patterns used for hand sketches (ITTC, 2002a) of cavitation tunnel test observations. Figure 2-5 below outlines the various types of cavitation that can be observed on a propeller.



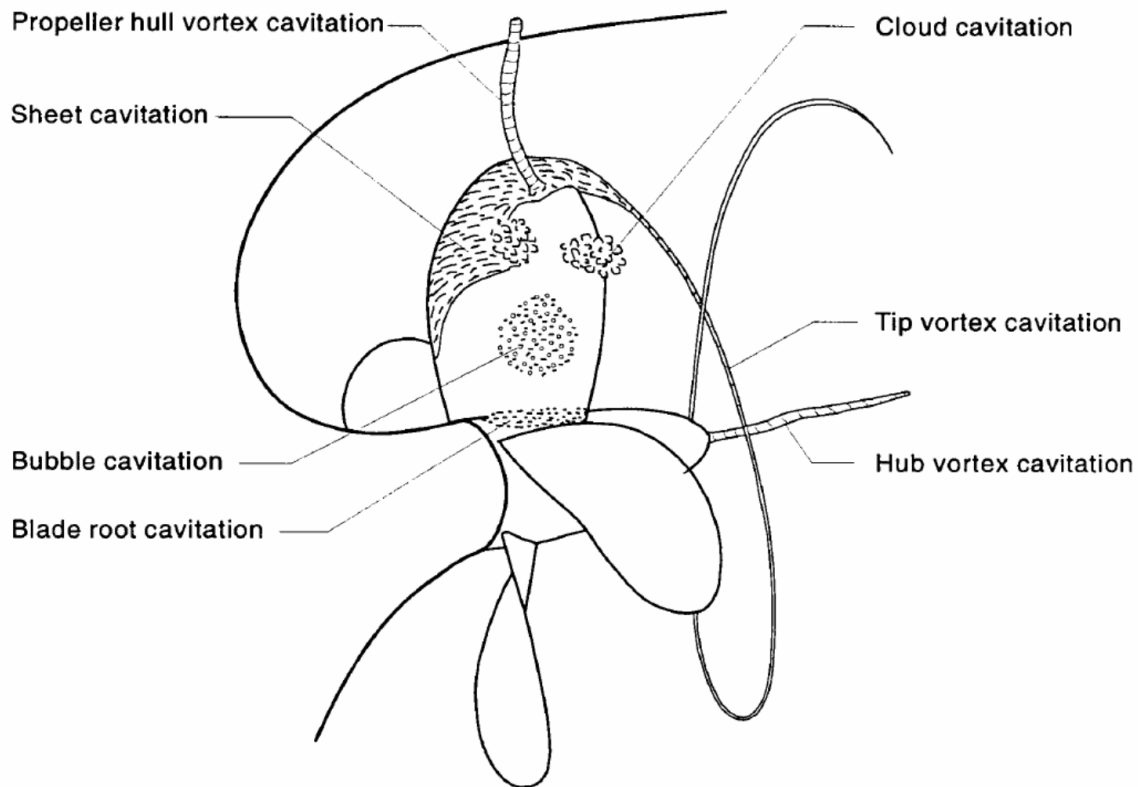


Figure 2-5 Representation of the most common types of cavitation (ITTC, 2002a).

### 2.7.1.1 Sheet cavitation

Sheet cavitation occurs when large suction pressures build up near the leading edge of the blade resulting in the back of the blade being covered with a layer (sheet) of cavitation bubbles. Sheet cavitation occurrence is largely a function of the variation of angle of attack of the propeller blade sections experienced due to the propeller rotation through non-uniform wake of the vessel. The low-pressure region has a value significantly lower than the critical pressure hence even the smallest nuclei are destabilized forming a singular large sheet cavitation. However, the unity of the cavitation is altered due to the propeller rotation out of the wake shadow region where local speed and hence angle of attack is significantly reduced. With the recovered speed the sheet cavitation experiences various types of break-off depending on the wake flow field due to the re-entrant jet formation as discussed in detail by Lange & Bruin, (1998). The break-off consequently results in the cavitation volume variation causing the acoustic pressure to be

produced (Ceccio & Brennen, 1995). While the volume of the sheet cavitation significantly contributes to the tonal levels emitted, dynamics experienced by the sheet cavitation, such as the break-off and collapse mechanisms, results in broadband noise. Typical break-offs are outlined by Bark together with the potential collapse scenarios for a number of different ship types and inflow conditions (Bark, 1986).

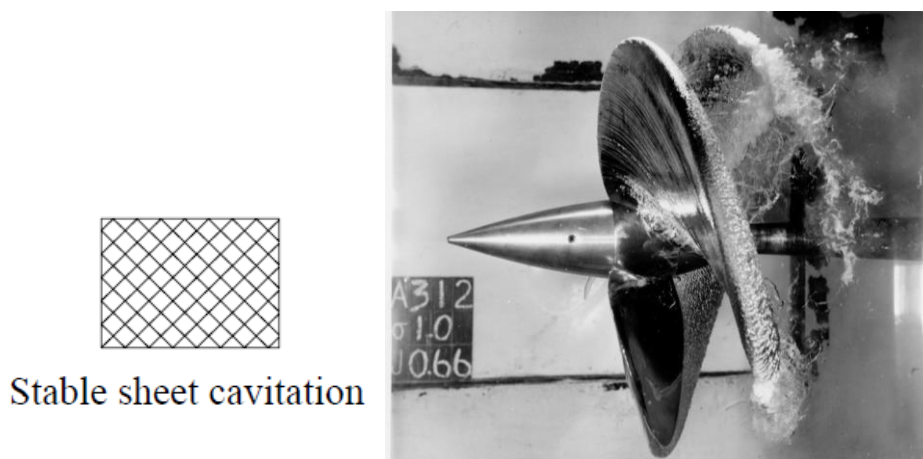


Figure 2-6 ITTC approved schematic patterns used for hand sketches and cavitation tunnel cavitation images for bubble cavitation (Courtesy of Emerson Cavitation Tunnel Archives).

### 2.7.1.2 Vortex cavitation

A vortex is a rotating flow that generally sheds from the tips of lifting foils with finite spans. The rotation causes a region of reduced pressure at the centre of the vortex which is also called the core. The reduction of the local pressure at the core of a vortex is due to the centrifugal forces acting upon it. If the vortex motion is strong enough, the reduction of the local pressure at the core will reach the critical pressure creating a cavitating kernel with the help of entrained nuclei due to the low-pressure region (Arndt, 2002). For uniform flow conditions such cavitation exhibits excellent stability and travels intact in the slipstream of a propeller or a lifting (Pennings, Westerweel et al., 2015; Pennings, Bosschers et al., 2015). However, if operating in a non-uniform flow, the vortex may be distorted or even collapse or burst due to the speed recovery upon the departure from the wake shadow region (Konno et al., 2002). Tip vortex cavitation, in particular, is mostly found to experience such dynamics, which in return causes large pressure fluctuations hence high levels of noise (Berghault, 2000). The emitted noise is

generally observed in the spectral domain as a hump in the mid frequency region (200 to 800 Hz) and broadband monopole type cavitation noise contribution due to the dynamics such as bursting and rebounding of the cavitation bubbles.

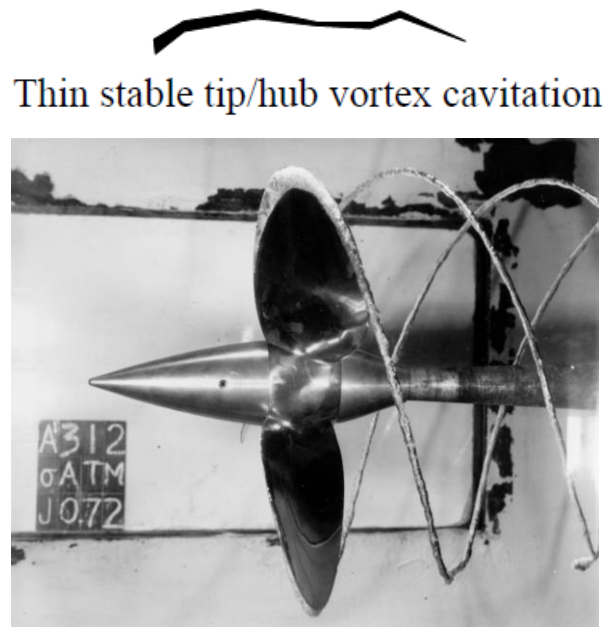
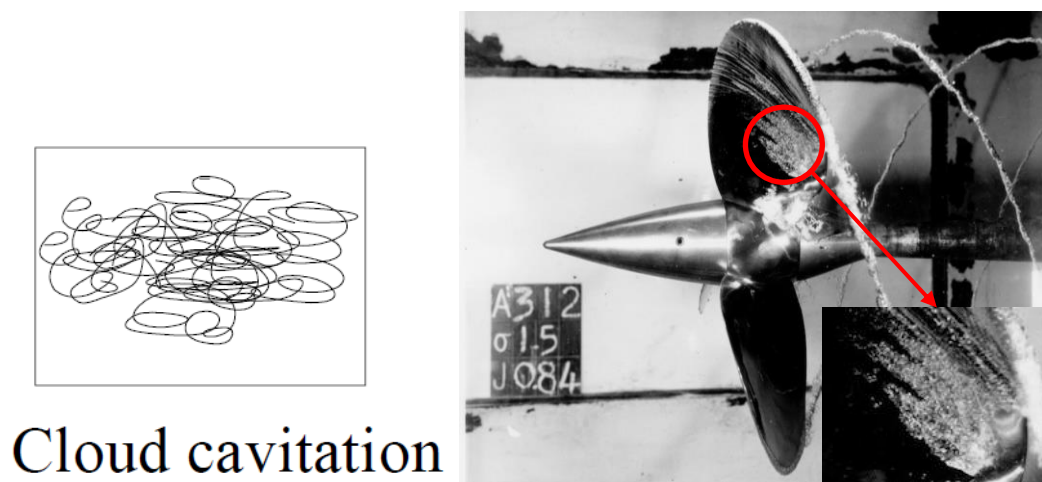


Figure 2-7 ITTC approved schematic patterns used for hand sketches and cavitation tunnel cavitation images for bubble cavitation (Courtesy of Emerson Cavitation Tunnel Archives).

### 2.7.1.3 Cloud cavitation

The sheet cavitation is usually found in the region of the wake shadow where locally reduced velocities provide a time interval for cavity volumes to grow and collapse. Upon the propeller blade leaving the wake shadow region due to its rotation, either the sheet cavitation is rolled up to form or join the tip vortex cavitation or it disintegrates in parts forming cloud cavitation. In this context, the formation of cloud cavitation from the sheet cavitation is mainly dependent on the wake inflow properties. Based on the unsteadiness of the flow, the sheet cavitation may experience a periodic cloud cavitation shedding and disintegration with variable intensity. The shed cloud cavitation would then experience a rise in the local pressure as it disintegrates resulting in a violent collapse producing high-pressure pulses emitting a high level of broadband noise (Wang & Brennen, 1995).



## Cloud cavitation

Figure 2-8 ITTC approved schematic patterns used for hand sketches and cavitation tunnel cavitation images for bubble cavitation (Courtesy of Emerson Cavitation Tunnel Archives).

### 2.7.1.4 Bubble cavitation

Bubble cavitation is caused by high suction pressures developing in the mid-chord region of the blade section due to combination of high camber and section thickness. Propellers with relatively thick blade sections which are operating at a small angle of attack are susceptible to bubble cavitation. Unlike sheet cavitation, bubble cavitation does not coalesce and form a single volume of cavitation. The large bubbles exist separately, following the flow direction on the blade surface. Early propeller design methodologies in the 1920's resulted in propellers which often experienced bubble cavitation due to the aerofoil sections used for the design purpose. However, this has later been avoided by local reduction of camber in the mid-chord region due to the high noise levels emitted by the collapse of this type as well as the erosive nature of the implosions (Kuiper, 1998).

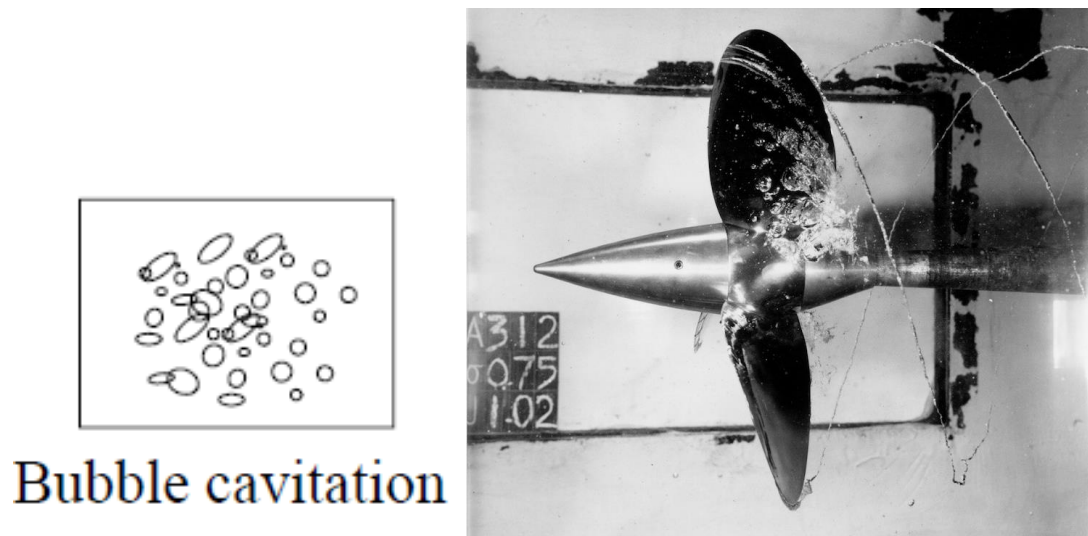


Figure 2-9 ITTC approved schematic patterns used for hand sketches and cavitation tunnel cavitation images for bubble cavitation (Courtesy of Emerson Cavitation Tunnel Archives).

### 2.7.2 Consequences of cavitation

Cavitation, in addition to underwater radiated noise, leads to a number of highly undesirable phenomena, such as propeller induced pressure pulses, erosion and loss of thrust (Kuiper, 2001).

Cavitation coverage of up to 25 to 30% of the blade area does not generally contribute to a significant loss of thrust on the blade. However, with increased cavitation coverage, there can be a significant loss in the pressure differential across the blade sections, leading to a loss of section lift. This loss adversely influences the thrust, torque and efficiency of the propeller (Pylkkanen, 2002).

Cavitating ship propellers may generate on-board noise and cause vibration that can be problematic for crew and passengers, in terms of both comfort and performance (Plunt, 1980; IMO, 2012). Pressure pulses caused by the propeller are the dominant source of on-board noise, produced by the displacement of the propeller blade and mainly due to the cavitation volume in the close proximity of the hull (Breslin & Andersen, 1996).

During the collapse process of sheet, bubble and vortex cavitation, bubbly structures can form micro-jets, which if sufficiently close to the blade surface, that can erode the blade material by the shock wave created by the imploding bubbles (Arndt et al., 1995). Cavitation erosion is one of the most serious consequences of the phenomena causing structural damage propeller blades and rudders (Fitzsimmons & Boorsma, 2007).

Amongst the various undesirable impacts of the cavitation, underwater radiated noise is the main focus of this thesis due to its potential impact on the marine fauna. However, the potential advancement that this experimental study may lead to alteration of propeller design methodology and hence result in improvement in terms of various consequences of cavitation as covered within this section.

## **2.8 Propeller noise prediction methods**

This section reviews the main empirical and semi-empirical methods available in the literature. Even though the interest in underwater radiated noise in the commercial domain is relatively recent, it has been widely investigated for naval applications and specialist research vessels. A considerable part of the noise generated by the ship system arises from the major sources: machinery, propeller and background hull flow noise as described by Ross (1976). Amongst these sources the propeller noise, particularly for the cavitating propeller, is the most harmful one as discussed previously, since the dominant noise levels can cover the broadband frequency (Leaper et al., 2009). Therefore, the design of a quiet ship necessitates the minimization of propeller noise and in particular cavitation related noise. To lower the SPL of propeller hydrodynamic noise, there has been a number of studies made thus far to predict it in the early design stage.

Although, the noise prediction methods can be categorized based on the cavitation presence or cavitation type, this review considers the available prediction methods in chronological order. This allows an understanding of the evolution of the estimation methods and is also expected to point a direction towards a method to use whilst undertaking a systematic test campaign concentrating on the propeller design parameters, previously reviewed, as is the objective of this study.

Fitzpatrick & Strasberg (1956), in their major study, reviewed various flow phenomena that produce hydro-acoustic sound. Their major contribution regarding marine propeller noise was the sound pressure prediction for a single cavitation bubble (Brennen & Ceccio, 1989). Based on the radial motion of a cavity bubble, that is assumed to go through spherical growth, acoustic pressure estimation is demonstrated. Another important fundamental recognition is made of the main noise creating mechanism being related to the second time derivative of the cavitation volume. As highlighted by the authors themselves, the prediction captures the main features of the spectra despite the simple assumptions made. However, they also point out areas for more accurate prediction, such as the non-spherical collapse, shock wave effect and rebounding dynamics of the cavitation bubble.

In the same vein, Baiter (1974) adopted a similar approach to Fitzpatrick and Strasberg. He assumed each cavitation bubble to be individual and by summation of the independent events of cavitation bubble collapse, noise radiated by the propeller may be predicted. The cavitation events are related to the stochastic distribution of the cavitation nuclei present in the water to enable the determination of the single cavitation number. Whilst, the simplifying assumptions are significant, and being one of the first theoretical based propeller noise estimation method, a great advancement in the subject was achieved.

Brown (1976), in his seminal manuscript, stresses the rising importance of propeller cavitation noise. Following the presentation of a typical propeller cavitation noise spectrum, Brown divides the spectrum into two regions. The low frequency region contains mainly tonal spikes due to the blade harmonics as well as a peak in the shape of a hump that is generally in the 40 to 300 Hz band. The tonal components are observed to appear at the lower end of the 40 to 300 Hz range when the propeller diameter is large and heavily cavitating. Brown also identifies the high frequency region to be mostly associated with cavitation, with a constant asymptote of -6 dB per Octave up to 10 kHz. Based on this concept, an equation is derived mainly dominated by the fraction of the propeller disc area swept by cavitation. While different types of cavitation and their impact on the noise are not explicitly recognized by this formulae, it has been commonly used by the shipbuilding industry for decades (Okamura & Asano, 1988; Ekinici et al., 2010). However with the developments in the field of propeller design, these estimated levels have tended to overpredict the RNL of newer ships.

Ross (1976), in his comprehensive book on the mechanics of the underwater noise, compiles his tremendous experience during the time he served in the US Navy. The book provides not only valuable insight into the overall subject of underwater radiated noise but also offers several simple noise prediction equations. The methods are based on ship noise measurements made during WWII. The equation given by Ross is suggested to be used for frequencies higher than 100 Hz and for ships longer than 100 meters. The equation utilizes the propeller tip speed as the main driving parameter. The tip speed is a significant parameter since it is influential in parameters that dominate a number of cavitation types such as circulation distribution for tip vortex cavitation as discussed above within the section dedicated to tip vortex cavitation. While this simple method had been useful for the ships of the time, the complex nature of the cavitation noise resulted in the prediction method being outdated and over predicting the actual noise levels of today's commercial ships.

The method developed by the British Maritime Technology (BMT) Cortec Ltd. utilizes knowledge from full-scale noise range data of 12 single screw fisheries research vessels. The model adopts a novel approach to model the cavitating and non-cavitating components of the spectrum (Angelopoulos et al., 1988). The prediction method is composed of three sub-modules including an inception module, non-cavitating noise module and cavitation noise module. The results of the modules are used to sum up the noise levels emitted by a ship based on the statistical analysis of the dataset. The prediction software was developed using a stepwise regression analysis to determine the influential and significant parameters to noise (BMT-Cortec, 1992). In this respect, the method is not only capable of making accurate predictions for fisheries research vessels but also contributes to the understanding on the effect of various parameters on the RNL (Aktas, Fitzsimmons et al., 2015).

Matusiak's pioneering study makes a valuable contribution to propeller cavitation noise prediction (Matusiak, 1992). Based on the assumption of dividing the spectrum into low and high frequency regions, Matusiak shares the initial partition of the spectrum with Brown (1976). The main contributing factors are defined to be tip vortex and sheet cavitation together with non-cavitating sources such as the blade thickness and loading. The high frequency region in this



respect is assumed to be dominated by the unsteady cavitation dynamics. Based on these assumptions he adopts the single cavitation bubble noise approach as introduced by Fitzpatrick and Strasberg (1959) combined with Baiter's (1974) multiplication by the cavitation event method. The cavitation events are predicted by a separate potential flow code as developed by Geurst (1961). The comparisons of the predictions are demonstrated against the benchmark data of the Sydney Express (ITTC, 1987). The predictions demonstrated significant potential and were then taken over by the Cooperative Research Ships (CRS) group to be developed further. More recent examples are demonstrated by Firenze and Valdenazzi (2015) and Hallander et al.(2012).

One of the latest methods that have found widespread use in the industry is the Tip Vortex Index (TVI) method by Raestad (1996). The predictions are made based on the extensive database of on-board noise measurements of cruise ships made by Det Norske Veritas (DNV). The importance of tip vortex cavitation has long been known by experience both from naval vessels and cruise/passenger ships. In light of this knowledge, DNV gathered a database of full-scale measurements for calculation of some statistical coefficients that are present in the tip vortex index method (Abrahamsen, 2005). According to Raestad, the pressure peaks at blade frequencies are due to blade cavitation and the following broadband nature of the spectrum is due to tip vortex cavitation. In addition to that, by presenting the pressure measurements conducted on Queen Elizabeth 2 cruise liner, Raestad demonstrated the impact of tip vortex cavitation in the propeller slipstream on the emitted noise levels. The method is limited to fully developed tip vortex cavitation for high powered ships with highly optimised propellers, but the methodology adopted carries greater importance as it proves the concept. The theory established in this context is the Intellectual Property of DNV and based on the pressure field calculation of cavity volumes on propeller blades using lifting line theory. The theory, however, was also adopted and developed by other major European facilities and demonstrated again by Firenze and Valdenazzi (2015).

Considering all of the reviewed major studies, development of a method for the prediction of underwater radiated noise induced by a cavitating propeller has experienced significant evolution. Yet, unsteady cavitation is a highly complex phenomenon that necessitates the implementation of non-linear equations. Whilst the current state of the art has reached a point where relatively more accurate predictions can be made, the CFD simulations that reproduce realistic

cavitation dynamics are still in their infancy (Lidtke et al., 2015). In this respect if the prediction methods presented are categorized; Baiter's and Matusiak's method requires information from another code that uses potential flow based methods to calculate mainly sheet cavitation extent, as it fundamentally neglects viscous effects. Raestad's method, however, concentrates on the tip vortex cavitation phenomenon and hence no account is made regarding the sheet cavitation. Thus, there is no existing method that can calculate the noise emissions from both sheet cavitation and tip vortex cavitation. This is due to their complex nature and dynamics such as the shock waves formed, rebounding of the cavitation bubbles and interaction and entrainment of super-cavitating sheet cavitation into the tip vortex (Wijngaarden et al., 2005).

### **2.8.1 Computational propeller noise prediction methods**

In addition to the above empirical, semi-empirical and statistical approaches for the prediction of ship propeller noise, with the recent developments in computational power, is also possible to be predicted using various CFD tools. Currently, computational prediction of the radiated noise is divided into three parts. The first part is devoted to the calculation of the ship wake field often obtained by Reynolds Averaged Navier-Stokes Equations (RANS) simulations. Following this, the propeller operation is then analysed using a Boundary Element Method (BEM) or vortex lattice method, or by utilizing the RANS platform used for the wake field calculation. Finally, a prediction is made for the far field radiated noise due to the cavitating propeller or hydrodynamic noise sources in general. For this purpose; an acoustic BEM that solves the Helmholtz or FW-H equations (Williams & Hawkings, 1969) are employed (van Wijngaarden, 2011; Firenze & Valdenazzi, 2015; Hallander et al., 2012).

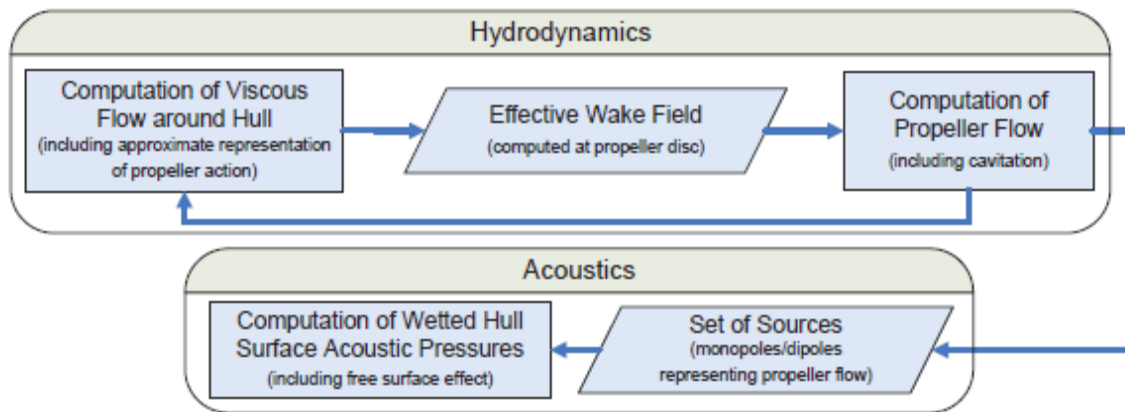


Figure 2-10 Flow chart for the computational prediction of cavitation noise (Reproduced from (van Wijngaarden, 2011))

With such an approach as outlined in Figure 2-10, prediction of the cavitation noise of a marine propeller is possible through coupling of up to five different software modules, while there are other software platforms that enable the prediction through only one as demonstrated by Kowalczyk & Felicjancik (2016). Overall, the prediction using CFD methods are time-consuming, cumbersome and expensive. Furthermore, the accurate prediction of the cavitation noise requires a very detailed analysis of unsteady cavitation behaviour, such as cavity clouds and cavitating vortices generated by the collapse of sheet cavitation. This necessitates a time accurate modelling of turbulence for which Large Eddy Simulations (LES) are even more expensive in terms of the computational time (Bensow & Goran Bark, 2010). Thus, whilst such developments are of great importance and carries great potential with the further development of the computational power, for the current state of the art it is in its infancy.

### 2.8.2 Experimental propeller noise prediction

Model scale experiments focusing on noise are usually performed to predict the full-scale acoustic source strength of a given design of cavitating propeller with respect to the underwater radiated noise for a broad range of frequencies (Blake, 1986, 1984). Since the main focus of such tests is the cavitation noise, the experiments are conducted either in a cavitation tunnel or a depressurized towing tank. During the set-up of such tests and the post-processing of the data, there are various components and procedures that require utmost attention and experience to ensure accurate measurements and reasonable predictions are made (Bark, 1985).

The most important component of propeller cavitation noise experiments is the propeller model. The model should be manufactured to meet the precision criteria for acoustic tests. The ITTC specifies the maximum offset for the blade sections to be in the range of  $\pm 0.05$  mm for a typical minimum diameter of 250 mm (ITTC, 2011c). Furthermore, the propeller blade edges should be manufactured with great care to avoid singing (Brennen, 2007; Fischer, 2008).

The most influential parameter after the propeller is the wake inflow. The propeller operates in the wake of the ship hull which leads to loading variations on the propeller blade (Harvald, 1981). These loading variations are the principal factor while simulating cavitation inception and dynamics which emit high level of cavitation noise (Brennen, 1995). The loading variation thus needs to be adequately modelled for the cavitation tunnel testing. The wake to be simulated in cavitation tunnels is either achieved by means of nominal wake measurements in towing tanks and extrapolation to full scale using ITTC guidelines (ITTC, 2011b) or by using CFD tools. Following the determination of the target wake, the wake field can be generated for the experiments using the following configurations;

- Wire screen meshes for the cavitation tunnels with small test sections. Cost effective and relatively simple method, simulating only axial velocity component of the wake field.
- “Dummy” models are utilized at medium size facilities in conjunction with wire screens as the removed parallel mid-section due to dummy model concept results in relatively lower Reynolds Number and hence a boundary layer which is not sufficiently developed
- Full ship models, which are used for the towing tank tests, are also utilized for the cavitation tunnel testing in the facilities with large test sections. There may still be a need for wake screens if the differences due to the extrapolation of the wake to full scale are significant.

In addition to the above wake simulation methods, recently research (van Wijngaarden, 2011) has shown that the representation of the full-scale wake can be also achieved by purpose built models to replicate the full-scale wake based on the CFD calculations instead of geometrically similar (geosim) models.

The type of wake simulation method used is also important in terms of the turbulence intensity introduced. In general cavitation tunnel LDA measurements have shown that, as the net mesh area ratio is decreased (i.e. mesh size getting smaller), the level of turbulence increases. This demonstrates the effectiveness of the wire meshes to create different levels of the turbulence intensity.

The cavitation noise experiments also need utmost attention during the execution of the tests as there are a number of factors that require correction or disposal of the data. One of the most influential factor is the background noise of the facility. Background noise is determined in the tests at the exact operational conditions of the cavitation noise tests, and where a dummy boss replaces the propeller. The data needs to be removed if the difference between the background levels and the cavitation noise levels is less than 3 dB and a correction is applied if the difference is between 3 to 10 dB. No correction is required for differences higher than 10 dB (ANSI, 2009). The major noise sources contributing to the background noise are turbulent boundary layer noise, impeller noise and propeller dynamometer and motor noise.

As cavitation tunnels are closed circuits with a chamber type measuring section, they are highly reverberant environments. Therefore, the influence of the testing environment on the noise transfer function needs to be determined in order to properly relate measured SPLs to source levels at a normalized distance of 1 m (Park et al., 2009). Such a correction is determined by substituting a calibrated noise source for the propeller. The hydrophone measurement and the calibrated source levels are then compared in order to determine the transfer function of the sound within the testing section.

Following the application of the corrections discussed above, the ultimate noise measurements are extrapolated to predict full-scale cavitation noise. The scaling methodology is based on theoretical bubble dynamics for radial motion of a cavitation bubble (Bark, 1985). Extrapolation methods are either based on the spherical spreading loss (Starsberg, 1977) or constant acoustic efficiency (De Bruijn & Ten Wolde, 1974).

In addition to full-scale noise prediction, cavitation tunnel experiments also provide invaluable insight regarding the noise creating mechanisms of the cavitation phenomena. For this purpose, measured time signals are fed into Joint Time-Frequency Analysis (JTFA). The influence of the cavitation events in time signals are visualised using spectrograms and their corresponding response in the frequency domain (Fitzsimmons, 2009). The synchronization of the pressure signal and the cavitation observations enables the interpretation of the impact of instantaneous cavitation events as well as the determination of broadband and tonal noise source identification (Filcek, 2006). This type of analysis allows the user to interpret single signals in terms of their effect to the overall spectrum and enables a better understanding of the reasons for the spectral characteristic in the frequency domain (Fitzsimmons, 2014).

Cavitation noise tests are configured to match the required cavitation number. However, tip vortex cavitation inception is generally observed to be premature at model scale for the exact cavitation number condition (Latorre, 1982; Hsiao & Chahine, 2008). Since tip vortex cavitation is significantly influenced by the viscous core of the vortex and therefore by the Reynolds number (Kuiper, 2012), use has been suggested of a ratio based on the Reynolds numbers as seen in Equation 7.

$$\frac{\sigma_{i,full\ scale}}{\sigma_{i,model\ scale}} = \left( \frac{Re_{full\ scale}}{Re_{model\ scale}} \right)^m \quad \text{Equation 7}$$

The exponent “ $m$ ” is determined as a result of detailed investigations and comparisons of an extensive database for full-scale and cavitation test information. Such studies have been conducted using an experimental approach (Oshima, 1994) and by CFD simulations (Hsiao & Chahine, 2008). Whilst the above argument stands valid for the inception condition, Bosschers, (2010) argues that the cavitation number identity is still valid for the developed tip vortex cavitation since the vortex core is not influential on the cavitating vortex diameter.

Overall, amongst the several propeller noise prediction methods reviewed, cavitation tunnel experiments can be concluded to be most appropriate for the adoption of a systematic approach using a standard propeller series. This is due to the fact that while CFD methods hold a great potential for the future, they are computationally expensive and time-consuming for studying

an extensive simulation matrix. In addition to that, the simulations are rather incapable of capturing major noise creating mechanisms such as cavitation dynamics. Empirical and statistical based methods are not sensitive to detailed propeller design parameters hence neither they aid in recognizing the influences of such parameters on the RNL, nor they are sophisticated enough to capture cavitation dynamics.

## **2.9 Experimental propeller noise test cases**

Experimental noise studies with the propellers are of great importance as they represent the state of the art and lead towards the knowledge gaps within the literature. Whilst, there is no study that has used standard propeller series for noise testing, some studies have compared the effect of some major propeller designs and operation parameters and wake inflow effect on the radiated noise levels.

In his early study, Holden (1981) carried out an experimental campaign with six propellers out of four that have been tested in the same wake field and two in different inflow conditions. The study set out to investigate the effect of BAR, radial camber and pitch distribution and skew with the four propellers and to look into the effect of wake inflow with an additional two propellers. This work reported that higher BAR, tip offloading and skew reduced the emitted noise levels originating from the propeller cavitation. While the tests have led to some significant conclusions regarding the major propeller design parameters, it failed to take into account wake inflow variations. Moreover, it is not known if the propellers tested were members of a standard propeller series. Whilst detailed pitch and camber distributions are provided for all propellers; there is no mention to their blade section shapes.

Sharma et al. (1990) conducted extensive experiments with three basic propellers models of different design to investigate the effect of advance coefficient, cavitation number and propeller geometry on radiated noise levels in uniform flow conditions. Furthermore, one of the propellers was tested behind a typical single screw vessel wake which led to the conclusion that wake

is one of the most important parameter for noise generation. Although the study provides valuable information and is one of the most important studies conducted on this subject, the work was limited to testing three independent propellers with no systematic variation of parameters. The tests were only carried out in uniform flow. Thus, no relation can be drawn from this study with regards to the influence of major propeller design parameters on the radiated noise levels of ships.

A recent, influential study by Konno et al. (2002) studied sheet and tip vortex dynamics phenomena. The research considered the modern propeller design tendency to use highly skewed propellers for lowering pressure fluctuations. However, the skew distribution created a strong cavitating tip vortex which emitted high levels of acoustic pressure when deforming within the wake peak.

The experimental strategy of this study centred on the effects of various parameters on tip vortex cavitation dynamics (the so-called bursting phenomenon). One of the most important aspects of this study was the inclusion of four wake variations. The severity of each wake was determined by means of the wake fraction gradients. The developed wakes were tested with two propellers having different pitch distributions as shown in Figure 2-11. The experiments were conducted at different cavitation numbers and thrust coefficients in order to assess the influences of such parameters.



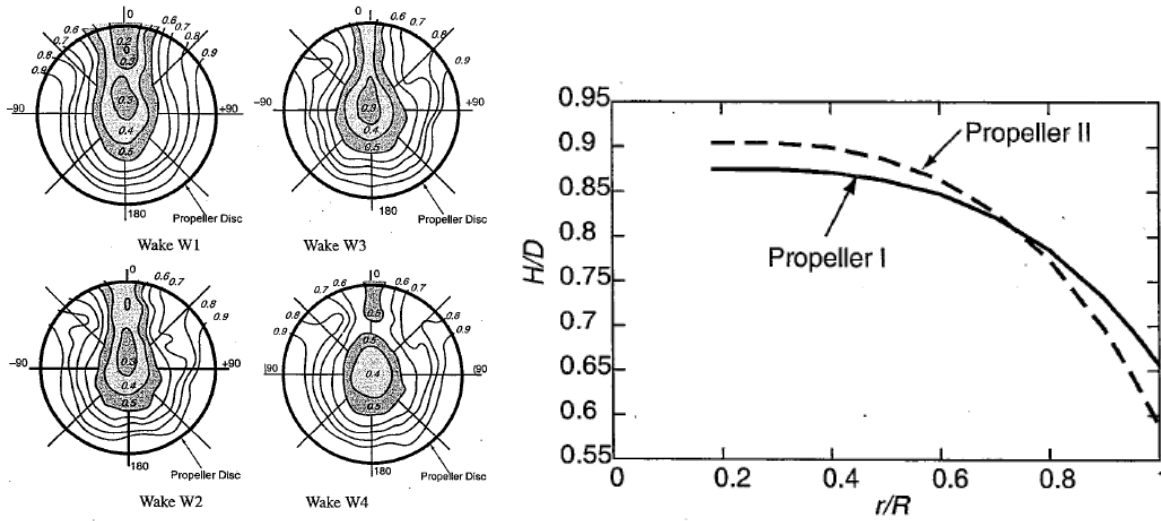


Figure 2-11 Wake non-uniformities (left) and propeller pitch distributions (right) of Konno et al., (2002)

The study draws some remarkable conclusions on the effects of such variants on the radiated noise levels. First of all, the wake inflow has a high influential on the radiated noise levels and the results of this study confirm that the cavitation noise increases with the increasing wake severity. Moreover, the study also indicates that the measured levels increase over the whole frequency range, as expected, with the decreasing cavitation number. Whilst certain trends are observed for the thrust coefficient and propeller pitch distribution they are more complex in nature due to the highly irregular cavitation interaction and dynamics. Although this work provides some vital evidence of how propeller cavitation noise changes with respect to propeller pitch distribution and operation parameters in conjunction with the flow non-uniformity alteration, it is limited by the absence of tests regarding the major propeller design parameters and small number of test conditions conducted.

The studies reviewed here point to a knowledge gap in terms of systematically designed experimental propeller tests. The research to date has explored the effect of single parameters on the radiated noise levels, however, there is no single comprehensive study of propeller geometry and wake structure that would enable implementation of a noise performance tool within the propeller design spiral and it is not practical to design and conduct such a complex experimental campaign. Thus, a series of experimental studies are required ranging from simple to complex in order to evaluate noise measurement capabilities of cavitation tunnel experiments.

One of the most simple to implement yet inherently unsteady experimental case is testing a propeller in oblique inflow condition. The inclined shaft introduces a cyclic variation of inflow conditions thus, a systematic variation of propeller cavitation performance and resulting noise signature. The implications of such a test case and previous studies on the subject are reviewed in the following subsection.

### 2.9.1 Inclined shaft effect on propellers

The inclined shaft effect and flow on a propeller is a well-known, fairly straightforward, unsteady flow phenomenon. It occurs either due to design choices in shafting configuration and afterbody shaping or due to motions of the vessels whilst underway. Shaft inclinations may be imposed in accordance with the engine arrangements, the need for sufficient propeller tip submergence, for increased minimum propeller tip clearance from the hull or for improving the wake flow to the propeller. On the other hand vessel motions can result from the stern wave, dynamic trim, pitching and heaving in heavy seas, and yawing and drifting of the vessel during manoeuvring. Figure 2-12 shows a sketch to describe some fundamentals of the inclined flow phenomenon.

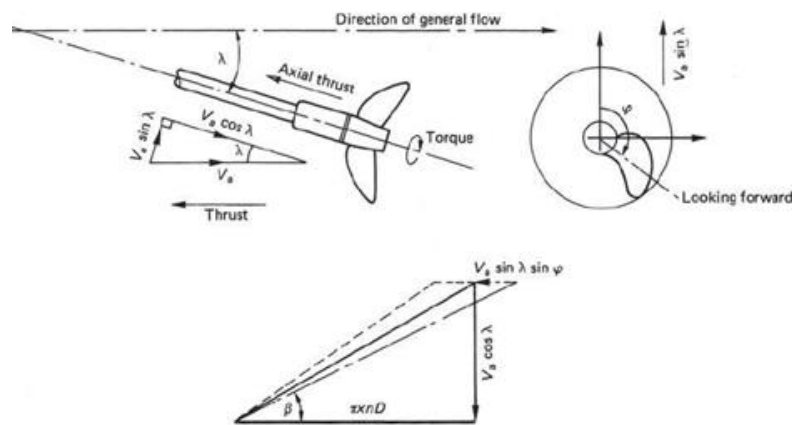


Figure 2-12 Inclined Flow Effect (Carlton, 2012)

Inclined flow imposes a cyclic variation of the incident tangential velocity and hence a change in the inflow angle to each aerofoil section comprising the propeller. This effect is more severe at the inner radii since the tangential velocity variation becomes a greater percentage of the shaft rotational vector compared to the blade tip speed. The oblique flow increases the variation in angle of attack and hence causes each blade section to operate farther from its design angle, inducing a range of cavitation and radiated noise issues.

The literature on propeller shaft inclination has hitherto explored the cavitation extent and overall performance forces and moments (thrust, torque) (Gutsche, 1964, Hadler, 1966, Taniguchi et al. 1969 and Kozhukharov & Sadovnikov 1983).

Gutsche's pioneering work included a combination of theoretical and experimental research work involving six model propellers. The propellers varied in terms of the BAR and P/D ratio, while all had a 200 mm diameter. The simulated shaft inclination angles were chosen as  $0^\circ$ ,  $20^\circ$  and  $30^\circ$ . The resulting experimental data was used to develop a quasi-steady flow analysis method. The explanatory English description of Gutsche's study can be found in (Hadler, 1966). Further experimental investigations were conducted in the Mitsubishi Experimental Tank (Taniguchi et al. 1969). using 5 super cavitating propellers with different P/D and expanded area ratios (EAR). These tests covered a relatively smaller range of shaft inclination angles:  $0^\circ$ ,  $4^\circ$  and  $8^\circ$ .

Although one may find further examples of other experimental studies as reported e.g. in (Carlton, 2012), the study conducted by (Kozhukharov & Sadovnikov, 1983) is of greater value due to its inclusion of detailed cavitation sketches for the conditions tested. The results obtained from this systematic series of propellers (designed using a lifting surface code) were used for populating the data and a validation study was conducted using the quasi-steady Gutsche method (Gutsche, 1964).

While the inclined flow effects can cause serious performance problems for a propeller - such as loss of thrust; erosion; intensified cavitation; and thrust and torque fluctuations - a comprehensive, systematic experimental investigation on inclined shaft phenomena is scarce. Underwater radiated noise data is even scarcer. Assessment of propeller cavitation and noise characteristics at different flow inclinations thus provides an essential body of such missing data.

### **2.9.2 ANN for data management & post processing of systematic experimental data**

Systematically designed propeller experiments comprise of a large testing matrix. Thus, it is unavoidable that such tests will result in a colossal amount of data. One of the most vital parts of carrying out experimental studies is the data management analysis procedure and post processing. Furthermore, such databases are also of utmost importance as they constitute a potential source for development of a database for statistical methods to enable prediction tools.

A survey of the various statistical methods has shown the potential of Artificial Neural Networks (ANN) with functionality to “learn” trends within the database using massive interconnection of simple computing cells referred to as “neurons”. Examples of ANN in the Marine field have been shown to excel not only in recognising complex patterns and trends but also with a high accuracy of predicting points that are outside the initial database. A plethora of studies have been conducted for a range of marine applications (Gougoulidis, 2008) in his comprehensive review. The versatility and power of the ANN is demonstrated through applications including: stability (Alkan et al., 2004), sea-keeping (Cepowski, 2007), preliminary ship design (Clausen et al., 2001), hull resistance prediction (Couser et al., 2004), diesel engine troubleshooting (Dimoulas & Nightingale, 1996). Whilst there are ample marine applications of ANN, the use of the neural network is also common for propeller design and performance prediction.

Noteworthy ANN studies were conducted by Neocleous & Schizas (1995, 2003, 1999) on a variety of propeller-based applications, including cavitation extent prediction, performance coefficient estimation for propeller design and performance comparison of Wageningen-B series propellers (Oosterveld & Van Oossanen, 1975) with United States Navy (USN) series propellers (Denny et al., 1989).

Another major work with ANN in the marine propeller field was made by Calcagni et al. (2010). An automated marine propeller design algorithm was developed based on data from a virtual standard propeller series using inviscid-flow model predictions. The method was then extended to the ducted propellers following confidence gained through initial comparisons.

One of the most distinguished applications of ANN for marine propellers was conducted by Seo et al., (2011). Based on the main standard series propeller design parameters, initially, an ANN was trained for the prediction of propeller performance coefficients. An additional network was also established for the extension to three-bladed propellers from the Meridian Standard Propeller series, (four, five and six-bladed propellers).

The studies reviewed in this section provide evidence that ANN is a well-established prediction and data management tool. Successful application of neural network methodology is clearly demonstrated through scientific applications in the marine field with specific focus on propeller cases. It is therefore concluded that ANN reveals itself as an outstanding tool to be utilized for the management of data produced through the execution of noise tests for a systematic propeller series.

## **2.10 Conclusions**

Chapter 2 has reviewed the literature in terms of the cavitation noise of a marine propeller. The literature review started with a brief history of underwater noise, then the background to the subject was provided, followed by an outline of the fundamentals of acoustics. Shipping noise was then considered as an anthropogenic source which causes disruption to marine fauna. Propeller design parameters and the subsequent cavitation effects on noise were then reviewed since cavitating propeller has been identified as the dominating source of underwater noise at service speeds. Other considerations such as propeller efficiency were also noted. Following this, various cavitation noise prediction methods were reviewed. Finally, systematically designed experimental propeller tests focusing on the cavitation noise were revisited together with the assessment of ANN as an efficient data management and associated prediction tool.

Based on the review conducted in this Chapter it has been noted that the subject of URN experienced a recent surge of research interest. This is due to increasing concerns about the noise emitted by commercial shipping and hence significant rise in the ambient noise levels of the world seas during the last seven decades as a result of global commerce and advancements in marine transportation. Whilst there are many environmental and anthropogenic contributors to the ambient noise spectrum the low-frequency regions are dominated by commercial shipping noise. Unfortunately, this frequency range is also used by marine mammals for various life-preserving activities. Thus, if the noise levels emitted by commercial shipping are not regulated, they may result in distress to these mammals and have longer-term implications which are still unclear but have the potential to be significant.

In order to be able to regulate and minimize the impact of commercial shipping on underwater radiated noise, accurate prediction at an early design stage is vital. Thus, this chapter critically reviewed various computational, empirical and semi-empirical methods. Regrettably, the review has revealed that although such above mentioned methods can give a rough indication of cavitating propeller noise, cavitation dynamics are the major noise sources which have not been represented by such methods.

Overall, it can be concluded that the state of the art is missing detailed information that can be produced by means of extensive experimental campaigns to enable the prediction of propeller cavitation noise. In addition, there is currently no practical way to provide a quick insight to the RNL performance of a vessel at an early design stage, due to the complexity of the dominant cavitation phenomena. Furthermore, a large body of publicly available URN data is non-existent, yet is vital for the development and validation of the more advanced prediction methods. The experimental approach to be adopted in this thesis can be thus justified. The nature of the tests are designed to both provide detailed information about experimental techniques and their validity as well as providing the public with valuable detailed URN data for ship and model scales.

## **Chapter 3   Experimental Facilities, Equipment & Data Analysis**

### **3.1   Introduction**

*Chapter 3 provides a description of the experimental facilities and equipment utilized within the framework of this thesis. Information on the major facilities is provided, such as the “Emerson Cavitation tunnel” and RV “The Princess Royal”. Following this, the main equipment inventory such as dynamometers, noise measurement, water quality monitoring, imaging devices, are introduced. Information regarding the complementary data analysis methodologies for the test results are provided, together with various guidelines.*

### **3.2   Emerson Cavitation Tunnel**

Newcastle upon Tyne has been a centre for cavitation research for more than 100 years and is credited with being the birthplace of the world’s first cavitation tunnel built by Charles Parsons in 1895 (Burrill, 1963) featuring a 2-inch tunnel. In 1910, Parsons built the first large tunnel (500mm square section) and following WWII a modern tunnel was erected in 1949. This was subsequently named the Emerson Cavitation Tunnel (ECT) (Atlar, 2000).

The tunnel has served the British ship industry and contributed to international research continuously since its inauguration in 1950, and it has undergone several major upgrades and modifications to maintain its status within the hydrodynamic research community as one of the living legends. The latest upgrade was in 2008 when significant portions of the facility were upgraded to ensure that state of the art experiments, of high accuracy, could be carried out.

The tunnel is a closed circuit depressurized tunnel with a measuring section of 3.1m x 1.21m x 0.8m (LxBxH), as shown in Figure 3-1 and Figure 3-2. More detailed information about the tunnel in detail after the recent upgrade is given by Atlar (2011) and general specifications can be found in Table 3-1.

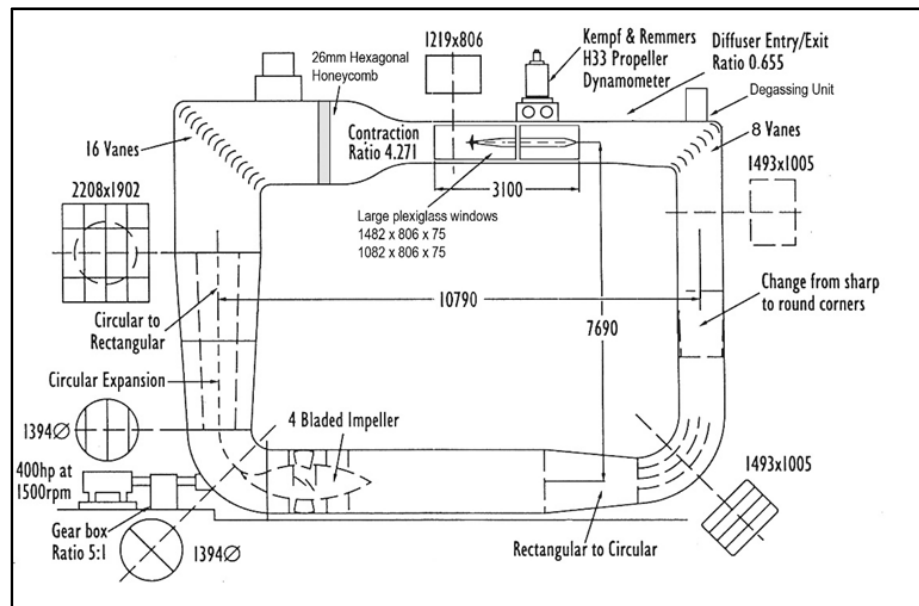


Figure 3-1 Sketch of Emerson Cavitation Tunnel.

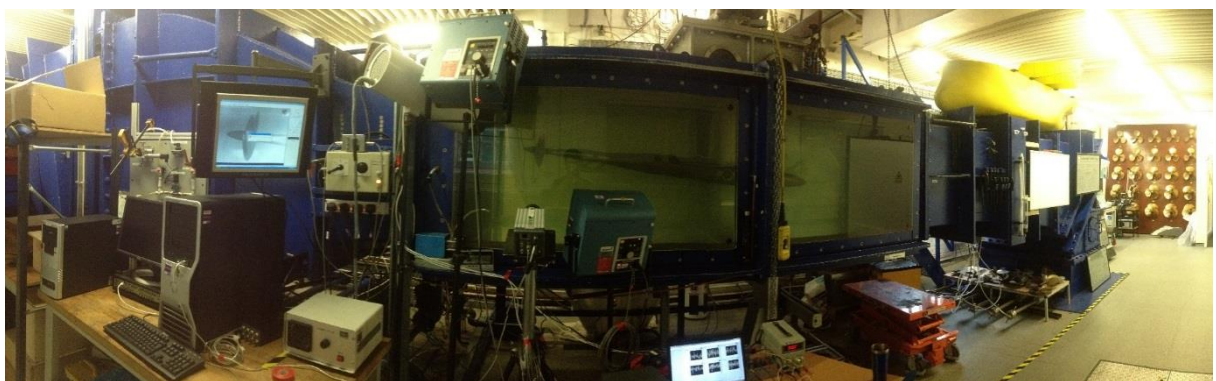


Figure 3-2 Panoramic view of Emerson Cavitation Tunnel and test set-up.



Table 3-1 Emerson Cavitation Tunnel specifications.

Tunnel	Emerson Cavitation Tunnel
Establishment year	1949
Description of facility	Vertical plane, closed circulating
Test section size (LxBxH)	3.10x1.22x0.81 m
Test section area	0.99 m <sup>2</sup>
Contraction ratio	4.271
Drive system	4 Bladed axial flow impeller with thyristor control
Main pump power	300 kW
Main pump rotational speed	294 Round Per Minute (RPM)
Impeller diameter	1.4 m
Maximum velocity	8 m/s (15.5 knots)
Absolute pressure range	7.6 kN/m <sup>2</sup> (min) to 106 kN/m <sup>2</sup> (max)
Cavitation number range	0.5 (min) to 23 (max)

### 3.3 Research Vessel “The Princess Royal”

Newcastle University replaced its aged, slow-speed mono-hull research vessel with a modern and relatively high-speed catamaran, named “The Princess Royal”, to support marine research, teaching and consultancy activities currently ongoing in the North East of England. The hull form of the new research vessel was designed by the staff and students of the School of Marine Science and Technology (MAST). The catamaran design was based displacement type Deep-V hull forms but with a novel anti-slamming bulbous bow and a tunnel stern as described in detail by Atlar et al. (2013). The vessel was built in aluminium alloy by a local North East Yard. Figure 3-3 shows the views of the research vessel whilst, Table 3-2 displays its main particulars.



Figure 3-3 Views of Newcastle University’s new research vessel, “The Princess Royal”.

Table 3-2 Main particulars of “The Princess Royal” as built.

Launching date & place	11 August 2011 & Alnmaritec, Blyth (UK)
Hullform	Displacement type Deep-V catamaran with symmetric demi-hulls
Length overall	18.88m
Length BP	16.45m
Breadth Moulded	7.03m
Breadth Extreme	7.34m
Depth moulded	3.18m
Demi-hulls separation ( $C_L$ to $C_L$ )	4.9m
Displacement (Lightship)	36.94tonnes
Draught (Lightship) (Amid - FP - AP)	1.65m – 1.6m – 1.7m
Deadweight data	7.32tonnes (Excluding 2tonnes of deck cargo)

Table 3-3 Propeller, engine and gearbox particulars of “The Princess Royal”.

Propeller particulars	
Number of propellers & type	2 (one per shaft) & fixed pitch
Propeller diameter	0.75m
Pitch to diameter ratio at 0.7R	0.8475
Expanded blade area ratio	1.057
Number of blades	5
Rake angle	0°
Skew angle (back)	19°
Direction of rotation	Port-left turning / SB-right turning ; outwards
Hub dia. to propeller dia. ratio	0.18
Blade thickness to propeller dia. ratio at 0.2R	0.04
Blade loading distribution (radially)	Wake adapted
Blade loading distribution (chordwise)	NACA $a=0.8$
Thickness distribution	NACA 66 modified
Material	Ni-Al-Br

<b>Engine particulars</b>	
Number of engines & Type	2 & QSM11-610 HO Cummins Mercruiser Diesel
Power rating (each)	449 kW (602 BHP) @ 2300 rpm
Cylinder-Displacement-Bore-Stroke	6 - 10.8lt – 125mm – 147mm
Fuel system	CELECT
Aspiration	Turbocharged – seawater after cooled
Fuel consumption at rated speed	117 lt/hr
<b>Gearbox particulars</b>	
Number of gearbox & Type	2 & QuickShift (Twin disc marine transmission) – MGX 5114 A (intermediate duty)
Reduction ratio	1.75:1
Input speed limits	330 rpm (min) / 3000 rpm (max)

### 3.4 The Equipment inventory

The experimental approach devised for this study required a large variety of instrumentation. While some equipment was already present within ECT (i.e. flow measurement devices, water quality monitoring system, propeller dynamometers, visual recording devices, noise measurement system), some new equipment was also found necessary (i.e. Pressure sensors and Data Acquisition system). This equipment is presented in this chapter together with the selected acquisition system, data presentation method and data analysing techniques.

#### 3.4.1 Flow measurement

Cavitation tunnel experiments involve detailed measurement and monitoring of flow properties such as the air content, velocity and turbulence intensity. Whilst flow measurements used pitot tubes in the past, today's technologies enable measurements without interrupting the flow; resulting in higher accuracies. Within the present studies, flow measurements were necessary for two instances. One was the simulation of the target wake in conjunction with a dummy model, as presented in Chapter 5 for which a Particle Image Velocimetry (PIV) system was used. The second was the construction of systematic axial wake variations for which wake screens were used together with Laser Doppler Anemometry (LDA) as presented in Chapter 6.

### 3.4.1.1 Particle Image Velocimetry

During the process of simulating a wake map in a cavitation tunnel, the traditional method of measuring the wake flow velocities was to use Pitot tubes. These have been replaced in recent years by laser-based systems allowing non-intrusive measurements. A PIV type field flow measurement device is one such time-saving, practical system. The Stereoscopic PIV (SPIV) device used in the ECT is a Dantec Dynamics Ltd system and a summary of its technical details is given in Table 3-4.

Table 3-4 Details about the Stereoscopic PIV.

Laser	NewWave Pegasus
Light sheet optics	80x70 high power Nd:YAG light sheet series
Synchronizer	NI PCI-6601 timer board
Camera	NanoSense MK III
Sensor size	1280x1024 pixels
Maximum capture frequency	1000Hz
Maximum images	3300
Calibration target	Multi-level 270x190 mm, 2 <sup>nd</sup> level -4
Seeding particles	Talisman 30 white 110 plastic powder

The SPIV setup used during the experiments for this thesis includes a laser illumination system; two high-speed PIV cameras; and a timer board to synchronize the whole measuring system. A Pegasus-PIV laser system, which consists of two IR laser heads, can generate high-energy laser light to illuminate the measuring area for a double-frame image-capturing task. And a closed laser light guide arm transfers the light to an 80x70mm light sheet optic to produce a light sheet and the velocity of seeding particles passing through the light sheet is measured. Therefore, the thickness of the light sheet is set 4 mm so that the camera can have enough time to capture the movement. Two high-speed cameras are used to capture the image from both sides of the light sheet and a traverse system is also included to move the light sheet and the cameras. The setup of the SPIV system in the ECT is shown in Figure 3-4. Although, PIV is a relatively expensive system in contrast to the traditional Pitot-tube measurements, it enables scanning a large area of the tunnel volume allowing streamline tracing and rapid positioning of the wire mesh screens for the simulation of the target wake as well as being non-intrusive to the flow.

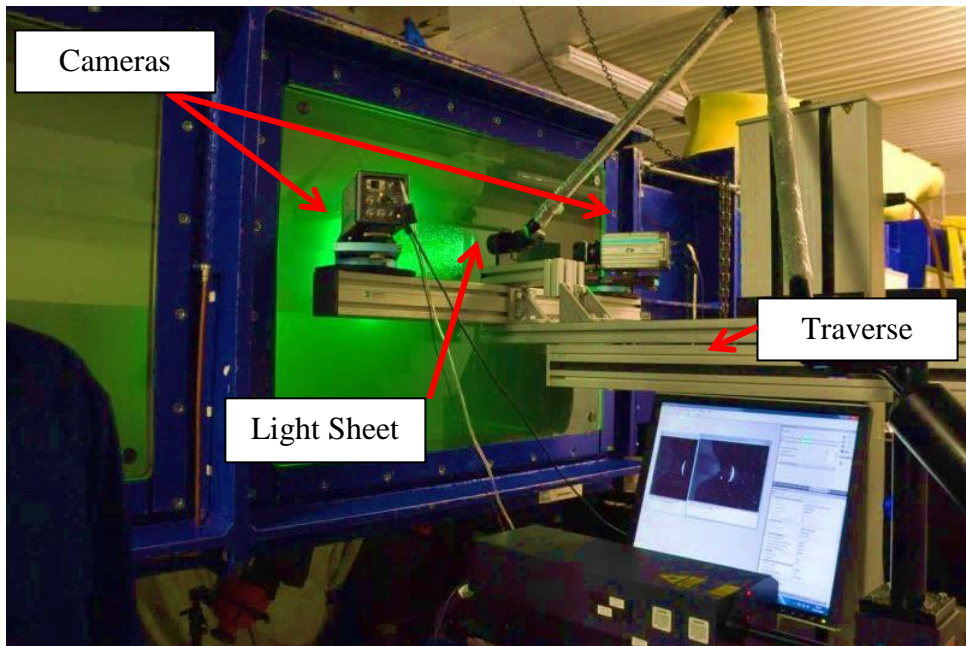


Figure 3-4 Setup of Stereoscopic PIV for measurement of Dummy Hull wake.

In order to calibrate the SPIV system, a multi-level 270x190 mm calibration target had to be used and therefore installed beside the propeller shaft at the wake plane, as shown in Figure 3-5. In the calibration process, it is generally assumed that the  $X,Y$ -plane where  $Z=0$  corresponds to the centre of the light sheet, but in practice this assumption may not hold since it can be tough to align the calibration target properly with the light sheet. In order to improve the accuracy of the calibration, the initial calibration results needed to be refined by combining the images acquired simultaneously from both cameras with a built-in calibration refinement function. The comparison is presented in Figure 3-6 along with the coordinate system definition. The green grid the initial calibration results, whereas the red grid represents the refined calibration results.

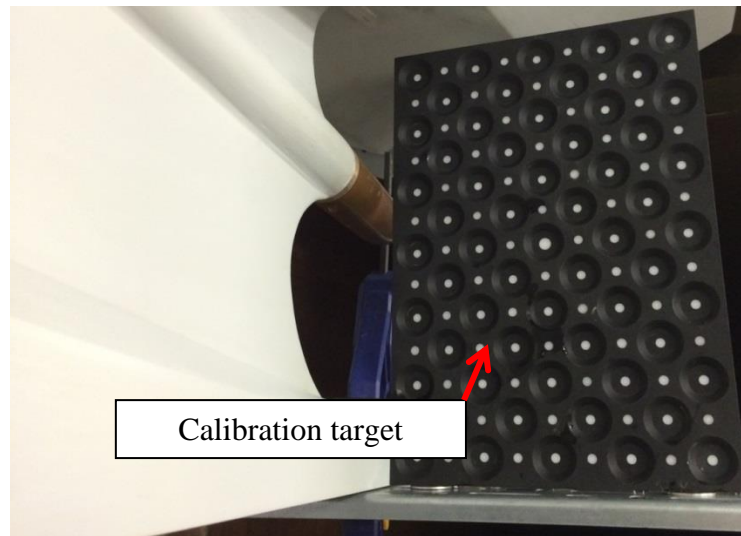


Figure 3-5 Calibration target installed on the dummy-hull model

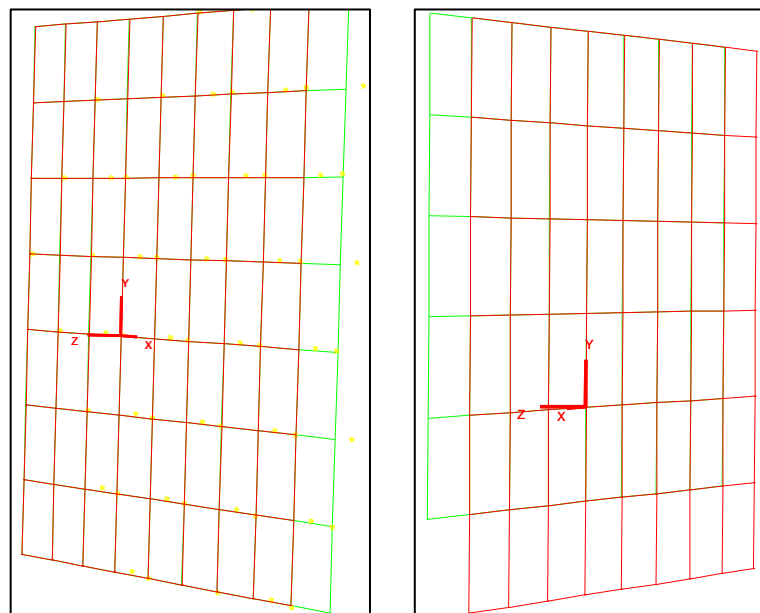


Figure 3-6 Calibration result (left image for the forward camera and right image for backward camera)

Throughout the measurements, 100 double frame image pairs are captured with a 100Hz frequency and 240 $\mu$ s delay between two frames. A sample of the captured images and a sample of the normalized cross-correlation map between two frames are illustrated respectively in Figure 3-7 and Figure 3-8. As shown in Figure 3-8, the peak value is much higher than the others in the interrogation area 64 $\times$ 64 pixels. Accordingly, the image quality and the seeding control are qualified for PIV measurement.

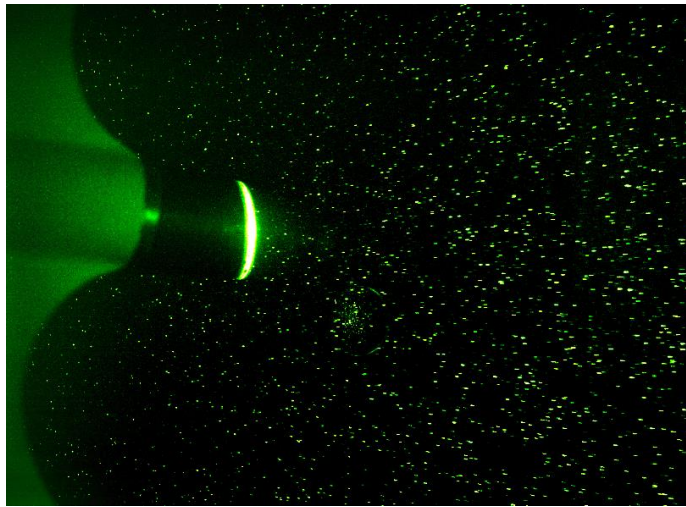


Figure 3-7 An example of PIV Images

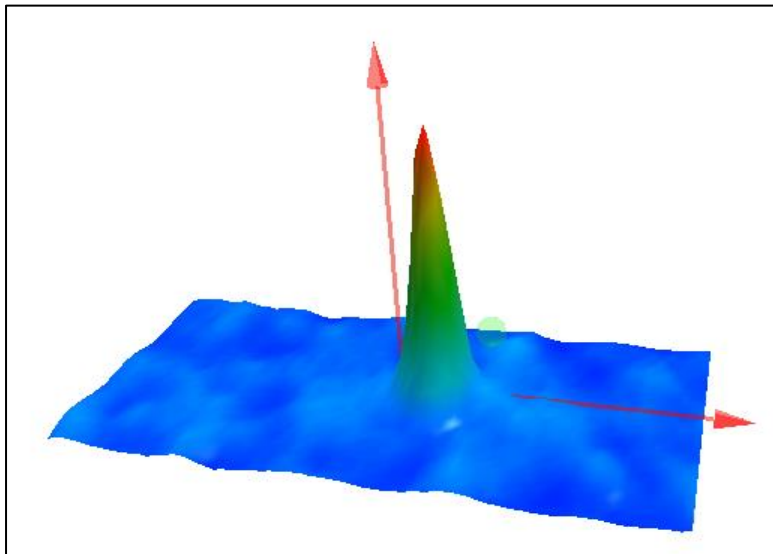


Figure 3-8 Normalised cross-correlation map

In order to analyse the images and hence to determine the flow velocities, at the beginning of data analysis, adaptive PIV analysis is used for the two-dimensional images from each camera. Range-validation and moving-average validation are used to eliminate invalid data. Afterwards, by combining the calibration results and the two-dimensional image data, SPIV results could be achieved. Finally, the results of the 100 samples are averaged to obtain the final SPIV result.

### 3.4.1.2 Laser Doppler Anemometry

LDA is an optical technique ideal for non-intrusive 1, 2 and 3 dimensional point measurement of velocity and turbulence distribution. The basic configuration an LDA/Phase Doppler Anemometry (PDA) is composed of a continuous wave laser, transmitting optics, receiving optics, signal conditioner and a signal processor. The laser beam is split in a Bragg cell (beam splitter) to produce a probe volume that is few millimetres long. The tunnel water is mixed with seeding particles, which scatters the laser light as they pass through the probe volume. The changing light intensity is then collected back by the receiver to be processed and transformed into the velocity and turbulence information. In the ECT LDA measurements are conducted with laser Doppler velocity device from Dantec Measurement Technology. A summary of its technical details is given in Table 3-5.

Table 3-5 Technical details of the LDA system.

LDA/PDA flow measuring device	Dantec Measurement Technology (upgradeable to 3 Dimensional LDA)
Electronics	Multi-PDA Signal Processor
Laser type and power	Genesis Air cooled Laser Diode System- Max 1.1W output
Probe details	60mm diameter 2 Dimensional submersible type with 500mm working distance
Traversing system	3-dimensional computer driven with a range of 590 mm x 690 mm

The development of novel systematic variations of axial wakes using wake screens is achieved using the LDA unit set up and run through BSA Flow Software (Figure 3-9). A measuring grid is defined at 1.5 propeller diameters downstream of the wake screen and included points on the non-dimensional radius ( $r/R$ ) values of 0.3, 0.5, 0.7, 0.9, 1.1 for every 10 degrees making up a total of 180 point measurements as shown in Figure 3-10.



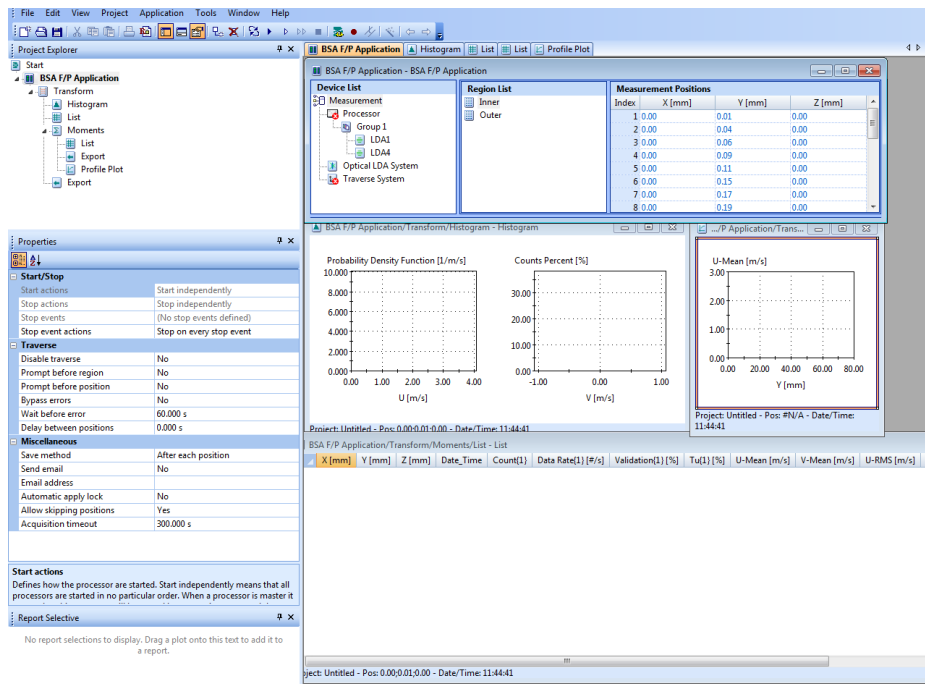


Figure 3-9 BSA Flow software user interface.

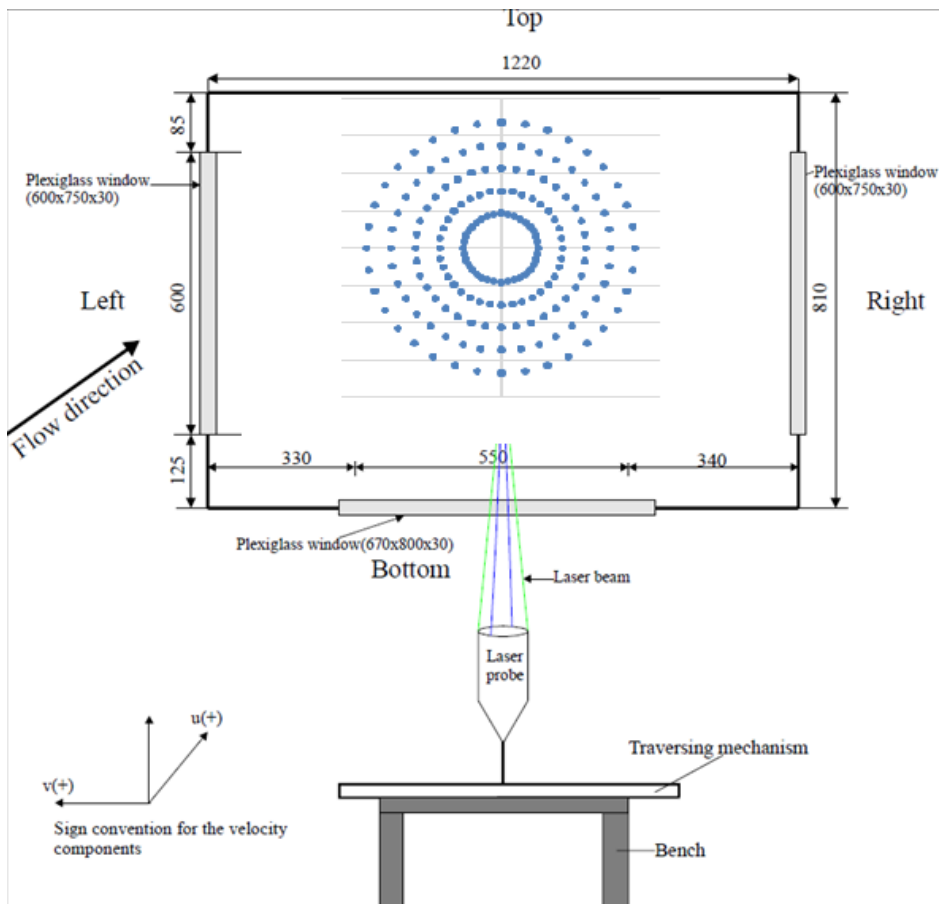


Figure 3-10 Grid of measurement points used for the wake screen development (reproduced from (Korkut, 1999)).

The measurement grid defined for the BSA software is modified to account for refraction of the beams in the water, hence there is a discrepancy between the set grid and the effective (actual) grid, i.e. the information relayed to the automated traverse system that controls the laser probe and the actual grid inside the measuring section. As the measurements were taken through the bottom window of the ECT only the 'z' (vertical component) is affected by the water refraction. At each measurement point conditional measurement is set as, 10000 samples or 30 seconds, whichever came first.

### **3.4.2 Water quality**

The cavitation experiments should always be performed under certain water quality conditions (ITTC, 2011c). The water quality of the ECT is monitored throughout all cavitation tests as it has a significant impact on the measurements. ECT has a dedicated water quality monitoring system and degassing system to keep the oxygen saturation level of the tunnel at desired level. The tunnel water quality is recorded using two systems in conjunction. The first device enables continuous monitoring of the water quality using the MS5 mini sonde (Figure 3-11) and the dedicated Hydrolab software. The probes attached to the tip of the mini sonde measure the water quality within a tubing arrangement through which tunnel water is pumped. The second device is a handheld meter for dissolved oxygen, from YSI instruments (Figure 3-12). This enables instantaneous on-demand measurements of the water quality for cross checking with the continuous monitoring system.



Figure 3-11 Hydrolab mini sonde MS5.



Figure 3-12 YSI 550A Handheld DO<sub>2</sub> Meter.

The ECT tunnel water is replaced annually with fresh water saturated in terms of the gas content. As such quantities of gas present in the tunnel water introduce measurement discrepancies, the gas content is regulated by means of a degassing system. The tunnel water is thus brought to the levels suggested by the ITTC (1987, 2011c). Gas content is one of the most influential parameter for the hydro-acoustic properties of the facility as well as dominating the cavitation dynamics, inception and extent. Higher levels of gas content will lead to a reduction in sound speed which changes the Mach number and the acoustic impedance of the fluid. The gas content should be kept to a minimum in model scale testing since too high of a gas content leads to a reduction of noise levels at high frequencies (Bark, 1986).

The ECT degassing method consists in creating an interface between the water and the local atmosphere and applying a vacuum. An expanded interface between the water and local atmosphere is obtained through the injection of millimetre air bubbles into the water through porous walls of submerged cylinders. The method is based on the idea of using the cavitation tunnel itself as the volume in which the water-atmosphere interface is formed. The tunnel provides a convenient environment for water degassing as it is already adapted to work under vacuum. The air bubbles are injected through a porous wall into water at the certain depth as shown in Figure 3-13. As the bubbles move vertically towards water free surface the dissolved air transfers from the water into the bubble's volume.

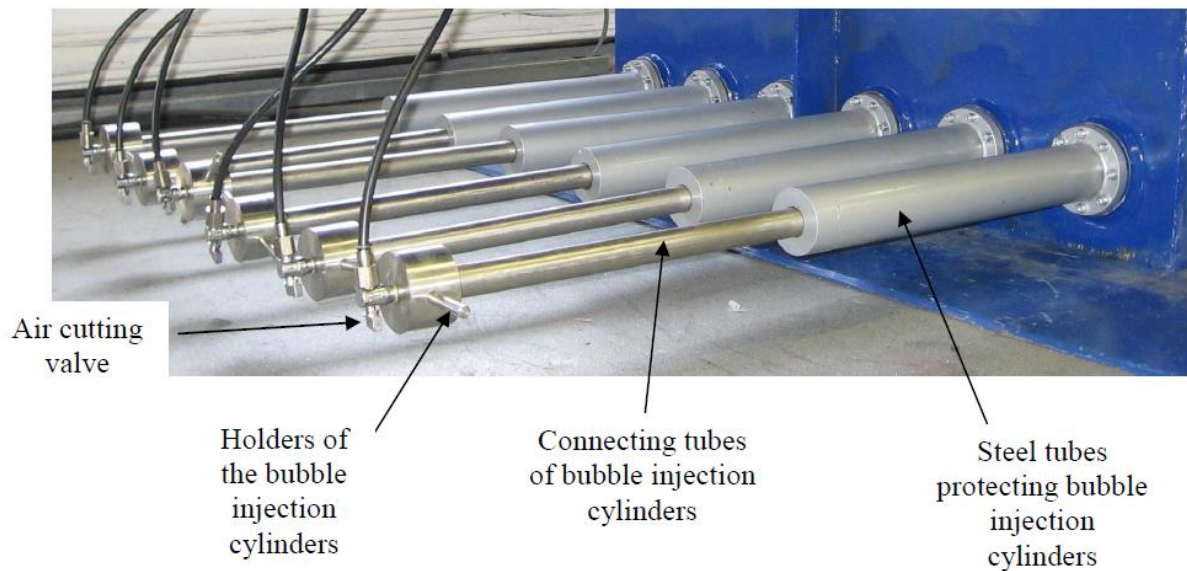


Figure 3-13 Bubble Injection cylinders of the ECT.

The injection of bubbles in the descending leg of the tunnel creates a slow, reverse flow due to the airlift effect. This process is shown schematically in Figure 3-14. The air buoyancy effect obliges the whole volume of the cavitation tunnel to cross the volume of the degasser. This enables de-aeration of the tunnel water without having the main pump working.

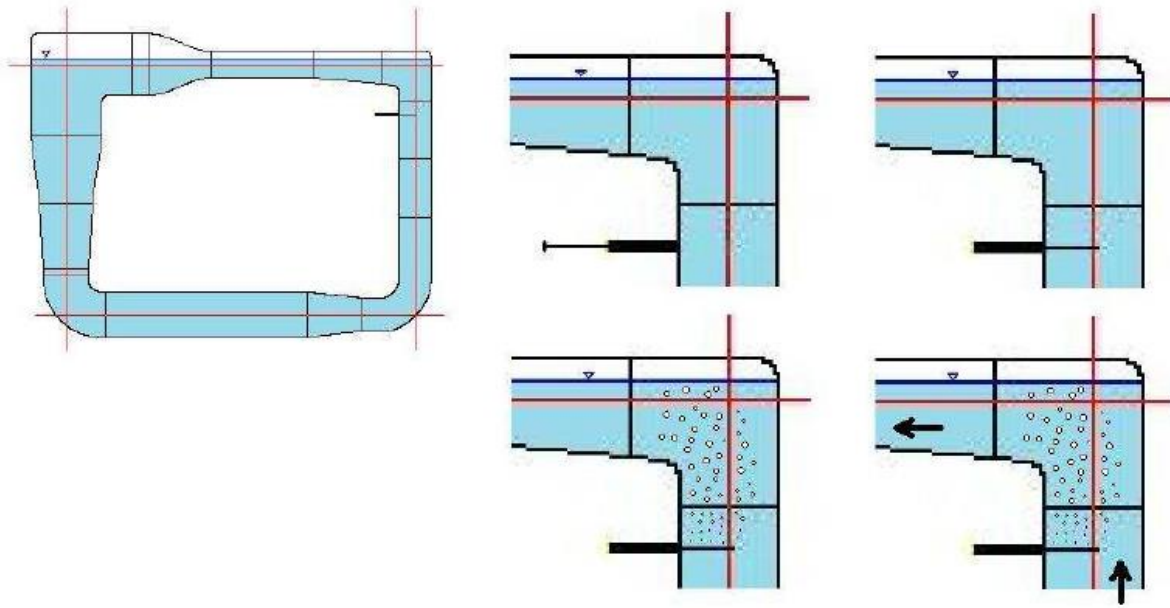


Figure 3-14 Degassing process of the ECT by application of millimetre bubbles under vacuum condition.

### 3.4.3 Dynamometers

ECT propeller tests are conducted using two high accuracy dynamometers. The experiments such as open water propeller tests are performed with H33 due to its higher torque and thrust range. Whereas, ship model cavitation tests and tidal turbine measurements are made with R45 as the measurement range of torque and thrust is smaller for such cases.

#### 3.4.3.1 Kempf & Remmers H33

The Kempf & Remmers H33 dynamometer, with its torpedo-shaped outline, is commonly used for open water experiments due to its relatively bigger range of thrust and torque compared to the Kempf & Remmers R45. The dynamometer is attached to the driving motor by means of a Cussons type H101-27 system for shaft height and angle adjustment, which facilitates testing for propeller inclination as well as yawing and heaving effects. The H33 is able to measure torque values up to 147 Nm and thrust values up to 2943 N with maximum permissible revolutions of 4000 RPM.

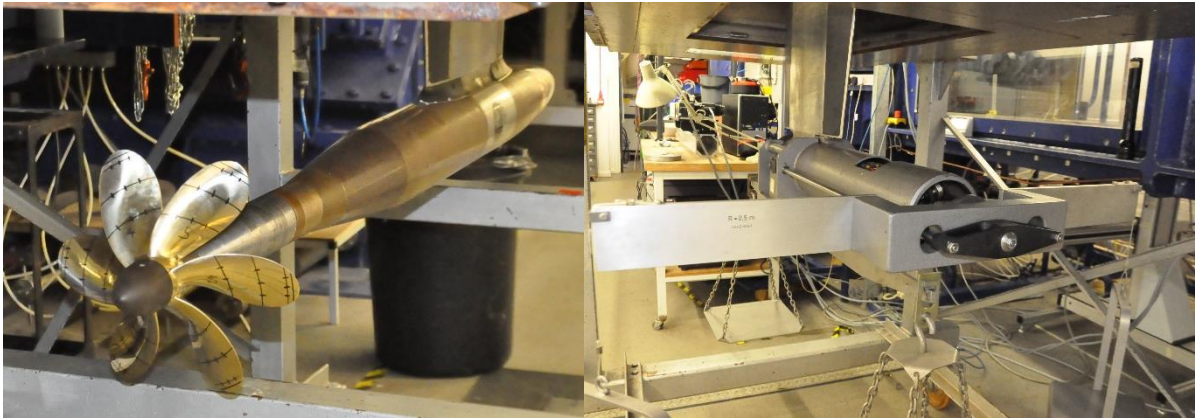


Figure 3-15 Kempf & Remmers H33 dynamometer attached to the bevel gearbox (Left) and during calibration (right).

### 3.4.3.2 Kempf & Remmers R45

Kempf & Remmers R45 dynamometer is dedicated to the relatively smaller ranged experiments such as model ship cavitation tests and tidal turbine testing. It has greater accuracy for low forces and moments and is suited to fit in the size of hull models installed in the ECT. The R45 is able to measure torque values up to 15 Nm and thrust values up to 400 N with maximum permissible revolutions of 3000 RPM whilst being run through a driving motor by means of a bevel gearbox as shown in Figure 3-16.



Figure 3-16 Kempf & Remmers R45 dynamometer attached to the bevel gearbox (Left) and during calibration (right).



### 3.4.3.3 Propeller performance data acquisition and analysis

The dynamometer measurements are used to calculate the propeller performance characteristics which enable extrapolation of the non-dimensional coefficients for the full-scale prediction. The acquisition from the dynamometer is made through National Instruments software and hardware as shown in Figure 3-17. An outline of the analysing procedure is described in order to give further insight into the propeller analysing methodology that is adopted.

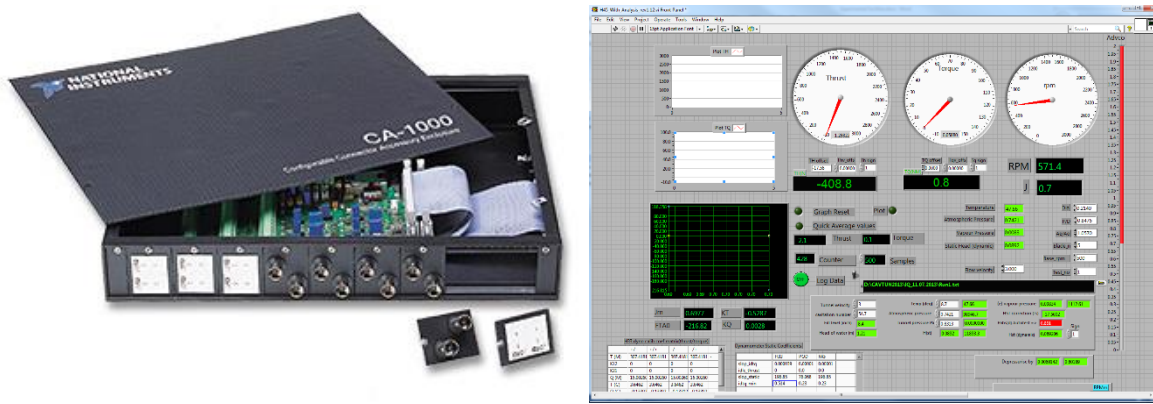


Figure 3-17 National Instruments hardware and software.

Following static calibration of the dynamometers, using the dedicated calibration rig, the propeller is replaced with a dummy hub of similar mass and diameter in order to conduct “idle” torque calibration to take into account of the shaft friction forces. Corrections to the measured torque are obtained from the idle torque calibration curve and applied using Equation 8:

$$Q = Q_m - q_0 \quad \text{Equation 8}$$

Following correction; the non-dimensional torque coefficient  $K_Q$  is calculated using Equation 9:

$$K_Q = \frac{Q}{\rho n^2 D^5} \quad \text{Equation 9}$$

The water speed is determined from the detailed LDA calibrations conducted and cross-checked with data from the Venturi manometer head and used to calculate the advance coefficient  $J$  using Equation 10:

$$J = \frac{V_A}{nD} \quad \text{Equation 10}$$

The thrust measurements are then corrected for two terms affecting the acquired data. The pressure differential effects on the thrust in terms of the static pressure head are calculated using Equation 11. The boss drag, due to the water speed is found with Equation 12.

$$T_S = 196.85 \times H_{ST} \quad \text{Equation 11}$$

$$T_D = 0.4267 \times V \quad \text{Equation 12}$$

The correction to the measured thrust is applied by adding the boss drag and static pressure head correction. The corrected value of thrust is be found by  $T_{cor}$  using Equation 13:

$$T_{Cor} = T_{measured} + T_S + T_D \quad \text{Equation 13}$$

Following the correction applied the non-dimensional thrust coefficient  $K_T$  is calculated using Equation 14:

$$K_T = \frac{T_{Cor}}{\rho n^2 D^4} \quad \text{Equation 14}$$

One of the important non-dimensional coefficients for the cavitation tunnel tests is the Reynolds number at a reference location on the propeller blade. The general tendency is to calculate it at the non-dimensional radius 0.7 r/R using the Equation 15. The Reynolds Number does not necessarily need to be equal to the full-scale value, but it should be as high as possible in order to maintain turbulent flow over the blade surfaces and to minimize the scale effects. It is important that the Reynolds Number for the test should have a minimum value of  $5 \times 10^5$  whenever possible to avoid scale effects occurring (ITTC, 2011c).

$$R_e = \frac{C_{0.7R} \sqrt{V^2 + (0.7\pi nD)^2}}{\nu} \quad \text{Equation 15}$$

The main purpose of cavitation tunnels is the accurate simulation of cavitation phenomena. However, the definition of the cavitation numbers varies according to the main interest in an experimental campaign; namely, the free stream, rotational or resultant cavitation number.



A cavitation number based on the free stream velocity is used for the experiments where propeller RPM is fixed and the tunnel flow velocity is altered. Thus, the equation is independent of the RPM term focusing on the velocity inflow as given by Equation 16.

$$\sigma_v = \frac{P_a + \rho g h_s - P_v}{0.5 \rho V^2} \quad \text{Equation 16}$$

A rotational cavitation number is used when the cavitation phenomenon of interest mainly relates to the rotational speed of the propeller. Although no term for the free stream velocity is included, this factor implicitly accounts for static head variations due to the flow speed. Being able to represent both flow velocity and inflow variation, the rotational cavitation number is commonly used for propeller cavitation tests and is calculated from Equation 17.

$$\sigma_n = \frac{P_a + \rho g h_s - P_v}{0.5 \rho (\pi n D)^2} \quad \text{Equation 17}$$

Amongst these variations in cavitation number formulations, the most accurate and definition is the resultant cavitation number due to its relatively more complex formulation. The calculation includes terms for both rotational speed of the propeller as well as the axial velocity component as in Equation 18.

$$\sigma_{vr} = \frac{P_a + \rho g h_s - P_v}{0.5 \rho (V^2 + 0.7 \pi D n^2)} \quad \text{Equation 18}$$

Throughout this thesis, different cavitation numbers are utilized depending on the nature and focus of the experiment. For example, Chapter 4 of this thesis involves open water tests which cavitation number is defined as the free stream version whilst Chapter 5 utilizes rotational cavitation number as it presents the ship model cavitation tests.

### 3.4.4 Cavitation observations

Since Parson's first cavitation tunnel experiments, visual observations and recordings have allowed a plethora of cavitation phenomena to be understood and interpreted both quantitatively and qualitatively. The observation techniques have ranged from sketches to high-speed video and PIV imaging.

Within the current work, a large number of different types of cavitation observation have been applied in order to gain insights into the nature and dynamics of propeller cavitation. Photographing propellers is a notoriously difficult application, so a range of cameras and methods were used in order to cover as many possibilities and opportunities to get decent and useful images.

The imaging techniques, however, differed for ship and lab based applications. Therefore, although inventory of the photography equipment was the same, the imaging techniques were relatively different and hence are covered separately. Table 3-6 shows the specifications of the cameras and lenses used.

Table 3-6: Camera Specifications.

Nano Sense MkII 512×512 Pixels, USB and GigE	<u>10000 Hz 8Gb ram</u> 32800 Images, 3.3 Sec
Nano sense MkIII 512×512 Pixels, USB and GigE	<u>2000 Hz 8Gb ram</u> 6600 Images, 3.3 Sec
Nikon D700 + 20mm f2.8 lens	6400 ASA giving 1/1000 sec at f 2.8 still images
Nikon D90 Digital SLR Camera	4800 ASA giving 1/4000 sec at f 1.4 still images
Olympus Swing prism borescope with Watec camera	30 fps video

The full-scale imaging techniques included a borescope inserted through the hull using a hollow bolt and ball-valve fitting, high-speed video recording, through flush-mounted windows, with continuous lighting and with shaft-triggered strobe lighting, still imaging using a digital single-lens reflex camera (DSLR) and compact digital camera recordings with stroboscopic lighting.

Borescope observations on the vessel were made using dedicated housings inserted through M20 tapped holes and a ball-valve fitting. The fitting is initially put into the place alongside, while at the start of the trials the borescope is carefully inserted, the valve is opened and the eye piece is used for focussing. Video recordings are made using an eyepiece adapter with a C-mount thread for attaching the WATEC camera as shown in Figure 3-18. Re-focussing is necessary when using the camera since its focus plane differs from the observer's retina plane. Figure 3-19 shows the trials equipment including the eyepiece, light amplification unit, camera and exposure control unit. Images are acquired through a laptop using dedicated software. Although the camera is rated at 0.000015 Lux, the light amplification unit is essential when using a high shutter speed and due to severe light transmission loss in the borescope optics.



Figure 3-18 Full-scale borescope cavitation observation arrangement.



Figure 3-19 Borescope observation technique parts.

Nanosense high-speed video cameras were used with the porthole setup on the trials. The cameras were adapted from their usual PIV setup for use with 35mm lenses. The cameras were paired with a continuous, high-wattage lamp with sufficient in-built cooling to be used close to the porthole glass for continuous recording. Additionally, the cameras and a strobe unit from the tunnel were linked through a synchronising trigger system. Better images of the cavitation were obtained with stroboscopic lighting, but the cavity dynamics were better understood under continuous lighting.

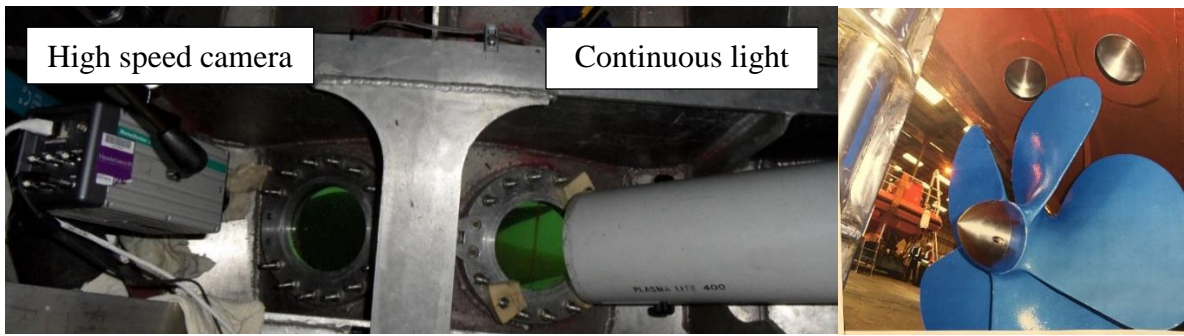


Figure 3-20 Full-scale high-speed camera cavitation observation setup through observation windows.

Still images were taken through the cavitation observation portholes with a full frame 35 mm Nikon D90 DSLR Camera fitted with a distortion-free 20 mm f 2.8 lens. This camera coupled with the high-intensity light gave the best resolution images. The images were limited only by the narrow scatter possible with the light source and the lack of a timing trigger.



Figure 3-21 Full-scale DSLR Camera sample image.

The model-scale imaging techniques included, high-speed video recording with continuous lighting or with triggered stroboscopic lighting, still imaging using DSLR and flash-cam video with stroboscopic lighting. Unlike the full-scale experiments the large Plexiglass observation windows of the tunnel allowed a clear view of the propeller blades with plenty area to determine the best position for image acquisition.

The most commonly used observation technique for the cavitation tunnel tests are the high-speed camera recordings aided with stroboscopic lighting synchronized with shaft position signal as shown in Figure 3-22. This enables freezing the image due to the triggered flash provided by the strobe lights. Stroboscope lighting also accommodates the still imaging with a DSLR camera by reducing the shutter speed in order to fit the image acquisition into the short bursts of the strobe flash.

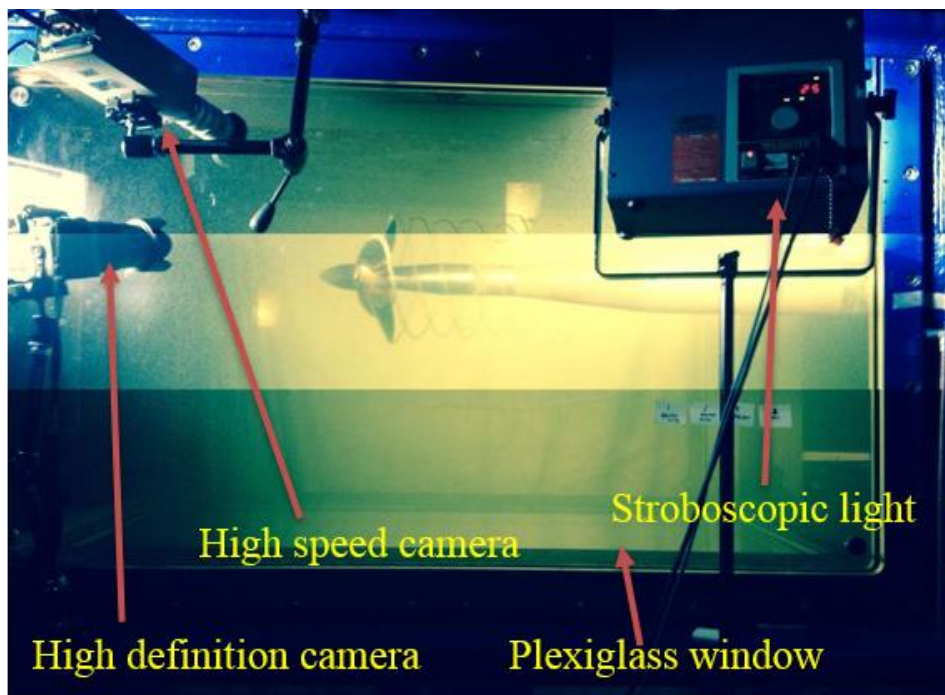


Figure 3-22 Cavitation observation using stroboscopic lighting.

Whilst observing blade images synchronized with the shaft speed simplifies the adjustment of the cameras, in non-uniform inflow, it is essential to record information on cavitation dynamics. Therefore, the high-speed cameras were also used at 5000 fps in a continuous recording mode for the non-uniform inflow conditions. A high-intensity light source was obtained from Plasma-Lite continuous light as shown in Figure 3-23, to allow a high acquisition rate for the high-speed cameras. The measurements were performed whilst capturing videos and pressure synchronously in an effort to relate cavitation images to characteristics of the measured pressure time-series. This was achieved by connecting the high-speed cameras and the Data Acquisition (DAQ) system to a signal generator, which helped filter out the signal from the motor shaft for triggering purposes.



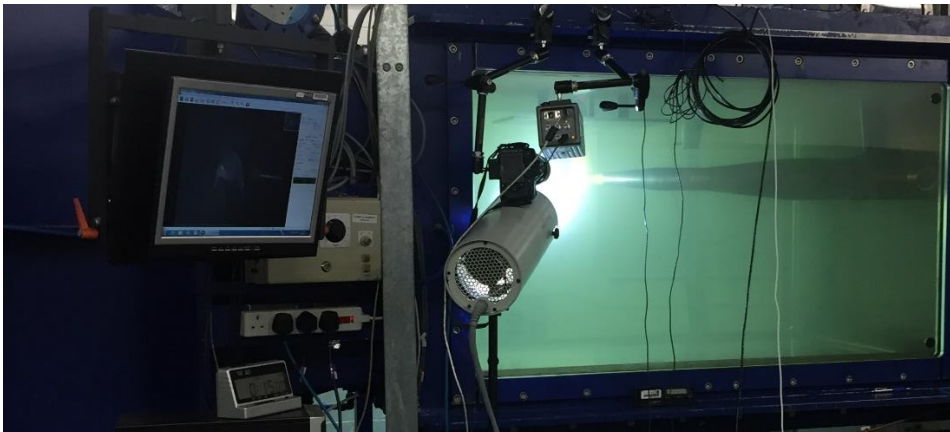


Figure 3-23 Model scale continuous light cavitation observation set-up at ECT.

### 3.4.5 Pressure sensors and data acquisition

The pressure pulse measurements are a vital part of propeller cavitation experiments. They relate to forced excitation of the stern part of the hull and consequent potential accumulation of fatigue cracks and an indication of potential erosion problems (van Wijngaarden, 2011, 2005). During the course of the present cavitation tunnel tests and full-scale trials, pressure pickups have been installed to measure the pressure pulses. Details are given in Table 3-8, Table 3-9 and Table 3-10. Through such measurements extrapolation methods may be applied to the model scale measurements for scaling and comparison with the full scale.

The pressure data from the sensors were acquired using the National Instruments (NI) DAQ system. The cDAQ 9178 chassis was used with the NI 9239 module for the output signal recording of the pressure sensors. The pressure sensors were excited using a laboratory direct current power supply being distributed to the each sensor by means of a dedicated pressure transducer excitation voltage and junction Box as shown in Figure 3-24. The spare module slots of the chassis were then utilized for various other measurements such as the acceleration measurements using NI 9234, various digital input/output signal recordings using NI 9401 and voltage measurements using NI 9215. The modular approach adopted, enabled the acquisition from different sensors to be executed using a single system as outlined in Table 3-7.

Table 3-7 Components of DAQ System.

Product Number	Description
781922-01	NI 9924 Front-mount terminal block for 25-pin D-Sub Modules
779593-01	NI 9239 4-Ch $\pm 10$ V, 50 kS/s/Channel, 24-bit, Channel-Channel Isolated AI Module
779351-01	NI 9401 8-Channel, 100 ns, Transistor-Transistor Logic (TTL) Digital Input/Output Module
779680-01	NI 9234, 4 Input, 24-Bit, 51.2 kS/s, SW Selectable IEPE & AC/DC
781156-01	cDAQ-9178, Compact DAQ chassis (8 slot USB)
779138-01	NI 9215 with BNC 4-Ch $\pm 10$ V, 100 kS/s/Channel, 16-b, SS Diff. AI

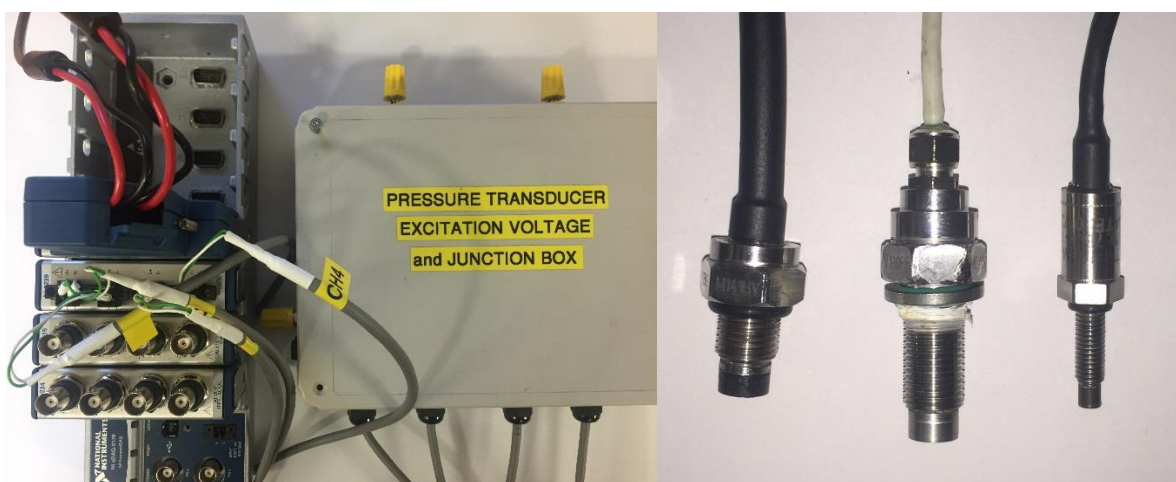


Figure 3-24 Pressure and vibration Data Acquisition Hardware including NI CDAQ Chassis with Modules and pressure sensors.



Fast Fourier Transform (FFT) analysis was applied using NI DIAdem software (National Instruments, 2014). The FFT applied had the Hanning window type and displayed the results in peak amplitudes with no average applied. The application of the FFT analysis provides the  $i$ -th harmonic of the blade rate for each shaft speed of the time signal. The analysed results of the pressure peak amplitudes are recorded for the blade rate harmonics as presented in Figure 3-25.

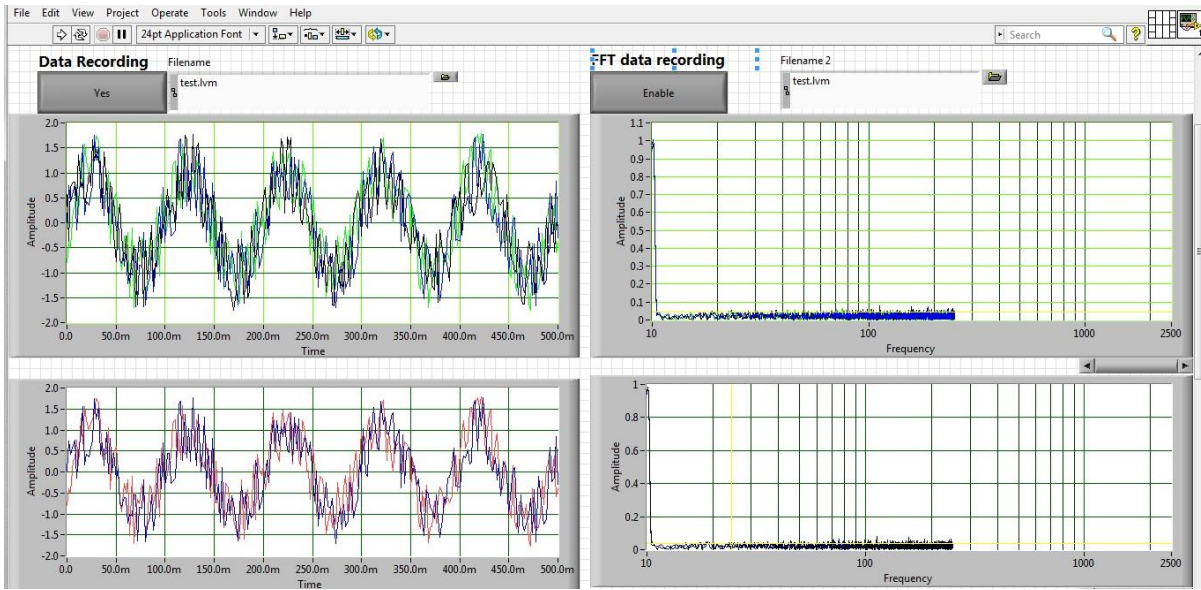


Figure 3-25 Appearance of typical simultaneous pressure Pulse Acquisition (left) and FFT analysis (right) in the Labview software domain.

The pressure signals for ship trials and model tests are presented as the non-dimensional pressure coefficient;  $K_p$  defined in Equation 19.  $K_p$  value is assumed to be constant for model  $K_{p,m}$  and full-scale  $K_{p,s}$  according to ITTC (1987). The pressure values presented throughout the thesis are extrapolated based on the above assumption and using Equation 19.

$$K_{p,m} = \frac{p_m}{\rho_m n_m^2 D_m^2} = K_{p,s} = \frac{p_s}{\rho_s n_s^2 D_s^2} = K_p \quad \text{Equation 19}$$

The pressure measurements are conducted with three different pressure transducers used in full-scale trials and model tests. Table 3-8 provides the details for the full-scale sensors. These were not used for the tunnel tests due to their limitation of working under vacuum and IP67 rating (i.e. waterproof up to 1m submergence into water). Therefore, for cavitation tunnel tests; prototype MEAS pressure sensors (Table 3-9) and Kulite pressure sensors (Table 3-10) are used.

Table 3-8 Full-scale Pressure sensors specification.

Part Number	Description	Quantity
XPM10-S107-05BS	Miniature Pressure Sensor	4
Range: 5 bar sealed Excitation: 10 to 30VDC Output: 0.5VDC to 4.5VDC Ingress Protection: IP67		

Table 3-9 Model-scale Measurement Specialities model Pressure sensors specification.

Part Number	Description	Quantity
XP1102-S107-05BS	Miniature Pressure Sensor	2
Range: 1 bar gauge Excitation: 10VDC Output: 0 to 100mVDC Ingress Protection: IP68		

Table 3-10 Model-scale Kulite Pressure sensors specification.

Part Number	Description	Quantity
Xtm-190M-3.5BARA	Miniature Pressure Sensor	2
Range: 3.5 bar Absolute Excitation: 10VDC Output: 0 to 100mVDC Ingress Protection: IP68		

The pressure pulse acquisition used a 5000 Hz sampling rate for 5 seconds, totaling 25000 samples for each recording. The acquisition rate was limited due to the transmission properties

of the pressure sensors, losing the linearity at the higher frequencies. The data recording was initiated by a signal from the dynamometer speed decoder, conditioned with a signal generator in order to enable synchronization with other simultaneous measurements. With a view to ensure accurate pressure transducer measurements, a thorough investigation has been carried out. The tests involving each element of the pressure data acquisition system and the effect of pressure sensitivity is conducted. The results confirmed the accurate measured levels of the cavitation induced pressure pulses.

### **3.4.6 Noise measurement equipment and analysing methodology**

Historically, the Emerson Cavitation Tunnel was designed as an acoustic research channel when it was originally established at *Pelzerhaken* in Germany. “The tunnel was one of the units of the underwater acoustic research complex *Nachrichten Versuchsanstalt; Pelzerhaken* constructed in 1938-40. This complex was situated on the shores of the Baltic Sea in Lubeck Bay and specialised in underwater acoustic research during the war, involving the inception of cavitation on sound domes, with the purpose of determining the physics of the phenomenon, as well as designing shapes for surface vessel and submarine sound locators. Other work at this complex included the development of a rubber coating for submarine hulls as an anti-locating measure, which could be tested in this tunnel. The development of hydrophones and that of depth charge proximity fuses operating on the Doppler principle for detonation below the plane of operation of an attacked submarine were part of these activities” (Atlas, 2000). However after shipping the tunnel to the Newcastle, the tunnel was reconstructed as a propeller testing facility; the initial tunnel measurements indicated that the noise level of the overall facility was high (Clarke, 1987). With the recent improvements and upgrades to the Emerson Cavitation Tunnel, the background noise levels have significantly reduced and can be considered as a reasonably silent commercial cavitation tunnel for practical propeller noise measurements (Korkut & Atlas, 2012b).

ECT noise measurements were made using the Bruel & Kjaer (B&K) PULSE Type 3023 data acquisition system with a 6/1 local area network (LAN) interface and the B&K Type 8103 miniature hydrophone.

A sketch of the B&K 8103 hydrophone is given in Figure 3-26 (left). Two different hydrophone location configurations for the noise measurement were adopted during the course of this study, one of which located the hydrophone inside the tunnel using a foil strut support as shown in Figure 3-26 (right). The other configuration attached the hydrophone in a water-filled, thick walled steel cylinder which is usually placed on the 70mm thick Plexiglass window of the tunnel parallel the propeller plane. The latter configuration is no longer utilized due to the poor high frequency response in comparison to the inside tunnel configuration following the experience through the inclined shaft tests that are presented in Chapter 4.

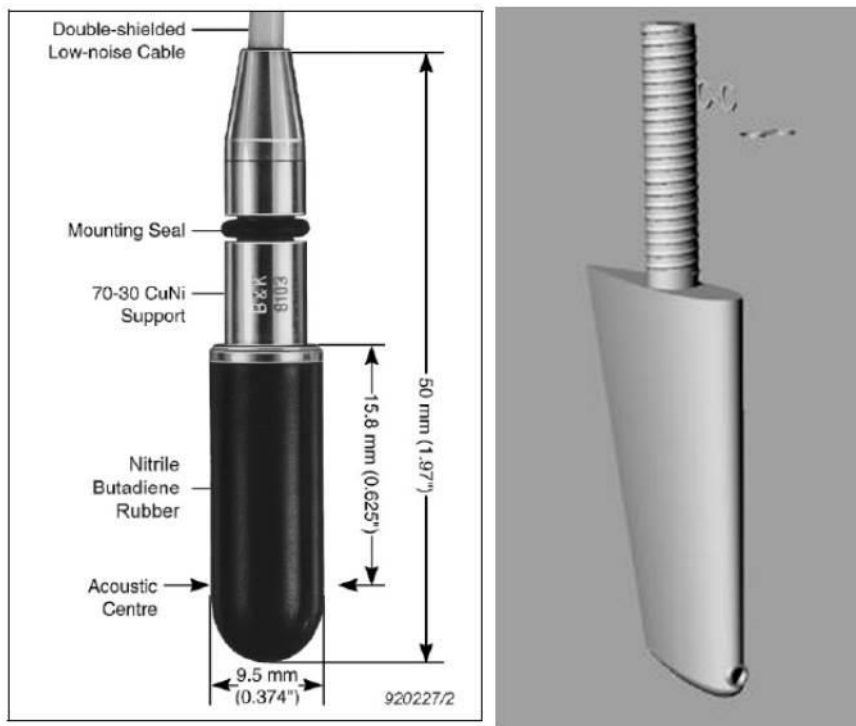


Figure 3-26 B&K Type 8103 Hydrophone (on the right) and its streamlined foil support to fit inside the tunnel test section (on the left).

Figure 3-27 presents further details of the B&K 8103 hydrophone; the top sketch in this figure shows the calibration configuration of the B&K 8103 with the Piston-phone Type 4223 and the coupler UA-0548. Even though the hydrophones were factory-calibrated, this set-up provided quick and accurate calibration and ensured the factory calibration was still valid. The calibration

frequency, nominally 250Hz, was  $251.2\text{Hz} \pm 0.1\%$  as defined by ISO 266. The sound level produced by the Piston-phone was nominally  $156.8 \pm 0.2 \text{ dB re } 1 \mu\text{Pa}$  at the reference conditions.

The middle sketch in Figure 3-27 shows the connection diagram. The hydrophone was submerged in the water up to the BNC connection end. The connection end should be avoided from water at all times. The bottom sketch of Figure 3-27 is the receiving frequency characteristics of the hydrophone indicating a linear response of the hydrophone up to 20 kHz.

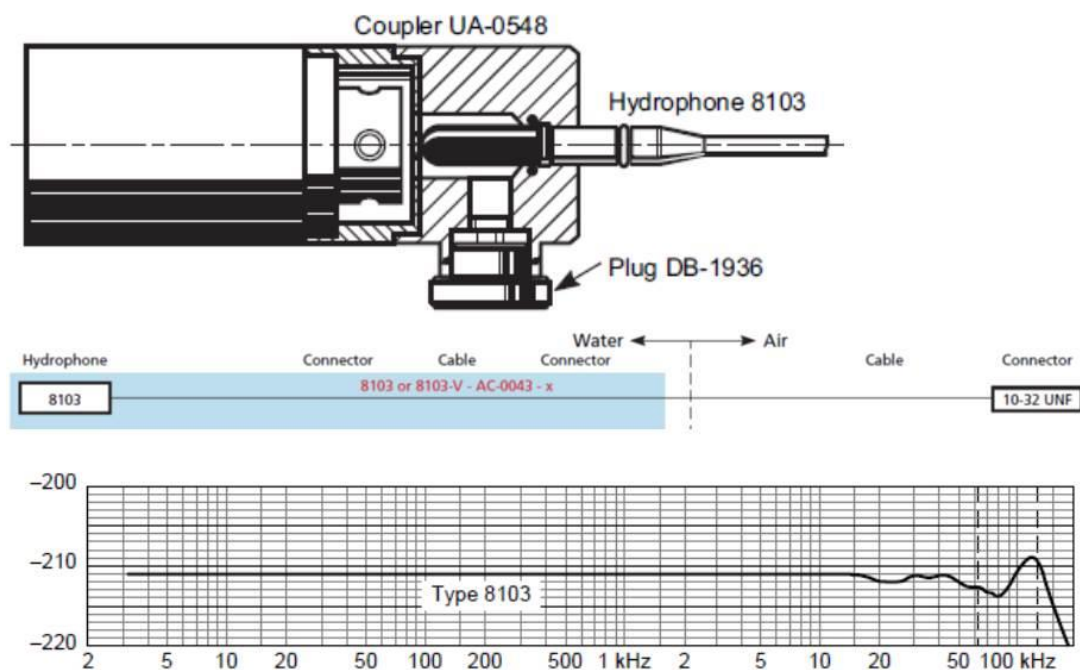


Figure 3-27 Calibration configuration of the Hydrophone (Top). The connection diagram of the hydrophone (Middle). Typical Receiving Frequency Characteristics of B&K 8103 (Bottom).

The noise signals were processed by the PULSE lab-shop by using Constant Percentage Bandwidth (CPB) and Fast Fourier Transform (FFT) analyser that were constructed in its dedicated software. The analysed results were presented in 1/3 octave bandwidth for 20 Hz to 20 kHz and 1Hz band levels for 1 Hz up to 6.4 kHz.

The noise data acquisition for 1/3 Octave band was conducted by using the waterfall format of the PULSE in order to eliminate the effect of any instantaneous sources as can be seen in Figure 3-28. This was achieved by using the multi-buffer option of the software which triggers the system every 0.25 seconds for the next measurement. The measurements were recorded for 200 triggers or 50 seconds at 45 kHz sampling rate. The noise measurements are carried out for 50 seconds and 200 individual recordings. The average of such a long measurement ensured the repeatability and determination of uncertainty for the conducted measurements.

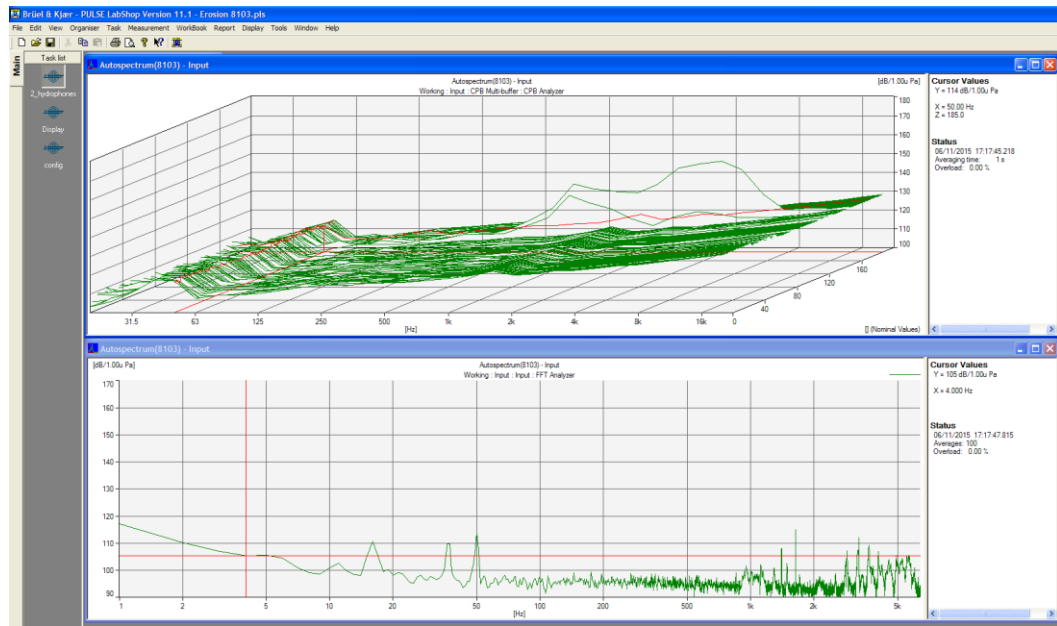


Figure 3-28 Pulse Labshop DAQ window.

The acquired data was considered to be in raw format since the measured values needed to be corrected to an equivalent 1 Hz bandwidth and 1m source level. A common practice in the analysis and presentation of the noise levels is to reduce the measured values of *SPL* in each 1/3 Octave band to an equivalent 1 Hz bandwidth by means of the correction formula recommended by ITTC (1987) as in Equation 20.

$$SPL_1 = SPL_m - 10\log\Delta f \quad \text{Equation 20}$$

where;  $SPL_1$  is the Sound Pressure level in 1 Hz band in dB relative to 1  $\mu$ Pa.  $SPL_m$  is the Sound Pressure level in 1/3 Octave band in dB relative to 1  $\mu$ Pa.  $\Delta f$  is the frequency bandwidth for the 1/3 Octave band for each centre frequency.

The ITTC also requires that the sound pressure levels be corrected to a standard measuring distance of 1 m using the spherical acoustic wave propagation relationship using Equation 21.

$$SPL = SPL_1 + 20\log(r) \quad \text{Equation 21}$$

where;  $SPL$  is the Sound Pressure Level in 1 Hz band in dB relative to 1  $\mu\text{Pa}$  at 1 m.  $r$  is the distance of the location of the hydrophone distance from the propeller centerline

The corrections for the tunnel background noise measurements are applied to the measured total noise levels in order to determine the net cavitation noise. The background noise measurements are made without the model propeller which was replaced by a dummy hub (Bertschneider et al., 2014). The background noise correction applied depending on the level of the difference following the procedure in ANSI/ASA S12.64-2009/Part1. When the difference is smaller than 3 dB, the result is discarded. In case of a difference between 3 and 10 dB, the results are corrected according to Equation 22 and no correction is applied in case of the difference being greater than 10 dB.

$$SPL_N = 10 \log \left[ 10^{(SPL_T/10)} - 10^{(SPL_B/10)} \right] \quad \text{Equation 22}$$

where; subscripts  $N$ ,  $T$ , and  $B$  indicate net, total and background respectively.

The noise measurements in a cavitation tunnel are actually intended for prediction of full-scale underwater RNL of a vessel. This can be achieved by utilizing some scaling procedures (Atlar et al., 2001). Extrapolation of model test URN can be attained using various scaling procedures to obtain the full-scale propeller noise levels (Bark & Berlekom, 1978; Bark, 2000, 1985). However, different tunnel-related factors can result in erroneous acoustical cavitation testing leading to inaccurate noise prediction. Two such factors are the reverberant nature of the cavitation tunnel and the high level of background noise due to the tunnel impeller and model propeller drive systems etc. These cause difficulties in interpreting the genuine propeller noise, as do other factors such as dissolved gas content, viscosity, etc. (ITTC, 1987). Therefore, accurate prediction of the full-scale propeller noise from model tests in a cavitation tunnel is not possible

without a detailed knowledge of the influence of the proximity of the tunnel walls and other factors, affecting the measured noise. On the other hand, the determination of correlation factors to be applied to model measurements would involve a large programme of model and full-scale tests. For this reason, such correlation factors do not exist for the Emerson Cavitation Tunnel. In the absence of such an in-depth scrutiny of the tunnel performance for noise, linear acoustical coefficients have been utilized for the extrapolation factors, as proposed by Starsberg (1977).

However, an approximation to the full-scale noise levels was made using the scaling laws recommended by the Cavitation Committee of (ITTC 1987). These laws are concerned only with differences in dimensions and operating conditions of the model and full-scale propellers and take no account of the fact that the model measurements may have been made in a cavitation tunnel. Furthermore, the scaling laws are based on Rayleigh's equation for the radial motion of a single spherical cavity which is assumed to be in an inviscid and incompressible fluid (Plesset, 1949; Plesset & Prosperetti, 1977). Equation 23 was used in combination with the ratio of the power spectral density expressions to represent the difference in the SPL in the model and full-scale as follows:

$$R \cdot \ddot{R} + \frac{3}{2} \cdot \dot{R}^2 = \left( \frac{\Delta P}{\rho} \right) = \left( \frac{P_0 - P_V}{\rho} \right) \quad \text{Equation 23}$$

Equation 23 is then manipulated to derive the expression for the extrapolation of model scale Power Spectral Density (PSD) to full scale as in Equation 24 (Nilsson & Tyvand, 1981). The PSD is then converted to SPL. An additional cavitation number term has been included into the extrapolation formulae assuming the cavitation bubble obeys the scaling method no matter its size.

$$\frac{G_s(f_s)}{G_s(f_m)} = \left[ \left( \frac{R_{M,s}}{R_s} \right)^2 \left( \frac{r_M}{r_s} \right)^2 \left( \frac{\Delta p_s}{\Delta p_M} \right)^{1.5} \left( \frac{\rho_s}{\rho_M} \right)^{0.5} \right] \quad \text{Equation 24}$$



Within this framework, various institutes have published scaling methods with different exponents for the terms in the extrapolation method. ITTC recommended the formula given in Equation 25 where the exponents used for the Emerson Cavitation Tunnel is  $x=1$ ,  $y=2$ , and  $z=1$  (ITTC, 2014).

$$\Delta L_S = \text{SPL}_S - \text{SPL}_M = 20 \log \left[ \left( \frac{D_S}{D_M} \right)^z \left( \frac{r_M}{r_S} \right)^x \left( \frac{\sigma_{N,S}}{\sigma_{N,m}} \right)^{y/2} \left( \frac{n_S D_S}{n_M D_M} \right)^y \left( \frac{\rho_S}{\rho_M} \right)^{y/2} \right] \text{dB} \quad \text{Equation 25}$$

The frequencies measured at model scale are also scaled using an approach based on the collapse time of a single bubble (Ross, 1976) given in Equation 26.

$$t_c = \sqrt{\frac{3}{2} \cdot \frac{\rho}{\Delta P}} \cdot \int_R^{R_M} \sqrt{\frac{R^3}{R_M^3 - R^3}} = 0.915 \times R_M \sqrt{\frac{\rho}{\Delta P}} \rightarrow \frac{f_s}{f_m} = \left( \frac{n_s}{n_m} \right) \times \left( \frac{\sigma_{n,s}}{\sigma_{n,m}} \right)^{0.5} \quad \text{Equation 26}$$

### 3.5 Conclusions

Chapter 3 presented the various major facilities, equipment inventory and analysis methods utilized for the experimental research study carried out in this thesis. The major facilities included the Emerson Cavitation Tunnel and RV, “The Princess Royal” which enabled the Author to conduct the entire model tests and full-scale trials presented in this thesis. The equipment inventory included laser-based flow measurement devices, water quality monitoring devices, propeller dynamometers, cavitation observation cameras and supporting tools, pressure sensors for the fluctuating hull pressures and noise measurement system for the URN.

The facilities and equipment described above are used to perform three sets of separately conducted, but complementary, experimental campaigns. The first group was designed and prepared to conduct systematic cavitation tunnel tests of a propeller in uniform and inclined flow conditions as presented in Chapter 4. These tests simulate the simplest variation for the

propeller operating condition by only introducing shaft inclination, hence providing a better understanding of the noise measurement capabilities and the potential for improvement as well as allowing familiarization with the testing equipment.

The second campaign group supported the investigations presented in Chapter 5. These involve underwater radiated noise investigations of cavitating propellers using a medium size cavitation tunnel and full-scale trials. These comparative tests and associated investigations not only provide an invaluable insight into the validation of the prediction capabilities of medium-sized cavitation tunnels but also place a large body of URN data in the public domain.

The knowledge accumulated through the two campaigns presented in Chapter 4 and 5 were used in Chapter 6 to design and conduct the third campaign group of tests in order to establish a prediction methodology for propeller cavitation noise using a standard series testing procedure. This third and final experimental campaign consisted of a variation of wake inflow produced by means of wake screens and a subset of the standard propeller series, chosen to evaluate major propeller design parameters. Such an experimental approach to cavitation noise prediction does not currently exist in the literature and hence justifies the novelty of the methodology proposed in this thesis.

# **Chapter 4    Systematic Cavitation Tunnel Tests of a Propeller in Uniform and Inclined Flow Conditions**

## **4.1    Introduction**

*Chapter 4 is dedicated to the systematic cavitation tunnel tests of a propeller in uniform flow under oblique flow conditions. The aim of the chapter is to describe the findings of systematic propeller tests in order to provide comprehensive data on propeller noise, cavitation inception, cavitation observation and propeller performance characteristics due to the effect of the shaft inclination. Little such experimental data is available in the literature, especially in regard to cavitation noise. This study also allowed the Author to become thoroughly familiar with cavitation tunnel testing, the ECT facility and its equipment.*

*First, the experimental setup and test conditions are covered including the devised test matrix, methodology and test procedure. Results are then presented and discussed in groups covering performance coefficients, noise measurements, cavitation inception and observation recordings and measurements. Finally, conclusions are drawn from measured and analysed experimental results.*

## **4.2    Experimental setup & test conditions**

Experiments were carried out in three groups of tests at the Emerson Cavitation Tunnel (ECT) of Newcastle University (UNEW). The first group of tests were conducted to obtain the open water efficiency performance of the model propeller in systematically varied shaft inclination angles at 3 different vacuum levels (cavitation numbers) and hence to investigate the effect of the flow inclination and cavitation on the propeller performance. The second group of tests involved cavitation inception measurements with the model propeller under the same inclination and vacuum conditions. The third group of tests comprised underwater noise measurements with the model propeller, once again, under the same flow and vacuum conditions.

All of the tests were conducted at a 4 m/s tunnel inflow speed recorded at the measuring section and for advance coefficients ( $J$ ) ranging from 0.4 to 0.75 under three different vacuum condition corresponding to three free stream cavitation numbers ( $\sigma_v$ ). Table 4-1 gives an overall summary of the test conditions.

Table 4-1 A summary of test conditions.

	Test Type		
	Open water performance tests	Cavitation inception tests and observations	Noise measurements
Shaft Incl. Angle (°)	0, 3, 6, 9, -3, -6 and -9		
Cavitation Condition	Atmospheric condition ( $\sigma_v=13.9$ )	Medium vacuum condition ( $\sigma_v=8.1$ )	High vacuum condition corresponding to vessel's fully loaded condition ( $\sigma_v=4.5$ )
J Range Tested	0.75, 0.70, 0.65, 0.60, 0.55, 0.50, 0.45 , 0.40		

The angle convention adopted for the shaft inclination during the tests was that a positive angle was obtained when the dynamometer shaft (at the propeller end) was inclined in an upward direction with the blade tip at the 6 o'clock position moving towards the incoming flow as shown in Figure 4-1. The experiments were repeated at both negative and positive angles in order to account for the tunnel's speed profile at the propeller plane as shown in Figure 4-2. The propeller centre was always positioned on the tunnel centerline.

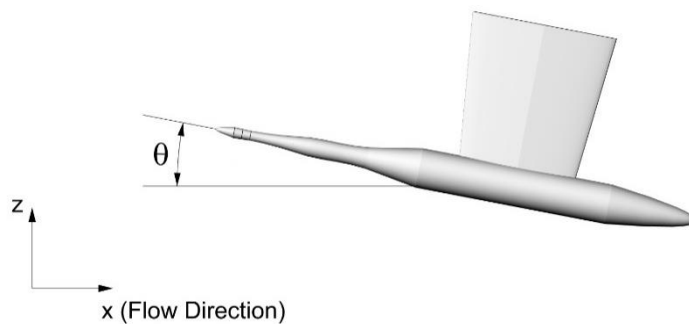


Figure 4-1 Angle convention for the conducted shaft inclination tests at ECT.

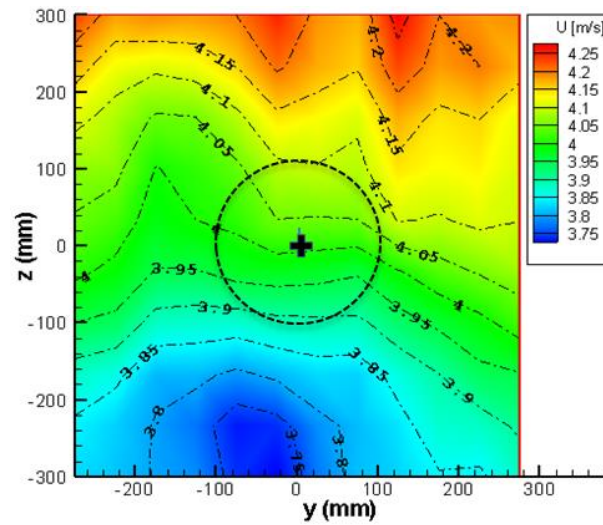


Figure 4-2 Axial speed profile of the Emerson Cavitation Tunnel for 4m/s inflow velocity measured at the propeller plane where the origin is the shaft centreline.

The tunnel inflow to the propeller model thus contain some non-uniformities as presented by Figure 4-2. However, the consistency of the conducted tests are achieved by means of height adjustment following the angle configuration to ensure propeller model is kept in the centre of the tunnel for all test conditions.

During the course of the experimental campaign repetition of the measurements are carried out back to back in order to ensure a satisfactory level of measurement uncertainty. The open water performance tests are repeated 6 times for zero degree inclination angle and resulted in a total uncertainty of 1.03% for thrust coefficient and 2.53% for torque coefficient using the proposed guidelines by ITTC (2002b).

#### 4.2.1 Propeller design and model propeller

The propeller model utilized for the cavitation tunnel tests represented the starboard propeller of “The Princess Royal”, having a scale ratio of 3.5, giving a 214 mm model propeller diameter. This model was manufactured with high accuracy for cavitation testing. Figure 4-3 shows the model propeller together with the full-scale port propeller. The propeller’s main particulars and offset table given in Appendix A.



Figure 4-3 Scale comparison of the full-scale (port) and model-scale (starboard) propellers of “The Princess Royal”.

### 4.3 Open water performance tests

Open water performance tests to measure the thrust and torque of the model propeller were carried out according to the ITTC procedures for open water tests (ITTC, 2011c), using a Kempf & Remmers (K&R) H33 dynamometer and Cussons Type H101-27 shaft height and angle adjustment system of the Emerson Cavitation Tunnel. The tests were performed to cover the whole advance coefficient ( $J$ ) range of the tunnel and systematic shaft angle combination under Atmospheric and 2 additional different vacuum conditions as specified in Table 4-1. The tunnel inflow speed ( $V$ ) was kept at 4 m/s and the advance coefficients ( $J$ ) were varied systematically by changing the rotational speed of the propeller ( $n$ ).

In order to achieve accurate results in the open water tests, the sampling rate for the measurements was 1000 Hz. The tests were repeated 6 times for the level shaft ( $0^\circ$ ) under Atmospheric condition, for determination of uncertainty of the propeller performance measurements, and 3 times for all other conditions, as stated in Table 4-1. The average thrust and torque values were then calculated and presented in non-dimensional coefficients:  $K_T$  for thrust,  $K_Q$  for torque and  $\eta_0$  for propeller efficiency.

For the plotted advance coefficients a simple cosine correction was applied to the advance coefficients as  $J_{corrected} = J \cos \theta$ , where  $\theta$  is the shaft inclination angle. A typical representation of the open water performance curves for the high vacuum condition, whilst varying the shaft inclination angle, is shown in Figure 4-4. During the tests the propeller Reynolds number ( $Re$ ) range varied from  $4.03 \times 10^6$  to  $8.22 \times 10^6$ . Here  $Re$  is defined based on the propeller chord length at  $0.7R$  using Equation 15

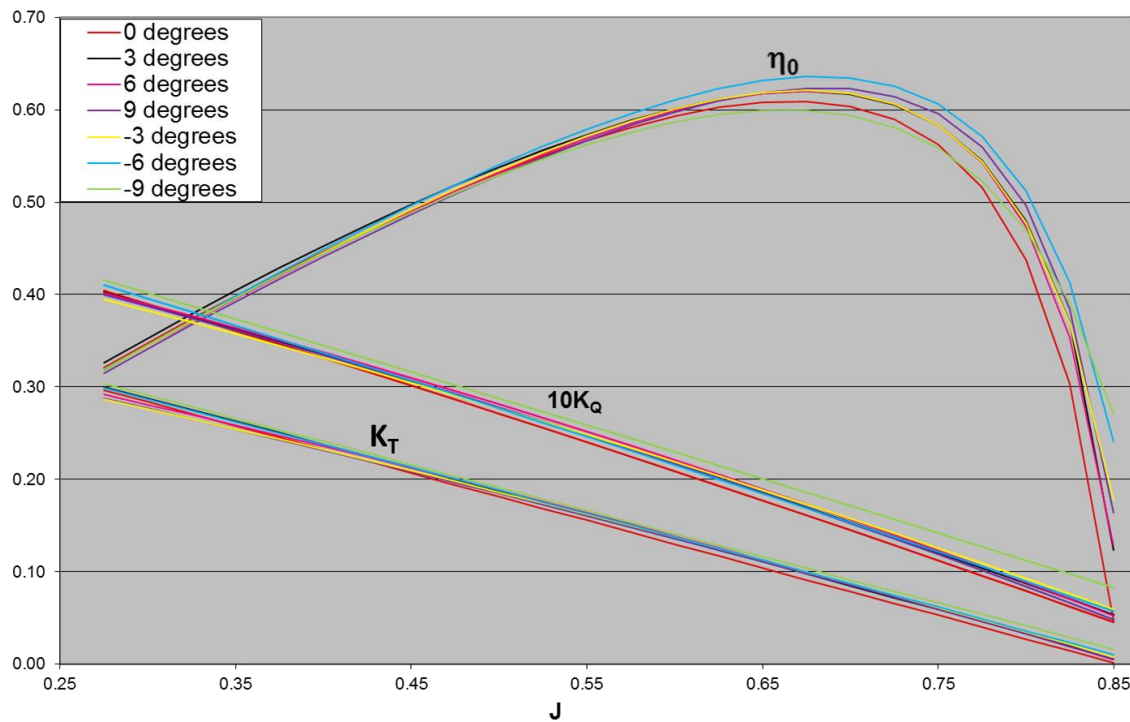


Figure 4-4 Open water performance of model propeller, for various inclination angles under high vacuum condition.

## 4.4 Cavitation observations

The cavitation observation recordings were made during the experiments both for cavitation inception/desinence detection and for well-developed cavitation. Two different configurations for the recordings were used: one using a strobe synchronised with a high-speed video camera; and the other using a continuous light source with the high-speed video camera. In the former configuration, the cavitation images were captured using the Transistor-Transistor Logic (TTL) signal from the electric motor driving the shaft to trigger both the strobe and the high-speed video. In the latter a powerful continuous light was used with the high-speed video to obtain a

better understanding of the cavitation dynamics. Figure 4-5 shows typical frames from the recordings made with a Dantec Dynamics Nanosense Mk II high-speed video camera (running at 2000 frames per second) in combination with triggered strobe lighting for the cavitation developments at  $-9^\circ$  inclination angle under the high vacuum condition for varying advance coefficients.

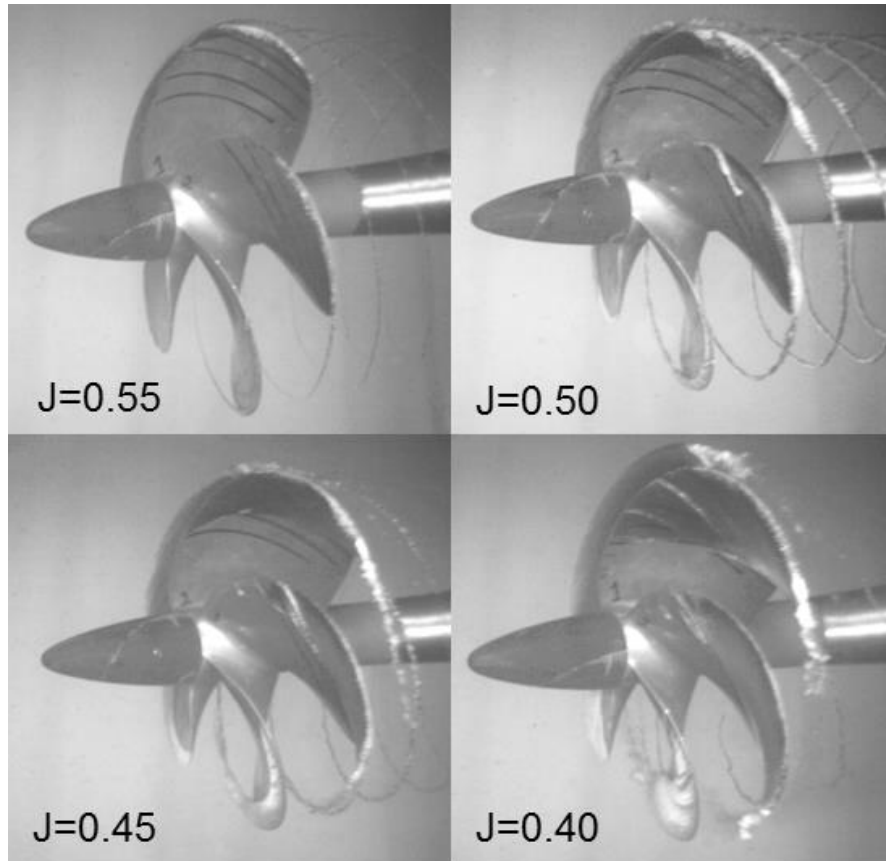


Figure 4-5 Cavitation developments at  $-9^\circ$  inclination angle under high vacuum condition.

#### 4.4.1 Cavitation inception

Inception and desinence points for respective cavitation events were recorded on video as well as by eye. The procedure for the inception measurements was performed such that the tunnel flow velocity was kept constant at 4 m/s. The tunnel static pressure was also set to a constant value and the rotational speed of the propeller was initially increased until a visual appearance of an unattached cavitating tip vortex cavitation was observed. This was recorded as the inception point of the respective cavitation. The rotational speed was then increased up to the point



that the tip vortex attached to the blades and then was decreased until the vortex disappeared from the tip of the propeller. This was accepted as the desinence point of the cavitation. Typical images of the inception and desinence points are shown in Figure 4-6 for the propeller model at  $0^\circ$  inclination angle under the high vacuum condition. The inception/desinence points for all of the tested conditions are presented in Table 4-2.

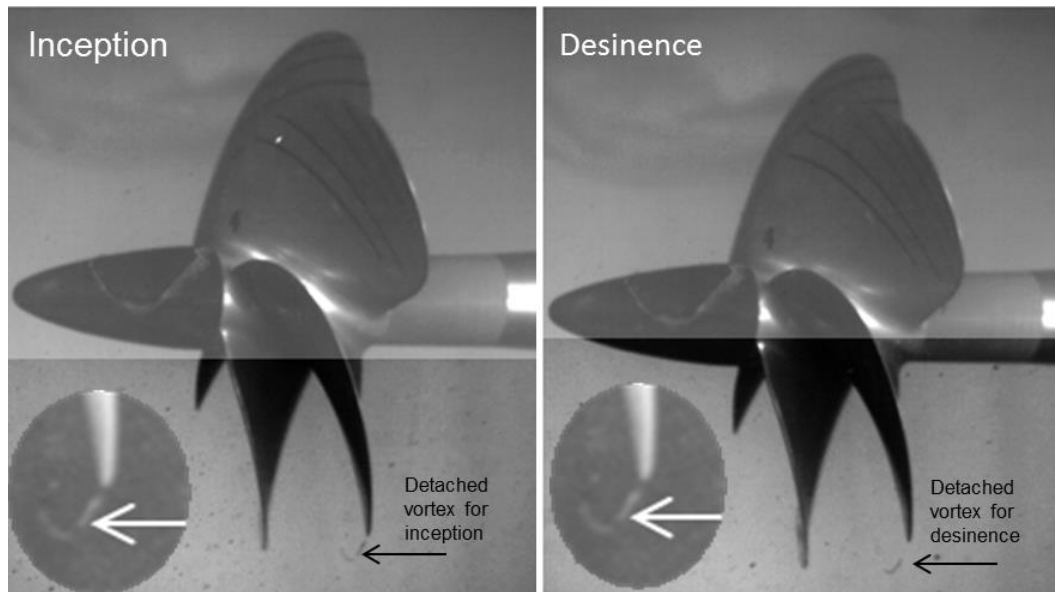


Figure 4-6 Images of the cavitation inception and desinence points for propeller model at  $0^\circ$  inclination angle under high vacuum condition.

Table 4-2 Cavitation inception and desinence points of propeller model at varying inclination angles and cavitation numbers

Atmospheric condition							
Inclination angle	0°	3°	6°	9°	-3°	-6°	-9°
Cavitation Type	Tip Vortex	Tip Vortex	Tip Vortex	Tip Vortex	Tip Vortex	Tip Vortex	Tip Vortex
Inception (RPM)	2128	2102	2047	2003	2138	2165	2095
Desinence (RPM)	2188	2126	2076	2093	2165	2186	2110
$J_{\text{Inception}}$	0.527	0.534	0.548	0.56	0.525	0.518	0.535
$\sigma_{\text{Inception}}$	0.758	0.772	0.811	0.845	0.748	0.737	0.782
Medium Vacuum Condition							
Inclination angle	0°	3°	6°	9°	-3°	-6°	-9°
Cavitation Type	Tip Vortex	Tip Vortex	Tip Vortex	Tip Vortex	Tip Vortex	Tip Vortex	Tip Vortex
Inception (RPM)	2013	1916	1900	1860	2004	2013	1921
Desinence (RPM)	2030	1946	1930	1938	2002	2030	1962
$J_{\text{Inception}}$	0.557	0.585	0.59	0.603	0.56	0.557	0.584
$\sigma_{\text{Inception}}$	0.489	0.537	0.541	0.566	0.492	0.498	0.542
High Vacuum Condition							
Inclination angle	0°	3°	6°	9°	-3°	-6°	-9°
Cavitation Type	Tip Vortex	Tip Vortex	Tip Vortex	Tip Vortex	Tip Vortex	Tip Vortex	Tip Vortex
Inception (RPM)	1903	1856	1828	1793	1875	1860	1803
Desinence (RPM)	1914	1860	1832	1797	1879	1870	1807
$J_{\text{Inception}}$	0.589	0.604	0.614	0.625	0.598	0.603	0.622
$\sigma_{\text{Inception}}$	0.303	0.316	0.325	0.337	0.31	0.314	0.332

In Table 4-2 the cavitation inception number ( $\sigma_i$ ) is defined based on the resultant velocity as using Equation 18. In addition to the RPM values corresponding to the cavitation inception and desinence points, Table 4-2 also includes the corresponding advance coefficients ( $J_{inception}$ ) to be able to relate them to the RNL. Table 4-2 illustrates the effect of the varying shaft inclinations on the inception and desinence points.

Figure 4-7 shows inception trends for positive and negative angles of shaft inclination angle. Inception occurred earliest at the higher inclination angles. While this effect was not symmetrical with the angle at Atmospheric condition, it became more so with the increasing vacuum in the case of the medium and high level of vacuum conditions.

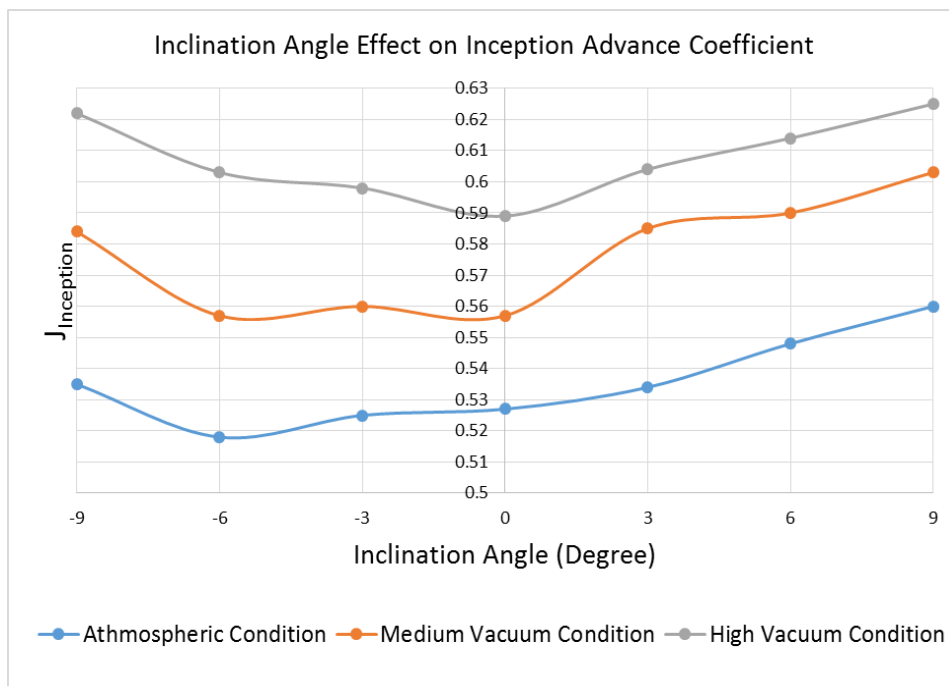


Figure 4-7 Variation of cavitation inception J number (Advance Coefficient) with respect to inclination angles.

## 4.5 Noise measurements

Noise measurements were also carried out at the 7 different shaft inclination angles and 3 different cavitation conditions. The measurements were recorded using a Bruel and Kjaer type 8103 miniature hydrophone mounted in a water filled, thick walled steel cylinder placed on the outside of the tunnel's Plexiglas window. This cylinder was glued onto the starboard window level with the centre of the propeller boss when the shaft inclination is zero and at a horizontal distance of 0.61 m from the shaft centreline, as shown in Figure 4-8 (top picture). The hydrophone signals were collected by further Bruel and Kjaer hardware and software; in this case, a PC based "PULSE" digital acquisition and analysis software system up to a frequency of 20 kHz, was used.



Figure 4-8 A view of hydrophone glued on the side window (top); An overall view of the dynamometer with inclined shaft arrangement in test section of the tunnel (bottom).

### 4.5.1 Analysis and presentation of the noise results

The analysing methodology outlined in Chapter 3 is applied to the acquired data. Therefore, the measured values of SPL in each 1/3 octave band is adjusted to an equivalent 1 Hz bandwidth using Equation 20. Following this, the 1Hz equivalent levels are corrected for the reference 1m measuring distance using the spherical acoustic propagation formulae given with Equation 21. The presented levels throughout the chapter are the total noise levels. Hence no correction for the background levels are applied. The total noise levels, however, are presented together with the corresponding background noise levels in order to provide further insight into the nature of the measuring environment of the ECT. Furthermore, the noise levels are cross plotted for certain frequencies where the measured SPL are significantly higher than the background noise levels since this does not require correction according to ANSI procedure. Figure 4-9 is a typical presentation of the noise spectra over a 20 kHz frequency range displaying the effect of varying shaft inclinations at a fixed J and high vacuum condition (low cavitation number).

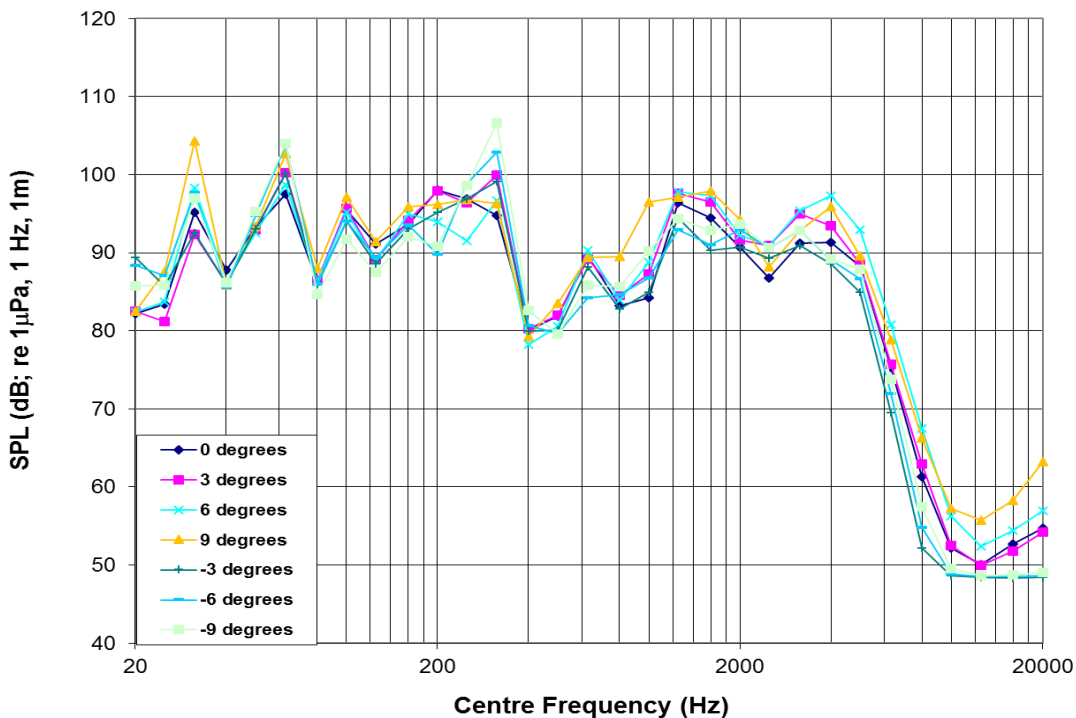


Figure 4-9 Comparison of noise levels at varying inclination angles at advance coefficient of  $J=0.60$  under high vacuum condition.

Figure 4-10 gives quantitative information on the background noise level of the Emerson Cavitation Tunnel. The figure also presents SPL spectra of the propeller corresponding to the  $+6^\circ$  inclination angle at advance coefficient 0.4 for the three cavitation conditions as given in Table 4-1.

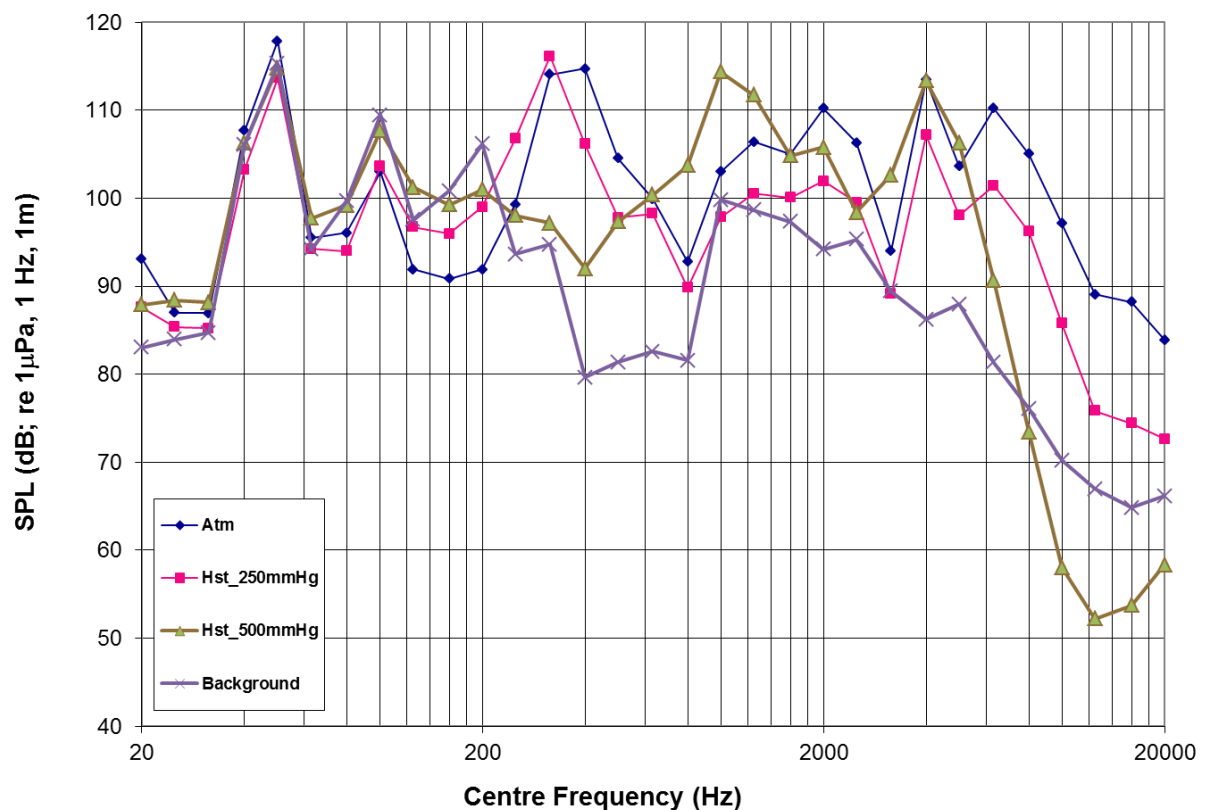


Figure 4-10 Background noise level spectrum (at Atmospheric condition) and SPL for  $6^\circ$  inclination at  $J$  0.4 (at various cavitation condition).

In order to have a better understanding of the trends in the noise spectra at various conditions, the measured noise data were extracted and presented in Figure 4-11 at two fixed frequencies: 630 Hz and 6.3 kHz. These correspond to frequency ranges where the SPL amplitudes were significantly distinct from the background noise and showed strong variations with the advance coefficient and shaft inclination angle.

In Figure 4-11 the effect of varying advance coefficients on the SPL's are shown for the systematically varied shaft angles and for three cavitation conditions at 630 Hz. The SPL's show relatively less sensitivity to the variations in  $J$  except for three distinct  $J$ 's, where the peak SPL's were recorded. It is considered that these peaks were due to the strong tip vortices are shown in the selected cavitation images in Figure 4-12.

This frequency was also close to the 4th blade harmonic. In order to assess the effect of the shaft inclination further, three cross-plot curves were extracted and shown in Figure 4-13 for systematically varied advance coefficients and for three cavitation conditions at 630 Hz. These cross plots do not show any significant asymmetry for the positive and negative angles of the shaft inclination across the three cavitation conditions imposed. Similar plots for the SPL's are also illustrated in Figure 4-14 for 6.3 kHz. In the first group of these plots, Figure 4-13, the noise levels appear to increase in a near monotonic manner from high to low  $J$ -values at each of the three-cavitation conditions whilst in the second group of the plots, Figure 4-14, a little asymmetry with the angle of inclination can be observed, although there is a weak tendency towards higher levels for the positive inclination angles.

During the tests, tip vortex and sheet cavitation were the main types observed, together with their complex interaction at the blade trailing edge. This interaction was also reflected in the noise levels for certain operating conditions. This was particularly strong at  $J=0.4$  for trailing edge vortex breakdown due to interaction with the sheet cavity extending downstream and was independent of the flow inclination angles. This phenomenon is illustrated for the zero and  $6^\circ$  shaft inclination together with its consequent effect on the SPL levels given in Figure 4-14. Here the impact of the phenomena is seen in a significant increase in the spectral levels for all inclination angles at  $J=0.4$  for the high vacuum condition (i.e. bottom graph). Similar observations were also given in e.g. (Bark, 1988, 1986; Konno et al., 2002).

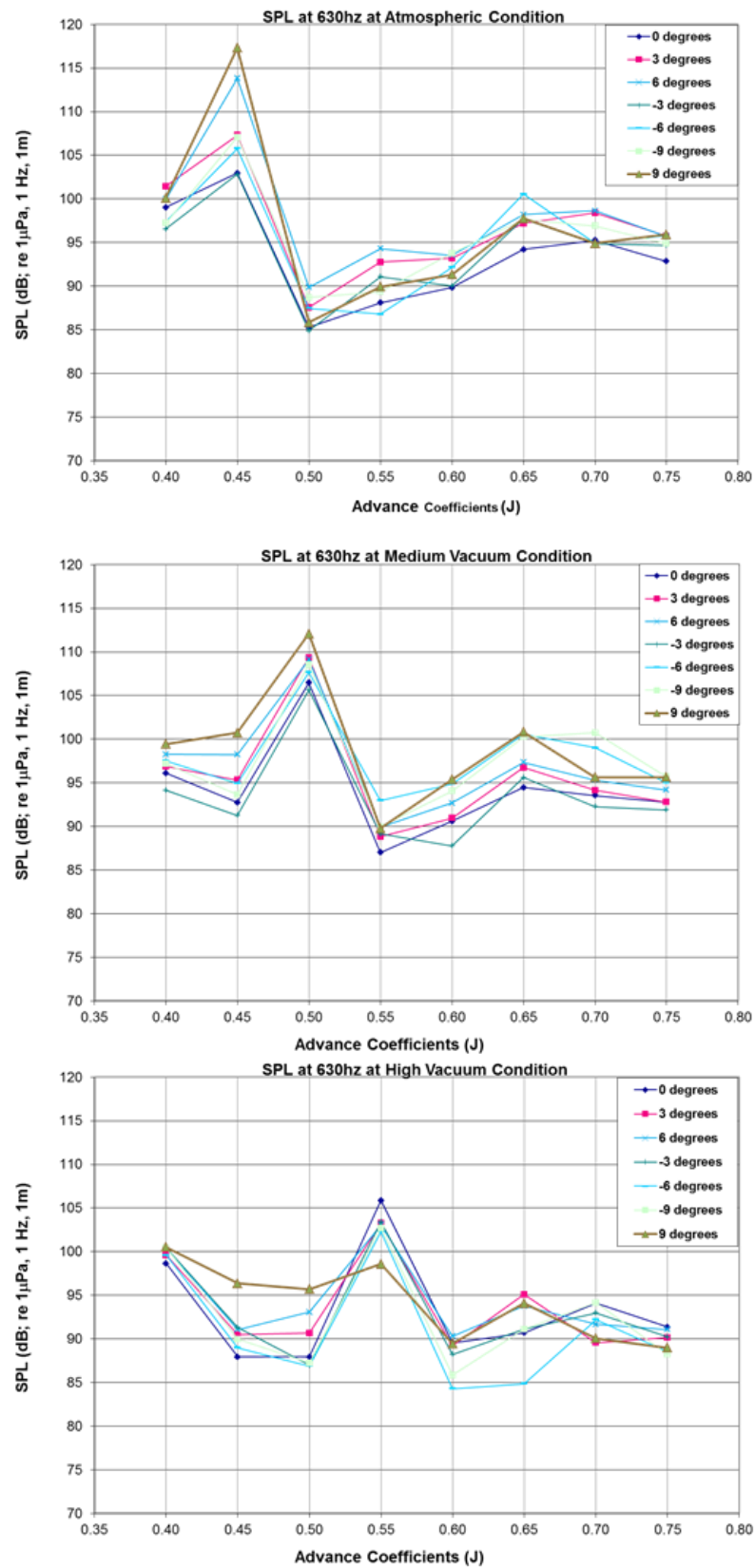


Figure 4-11 Comparison of noise levels for varying shaft inclination angles on advance coefficients under different cavitation conditions at 630 Hz.



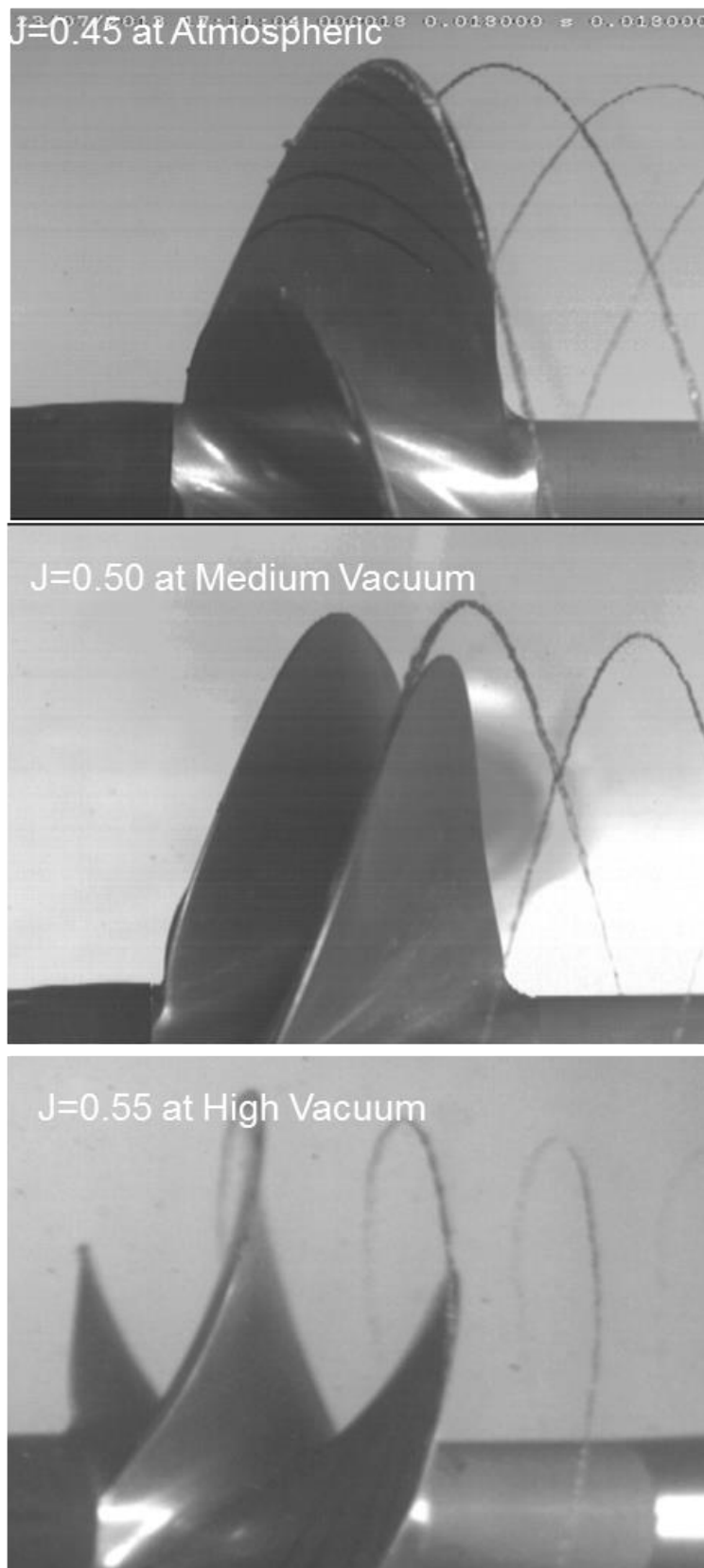


Figure 4-12 Cavitation observation for varying shaft inclination angles on advance coefficients under different cavitation conditions.

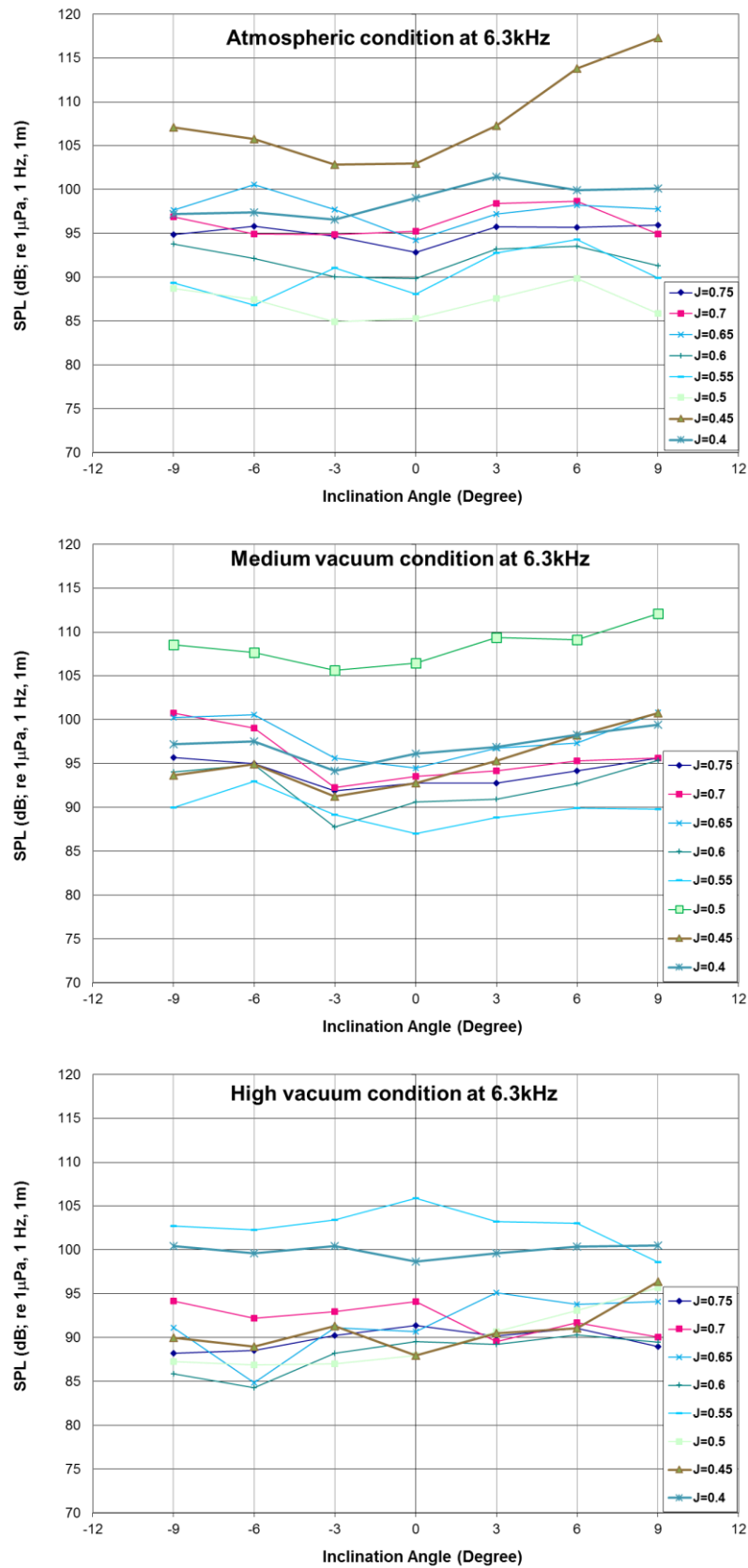


Figure 4-13 Comparison of noise levels for varying advance coefficients on shaft inclination angles under different cavitation conditions at 630 Hz.

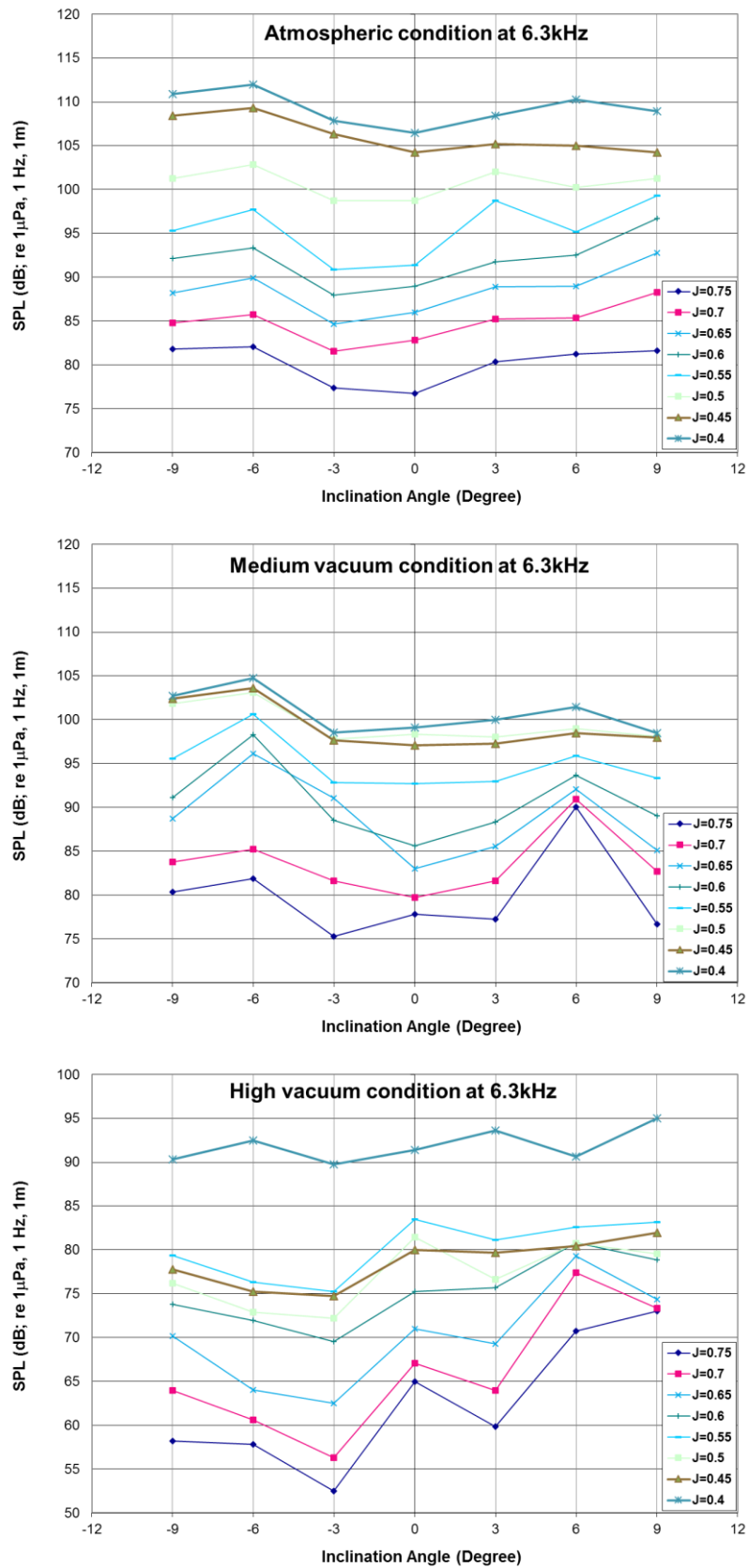
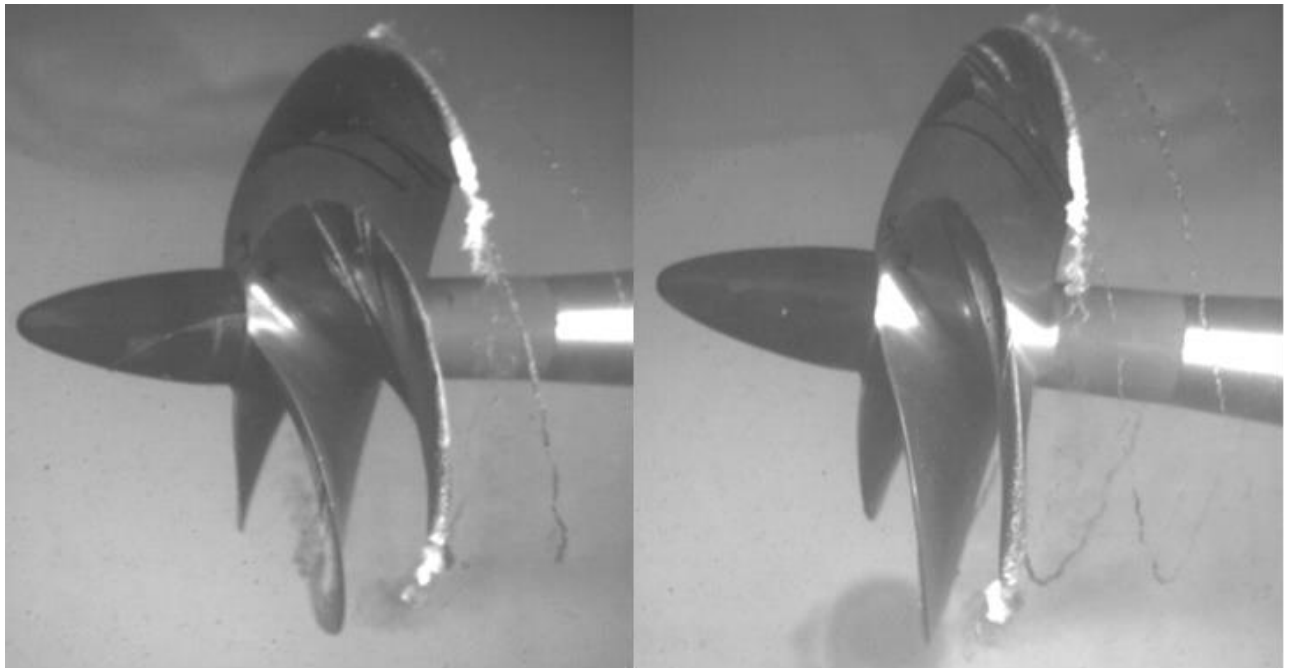


Figure 4-14 Comparison of noise levels for varying advance coefficients on shaft inclination angles under different cavitation conditions at 6.3 kHz.



Zero shaft inclination, high vacuum

+6 deg shaft inclination, high vacuum

Figure 4-15 Tip vortex breakdown due to interaction with the sheet cavitation extension at  $J=0.4$ .

## 4.6 Discussion

### 4.6.1 Open water efficiency performance

Effects of the shaft inclination on all test cases are similar for the propeller open water performance curves, namely showing discernible differences in the torque coefficient ( $K_Q$ ) at  $-3^\circ$ ,  $-6^\circ$  and  $-9^\circ$  inclination angles and hence on the propeller efficiency ( $\eta_0$ ) curves. Figure 4-4 typically shows this trend in the high vacuum condition. As theoretically expected, the inflow velocity is not responsive to the direction of the inclination angle since the advance velocity is the cosine of tunnel velocity and hence is the same for both negative and positive inclination angles. This can be shown in Figure 4-16 where no discernible variation in the performance coefficients can be detected with the variations in the inclination angles whilst for the high vacuum condition the loss of thrust and torque is evident due to the cavitation extent. The effect of the different vacuum (cavitation) conditions had similar trends in  $K_T$ ,  $K_Q$  and  $\eta_0$  for the Atmospheric and medium cavitation conditions, hence making it difficult to quantify the effect of the inclination

under these circumstances. It was observed that the increasing vacuum generally reduced the open water efficiency of the propeller at all inclination angles and this effect was also found to be dependent on the  $J$  range. For instance comparison of the efficiency of the propeller for  $0^\circ$  and  $6^\circ$  has shown as high as 10% difference at the higher end of the advance coefficient range. But this variance diminishes as the advance coefficient is lowered.

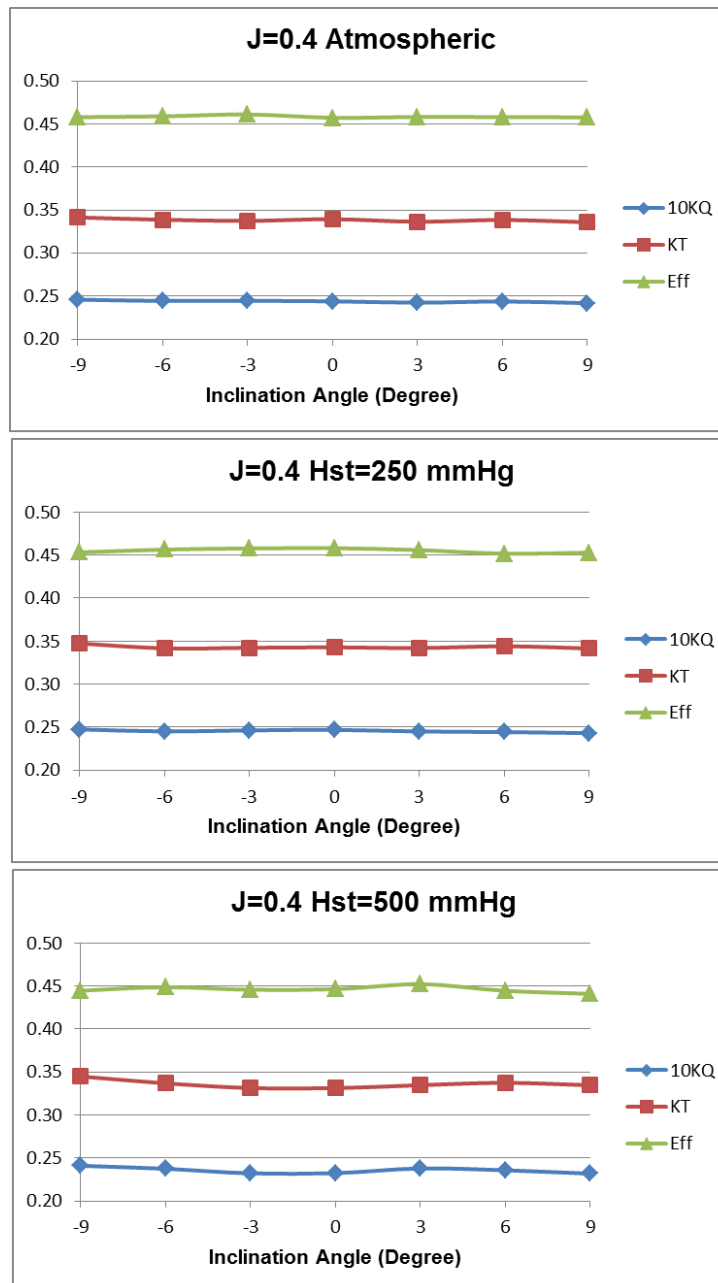


Figure 4-16 The Non-Dimensional Performance Coefficients at  $J=0.4$  for different vacuum conditions.

### 4.6.2 Cavitation observations

The inception RPM values determined with the help of cavitation inception and desinence observations (Figure 4-6) showed that as the inclination angle was increased the cavitation inception  $J$ -value increased for the medium and high vacuum conditions as outlined in Table 4-2 and presented in Figure 4-7.

Positive shaft inclination stimulated earlier inception on the blades. Overall the inclination angle was observed to initiate an earlier inception for all angles and at all cavitation conditions except the Atmospheric condition. The difference seen in the Atmospheric condition are most likely to be due to the axial flow speed map of the tunnel and to the reduced number of nuclei available in the circulating water.

Trends in the observed cavitation patterns are discussed for the three vacuum conditions as follows:

Atmospheric condition: the cavitation-free range lays above  $J=0.515$  for all values of the shaft inclination angle. Below this  $J$  value, two distinct types of cavitation patterns, i.e. tip vortex and sheet cavitation were observed. Only slight differences were observed in the extent and strength for the inclined cases relative to the level shaft inclination case. Figure 4-17 shows images for zero shaft angle.

Medium vacuum condition: The cavitation-free range was observed above  $J=0.55$ . Below this range, it was observed that the size of the tip vortices was increased compared to the Atmospheric condition and also displayed distinct nodes in their structures behind the blade training edges, as shown typically in Figure 4-18. However, similar to the Atmospheric condition, it is hard to observe clear differences in the cavitation structures for the same positive and negative shaft angles.

High vacuum condition: The cavitation-free range was above  $J=0.59$ , including variations in the inclination angle. Figure 4-15 and Figure 4-19 show typical examples of this condition with larger tip vortex structures than observed at the lower vacuum conditions. The cavitation appeared to be similar over the range of shaft inclination angle. However, there appeared to be more sheet cavitation at  $J=0.4$  and  $-6$  degrees shaft inclination than at the moderate cavitation condition. A wide extent of sheet cavitation was also shown over the blade area combined with severe trailing edge sheet cavitation and tip vortex cavitation interaction and resulting dynamics.



Figure 4-17 Cavitation patterns at  $0^\circ$  inclination angle under Atmospheric condition

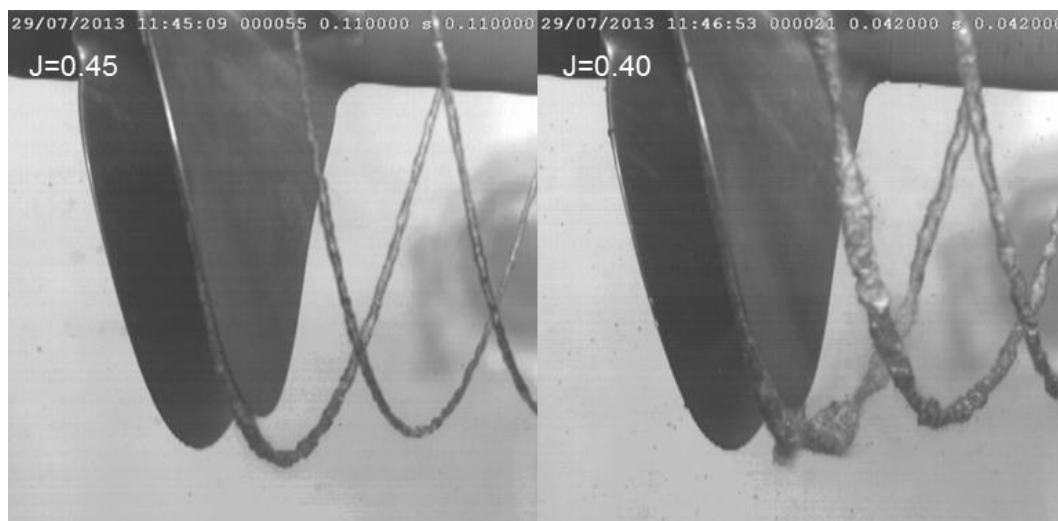


Figure 4-18 Cavitation patterns at  $6^\circ$  inclination angle under medium vacuum condition.

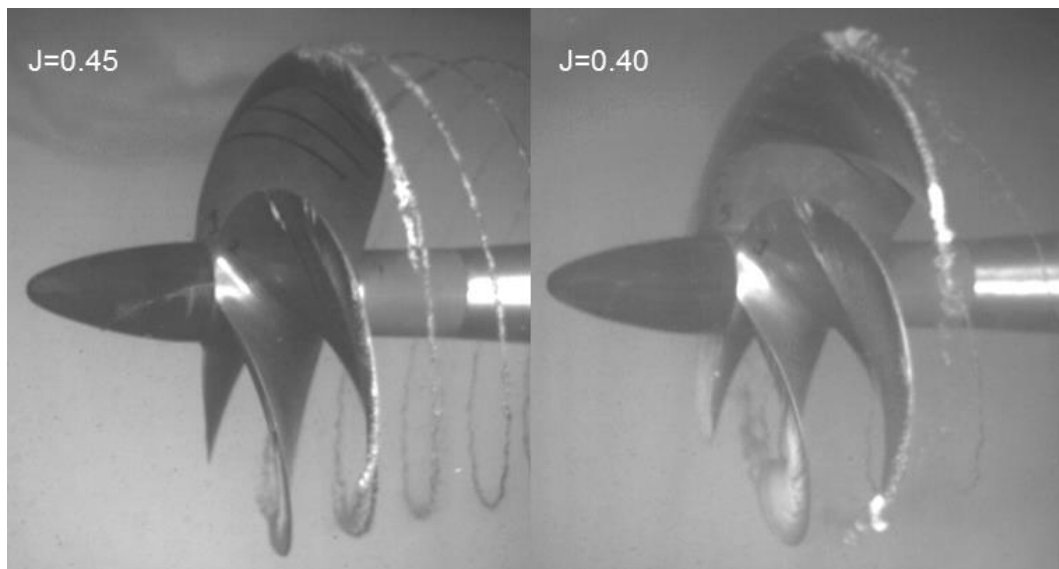


Figure 4-19 Cavitation patterns at  $-6^\circ$  inclination angle under high vacuum condition.

### 4.6.3 Noise measurements

The noise measurements presented contain the combined propeller and background noise; no correction was made for the background noise of the tunnel. A vibration survey of the tunnel carried out earlier showed that the frequencies of the structural vibration generated by the dynamometer and impeller to be in the region below 100 Hz. Therefore, it is most likely that the noise levels due to the blade rate frequency ranging from 125 Hz to 250 Hz and its harmonics, together with structural vibration, would be affected by these effects in the frequency region up to 200 Hz. The contribution of these major operating noise sources produced a rather noisy environment for frequencies below 200 Hz as shown, typically in Figure 4-10. Based on the above information regarding the background noise signature of the ECT, certain 1/3 Octave centre frequencies (630 Hz and 6.3 kHz) with SPL's well above the background noise levels are chosen and compared.

The analysed results in Figure 4-11 shows that, as the advance coefficient is reduced, the noise levels at 630 Hz decreased for  $J=0.75$  to 0.50 under the Atmospheric condition. At  $J=0.45$  the noise levels experience a distinct peak which is then followed by a decline at  $J=0.40$ . For the medium cavitation condition as presented by the middle part of Figure 4-11, a similar trend was



also observed from  $J=0.75$  to  $J=0.50$  at 630 Hz. However, at  $J=0.45$  again a distinct peak is experienced followed by a reduction in the measured noise levels at  $J=0.40$ . Progressively, the peak experienced by the cross plots are moved towards the  $J=0.55$  for the high vacuum condition as presented by the bottom part of Figure 4-11. The peak formation was found to be coinciding with the exact same formation and extent of tip vortex cavitation as presented in Figure 4-12. The peak is again followed by a reduction at high vacuum condition in the measured levels for the  $J=0.50$  and  $J=0.45$ . Then the levels experience a second peak at  $J=0.40$ , which is caused by the tip vortex cavitation and sheet cavitation interaction as discussed in the cavitation observation section and presented in Figure 4-19.

Figure 4-13 and Figure 4-14, presents the cross plots at 630 Hz and 6.3 kHz for variations of inclination angle and advance coefficient. In this respect, Figure 4-13 is a reproduction of Figure 4-11. Hence, same conclusions are clearly visible from these plots too. Figure 4-13, presents results at a high frequency. Thus, the corresponding cross plots are strongly influenced by cavitation dynamics due to their broadband noise characteristics. For example whilst the levels have shown not so significant change with the decreasing advance coefficient at 630 Hz as illustrated in Figure 4-13, the plots show elevation in terms of the spectral levels with the decreasing advance coefficient as presented in Figure 4-14. The most noticeable increase is experienced at  $J=0.40$  at high vacuum condition as shown by the bottom part of Figure 4-14. The elevation of up to 15 dB in comparison to  $J=0.45$  is observed due to the previously mentioned interaction of tip vortex and sheet cavitation.

Overall, it can be deduced from the discussions regarding the measured levels that, the measured spectral levels and the frequency band contribution are highly pertinent with the cavitation type present. Moreover, the interactions between different cavitation types result in complex cavitation dynamics resulting in significant increases to be experienced by the propeller in terms of the RNL.

## 4.7 Conclusions

Chapter 4 presented the systematic cavitation tunnel tests were carried out to investigate the open water (efficiency) performance, cavitation and noise characteristics of the model propeller of the UNEW research vessel, “The Princess Royal”, in uniform (open water) and in inclined flow conditions.

The main focus of this chapter has been on flow-unsteadiness caused by systematically varying shaft inclination especially and in particular its effect on the underwater radiated noise of a model propeller. The inclined shaft effect is mainly associated with small craft at relatively high-speed as in the case of “The Princess Royal”. Although no effect of the hull wake is studied in this investigation, invaluable and comprehensive data has been produced using a systematic approach. The results have shown that the simplest variation of the inflow, which is shaft inclination, in this case, can be recognized and studied thoroughly using cavitation tunnels. This has provided justification and encourage to pursue an experimental approach with added inflow complexity for accurate noise prediction. The following conclusions are deduced from the first test campaign conducted in ECT.

- A set of systematic experimental data for the effect of shaft inclination on the URN of a propeller is created in combination with the cavitation observations and efficiency performance to contribute to the state-of-the-art to provide further insight on this effect for the URN.
- The effect of shaft inclination on the propeller open water performance was greater on the torque and hence the propeller efficiency. The effect was asymmetric with shaft positive and negative angles and across the  $J$  range. The thrust was relatively insensitive to the change in the shaft angles. The propeller efficiency was reduced with increasing vacuum over the range tested.
- The effect of shaft inclination on the cavitation inception (and desinence) of the tip vortices was evident and this effect was asymmetric; in general, depending on the direction of the inclination. However, this asymmetry was less pronounced towards the higher vacuum levels. The asymmetry for the Atmospheric and medium cavitation condition

can be attributed to the axial flow profile of the tunnel and to the reduced number of nuclei available in the circulating water.

- Two distinct types of well-developed cavitation patterns (tip vortex and sheet cavitation) were observed together with their complex interactions at the trailing edges of the blades. The extent and strength of these cavitation phenomena were influenced by the change in the inclination angles.
- The presented total noise levels (including the tunnel background noise), showed that, in the low-frequency range, the effect of changing the shaft inclination seemed not to be significant, since all the inclined conditions displayed similar noise levels and trends. However, this trend changed in the high frequency range, as presented by the 6.3 kHz cross plots with Figure 4-14, depending on the direction of the shaft inclination as well as the vacuum levels applied.
- The recorded RNL were found to be highly sensitive to the type and extent of cavitation as well as the frequency range to which the particular cavitation contributed.

On a final note, this experimental study also enabled a better understanding of the noise measurement capabilities of the Emerson Cavitation Tunnel. The areas that may be improved have been identified and possible methods of measurement technique for improved measurement accuracy have been determined. Furthermore, the nature of the tests has provided a better understanding of the practicalities of undertaking such a systematic tests with particular focus on noise.

## **Chapter 5 Underwater Radiated Noise Investigations of Cavitating Propellers Using a Medium Size Cavitation Tunnel and Full-Scale Trials**

### **5.1 Introduction**

*Chapter 5 presents details of the propeller cavitation noise investigations for a research vessel using a cavitation tunnel and full-scale trials. The main aim of the chapter is to demonstrate and prove the noise prediction capabilities of medium size cavitation tunnels. The conducted tests provided enhanced understanding from the cavitation testing point of view justifying the adopted experimental approach. Moreover, familiarity with the facilities and equipment is gained whilst providing publicly scarce URN data from both model and full scale to public domain. Within this framework, the full-scale noise trials conducted with the RV “The Princess Royal” has been simulated in the Emerson Cavitation Tunnel to validate the cavitation tunnel predictions. The cavitation tunnel measurements necessitated a dummy model and wake simulation which is initially covered within the chapter. Following this test conditions and the determination of the tunnel operating conditions is given. Then the results of the noise prediction in comparison with the full-scale counterparts are given together with a dedicated section discussing the results. Finally, conclusions drawn from the chapter is presented.*

### **5.2 Further details of experimental facilities and setup**

ITTC recommendations for model scale testing of cavitation phenomena on ships include an accurate representation of the hull geometry in the way of the propeller and accurate representation of the 3-D velocity field. In the largest tunnels, worldwide, this is achieved using a full, scaled model of the hull, with appropriate turbulence stimulators, if required. The length of the ECT measuring section is too short for such a procedure. Hence, the usual approach was

adopted for small and medium size cavitation tunnels. The usual approach makes use of a truncated “dummy-hull” model to achieve correctly scaled afterbody shaping and transverse flow velocities, while wake grids are used to achieve the correct axial flow velocities. For twin hull and twin-screw vessel, it is permissible to represent one-half of the vessel.

### 5.2.1 Main particulars of “The Princess Royal” and propeller

“The Princess Royal” is a displacement type of Deep-V catamaran, which was designed in-house and built locally, as described in details by (Atlar et al., 2013). For the present study, the starboard demi-hull of the vessel was used as a basis for simulating the hull. The model scale factor of  $1:3.5$  was set by considering various limiting factors such as avoiding an undesirable blockage effect, achieving a reasonable Reynolds number range for minimizing the scale effects and attaining a respectable size for avoiding practical size limitation. The size of the model propeller and hull should be determined, within the capacity constraint of the test facilities and within an acceptable range of test-section blockage (i.e. less than 20%), to achieve the highest possible Reynolds number (i.e. using largest size propeller as possible). At this scale, the demi-hull was too long (5.39 meter) to fit the tunnel’s test section and was truncated to 3 meters by removing a portion from the parallel mid-section, to be combined with properly scaled fore and aft sections. This is a well-recognized practice throughout the industry. The chosen dimensions combined with the required tunnel conditions resulted in a propeller Reynolds number ranging from  $8.67 \times 10^5$  to  $1.47 \times 10^6$ . The largest blockage of the tunnel cross section was 16.5%, which is well within the ITTC guidelines (ITTC, 2011a). Based on the above selections; the general specifications of the dummy-hull model and the full-scale vessel are given in Table 5-1.

Table 5-1 Full-scale vessel and dummy-hull model particulars.

<b>Main particulars</b>	<b>Full scale (Start of Tri- als)</b>	<b>Full scale (End of Tri- als)</b>	<b>Model scale (Dummy model of Starboard Hull)</b>
Length overall	18.88	-	3.007
Length between perpendiculars, $L_{PP}$ (m)	16.45	-	N/A
Beam, moulded, $B$ (m)	7.3	-	0.558
Draft at forward perpendicular, $T_F$ (m)	1.745	1.72	0.448
Draft at aft perpendicular, $T_A$ (m)	1.845	1.82	0.557
Propeller distance from aft perpendicular (m)	0.9	-	0.262
Number of propellers, NP	2	2	1

These data show two loading conditions of the vessel, namely, at the start and end of the full-scale trials. This was because the trials were conducted over three consecutive days, thus, the fuel consumptions and various other changes on-board resulted in slight changes in the drafts and hence running conditions of the vessel. The loading conditions of the vessel were taken from the bridge logbook and then used as an input to the stability booklet to interpolate the draft readings for each loading condition. The procedure was then repeated taking into account the fuel consumption during the course of the trials. The draft values in Table 5-1 represent only the static trim condition. Further manipulation of this data to take account of the dynamic trim is discussed in Section 3. Based on the selected scale ratio the main characteristics of the model and full-scale propeller are given in Table 5-2.

Table 5-2: Full-scale propeller and model propeller particulars

	In full scale	In model scale
Propeller diameter, D (m)	0.75	0.214
Number of blades, Z	5	
Direction of rotation	Port: left turning - SB: right turning -	SB: right turning - outwards
Type of propeller	Fixed pitch	
Pitch ratio at 0.7R P/D	1.057	
Chord length at 0.7R, (m)	0.352	0.1006
Skew angle, $\theta_s$ (Deg)	19°	
Rake angle (Deg)	0°	
Expanded Blade Area Ratio, EAR	1.057	
Boss diameter ratio, $D_{Hub} / D$	0.2	
Scale ratio, $\lambda$	3.5	

### 5.2.2 Wake simulations

A dummy hull plus 2D wake screens offer a better method of representing the 3D towing tank flow effects compared to a simple two-dimensional wake screen approach, although the latter is more economical in time and cost. Hence, two-dimensional wake screens were added at the aft end to account for the flow retardation lost by truncation of the hull in the middle section as shown in Figure 5-1. During the wake simulation exercise in a cavitation tunnel, the traditional method of measuring the wake flow velocities is to use the Pitot tubes. By considering the intrusive nature of these devices, the use of a Particle Image Velocimetry (PIV) type field flow measurement device is adopted. The density of the screen meshes was adjusted through an iterative exercise by using the SPIV system of the ECT. The target wake for these simulations was obtained from the wake survey tests with a 1:5 full-model of “The Princess Royal” in the Istanbul Technical University towing tank excluding the rudder and interceptor plates (Korkut & Takinaci, 2013). Detailed wake measurement results are provided in numeric format in Appendix A.

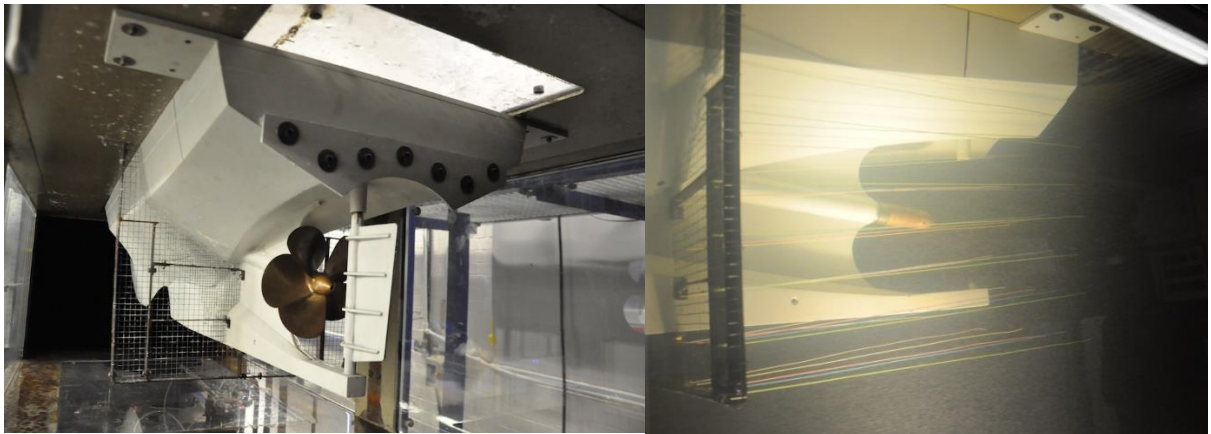


Figure 5-1 : Dummy-hull model fitted in Emerson Cavitation Tunnel.

Wake simulation started with a “base wake screen”, which was made of  $10 \times 10 \text{ mm}$  size of wire mesh grids, was used. The base screen was laid over a steel framework, which was located in a transverse plane at a distance of 1.5 propeller diameter upstream of the propeller’s hub centre, as seen in Figure 5-1. To make the wake screen construction more efficiently, a streamline tracing experiment was conducted to determine the corresponding position from the wake screen to the wake plane. In order to trace the streamlines visually, sufficient numbers of soft threads with different colours were attached to the base mesh at strategic positions. The projections of the trailing ends of these threads provide a very useful practical guide for strategically positioning of wire mesh grids on the base mesh as presented by the right-hand side of Figure 5-1.

In the simulation exercise, more emphasis was put on the accuracy of the wake velocities at the higher radius ( $r > 0.8r/R$ ) and at the top dead centre (TDC) and bottom dead centre (BDC) due to the influential effect of the wake shadow region and substantial skeg, respectively. Whilst there happens to be some discrepancy at lower radius region, agreements for radii  $r/R > 0.5$  are particularly encouraging and considered satisfactory for the hydro-acoustic cavitation tunnel tests. Figure 5-2 shows the contour plots of the target wake and simulated wake while Figure 5-3 and Figure 5-4 show the expanded comparative plots of the wake velocities at two critical outer radii. The latter two figures demonstrate that reasonable simulation of the target wake has been achieved.



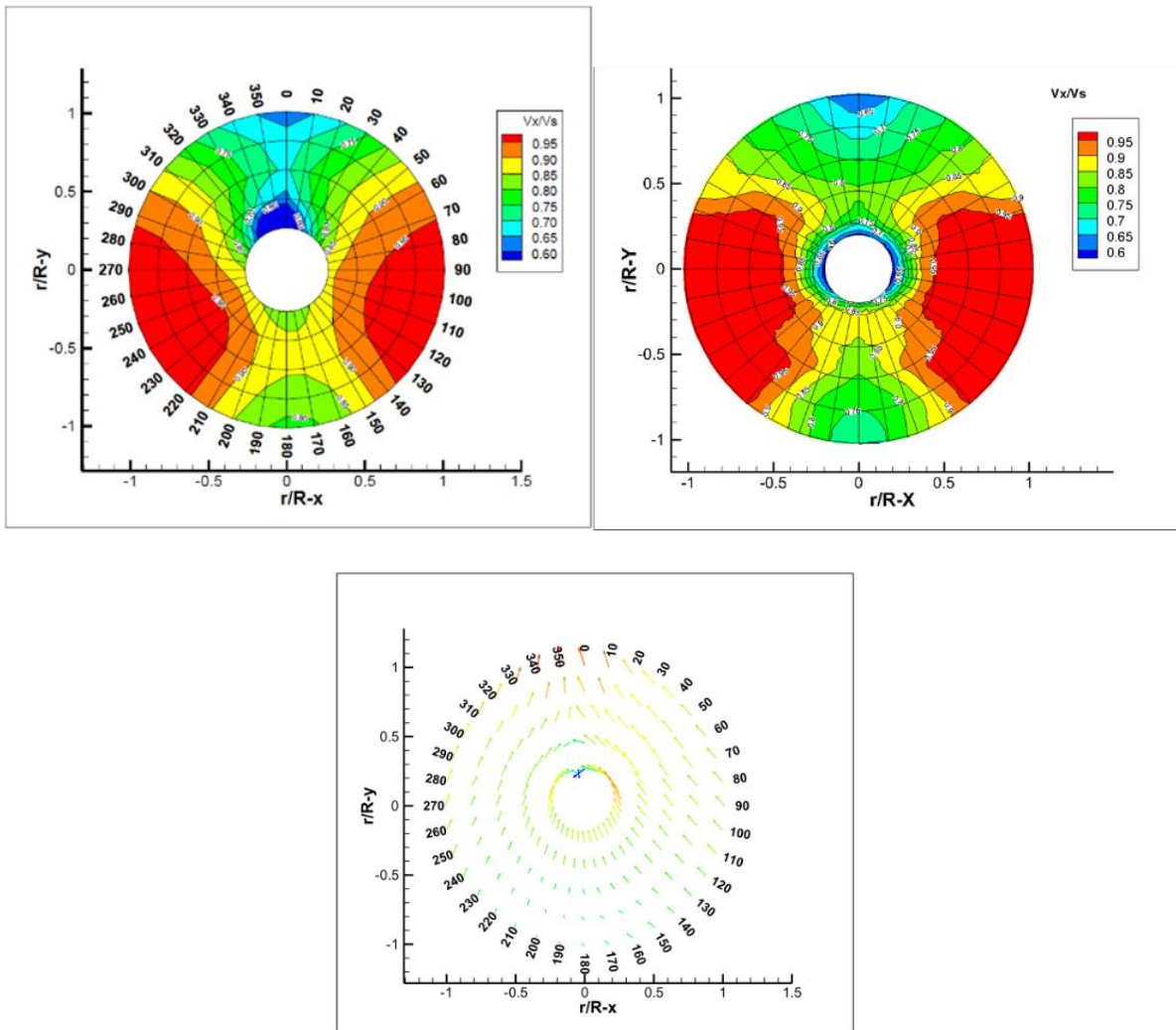


Figure 5-2 : Contour plots of target wake (left) and simulated wake (right) together with the vector plot of the radial and tangential components of the target wake (bottom).

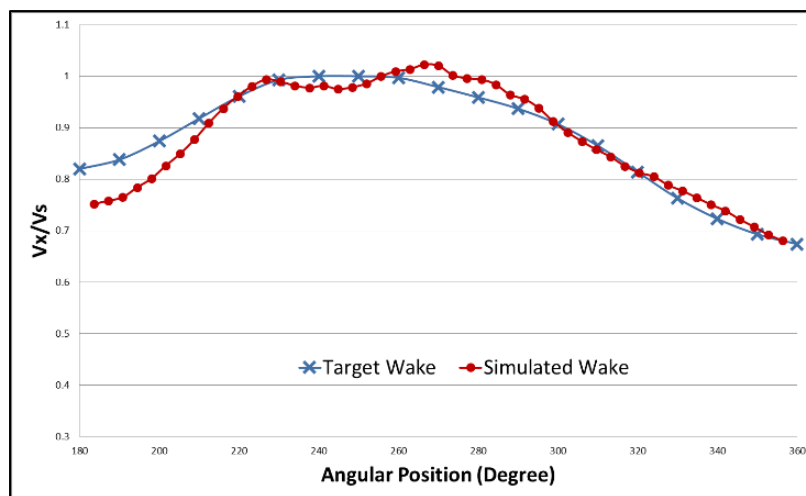


Figure 5-3 : Comparative plots of axial wake velocities at  $r/R=0.827$ .

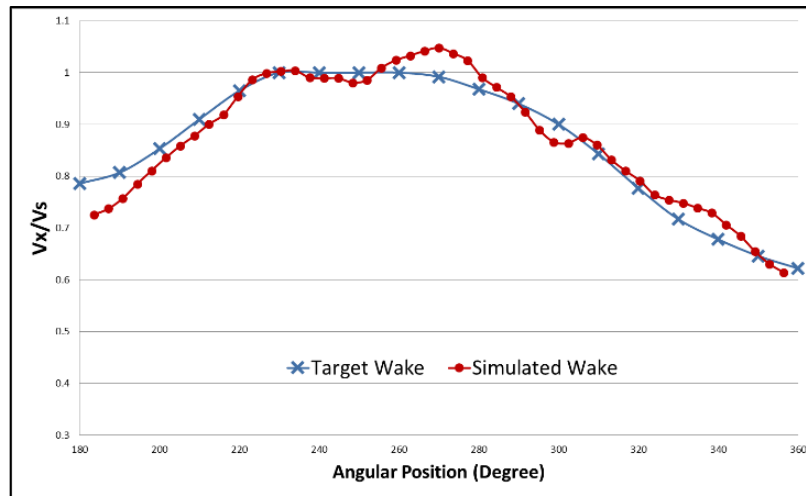


Figure 5-4 : Comparative plots of axial wake velocities at  $r/R=1.013$ .

A scaled hull model used for the wake simulation is not enough to completely represent a developed flow boundary layer in comparison to full-scale wake. This results in discrepancies in terms of Reynolds number to exist which leads to a relative difference in the boundary layer thickness between the model and the full-scale ship. This is generally accounted for by applying corrections as proposed by Sasajima as presented by Carlton (2012) especially for models with high scale ratio. The full-scale extrapolation of the wake is not carried out for this case due to the small scale factor of the model used for the case.

### 5.3 Cavitation test conditions

The trial runs simulated in the tunnel were determined based on the four most representative and reliable runs selected from the full-scale trials conducted under the SONIC project. These conditions had sufficient repetitions and reciprocal runs to filter out the tidal current effects and included one non-cavitating condition and three cavitating conditions corresponding to engine speeds of 600, 900, 1200 and 2000 rpm, respectively. Readings are for the Port propeller since its shaft torque gauge was deemed more reliable. The corresponding propeller shaft speeds were lower, in the gearbox ratio of  $1.75:1$ . A summary of the selected full-scale conditions and relevant data for the vessel is given in Table 5-3.

Table 5-3 : Selected full-scale test conditions and relevant data for “The Princess Royal”.

DATA / PARTICULARS	VALUES			
Power rating (% of MCR)	Service Condition at 2.23% MCR	Service Condition at 6.9% MCR	Service Condition at 16.1% MCR	Service Condition at 73.4% MCR
Dynamic draught $T_A / T_F$ (m)	1.95 m /1.57m	1.95 m /1.57m	1.95 m /1.57m	1.95 m /1.57m
Ship speed through water, $V_s$ (knot)	4.775	7.100	9.350	15.108
Engine speed, N (RPM) (As set on the wheelhouse by the skipper)	600	900	1200	2000
Delivered power at propeller, $P_D$ (kW) (Port side in full Scale)	10.0	31.0	72.25	329.5
Propeller speed, actual $N_{act}$ (RPM) (Port side in full Scale)	342.8	514.2	682.1	1141.5
Cavitation number, $\sigma_n$	1.20	0.53	0.30	0.11
Torque (kNm) - (Port side in full scale)	0.3	0.6	1.0	2.8
Torque Coefficient, $10K_Q$	0.378	0.336	0.318	0.318

For the tunnel tests, similarity was achieved using key parameters for each operational condition such as advance coefficient, torque coefficient and rotational cavitation number using the Equation 17.

Using the relevant expressions and associated data given in Table 5-3 the key parameters for setting the corresponding tunnel test conditions are presented in Table 5-4. In setting these conditions, either the model propeller shaft speed or the applied vacuum level requires to be fixed for each test condition; the former was selected. Thus, for each condition presented in the Table, the propeller shaft speed,  $n_m$ , was first selected, then the corresponding vacuum level calculated based on this speed. The tunnel speed,  $V_m$ , was then adjusted to meet the required shaft torque,  $Q_m$ , based on the equivalent ship  $K_Q$ .

Table 5-4 : A summary of cavitation tunnel test conditions.

DATA / PARTICULARS	VALUES			
Power rating (% of MCR)	Service Condition at 2.23% MCR	Service Condition at 6.9% MCR	Service Condition at 16.1% MCR	Service Condition at 73.4% MCR
Test conditions	Condition 1	Condition 2	Condition 3	Condition 4
Cavitation number, $\sigma_n (\pi nD)$	1.2	0.54	0.3	0.11
Dynamometer, $n_m$ (revolutions per second (rps))	15	20	20	30
Vacuum applied to tunnel, $H_{st}$ (mmHg)	-254	-351	-510	-551
Model scale torque, $Q$ (Nm)	3.84	6.07	5.75	12.92
Adjusted tunnel speed, $V_m$ (m/s)	1.39	2.25	2.41	3.75

In Table 5-4 the test condition numbers: 1, 2, 3 and 4 corresponding to the selected trials conditions (i.e. engine speed of) 600, 900, 1200 and 2000rpm, respectively given in Table 5-3. The tunnel tests conditions cover a broad range of speeds. Therefore, although the fixed rotational speed and fixed vacuum application method was employed, it was concluded that the best way to cover such a wide cavitation range was to alter the propeller shaft speed in correspondence with the full-scale propeller scaled shaft speed. This also enabled better cavitation observation in test Condition 4 by achieving required cavitation number through increased rpm rather than increased vacuum and thus reducing the number of light scattering bubbles in the viewing section.

During the whole course of the testing campaign, the water quality of the facility was monitored for gas content, since it is well known to affect cavitation. The dissolved oxygen content of the tunnel was kept at 30% during the experiments as recommended by ITTC (2011a, 1987).

## 5.4 Cavitation observations

Nano-Sense high-speed video cameras and Nikon DSLR camera were used for the cavitation observation and recording at ship and model scale. The recordings were made in two different lighting configurations. First one was with the high-speed camera mode with continuous lighting; the second one was with stroboscope lighting where both the strobe and cameras were triggered from propeller speed. Figure 5-5 to Figure 5-12 show sample cavitation observations for each condition, both from the cavitation tunnel tests and full-scale trials. Overall, qualitative comparisons of the cavitation extent show reasonable similarity except the tip vortex diameter, which is observed to be relatively small during tunnel tests.

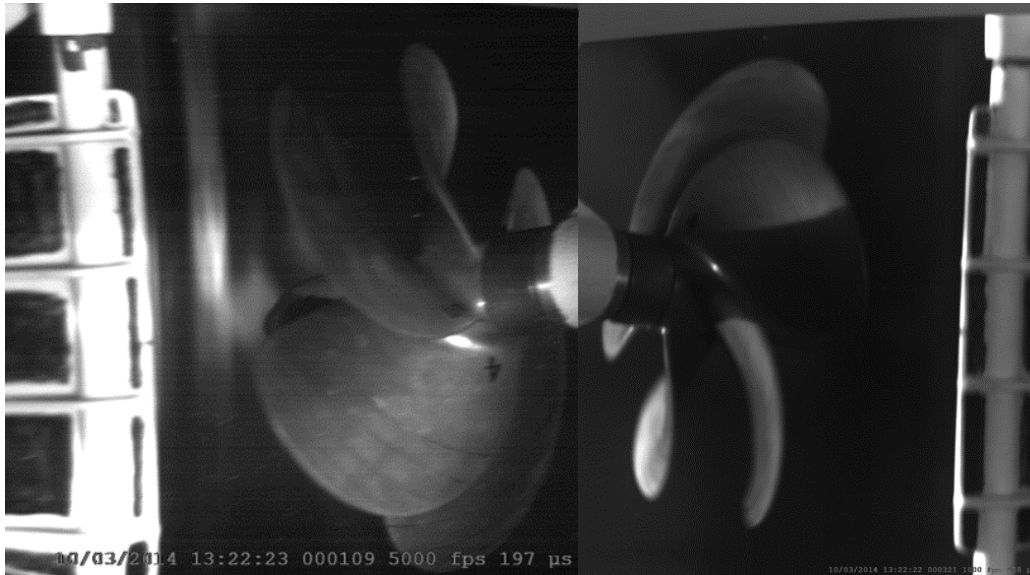


Figure 5-5 Cavitation observations from tunnel tests for Condition 1;  $\sigma_n = 1.20$ ,  $K_Q = 0.378$ .

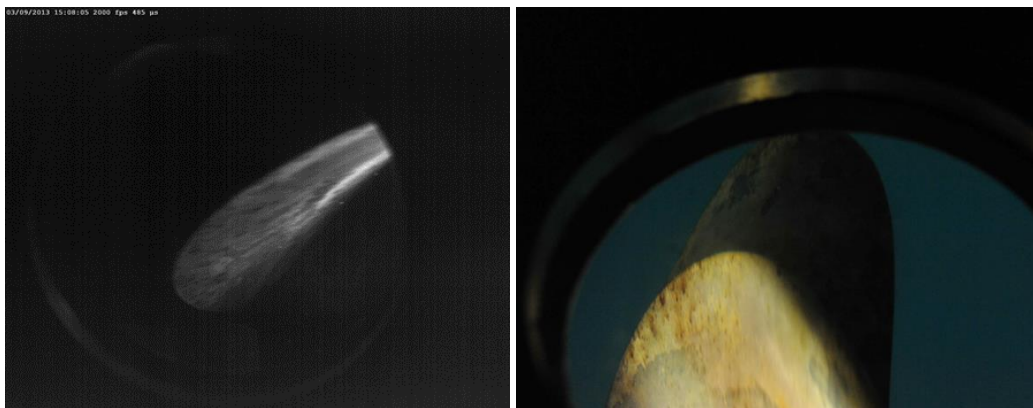


Figure 5-6 Cavitation observations from full scale trials for Condition 1;  $\sigma_n = 1.20$ ,  $K_Q = 0.378$ .

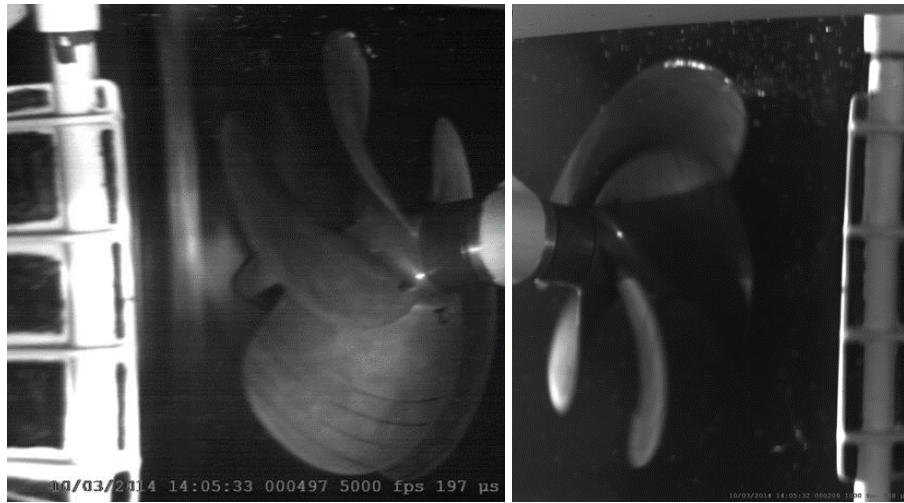


Figure 5-7 Cavitation observations from tunnel tests trials for Condition 2;  $\sigma_n=0.54$ ,  $K_Q=0.336$ .

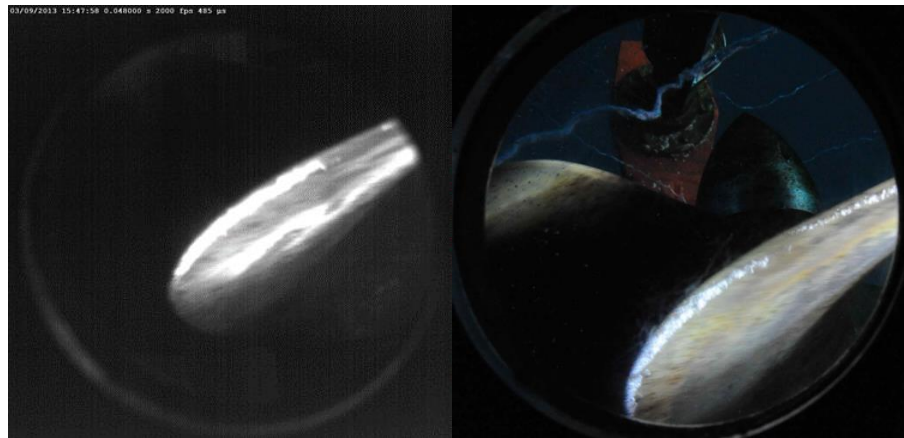


Figure 5-8 Cavitation observations from full scale trials for Condition 2;  $\sigma_n=0.54$ ,  $K_Q=0.336$ .

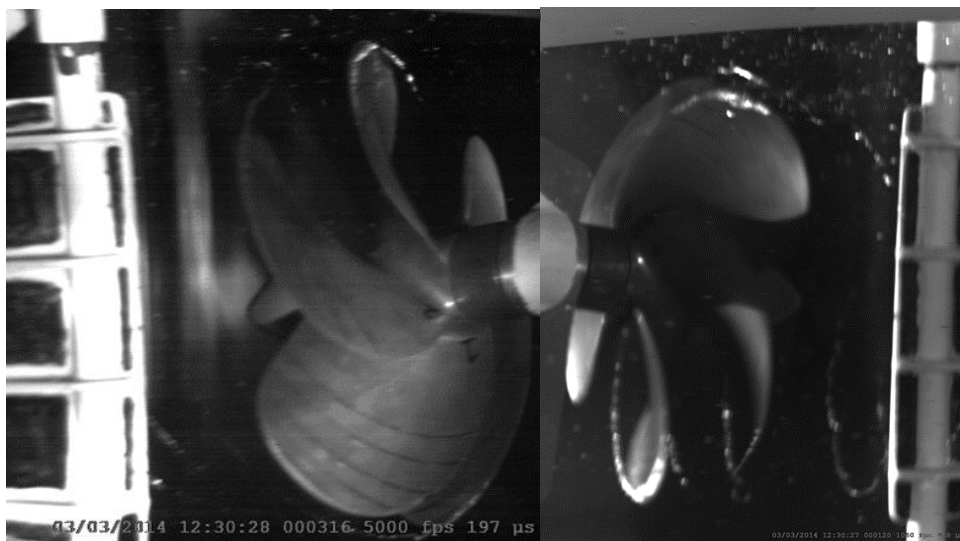


Figure 5-9 Cavitation observations from tunnel tests for Condition 3 Condition 3;  $\sigma_n=0.3$ ,  $K_Q=0.318$ .



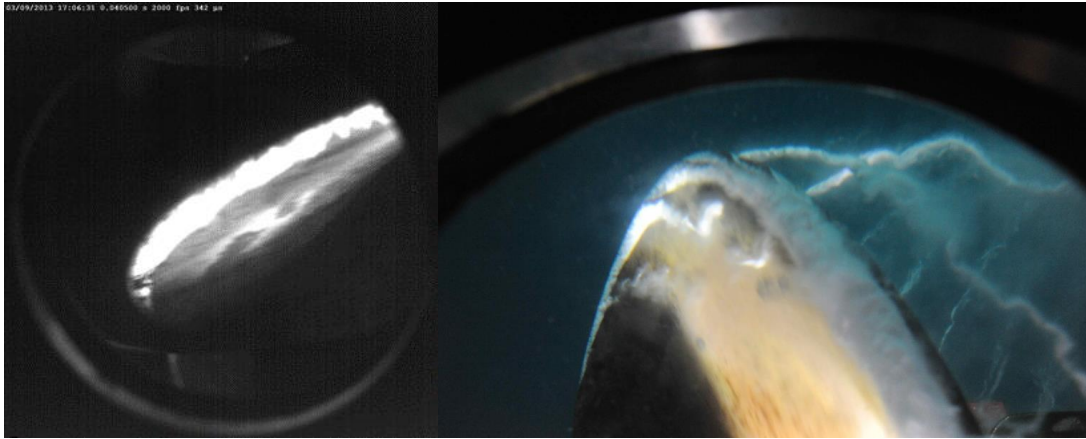


Figure 5-10 Cavitation observations from full scale trials for Condition 3;  $\sigma_n=0.3$ ,  $K_Q=0.318$ .

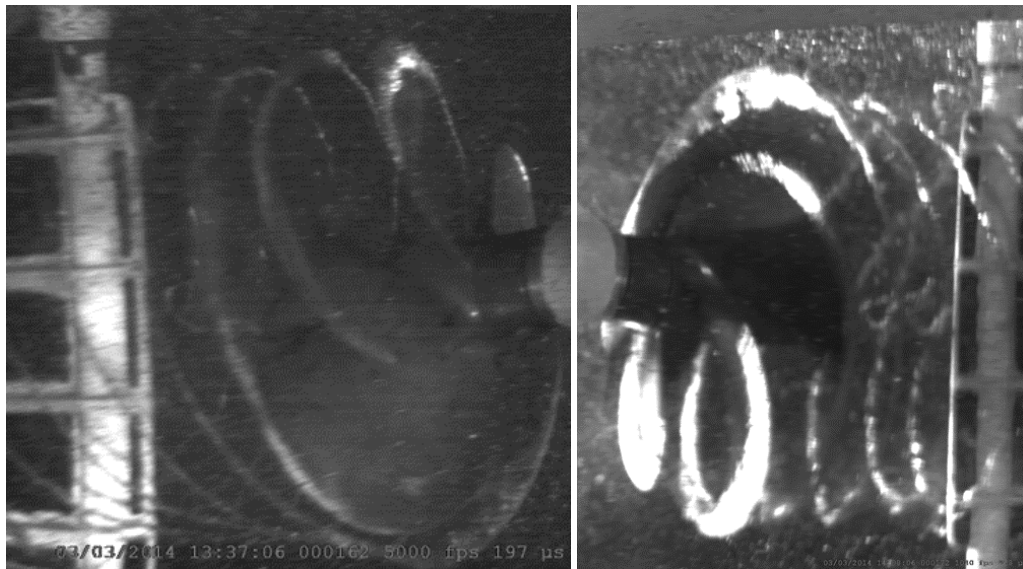


Figure 5-11 Cavitation observations from tunnel tests for Condition 4;  $\sigma_n=0.11$ ,  $K_Q=0.318$ .

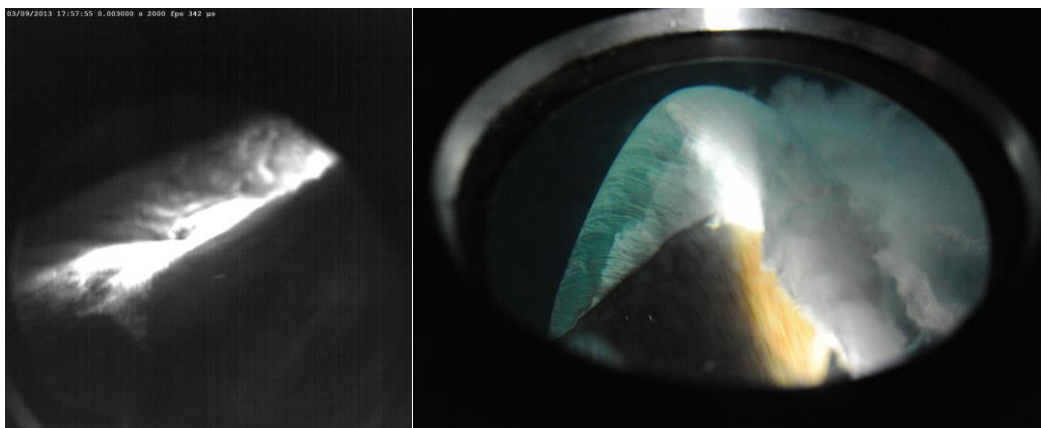


Figure 5-12 Cavitation observations from full scale trials for Condition 4;  $\sigma_n=0.11$ ,  $K_Q=0.318$ .

## 5.5 Pressure pulse measurements

Propeller induced pressure pulse measurements were conducted both on board “The Princess Royal” and with the pressure transducers installed in the dummy hull model. The locations of the pressure sensors on the dummy model were determined by scaling the full-scale distances of the pressure sensor holes from the centre scantling as in Figure 5-13. Extrapolation of the model scale measurements are made using Equation 19.

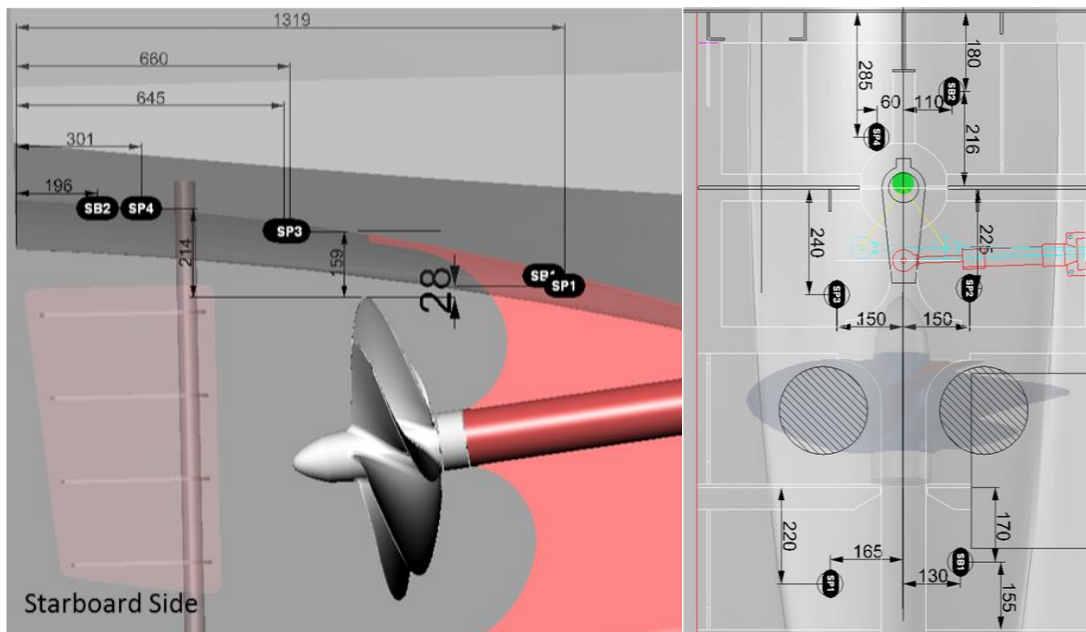


Figure 5-13 Starboard side pressure sensor (indicated by SP\*) and borescope hole (indicated by SB\*) arrangement of “The Princess Royal”.

### 5.5.1 Presentation of results

The propeller induced pressure measurements in the ECT using a dummy model were made using 4 pressure transducers. Figure 5-14 to Figure 5-17 presents measured levels after extrapolation showing the influence of the pressure sensor location on the measured levels. The pressure pulses increase significantly with decreasing cavitation number due the effect of the cavitation. Figure 5-18 to Figure 5-21 show comparisons between the full-scale pressure amplitudes and the extrapolated model scale measurements. The comparisons are made only for the P2 position due to poor signal quality from the other full-scale sensors.



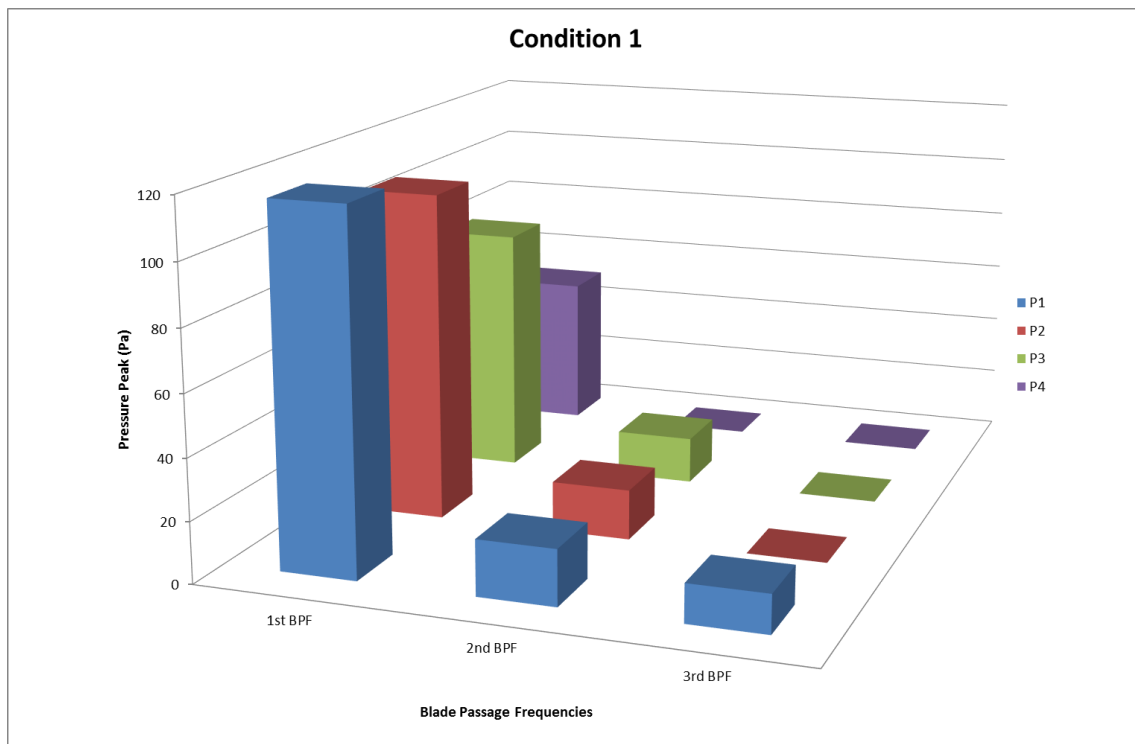


Figure 5-14 Comparative full-scale pressure peaks based on the extrapolation from model tests for Condition 1;  $\sigma_n = 1.20$ ,  $K_Q = 0.378$ .

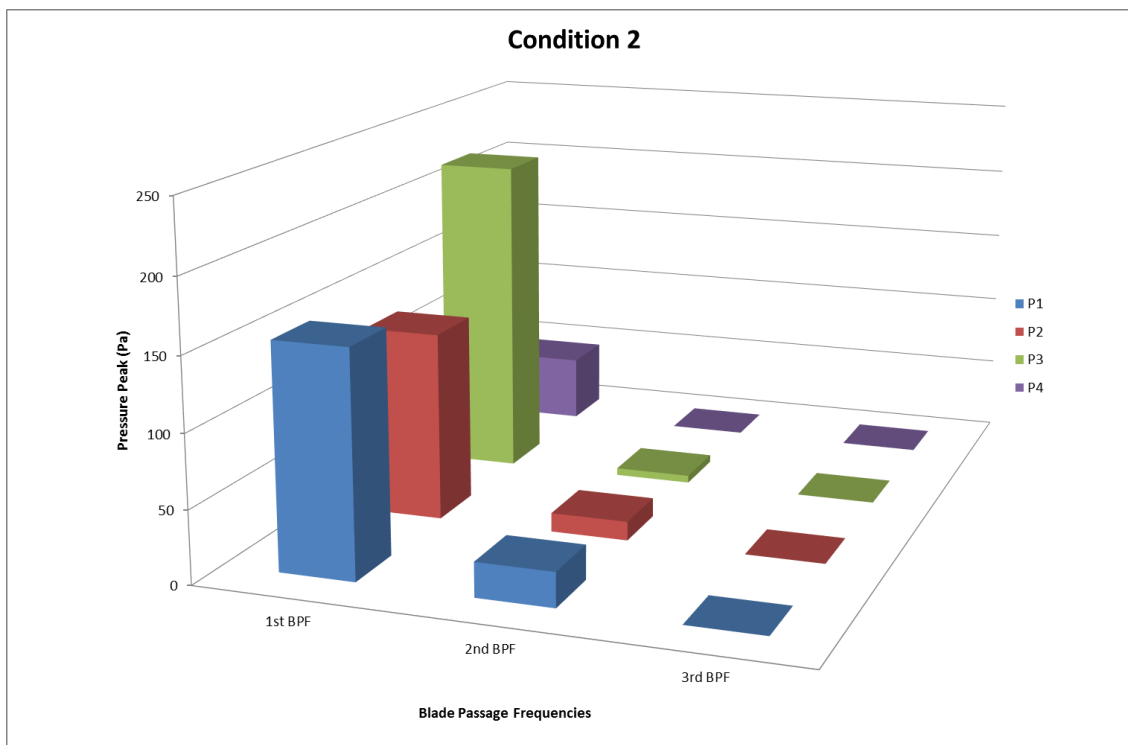


Figure 5-15 Comparative full-scale pressure peaks based on the extrapolation from model tests for Condition 2;  $\sigma_n = 0.54$ ,  $K_Q = 0.336$ .

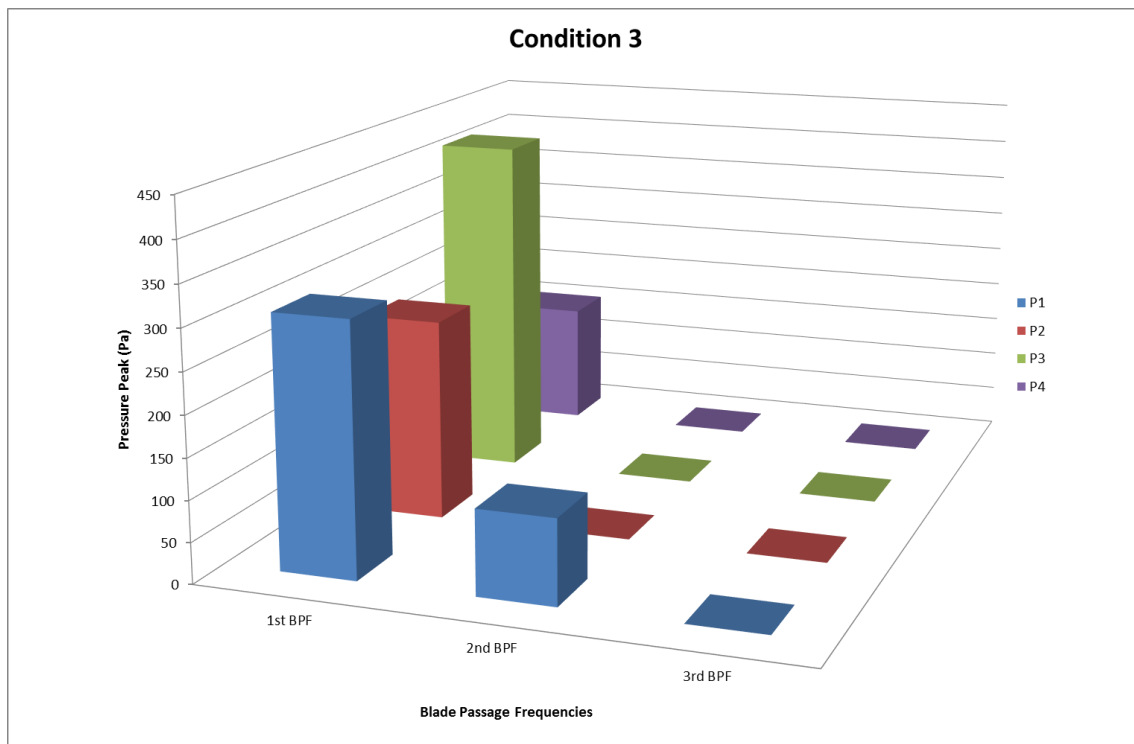


Figure 5-16 Comparative full-scale pressure peaks based on the extrapolation from model tests for Condition 3;  $\sigma_n=0.3$ ,  $K_Q=0.318$ .

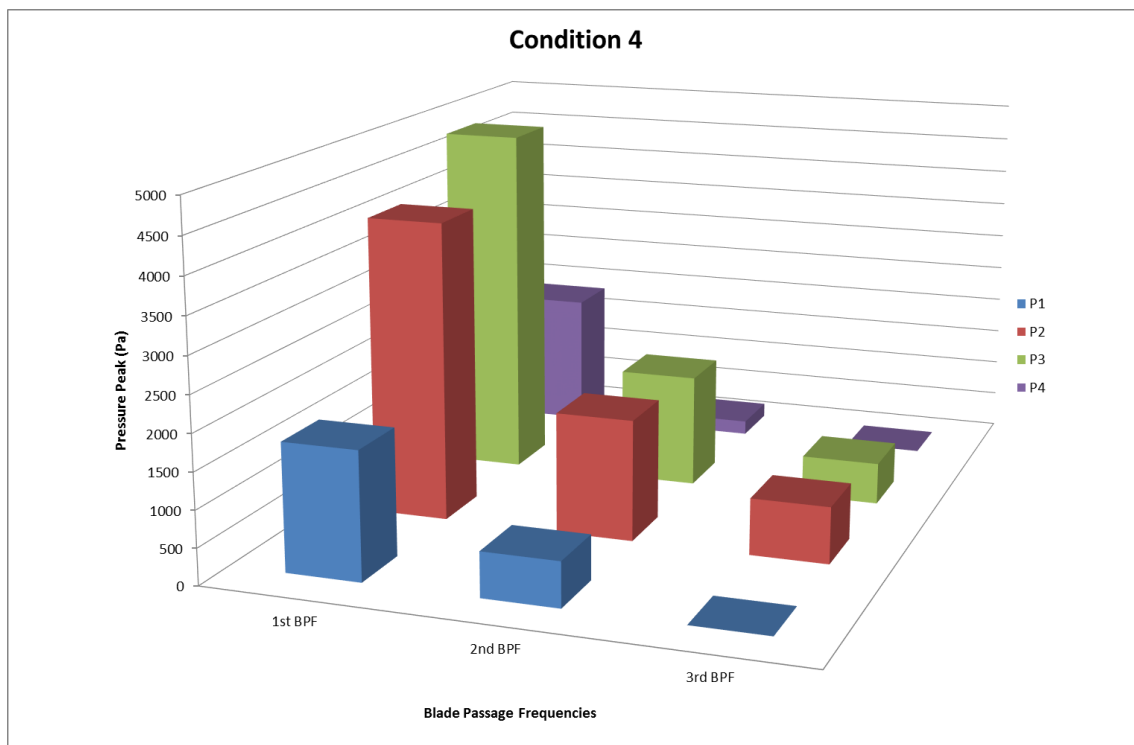


Figure 5-17 Comparative full-scale pressure peaks based on the extrapolation from model tests for Condition 4;  $\sigma_n=0.11$ ,  $K_Q=0.318$ .

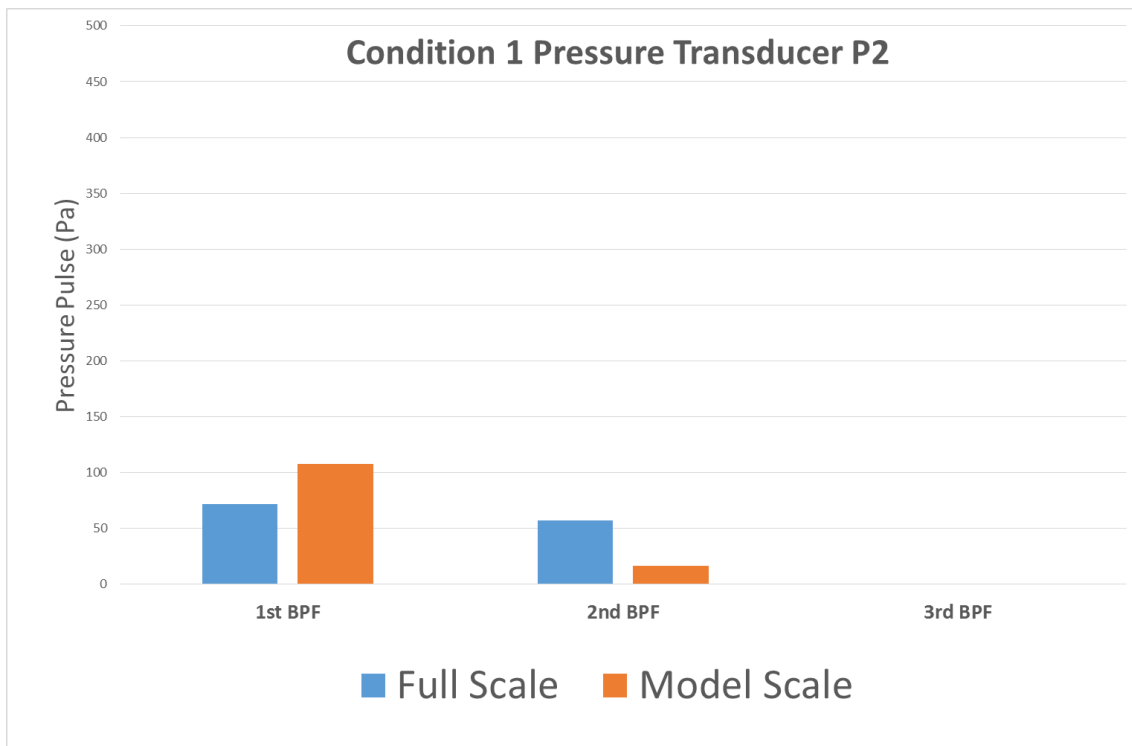


Figure 5-18 Comparison of the full scale and extrapolated model scale measurements for P2 position  
Condition 1;  $\sigma_n = 1.20$ ,  $K_Q = 0.378$ .

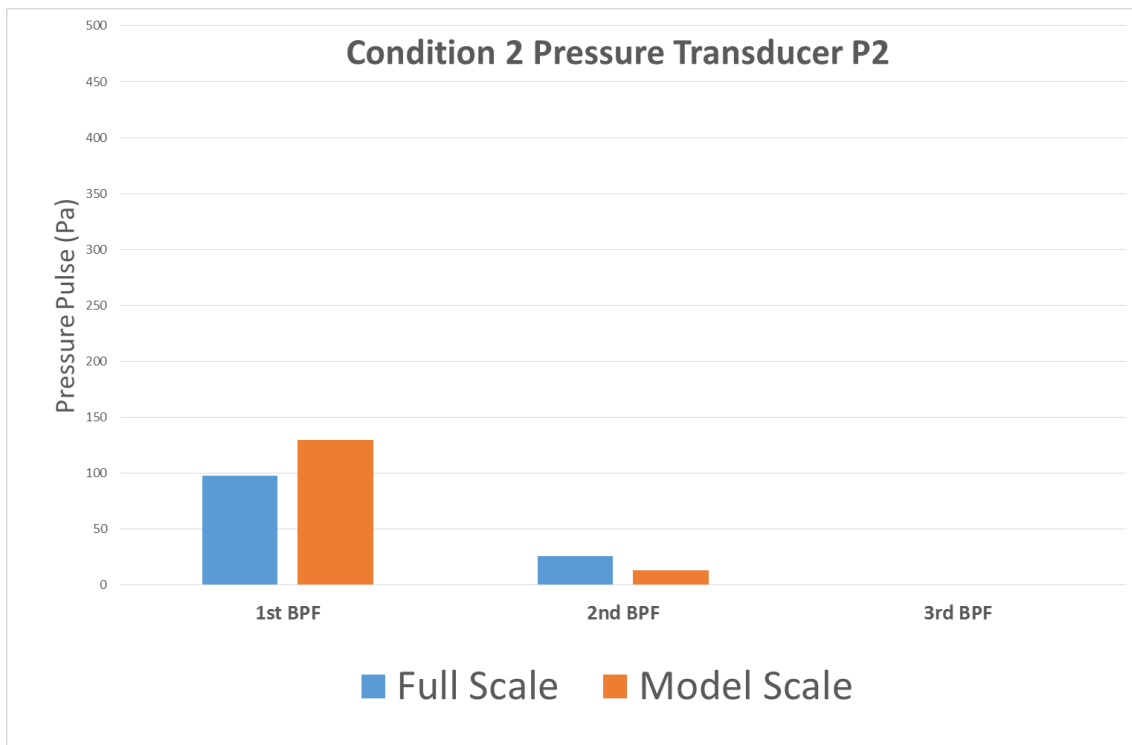


Figure 5-19 Comparison of the full scale and extrapolated model scale measurements for P2 position  
for Condition 2;  $\sigma_n = 0.54$ ,  $K_Q = 0.336$ .

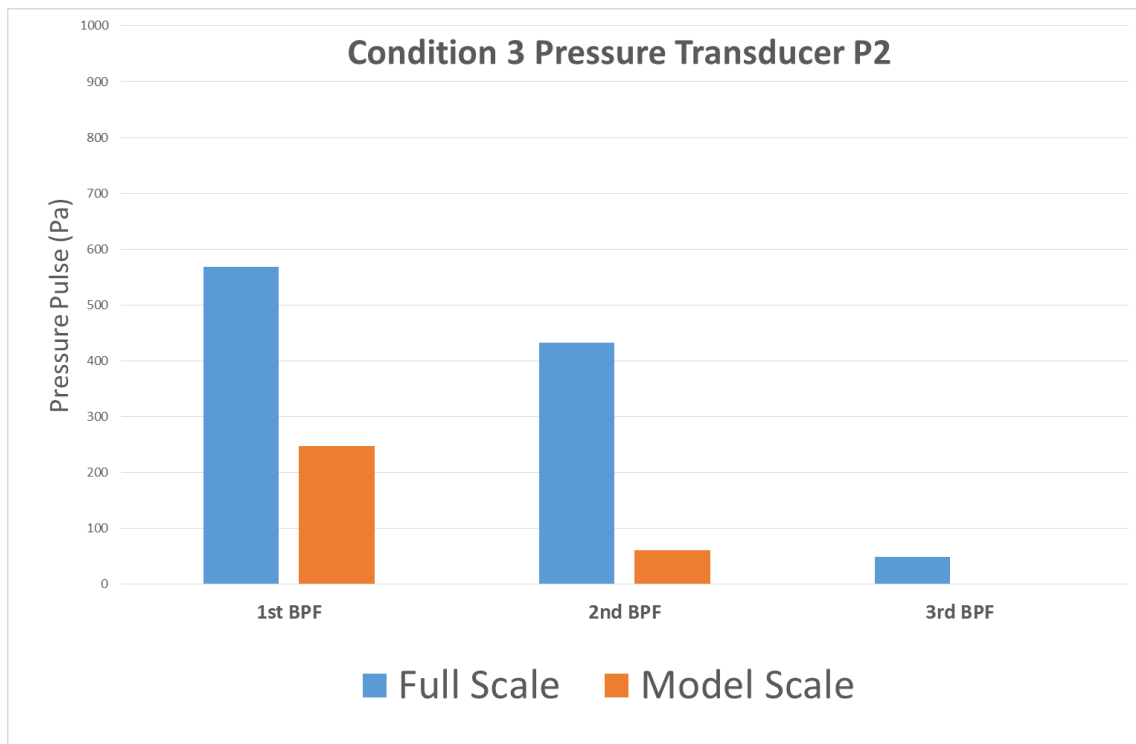


Figure 5-20 Comparison of the full scale and extrapolated model scale measurements for P2 position for Condition 3;  $\sigma_n=0.3$ ,  $K_Q=0.318$ .

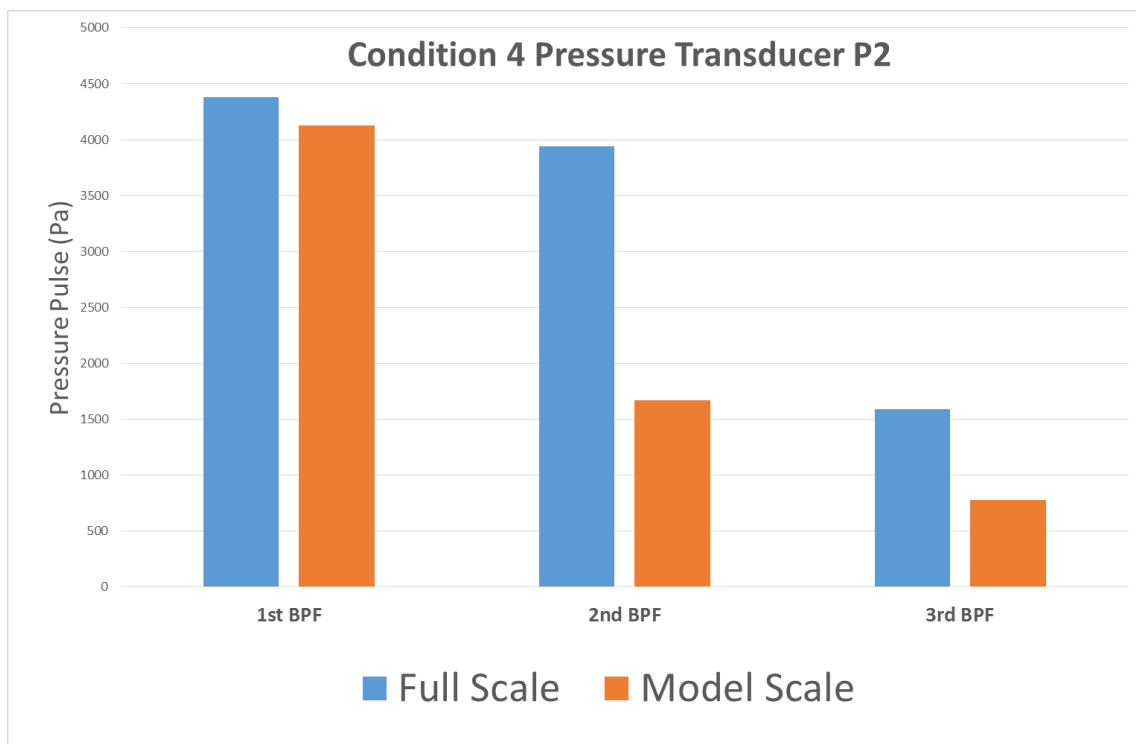


Figure 5-21 Comparison of the full scale and extrapolated model scale measurements for P2 position for Condition 4;  $\sigma_n=0.11$ ,  $K_Q=0.318$ .

## 5.6 Noise measurements

Noise measurements were made using the B&K PULSE Type 3023 data acquisition system with a 6/1 LAN interface and a B&K Type 8103 miniature hydrophone which was located inside the cavitation tunnel and supported by a streamlined strut. The offsets of the hydrophone location are given in Table 5-5.

Table 5-5 Offset of hydrophone location in the tunnel.

8103 Hydrophone location relative to Propeller Plane & shaft line intersection	
x	415mm
y	455mm
z	150mm

In order to ensure the repeatability and reliability of the measurements, Condition 4 was repeated three times since this was the condition where the most severe cavitation was experienced and hence might have had a higher risk of errors (Coleman & Steele, 2009; ISO, 2009). The uncertainty analysis for this condition has indicated a maximum error of 4.39 dB, calculated using back to back repetition tests using the same mountings and configuration, in the measured URN levels and is within the range of the recommendations (1-5 dB) made by the ITTC (Bertschneider et al., 2014).

One important practical issue in the analysis of the data is associated with the catamaran configuration of the target vessel, which has two propellers and hence two dominant noise sources. However, in the tunnel tests, only one of these sources was represented by the use of the starboard demi-hull. The missing propeller effect was accounted for by doubling the measured levels. This was achieved in the logarithmic scale by adding 3dB to the measured levels.

### 5.6.1 Presentation of results

Figure 5-22 to Figure 5-25 present comparisons of the total RNL, measured on the full-scale trials (SOTON) by Brooker & Humphrey (2014). The total RNL (UNEW) was extrapolated based on Newcastle's tunnel measurements for each of the four operating conditions given in Table 5-4. Two double runs were conducted for each condition given in Table 5-3; a Northwards and Southwards course heading for both starboard and port aspect. The trial area depth was chosen to be approximately 100m with a seabed of soft mud. The measurements are made using a 3 hydrophone array with the deepest hydrophone at 50 m. The full-scale measurements were analysed assuming a dipole source level, which is also referred to as the affected (Ainslie, 2010; Jong, 2009) source level or RNL. Whilst the RNL representation does not account for the influence of the well-known Lloyd's Mirror effect, the error was minimised by adopting the ANSI standard analysis procedure and averaging the measurements made with three hydrophones (ANSI, 2009; ISO, 2012).

Figure 5-22 to Figure 5-25 also include the measured background noise levels in both the full-scale trials and cavitation tunnel experiments. Although the nature of the background noise for the model and full-scale noise measurement is different, it is relevant to note the levels contributed from these sources. Whilst there is a significant contribution from the background in the tunnel measurements, ambient noise in the full-scale measurements is rather small. Further information on the definition of the background noise levels for the full-scale trials and model tests is given in Section 3.4.6 under the headline "Noise measurement equipment and analysing methodology".

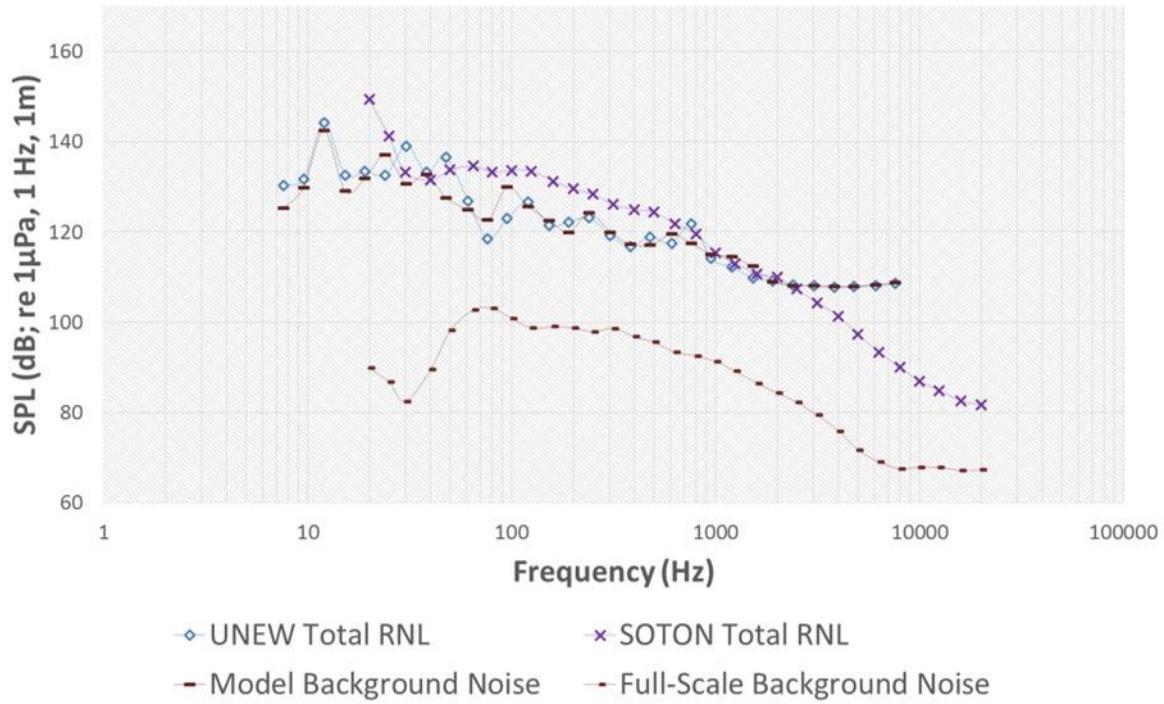


Figure 5-22 Condition 1 - Comparison of total RNL from full-scale trials and tunnel test measurements based extrapolations at  $\sigma_n = 1.20$ ,  $K_Q = 0.378$ .

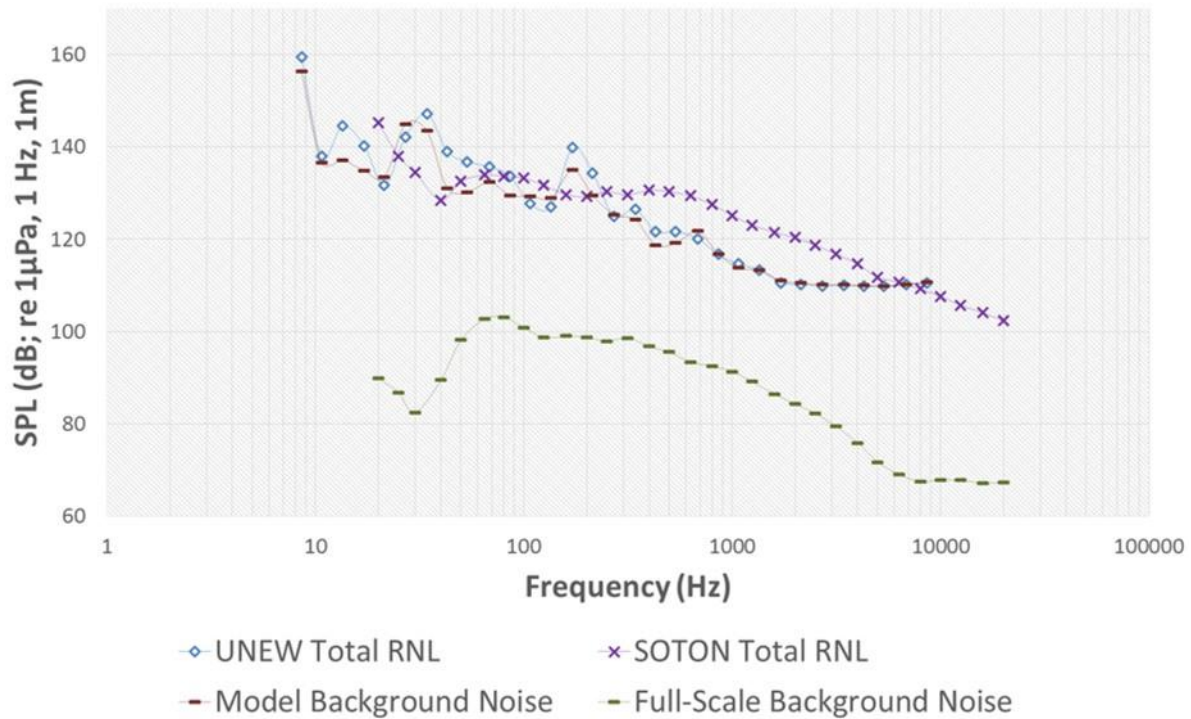


Figure 5-23 Condition 2 - Comparison of total RNL from full-scale trials and tunnel test measurements based extrapolations at  $\sigma_n = 0.54$ ,  $K_Q = 0.336$ .

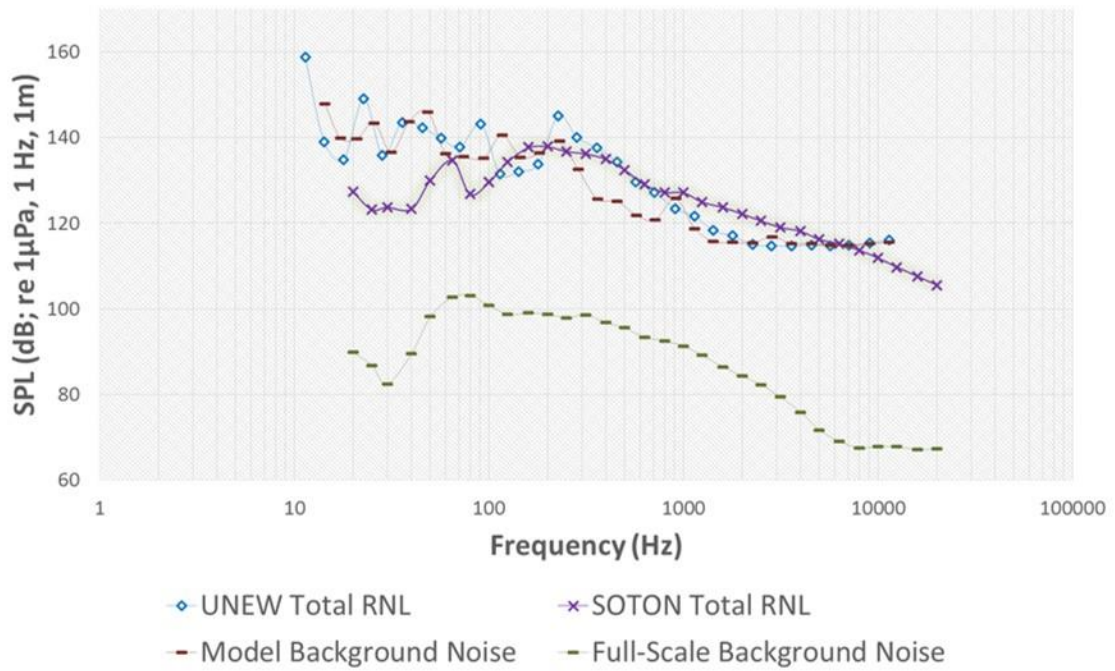


Figure 5-24 : Condition 3 - Comparison of total RNL from full-scale trials and tunnel test measurements based extrapolations at  $\sigma_n=0.3$ ,  $K_Q=0.318$ .

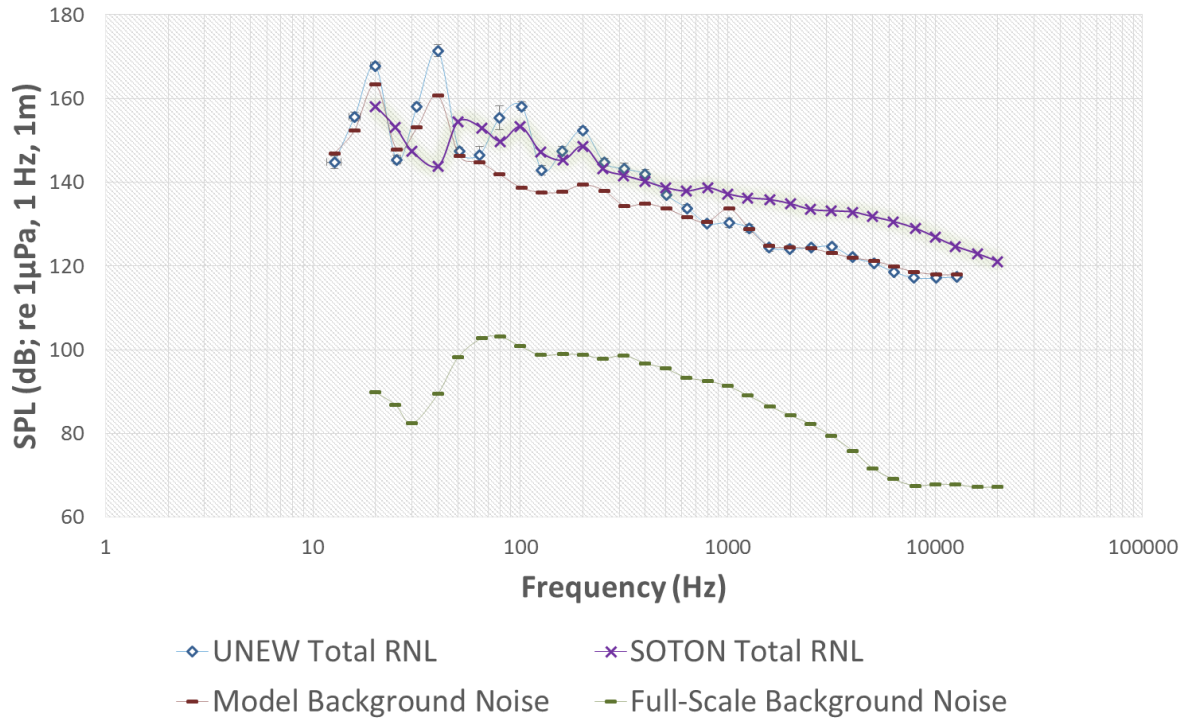


Figure 5-25 Condition 4 - Comparison of total RNL from full-scale trials and tunnel test measurements based extrapolations at  $\sigma_n=0.11$ ,  $K_Q=0.318$ .



Figure 5-26 to Figure 5-29 compare “net” RNLs for the same four operating conditions after including corrections for the background noise following the recommendations given by ITTC (ITTC, 2014) and ANSI (ANSI, 2009). Moreover, during the tests, investigations of the effect of varying torque loading on the measured noise is also carried out. Figure 5-29, includes a dashed line representing the Net noise levels measured for the condition where the propeller is operated for 15% higher torque than the required level.

The use of a dummy model and wake screen (1.5 propeller diameters upstream of the propeller plane) to simulate the correct inflow conditions for propeller cavitation raises questions over the noise creating mechanisms thus introduced. These may include cavitation, increase in turbulence intensity and singing. The effects of these sources on the measured noise levels were accounted for through the background noise correction.

Although the ITTC guidelines recommend further correction of the measured data to account for the influence of the testing environment such as the reverberation and reflections due to the walls (Bertschneider et al., 2014), such corrections were not applied to the presented results. This was purely due to the time restrictions imposed on the project and tight tunnel schedule that was not able to accommodate a detailed investigation for this dummy model.

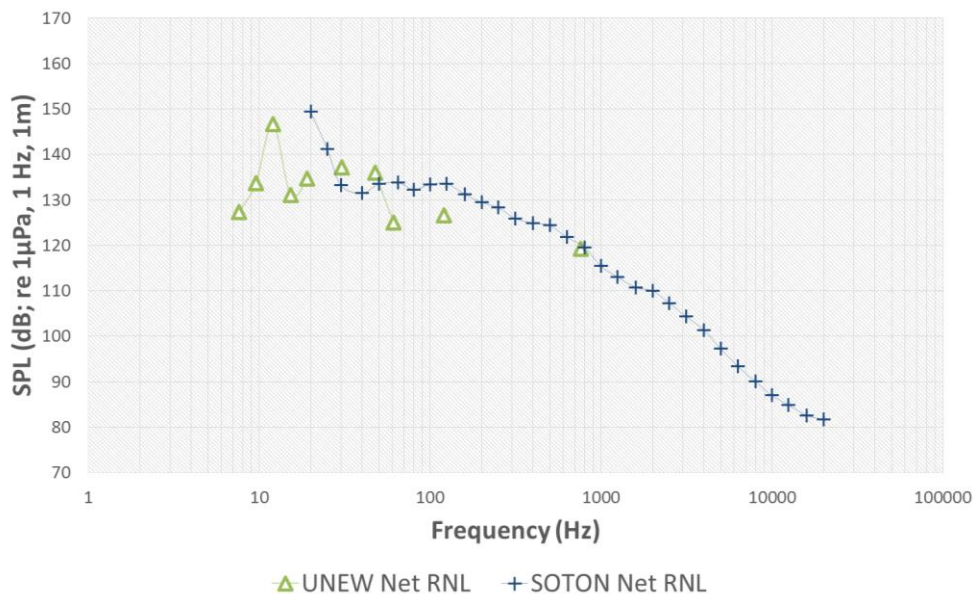


Figure 5-26 Condition 1 - Comparison of net RNL from full-Scale trials and tunnel test measurement based on extrapolations at  $\sigma_n = 1.20$ ,  $K_Q = 0.378$ .

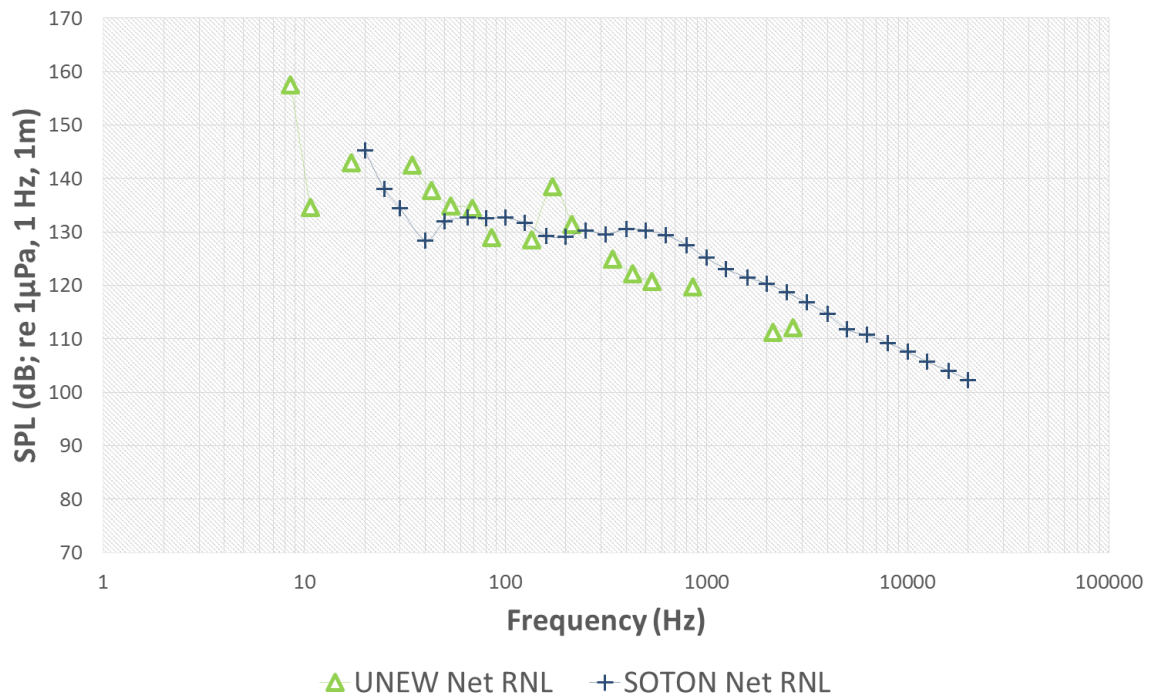


Figure 5-27 Condition 2 - Comparison of net RNL from full-scale trials and tunnel test measurement based on extrapolations at  $\sigma_n = 0.54$ ,  $K_Q = 0.336$ .

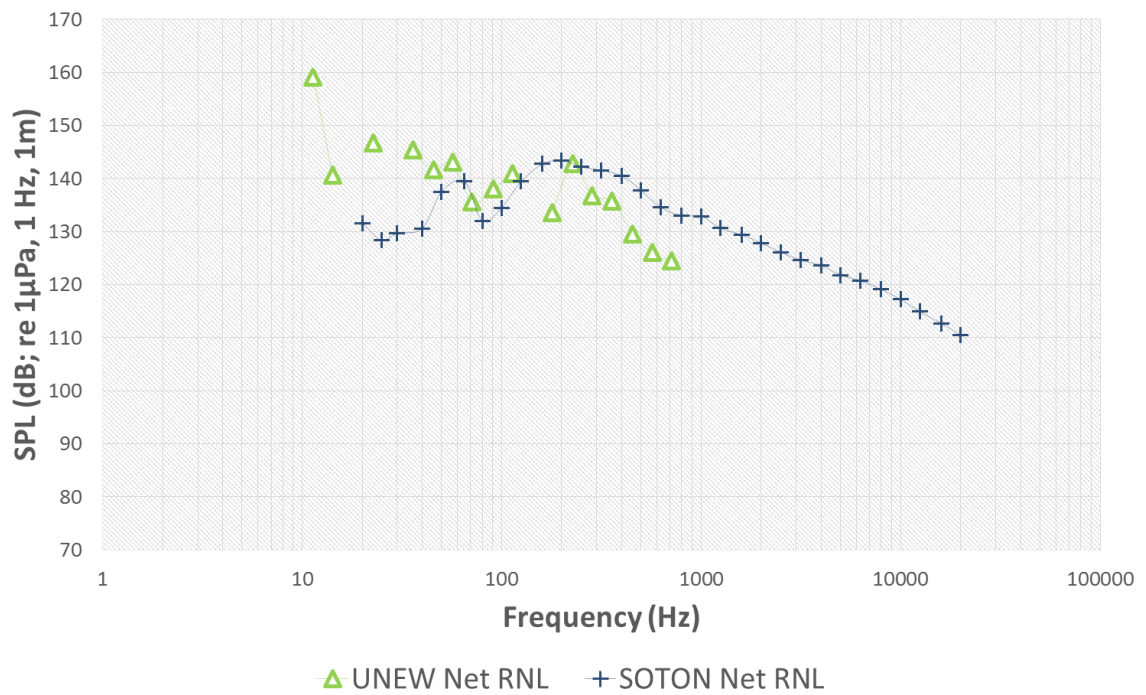


Figure 5-28 Condition 3 - Comparison of RNL from full-Scale trials and tunnel test measurement based on extrapolations at  $\sigma_n = 0.3$ ,  $K_Q = 0.318$ .

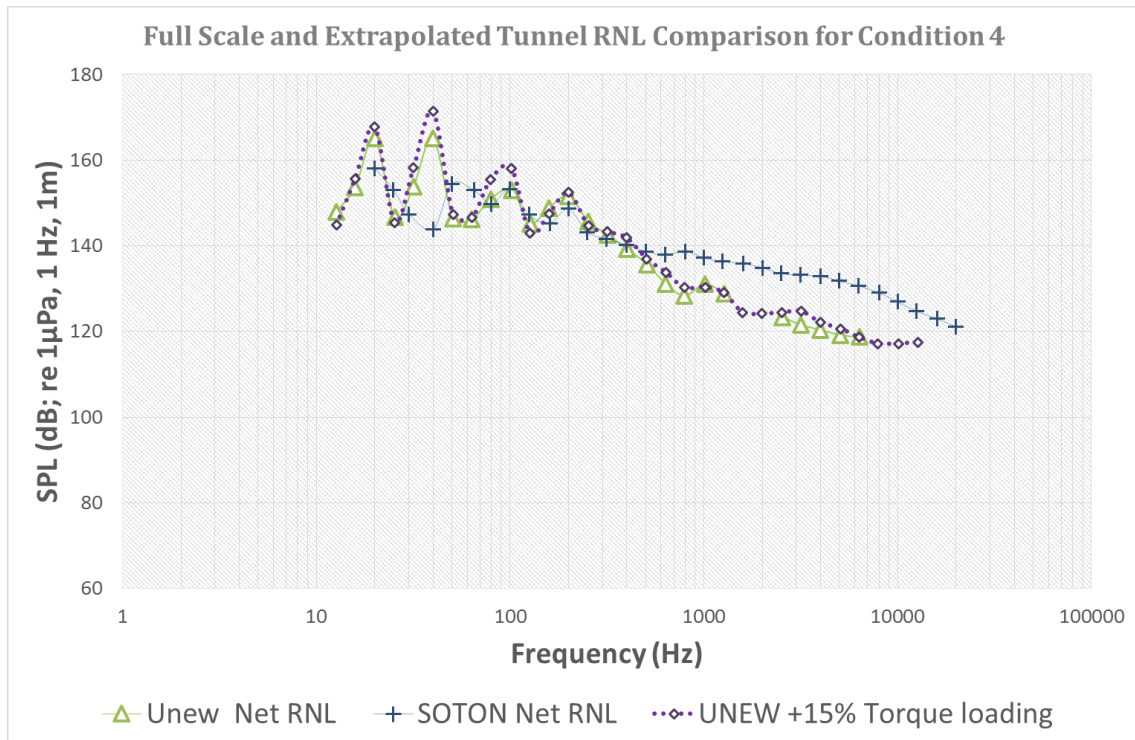


Figure 5-29 Condition 4 - Comparison of net RNL from full-scale trials and tunnel test measurement based on extrapolations at  $\sigma_n=0.11$ ,  $K_Q=0.318$ .

## 5.7 Discussion

The discussion regarding the measurements are structured to initially elaborate on the cavitation observations. The qualitative interpretation of the cavitation observations aid comparisons of the propeller induced pressure pulses and underwater RNL between full-scale and model tests.

“The Princess Royal” had sub-cavitating propellers with very low inception speed and strong tendency to develop cavitation with increasing propeller loading. During the full-scale trials, no cavitation was observed for “Condition 1” at the engine speed of 600 RPM as in Figure 5-6. This was also confirmed by the tunnel tests as can be seen in Figure 5-5.

As the speed increased to 900 rpm (i.e. Condition 2), in the full-scale, relatively continuous leading edge vortex emanating from the blade suction side and trailing in the slipstream up to rudder was observed. The comparison of the cavitation observations from the full-scale and

cavitation tests present a relatively weaker tip vortex during model tests as shown in Figure 5-7 and Figure 5-8 for tunnel tests and from the portholes of “The Princess Royal” respectively.

At the engine speed of 1200 rpm (i.e. Condition 3), in the full-scale, a relatively strong suction side Sheet cavitation emanating from the entire blade leading edge with increased extent (hub to tip) terminated the blade by rolling-up in the form of trailing tip vortex extending to the rudder. The partial break-up of the sheet cavitation, as well as the occasional appearance of hub vortex cavitation and propeller-hull vortex cavitation, were observed as in Figure 5-10. In the tunnel tests, the similar patterns could be observed at corresponding condition whilst the extent of the cavitation has been judged to lesser in terms of the volume in comparison to the full scale as presented in Figure 5-9.

Condition 4 has an engine speed of 2000 rpm and is closest to the engine MCR (2300) condition. The full-scale propeller, in this condition, displayed a rather large extent (almost 25-30% of the blade area, Figure 5-12), volume and intensity of suction side sheet cavitation. This was extremely unsteady, breaking-up (and bursting) intermittently with a cloudy appearance. This sheet cavitation terminated at the blade tip region by rolling-up in the form of a rather thick, intense and cloudy tip vortex trailing to the rudder. This trailing vortex was bursting from time to time. The hub-vortex cavitation was much thicker, intense and continuous. The tunnel test observations compared favourably with the full-scale observations, as shown in Figure 5-11 and Figure 5-12. There was a good correlation in terms of the type, strength and dynamic behaviour of the types of cavitation observed.

The four pressure measurement locations at model scale (Figure 5-14 to Figure 5-17) display amplitudes which are significantly smaller for the non-cavitating Condition 1, however, as expected these increased significantly with the development of cavitation. In addition to this, the amplitudes for sensor positions P1 and P4 are considerably smaller in comparison to P2 and P3 due to being located further from the cavitating region. As the displacement of the propeller blade and cavitation volume and its dynamics are the major sources of pressure pulses, these results show a reasonable tendency. Also, amplitudes from P2 and P3 indicate that P3 is always

higher except in the non-cavitating Condition 1. This is consistent with P3 being located after the wake shadow region. Here the developed cavitation is collapsing and rebounding as the blades leave the wake shadow region and passes into the area of higher axial velocity where the blade inflow angle decreases thus reducing the flow conditions which maintain the volumes of the sheet and vortex cavitation.

Model-scale extrapolated predictions of propeller induced pressure amplitudes were compared with the full-scale results in Figure 5-18 to Figure 5-21. Results for the non-cavitating Condition 1 and for Condition 2, which displays a weak tip vortex presence, display reasonable agreement as shown in Figure 5-18 and Figure 5-19, respectively. However, for the Condition 3, the predictions underestimate the full-scale levels. This may be attributed to differences in observed cavitation extent as discussed previously. Model-scaled predictions for Condition 4 show good agreement with those measured at full scale.

Total noise measurements presented through Figure 5-22 to Figure 5-25 are given together with the background noise measurements to provide further insight especially in the tunnel measurements for which the background noise levels are much more significant. When the background noise corrections were applied, as shown in Figure 5-26. For “Condition 1” most of the noise spectrum had to be discarded since differences were less than 3 dB in the noise levels between the measured model scale data with propeller and the background noise. The non-cavitating noise spectrum was of the dominated by the background noise. Equations 4 and 5, are based on cavitating bubble dynamics and are most probably not appropriate for this condition. Consequently, no further investigation was made in this study of non-cavitating noise extrapolation laws, since the focus was on cavitation induced noise which dominated the full-scale spectra.

In Conditions 2 and 3, as shown in Figure 5-27 and Figure 5-28 respectively, the spectral levels are observed to be less affected by the tunnel background noise for frequencies lower than 1000 Hz. However, beyond this threshold, the spectral levels for both conditions are still affected significantly by the background noise. The cavitation patterns for Conditions 2 and 3, shown in Figure 5-7, Figure 5-8, Figure 5-9 and Figure 5-10 respectively, indicate that the developed

leading edge tip vortex and sheet cavitation are extremely unsteady, breaking-up (and bursting) only intermittently with a cloudy appearance. The sheet cavitation terminates at the blade tip region by rolling-up in the form of a rather thick, intense and cloudy tip vortex, trailing aft to the rudder. Comparison of both the tunnel cavitation observations and the URN predictions with the full-scale measurements for these two conditions seem to be in reasonable agreement up to 500 Hz for the noise predictions.

Underestimation of the SPL predictions at frequencies above 500 Hz may be due to various noise emitting mechanisms and cavitation dynamics created by the tip vortex cavitation at full scale. In order to ensure similar dynamics in model scale experiments, it may be possible to establish a relationship based on acoustical and cavitation similarity, as proposed by Latorre and Shen & Strasberg (Latorre, 1982; Shen & Strasberg, 2003) using McCormick's earlier work (McCormick, 1962); although this was not tried in this study. It was also noted that the cavitation dynamics in Condition 3 appeared more active in full-scale than in the model tests, as observed in the high-speed videos from both cavitation tunnel tests and full-scale trials. Differences in cavitation dynamics are reflected in the distinct differences between the cavitation tunnel SPL predictions and the full-scale values.

For Condition 4, as shown in Figure 5-29, the high level of URN noise spectra over the entire frequency range appears not to be significantly affected by the background noise since the RNL is dominated by significant sheet cavitation and its complex interaction with the tip vortex cavitation. Figure 5-11 and Figure 5-12, show that the propeller developed a rather large extent of suction side cavitation (almost 25-30% of the blade area) with increasing volume and intensity. This was observed to be rather unstable foamy sheet cavitation. The unsteadiness was more towards the blade tip where the sheet cavity terminated on the blade by rolling-up and increasing the strength and thickness of trailing tip vortex extending to the rudder. The trailing vortex sometimes broke-up intermittently, having a cloudy appearance. Also noted were a continuous, intensified cavitating Hub Vortex and, intermittently, a cavitating Hull-Propeller Vortex. The predictions for this condition underestimate the full-scale measurements at the high frequency region (500 Hz - 20 kHz). Although comparisons of cavitation extent are in reasonable agreement, such observed violent collapse events and partial break-off of the sheet cavitation, have



been identified as major noise emitting mechanisms (Bark, 1986), yet cannot be adequately represented in model scale tests. As such these may influence under prediction of the noise levels in the high frequency region.

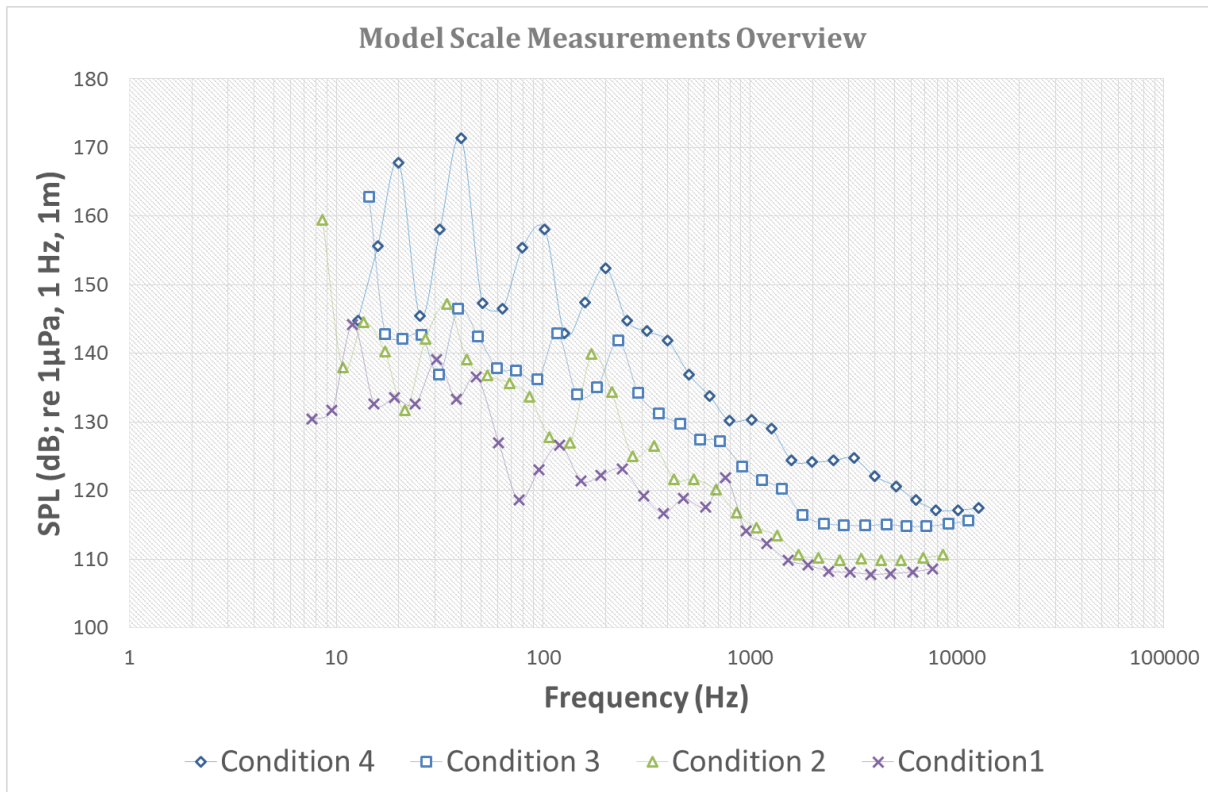


Figure 5-30 Model scale total noise measurements overview.

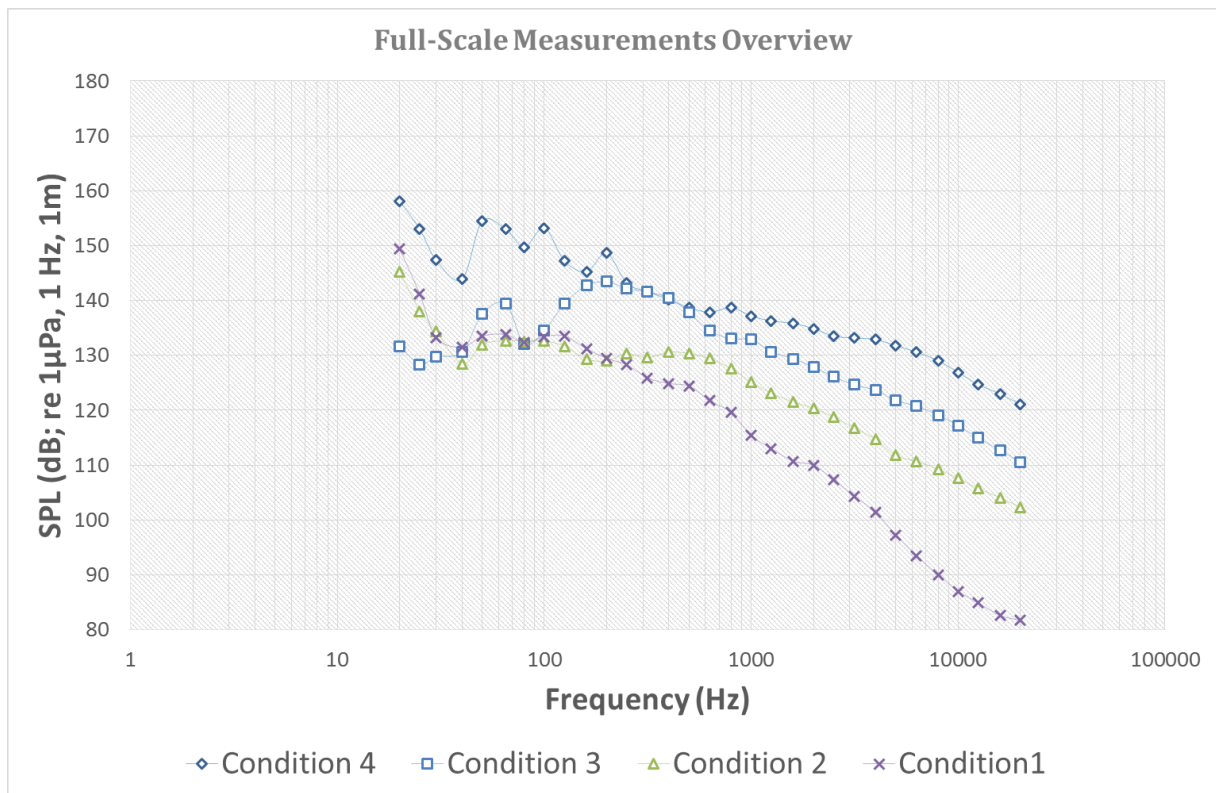


Figure 5-31 Full-scale net noise measurements overview.

Figure 5-30 and Figure 5-31 give a comparative overview of the spectral noise levels for the four operating conditions at model and full-scale, respectively. These allow further interpretation of the influence of the operating conditions and associated cavitation dynamics on the noise spectra. It is evident from the both figures that without cavitation, the URN levels are low. However, as soon as cavitation inception occurs, the spectral levels increase as is expected from trends in the literature (Arveson & Vendittis, 2000). Following discussions are made based on full-scale noise measurements as presented in Figure 5-31, as the relative shift in the measured spectral levels are easier to distinguish. In Condition 2, the increase in the URN levels starts at a frequency around 200 Hz and is considered to reflect the relatively smaller diameter of the cavitating tip vortex and less activity in its cavitation dynamics (Berghault, 2000). In Condition 3 the noise levels are observed to increase over the whole frequency range due the broadband nature of the dominant cavitation phenomena creating a direct impact on the spectral levels, especially in the high frequency range. The only test condition with the large extent of sheet cavitation is Condition 4, which shows a significant increase in the URN level over the whole frequency range. A series of peaks around multiples of the blade rates occur in association with increased volume variation of the sheet cavitation and with a larger diameter tip vortex cavitation also exhibiting increased cavity dynamics.



## 5.8 Conclusions

Overall, Chapter 5 has been a constructing block for the development of the systematic propeller series approach to be presented in Chapter 6 by the further experience and familiarity with the facility gained following the previous chapter. Moreover, invaluable data including the cavitation observations, pressure pulse measurements and noise measurements from both full scale and model test are provided together with the necessary accompanying information such as the operating conditions, wake data and propeller geometry which are publicly scarce if not non-existent.

Detailed experimental investigations have been conducted to predict URN levels for the Newcastle University's catamaran research vessel "The Princess Royal". The findings are based on a series of model tests carried out in the University's medium size facility "The Emerson Cavitation Tunnel" and on full-scale noise trials conducted with the vessel as part of a collaborative European research project SONIC. Based on the investigations it is concluded that:

- In a medium size cavitation tunnel, a truncated dummy-hull model with properly scaled bow and stern sections, combined with the wake screens strategically fitted at the stern, could be the closest alternative to a full (twin-hull) model configuration to simulate the wake flow effectively.
- In spite of various simplifications made in the dummy-hull configuration to represent the actual catamaran vessel, the tunnel test measurements for underwater RNL and cavitation observations can provide a reasonable basis to validate the full-scale trial measurements by using the ITTC procedures and guidelines.
- Extrapolated URN spectra, based on tunnel tests in the presence of cavitation displayed more reasonable agreement with the full-scale URN over the low and medium frequency ranges than over the higher frequency range.
- In the present study, the issues related to the effect of the reverberations of the cavitation tunnel facility and non-cavitating operating conditions have not been tackled due to time restrictions on the project and a focus on the cavitation induced noise. This may require further investigations.

# Chapter 6 Propeller Cavitation Noise Prediction

## Using a Standard Propeller-Series Approach

### 6.1 Introduction

*Chapter 6 presents an experimental approach to the cavitation noise predictions of commercial vessels in full-scale by using a subset of a standard propeller series and adopting a systematic testing method. The proposed approach has been validated using full-scale case studies and results are discussed. The systematic test data for the URN, fluctuating pressures and cavitation observations have been analysed jointly for further understanding of the URN phenomenon in terms of the cavitation dynamics as well as exploring the effects of some of the important design parameters and operating conditions on URN.*

*Following this introduction, Section 6.2 of the chapter describes the philosophy behind the prediction approach. Section 6.3 presents the adopted experimental approach to generate the experimental database. The development of the database is conducted in two stages: firstly, a small subset of the Meridian standard propeller series is tested to demonstrate the viability of the proposed approach, which is presented in Section 6.4; secondly, an extended subset of the Meridian series is tested to establish a larger database as presented in Section 6.5. In the same section (i.e. Section 6.5) an advanced experimental data analysis tool is also implemented to study the effect of some important propeller design parameters, operational conditions and cavitation dynamics on URN. In Section 6.6 an artificial neural network (ANN) based prediction tool is implemented to predict the URN of a vessel by using the large database established. The developed tool is tested and hence the prediction approach is validated by using two full-scale case studies in Section 6.7. Finally, the conclusions of the chapter are presented in Section 6.8.*

## 6.2 Philosophy of standard series approach to URN prediction of a propeller

The scope of this chapter is comprised of a number of sections that are contributing to the development of an experimental standard series approach to predict the propeller cavitation noise. In order to help the reader Figure 6-1 is provided to summarise the philosophy behind this approach and hence guidance for the layout of this chapter.

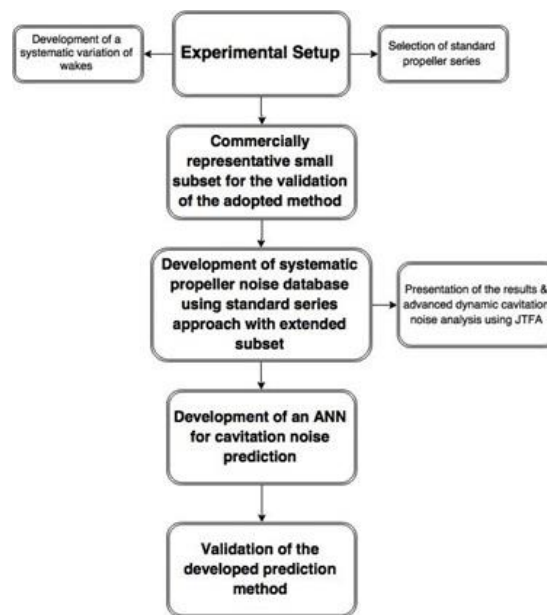


Figure 6-1 Philosophy behind the experimental approach for URN prediction.

In spite of their limitations and costs, the power of systematic propeller standard series and their role in propeller design is well-known. The proposed approach, therefore, aims to develop a noise prediction procedure based on the standard series and starts with the selection of a suitable series.

In order to implement the approach in a cost economical way, amongst the various standard propeller series that are readily available in the inventory of the ECT, the one with the best coverage for acoustic testing is considered to be the Meridian Standard Propeller series (Emerson & Sinclair, 1978). This family of propellers also has existing propeller performance data that enables cross-checking measurement reliability.

Since all standard propeller series are generated in uniform flow and since the effect of wake distribution on the cavitation and resulting noise is vital, the approach should include the wake

effect and hence a systematic variation of wake inflow for the propeller tests is proposed based on the BSRA wake criteria parameters.

Having specified the representative standard series and wake variations a comprehensive experimental set-up and associated systematic programme is adopted for the noise tests of the members of the series in ECT. This test programme also included the acoustic characterization of the ECT.

The experimental setup and developed inventory are initially put to test with the commercially representative small subset of Meridian standard propellers. The test matrix of this test campaign is determined based on the real oceangoing commercial vessel powering data and propeller design parameters (MAN, 2009, 2014). The URN measurements made with this small subset in ECT are then extrapolated to full scale using the same powering information to validate and confirm the adopted approach by comparing with average shipping noise data literature (Wales & Heitmeyer, 2002) as well as quantitatively confirming the significance of the wake inflow effect.

The developed confidence through the small subset is then extended to an extended, larger subset of the Meridian standard series propeller chosen with particular attention to major propeller design parameters such as BAR, P/D ratio and blade number. The tests are conducted in a systematic manner in order to be able to compile a sophisticated database for the development of a propeller cavitation noise prediction method.

With a view to improve the efficiency and accuracy of the database the artificial neural network (ANN) is used as the most suitable database management tool. Finally, an ANN based standalone tool is developed to predict the URN of a commercial vessel by utilising the database developed.

The developed code is applied for two real test case studies to predict the URN. The first test case is a Japanese training ship “Sein-Maru” with its conventional and highly skewed propellers while the second test case is “Merchant Tanker Olympus” with a controllable pitch propeller.

Moreover, as a by-product of the experimental investigations in this Chapter, the analysed results of the systematic propeller tests are also used for the implementation of an advanced cav-

itation dynamics analysis tool to provide better insight into the understanding of cavitation induced noise by using the synchronized pressure time signal recordings and cavitation observations. For this purpose, Joint Time-Frequency Analysis technique is used as a tool to establish a bridge between the time domain and frequency response. The developed methodology is demonstrated through comparisons of major propeller design and operational parameters to enhance the understanding of their roles as noise producing mechanisms of the propeller cavitation.

### **6.3 Adopted experimental approach**

As outlined in Section 6.2 the experimental approach to be adopted required the selection of a representative propeller series and the development of representative wake distributions. Newcastle University with its ECT facility has been the birthplace of a number of famous and most widely used systematic propeller series (e.g. KCA or Gawn-Burrill, KCD, Meridian, etc.) for which comprehensive open water performance charts have been published (Gawn & Burrill, 1957; Emerson & Sinclair, 1978). Some of these data were used in the development of Burrill's cavitation criterion (Burrill & Emerson, 1962) which relates sheet cavity extent to thrust, blade area and cavitation number. Such historical data have formed the background to the main objective of the present research, namely, to generate a representative systematic body of underwater noise data for a subset of the standard "Meridian propeller series" and to present it in a form which can be used as a tool for propeller noise prediction and mitigation in the early design stage.

The main noise-producing mechanism during the operation of a marine propeller has been identified by several authors as the variation of cavitation volume (sheet and vortex) in a non-uniform wake field produced by the hull-form and appendages ahead of the propeller (e.g. Konno et al., 2002). This significant effect has been included in this study through a systematic variation of wake inflow fields, constructed prior to conducting the cavitation tests. The synthesised wake characteristics were influenced by the BSRA wake criteria (Odabasi & Fitzsimmons, 1978) and critical parameters of this criteria were identified in the BMT empirical noise prediction study (Angelopoulos et al., 1988). In supporting the importance of the wake flow on the URN, the comparison of the tests in the uniform flow condition and behind three wake flows

have confirmed the basic hypothesis of the dominance of non-uniform inflow when focussing on the propeller radiated noise.

In the remaining parts of this section (6.3) the details of the selected standard series are presented in section 6.3.1. This is followed by the description of the representative wake inflows and their constructions for the experiments in section 6.3.2. Finally in section 6.3.3, detailed information about the experimental setup for the URN tests is given including the test programme for the determination of the acoustic transfer function of the ECT.

### 6.3.1 Selection of standard propeller series

Propeller design with the absence of computational power initially relied mainly based on experience and model tests. Eventually, in order to aid propeller designers, standard propeller series were developed and tested to give guidelines and a design methodology (Kuiper, 2010). These series have enabled the propeller designer to size the propeller quickly using charts whilst ensuring with sufficient thrust to achieve the contract speed and power. Table 6-1 (Carlton, 2012) shows some of the well-known standard series of propellers. The Emerson Cavitation Tunnel has been involved in the development of the KCA series with the support and funding of the British Admiralty and both the KCD and Meridian series with Stone Marine Manganese (Emerson & Sinclair, 1978; Gawn & Burrill, 1957).

Table 6-1 Fixed pitch, non-ducted propeller series (Reproduced from (Carlton, 2012)).

Series	Number of propellers in series	Range of parameters			$D$ (mm)	$r_h/R$	Cavitation data available	Notes
		$Z$	$A_E/A_O$	$P/D$				
Wageningen B-series	$\simeq 120$	2–7	0.3–1.05	0.6–1.4	250	0.169	No	Four-bladed propeller has non-constant pitch dist
Au-series	34	4–7	0.4–0.758	0.5–1.2	250	0.180	No	
Gawn-series	37	3	0.2–1.1	0.4–2.0	508	0.200	No	
KCA-series	$\simeq 30$	3	0.5–1.25	0.6–2.0	406	0.200	Yes	
Ma-series	32	3 and 5	0.75–1.20	1.0–1.45	250	0.190	Yes	
Newton–Rader series	12	3	0.5–1.0	1.05–2.08	254	0.167	Yes	Propellers not geosyms Propellers not geosyms
KCD-series	24	3–6 (mainly 4)	0.587 Principal 0.44–0.8	0.6–1.6	406	0.200	Yes	
Meridian series	60	6–4	0.45–1.05	0.4–1.2	305	0.185	Yes	

The Meridian propeller series is a unique standard series based solely on practical propeller designs for standardised variations in pitch to diameter ratio, BAR and number of blades ( $Z$ ). The series is unique in that actual propeller designs were chosen as the parent propellers for each blade number group and blade area group. These were largely obtained from the extensive database of Stone Marine Propulsion (SMP).

The designs were also refined through SMP's design methodology to extrapolate the designs, fill in the gaps and to check and adjust the designs. Standard Meridian forms were used for the blade width distribution, basic section shapes and radial thickness distribution (SMP, 2016). All of the parent propellers were designed to work in a uniform wake stream. In line with the current practice, the blade outline below  $0.5 r/R$  was expanded where necessary to give a  $t/c$  ratio of 0.2 at  $0.25 r/R$ , while the lift coefficients were limited to 0.65.

The original Meridian Propeller Series are the proprietary design of both Stone Manganese Marine Ltd (now SMP Ltd) and Newcastle University. They have a range of blade numbers ( $Z$ ) from 4 to 6 and BAR of 0.45, 0.65, 0.85 and 1.05. For each parent model, five mean  $P/D$  ratios of 0.4, 0.6, 0.8, 1.0 and 1.2 were generated. Model tests with 304.8 mm diameter propellers in manganese bronze, were conducted in the Emerson Cavitation Tunnel. These tests generated systematic open water performance curves, from which  $Bp-\delta$  diagrams were derived. The tests also included limited performance testing for a range of cavitation numbers (Emerson & Sinclair, 1978).

The catalogue of the available model propellers at the ECT was used to select an appropriate subset. Following detailed blade inspections, some propellers with minor damage were eliminated from the final chosen subset. Details of the selected propellers are discussed in Section 6.4 and 6.5.

### 6.3.2 Development of systematic variation of wake inflow

The significance of the hull wake and its distribution on propeller performance, especially for cavitation and inboard noise, has been noted in many research studies since the 1970's and is routinely taken into account in the design and analysis process (e.g. Oossanen, 1971; Young & Kinnas, 2001). Although all three components of the hull wake flow are critical to the performance analysis of a propeller, the axial wake is the most important component dominating the propeller's loading characteristics (e.g. Huse, 1974; Harvald, 1981), as was also discussed in the Literature Review in Chapter 2. Based on this fact and considering the time and resource limitations of this project, only investigation of the axial wake distribution on the propeller performance has been justified.

Consequently, it was decided that the desirable wake configurations could be simulated by using two-dimensional wake screens in combination with different grades of "chicken-wire" meshes, strategically patched onto a base frame which is in line with the established practice within the ECT.

In order to select suitable wake configurations, an extensive literature survey was conducted. These included seminal studies such as Konno (Konno et al., 2002) in which cavity collapse events were observed to increase amplitudes and complexities of the pressure pulse time-series for the propeller operating behind a peaked, non-uniform inflow. The study further highlighted the effect of altering the gradient of the wake distribution. The wakes with steeper velocity change were shown to produce higher tonal amplitudes of pressures as well as high frequency contributions from increased dynamic cavity collapses, both on and off the blade surface. A characteristic pressure pulse feature was a double peak configuration in the time domain signals. Inspiration from Konno's study led to the utilization of BSRA wake criteria suggested by (Odabasi & Fitzsimmons, 1978; Angelopoulos et al., 1988) to quantify and develop a family of 3 representative wake grids, to complement the parametric variations in the standard propeller series geometries. According to Odabasi & Fitzsimmons, the severity of the wake, which can be quantified by the wake non-uniformity parameter given by Equation 27, is an important characteristic in generating propeller excited vibration and radiated noise.



$$W_{\Delta} = \left\{ \frac{W_{Max} - W_{Min}}{1 - \bar{W}} \right\} \quad \text{Equation 27}$$

where,  $W_{Max}$  and  $W_{min}$  are the maximum and minimum wake fraction and  $\bar{W}$  is the circumferential average wake fraction calculated by Equation 28. The above is defined at  $r/R = 0.7$  in this study. Whilst the BSRA wake criteria normally is defined at  $r/R = 1.0$ , the wake parameters at  $r/R = 0.7$  is preferred in the thesis since the developed wake grids presented higher gradients at this radius and hence better representation of the implemented wake variation.

$$\bar{W} = \frac{\int_{r_h}^R r \int_0^{2\pi} w_T d\phi dr}{\pi(R^2 - r^2)} \quad \text{Equation 28}$$

where,  $r$  is the representative radius of the propeller that is integrated over the propeller radius,  $w_T$  is the wake fraction that is integrated over the  $360^\circ$  and  $R$  is the radius of the propeller.

In order to have a better definition and control of the systematic wake variation, further wake parameters such as the mean wake, half-wake width and wake depth were included in the wake analysis as shown in Figure 6-2 for  $r/R = 0.7$ . The highest value of the wake depth and lowest value of the half-wake width would present the most non-uniform wake distribution. This resulted in the most dramatic change of the inflow velocity in the wake shadow region and consequently would induce the formation of unsteady cavitation in this region by the collapse and rebound of cavity volumes at exit from the wake shadow region.

Based on the above considerations, three related wake configurations were generated numerically (theoretically); these are designated as ECT1, ECT2 and ECT3, for varying wake non-uniformity parameters. The target variations are achieved through variation of the half wake width and wake depth parameters, ranging from severe to mild. Thus, the wake with the narrowest wake width and highest wake depth presents the most severe wake (ECT1) and the wake that has the lowest wake depth and largest half wake width represent the mildest wake (ECT3) while ECT2 is lying in between. Table 6-2 shows the main parameters of the three wake configurations, while Figure 6-3 compares the target wake variations (dotted lines) with the experimentally simulated wake distributions (solid lines) at one fractional radius ( $r/R = 0.7$ ). Cavitation dynamics outside the  $0.7 r/R$  are considered to dominate noise generation.

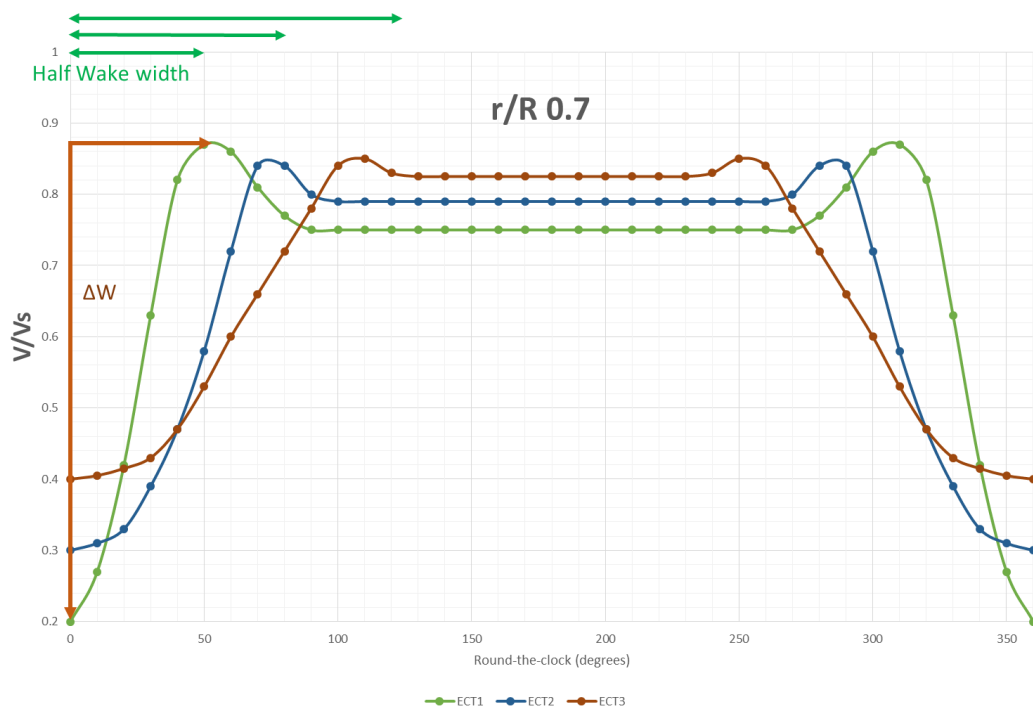


Figure 6-2 Representation of wake depth ( $\Delta W$ ) and half wake width for three representative wake distributions at  $r/R=0.7$

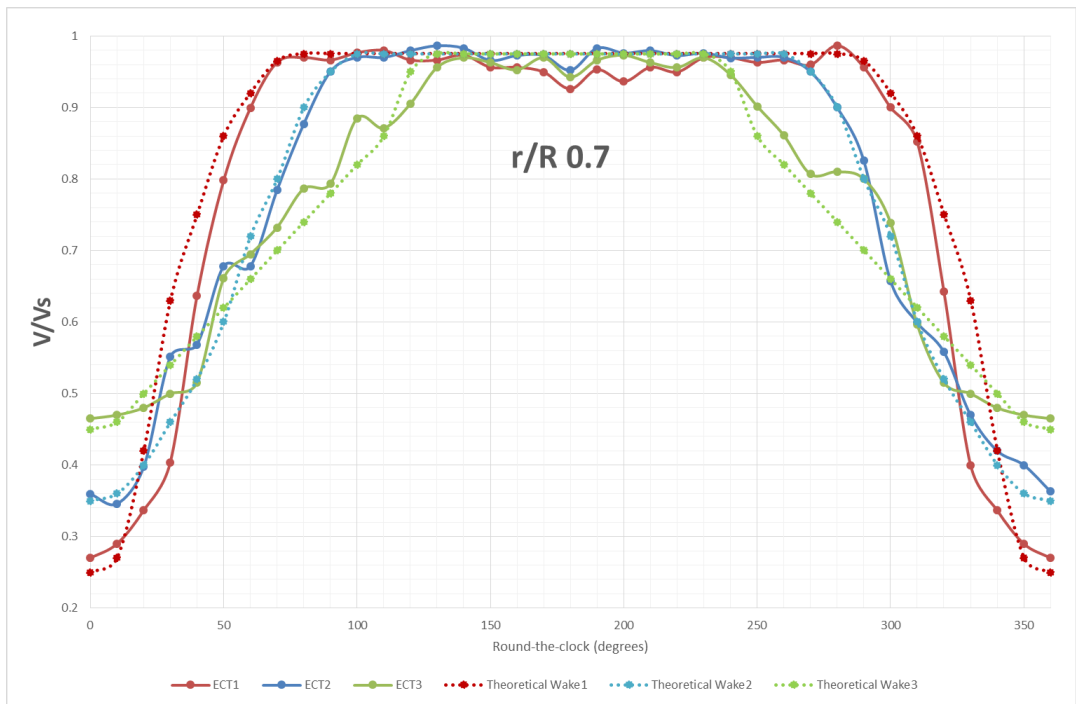


Figure 6-3 Comparison of target (theoretical) and simulated wakes (ECT) at  $r/R=0.7$

Table 6-2 Significant wake parameters for wake distributions selected.

Wake Parameters			
Wake screen type	ECT1	ECT2	ECT3
Wake depth	0.71	0.64	0.50
Half Wake Width (degrees)	60	95	132
Mean Wake (Propeller disc)	0.16	0.20	0.195
Wake non-uniformity parameter	0.86	0.81	0.63

The three wake screens manufactured and used for the experimental simulations are shown in Figure 6-4. During the experimental wake simulations these wake screens were placed ahead of the model propellers at a distance of 1.5 propeller diameters as shown in Figure 6-6 and ( $x$  and  $z$ ) wake velocity components were measured by using the ECT's two-dimensional LDA system and measurements were made as outlined in section 3.4.1.2 entitled Laser Doppler Anemometry.

The simulations of the target wake velocities by using the final grid arrangements shown in Figure 6-4 were achieved by 20 attempts in total for the three different wake variations. The measurements with the finalized wake grids, which are presented as contour plots, are shown in Figure 6-5 for the three representative wake flows.

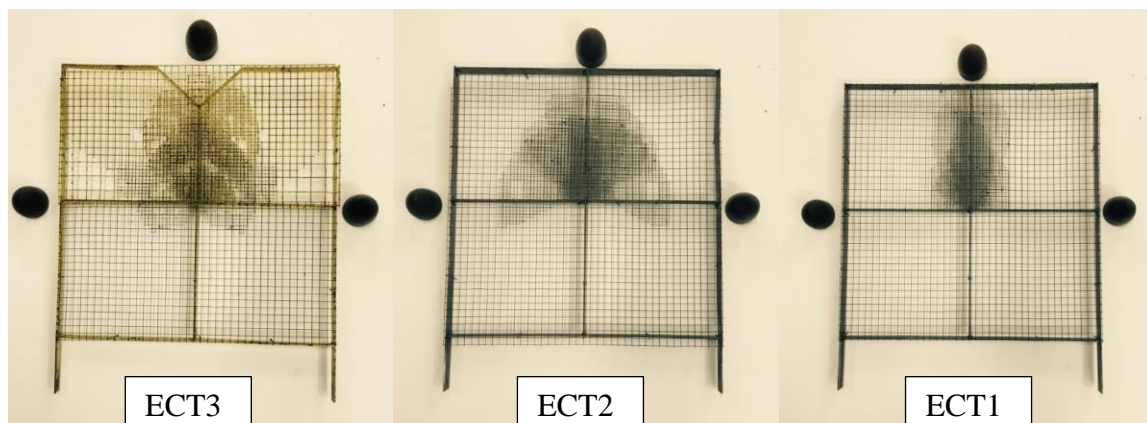


Figure 6-4 Constructed wake screens.

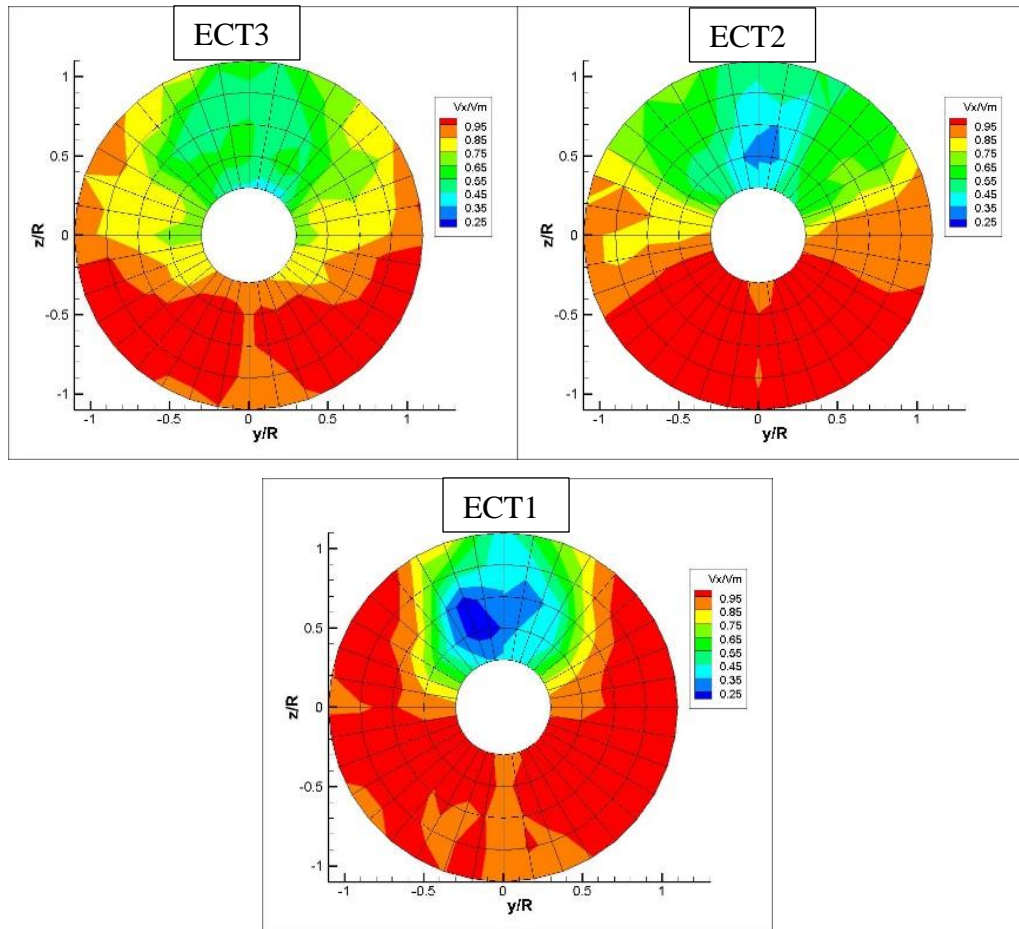


Figure 6-5 Contour plots of axial velocity distributions of the simulated 3 representative wakes.

### 6.3.3 Experimental setup

The conduct of the systematic propeller tests required easy implementation and change of the experimental parameters in order to make the process efficient. In this context, in order to be able to acquire a significant amount of data points, major variations to the experimental setup, such as the propeller and the wake screen, require short periods of downtime for the facility. Therefore, although using a full model or a truncated dummy model to generate the wake is preferable due to their advantage of representing the tangential components of a wake inflow to the propeller, a series of fixed axial-flow wake screens has been used to simplify the experimental setup and reduce the downtime.

As stated earlier, the wake screens are located in the tunnel at a distance of 1.5 propeller diameter upstream of the propeller model in order to avoid the high levels of turbulence intensities introduced by the presence of the wake screen, as can be seen in Figure 6-6.



Figure 6-6 Testing set-up of model propeller behind wake ECT2 at a distance of 1.5 propeller diameter.

The noise measurements are conducted using a B&K 8103 hydrophone mounted within the tunnel in a streamlined strut. The configuration and properties of the hydrophone setup and acquisition are outlined in section 3.4.6 entitled “Noise measurement equipment and analysing methodology”. The hydrophone is positioned facing the incoming flow and at an offset given in Table 6-3 and shown in Figure 6-7. Acoustic experimental procedure requirements are met by conducting the tunnel background noise measurements as well as tunnel acoustic frequency response due to reverberation. The details of the former study are presented in detail within the following subsection (6.3.3.1). The background noise measurements are also presented in Appendix C.

Table 6-3 Offset of hydrophone location used during tests in ECT.

8103 Hydrophone Distance from the Propeller Plane & shaft axis	
x	264mm
y	245mm
z	120mm



Figure 6-7 Locations of two B&K hydrophones relative to model propeller inside ECT.

The experimental setup was modelled digitally before the conduct of the experiments in order to ensure the feasibility and to give a better idea of the nature of the test setup. Figure 6-8 shows a 3-dimensional Computer Aided Design (CAD) view of the experimental set-up used in ECT. It displays the dynamometer, model propeller, hydrophone and wake screen.

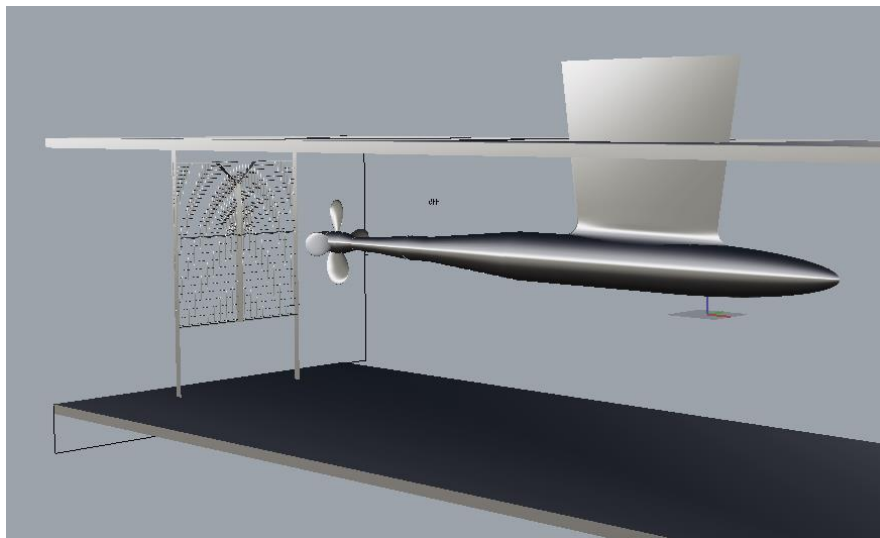


Figure 6-8 CAD model of the experimental setup in ECT test section.

Throughout the test campaign, the water quality of the ECT was monitored in order to ensure the satisfactory levels were attained as described in detail in section 3.4.2 entitled “Water quality”. The tunnel was deaerated by means of its dedicated degassing system as required. The saturated gas content was increased by using the degassing cylinders under atmospheric condition and by circulating the tunnel for long time periods to enable saturation of the gas in the tunnel water. The tunnel air content was kept between 30 to 40% throughout the periods that experiments took place following the ITTC guidelines.



### 6.3.3.1 Determination of acoustic transfer functions for the ECT

The cavitation tunnels are closed-circuit water circulation channels. As a result of the fixed boundaries of such facilities, noise measurements suffer from reverberations (reflected waves and boundary motions) (Park et al., 2009). In order to account for any related errors that may influence the accuracy of the measurements, a known noise source is first introduced with a view to determine the acoustic response of the tunnel at the measuring hydrophone (Tani, Viviani, Armelloni, et al., 2015). The correlation between the known noise source and the receiver hydrophone is defined as the transfer function of cavitation tunnel acoustic frequency response.

Measured transfer functions for the ECT have been determined for the systematic propeller cavitation tests. Determination of the acoustical properties of the testing environment has been performed reproducing the experimental setup as much as possible (Cochard & Arzelies, 1998). In order to achieve this, while the hydrophone is kept at the exact location given in Table 6-3 and shown in Figure 6-7, a calibrated known noise source was attached to the propeller dynamometer in the propeller plane as illustrated in Figure 6-9 and connected to an “Agilent” arbitrary waveform generator which produced sinusoidal sweep signals (Figure 6-10).

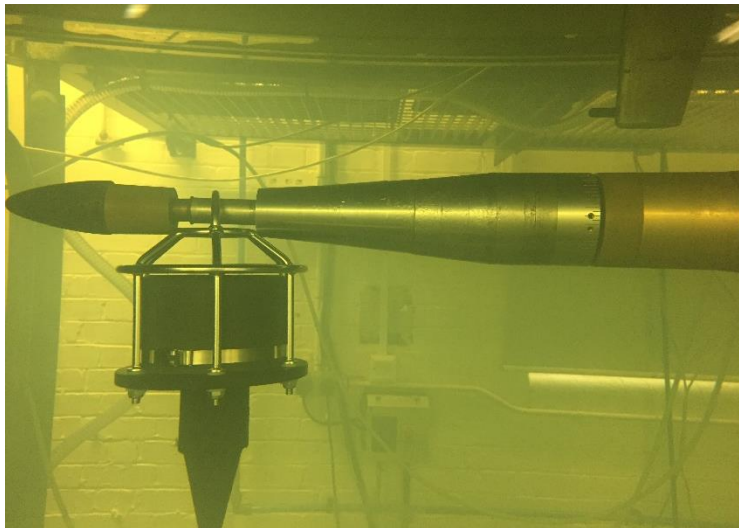


Figure 6-9 - Setup of the known noise source for the determination of the acoustical transfer functions

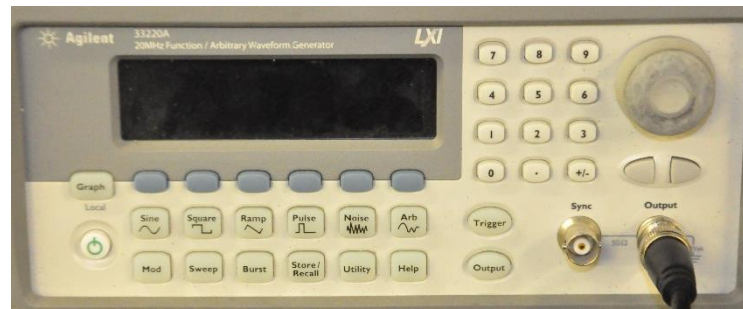


Figure 6-10 - Agilent arbitrary waveform generator

The channel impulse response is shown in Figure 6-11, was measured by transmitting a 5-20 kHz sweep signal over the 0.5-second duration and performing the cross-correlation of the hydrophone signal with the transmitted signal. There is detectable reverberation spanning at least 20ms but the time spread of significant arrivals is approximately 4ms. As a rule of thumb, signals whose period is greater than 10 times the time spread will not experience large amplitude variations due to destructive interference. Therefore, below  $\sim 25$  Hz the cavitation tunnel may be viewed as a waveguide and the losses between the source and receiver will be minimal (only 3 dB or multiplied by 0.5 as half the energy will travel away from the receiver). At frequencies above this threshold value, the tunnel will present a complex frequency selective fading channel.

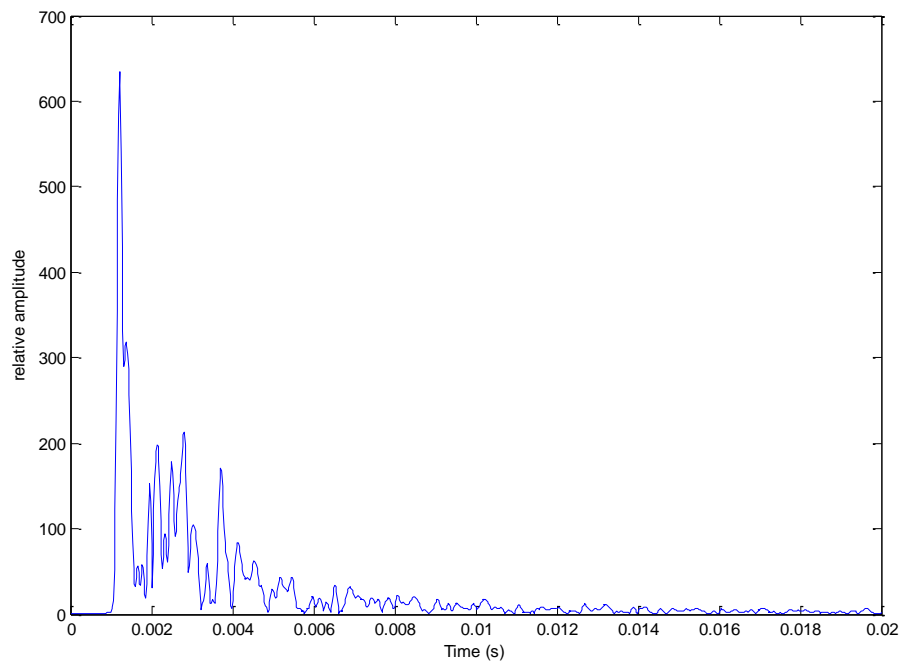


Figure 6-11 Channel impulse response in time domain for 5-20 kHz sweep signal over 0.5 second.



The Figure 6-12 and Figure 6-13 below show the spectrum of the signal received from the FFT of the frequency sweep. The result is only reliable from 7-15 kHz due to poor sensitivity in the source transducer outside this range and high signal to noise ratio. The first Figure 6-12 shows the transit transducer sensitivity in dB re  $1\mu\text{Pa}/\text{V}$  @  $1\text{ m}$  (red trace), the expected received level with a range of 0.38 m and the received signal level (blue trace). The second Figure 6-13 shows the response of the channel (gain in dB) relative to a free space measurement at a given range of 7-15 kHz.

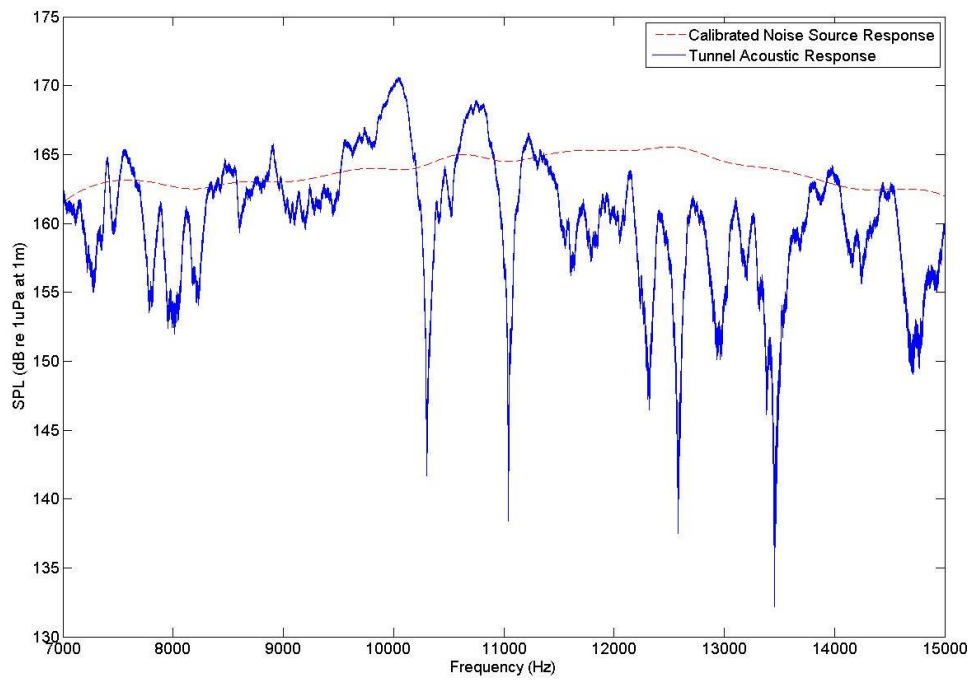


Figure 6-12 Narrowband frequency response of the tunnel with the calibrated noise source response.

The carried out investigation enabled the determination of the acoustic characterization of the ECT for the systematic standard propeller series tests. The obtained transfer functions are provided in narrowband frequency domain to ensure the completeness of the study conducted as it is stated by ITTC (2014). The resulting reverberation characteristics of the ECT has been observed to be significantly similar to other cavitation testing facilities (Tani, Viviani, Gaggero, et al., 2015) The conducted study is not applied as a correction to the experimental measurements carried out in the context of this section due to the limited frequency range that the signal to noise ratio of the measurements are reliable (i.e. only corresponding to three 3<sup>rd</sup> octave centre frequencies). In order to overcome this missing information, further investigations are planned to take place using a hydrophone array to enable the spatial averaging of the cavitation tunnel measurements.

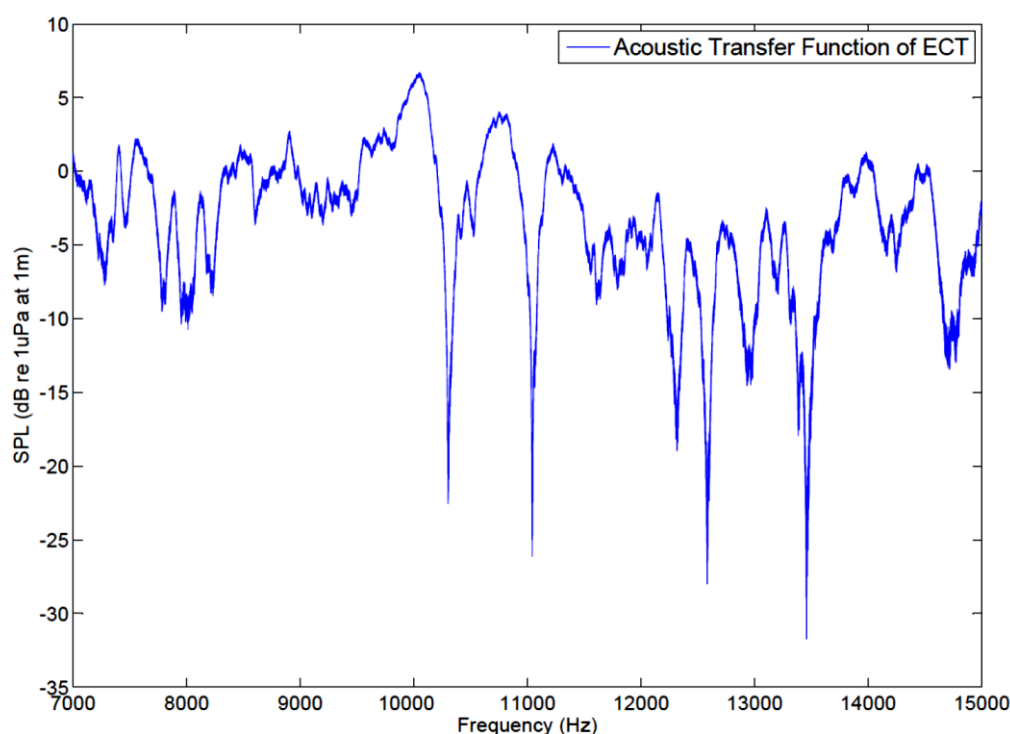


Figure 6-13 Narrowband frequency domain transfer function of the ECT.

## 6.4 URN data with commercially representative small subset of Meridian propeller series

This section presents a small, but commercially representative, standard series of propeller models tested in ECT using 3 members of the Meridian series for commercial ship propellers. The members were chosen to test significant propeller design parameters in relation to cavitation noise radiation. These parameters include pitch to diameter ratio, blade area ratio, number of blades and operating conditions implemented by the changing of the wake, shaft speed and applied vacuum level. The propellers selected were tested both in open water conditions and behind 3 different grades of non-uniform axial wakes described earlier in Section 6.2.2. Based on the measured noise data the results were extrapolated to full-scale using an available database for some real commercial vessels (MAN, 2014, 2009) with similar main propeller particulars as the members of the selected propeller series.

The initial aim of using this 3 member small subset was to test major propeller design parameters such as BAR, P/D ratio and blade number (Z). Based on some major commercial ship types (i.e. Container ship, Panamax bulker and Handy size bulker) the subset of 3 propellers was selected from the Meridian Series (KCD 193, 192, 191) as shown in Figure 6-14.


Pitch/Diameter Blade Area Ratio	0.6	0.8	1.0	
0.65	KCD191 (4 Blade)		KCD193 (4 Blade)	
0.85		KCD129 (5 Blade)		

Figure 6-14 Main propeller parameters from the 3-memeber Meridian Series subset (on the Left). Subset images: KCD 129 (top left), KCD 193 (Top right), KCD 191 (bottom).

#### 6.4.1 Test matrix and adopted approach for tests

The test matrix for this small propeller subset was devised based on the knowledge of some ships in service, since it was considered that the test cases should both represent a certain ship type with a realistic pitch to diameter ratio as well as realistic operating conditions. Bulk carriers, container vessels and tankers are the three largest groups of vessels within the world merchant fleet. Therefore, this study selected some sub-groups as the basis for compiling a noise database. The model propellers and associated test data were extrapolated based on the assumption that certain ship types tend to use certain pitch to diameter ratios and operate between certain torque coefficients that are also similar due to their mission profiles (MAN, 2014, 2009).

Consequently, Figure 6-15 is provided based on the actual operating conditions of a large number of full-scale commercial vessels where the representative operational conditions for certain ship types are plotted for the determination of the test matrix as presented in Table 6-4. The conditions are presented on the y-axis in terms of the rotational-speed based cavitation number and representative torque coefficients on the x-axis. The individual powering conditions of the vessels are also shown plotted against the vessel types for which the model test noise measurements are extrapolated.

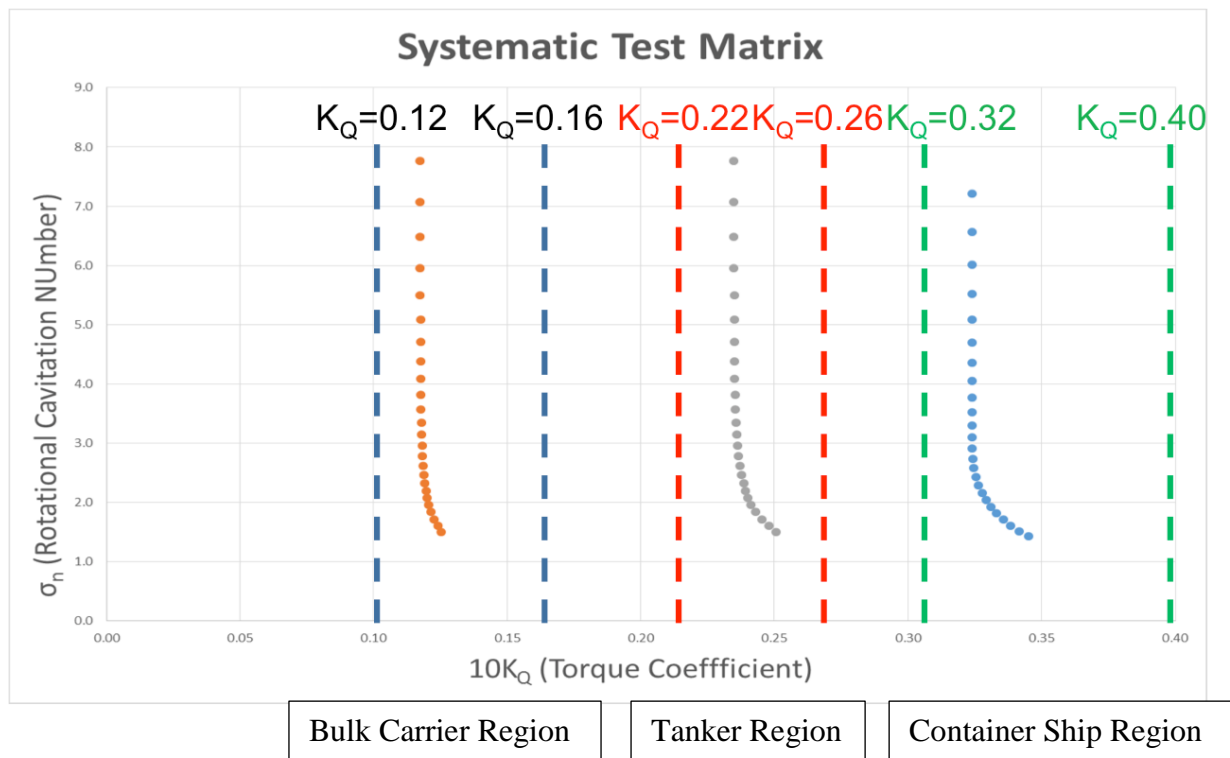


Figure 6-15 Measurement matrix given together with the operating conditions of the target vessels. (Operating conditions are denoted by circles while operating regions are denoted by dashed lines for each vessel type).

In general, the data on the right-hand side of Figure 6-15, which is confined between  $K_Q = 0.32$  and  $K_Q = 0.4$ , correspond to the operational conditions for typical container vessels while the data on the left-hand side, which are confined between  $K_Q = 0.12$  and  $K_Q = 0.16$ , correspond to handy size bulk carriers. The data range in the middle confined between  $K_Q = 0.22$  and  $K_Q = 0.26$  are for the Panamax size bulk carriers.

Table 6-4 Commercially representative small subset test matrix.

Propeller No	Wake Fraction	Vacuum Condition	Dynamometer Speed (RPM)	Inflow Speed (m/s)
KCD 191	Open water, "ECT1", "ECT2", "ECT3"	Atmospheric, 100 mmHg, 200 mmHg, 300 mmHg, 400 mmHg, 500mmHg.	two RPMs for each propeller based on the open water data	3
KCD 193				(for open water)
KCD 129				3.5 (for behind wake screens)

In order to cover as many possible vessel operational data as possible and hence to facilitate interpolations, the tests were conducted from relatively high to low representative torque coefficients as well as their representative cavitation numbers. The propeller open water characteristics were then utilized to calculate the test conditions using the chosen torque coefficients and tunnel operating limitations. Once the propeller test conditions were fixed the tests were conducted for six different cavitation numbers and corresponding noise data were recorded. The required cavitation number was adjusted by application of a vacuum to the tunnel. The range of the six cavitation numbers was achieved by applying 5 different vacuum levels from the Atmospheric condition to 500 mmHg, at 100 mmHg intervals as shown in Table 6-4. The definition of the non-dimensional coefficients comprising the test matrix are determined with Equation 9 and Equation 29 for torque coefficient and cavitation number, respectively.

$$\sigma_n = \frac{P_a + \rho g h_s - P_v}{0.5 \rho (nD)^2} \quad \text{Equation 29}$$

The overall test matrix included 3 model propellers (KCD 129, 191 and 193) behind 4 different inflow configurations (i.e. open water and 3 different wake screens) for 2 different torque coefficients and at 6 different cavitation numbers. Thus, 144 unique operating conditions were simulated in the cavitation tunnel in order to construct the systematic series database.


In order to meet the requirements of the test matrix, three different operating regions were specified for each ship for which the powering data was readily available. Thus, during the tests, the tunnel inflow speed was fixed at 3.5 m/s behind the wake screen conditions and at 3m/s for the open water test conditions. This meant that although the exact predefined torque coefficient was not achieved during the experiments, the intended region for each vessel type as presented in Figure 6-15 was covered by the recorded data.

### 6.4.2 Noise measurement results

The systematic database of experimental results collected for the propeller noise has the potential to be used as a noise prediction and mitigation tool in the early stage of a propeller design provided that the proposed design lies within the range of the database parameters. A designer with concerns for noise levels will be able to make a preliminary estimation of noise for a candidate propeller at the early design stages.

In order to demonstrate the above capability, bearing in mind the data range given in Figure 6-15, the noise data generated with the 3 KCD model propellers (KCD 191, 129 and 193) have been extrapolated to full-scale using the main particulars of three relevant ship types, namely a typical handy size bulk carrier, a Panamax size bulk carrier and a 4800 TEU Containership, as shown in Figure 6-16, Figure 6-17 and Figure 6-18, respectively.

Dimension		
Handy Bulkcarrier		
Loa	187.83	[m]
Lwl	182.46	[m]
Lpp	180.00	[m]
B	30.00	[m]
D	17.30	[m]
d	11.00	[m]
Cb	0.8312	



Propeller Dimension		
Dp	6.130	[m]
P/D	0.676	
EAR	0.400	
Z	4	
boss ratio	0.180	

Figure 6-16 Handy Bulk carrier dimensions used for extrapolation of the KCD 191 noise data.

Dimension		
PANAMAX BULK Carrier		
Loa	203.61	[m]
Lwl	198.50	[m]
Lpp	195.85	[m]
B	32.26	[m]
D	18.00	[m]
d	11.30	[m]
Cb	0.8353	



Propeller Dimension		
Dp	6.90	[m]
P/D	0.804	
EAR	0.520	
Z	5	
boss ratio	0.180	

Figure 6-17 PANAMAX Bulk carrier dimensions for extrapolation of the KCD 129 noise data.

Dimension		
CONTAINER SHIP 4800 TEU		
Loa	302.30	[m]
Lwl	295.46	[m]
Lpp	292.00	[m]
B	40.00	[m]
D	21.80	[m]
d	13.00	[m]
Cb	0.6265	



Propeller Dimension		
Dp	8.30	[m]
H/D_0.7R	1.029	
EAR	0.667	
Z	5	
boss ratio	0.180	

Figure 6-18 Container ship dimensions for extrapolation of the KCD 193 noise data.

The dataset generated within the framework of this experimental campaign is extremely large and hence to present all of the results is a challenge. However in order to give an insight into the nature of the data produced, the effect on RNL of some main primary propeller design parameters and operating conditions are shown in Figure 6-19 to Figure 6-21.

The noise data presented in Figure 6-19 and Figure 6-20 presents the full-scale noise levels with the KCD 129 and KCD 193 in an open water condition as well as behind the ECT1 and ECT2 wake grids in full-scale. Thus, the figures carry great importance as they demonstrate the effect of three different inflow conditions.

As one can see in both figures, the extrapolated spectral levels were significantly increased due to the effect of the simulated wakes, over the whole frequency range thus proving the validity of the approach adopted in the study in terms of the wake flow effect.

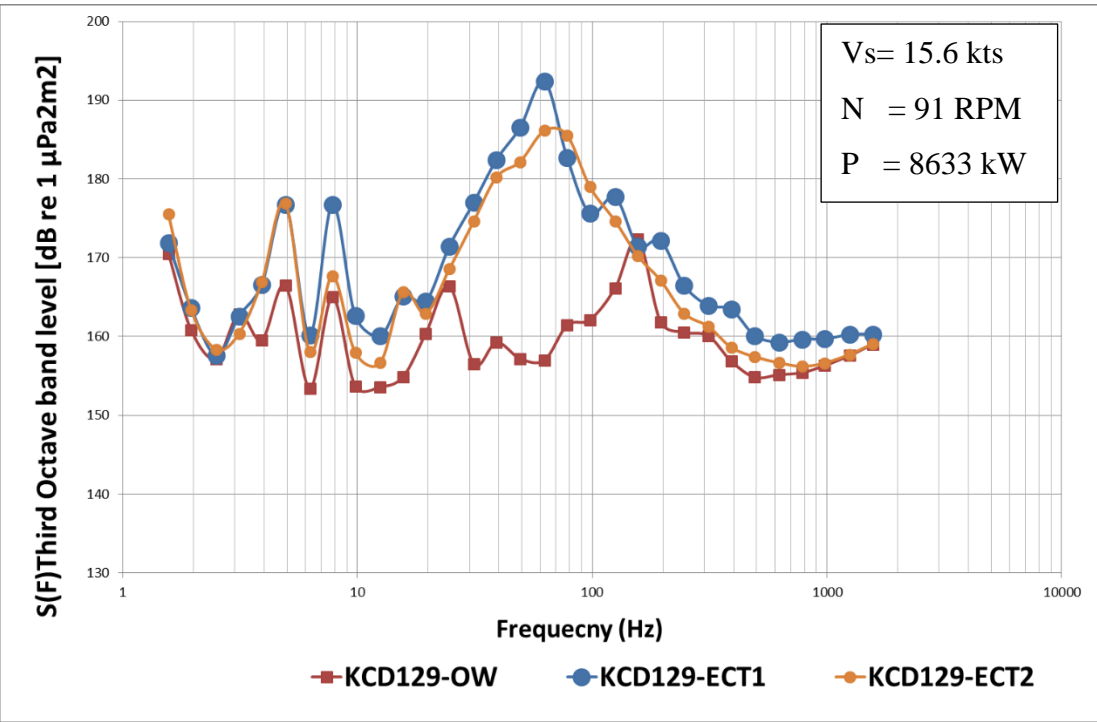


Figure 6-19 Extrapolated noise levels of KCD 129 in open water condition and behind wake screen ECT1 and ECT2.

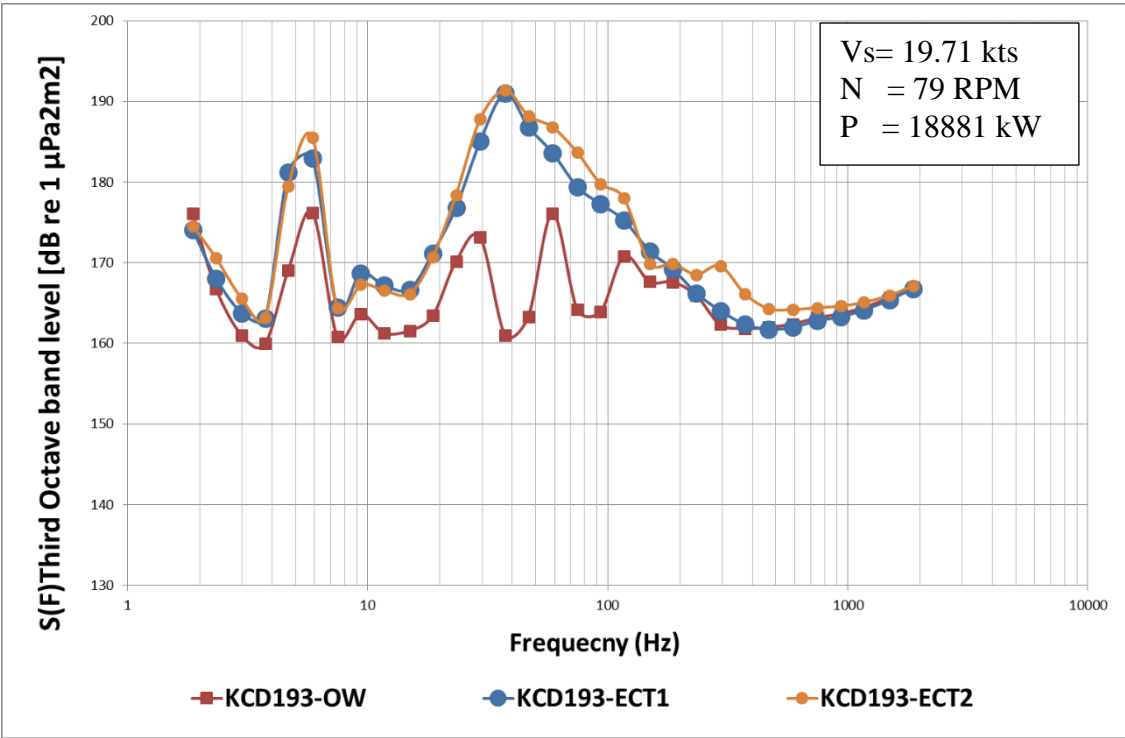


Figure 6-20 Extrapolated noise levels of KCD 193 in open water condition and behind wake ECT1 and ECT2.



In order to demonstrate the practical and qualitative accuracy of the data generated in this study, the extrapolated noise levels for the representative container ship (KCD 193) and Panamax bulk carrier (KCD129) are compared with the averaged shipping noise data recorded by Wales & Heitmeyer, (2002) as shown in Figure 6-21. The scaled noise predictions compare reasonably well with the ship statistical data above 100Hz, implying a certain level of correlation in the spectra levels. Moreover, the predictions indicate significant potential in predicting especially 1<sup>st</sup> BPF, as the spectral peak is present within the extrapolated spectrums.

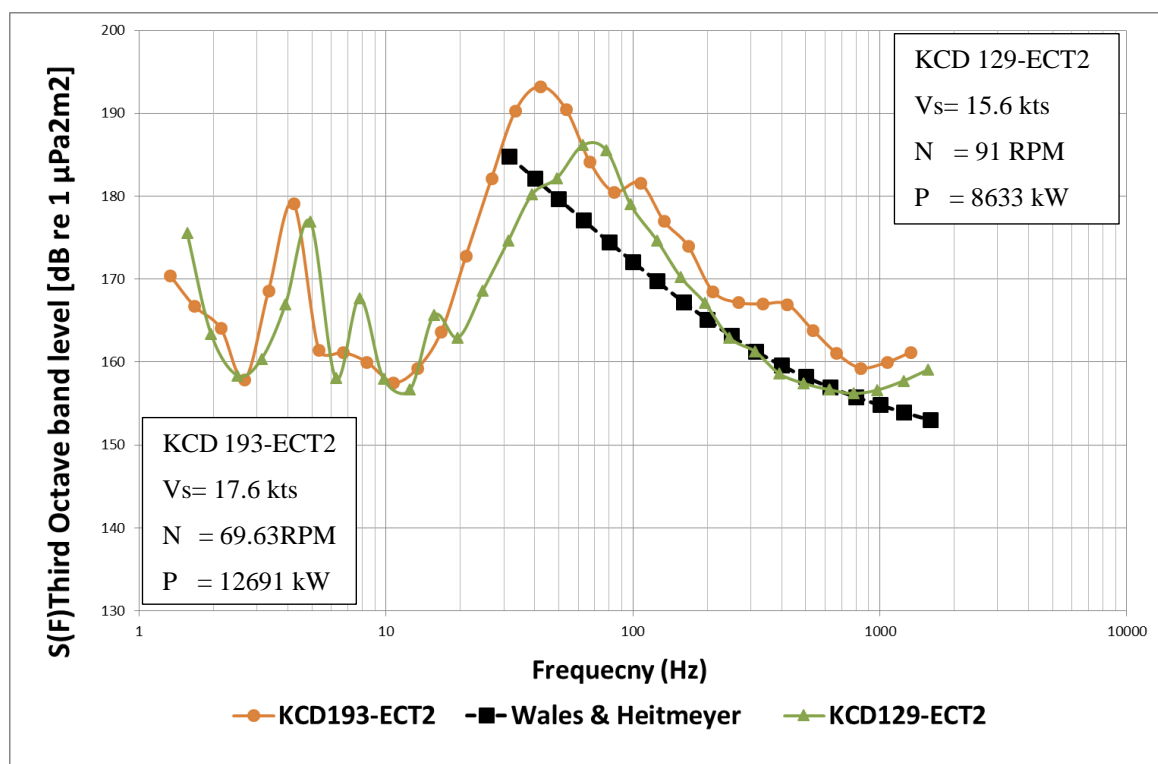


Figure 6-21 Comparison of predicted noise levels with average shipping noise data.

### 6.4.3 Remarks on test results with small subset of propeller series

An initial subset (3 model propellers) of the Meridian standard series was chosen to represent the main design variants such as P/D ratio, BAR and blade number of commercial vessels. These were combined with the selection of three different grades of wakes deficit ahead of the propellers. The resulting model propeller and wake subset were tested in the Emerson Cavitation Tunnel to generate associated noise data covering a broad range of operating conditions

representative of three commercial ship types. The test results were extrapolated to full scale using a database for the main particulars of real ocean-going vessels in order to validate the extrapolated URN results with available full-scale URN data. Based on the results presented here it can be concluded that:

1. Comparison of the measured noise levels behind the wake and in open water condition demonstrates the importance, and hence necessity, of introducing the effect of wake into the noise investigations of propellers even for the systematic series.
2. Qualitative comparisons of the predicted full-scale URN for representative commercial vessels based on the systematic noise database and published commercial shipping noise data from Wales and Heitmeyer (Wales & Heitmeyer, 2002), indicate a reasonable confidence in the predicted noise levels and trends over the frequency range of the comparison.

## **6.5 URN data with extended subset of Meridian propeller series**

Confidence in the results achieved with the small subset experiments, allowed a larger subset from the Meridian standard propeller series to be chosen and a more extensive experimental matrix to be devised. The following subsection, therefore, covers various aspects of systematic propeller testing and the eventual database to be produced based on the larger subset of model propellers. Thus, initially, the larger test matrix and the subset are specified as given in Table 6-5. Following this, data representing the main variants of the conducted experimental campaign are picked and compared in order to investigate the effect of these parameters on propeller cavitation noise (Section 6.5.1). Within Section 6.5.1 further scrutiny of the experimental results by means of the synchronized pressure time signal and cavitation observation recordings together with the joint time-frequency analysis using the Short-Time Fourier Transform technique.

Six members of the Meridian series were hand-picked to assess key propeller design parameters as such; models KCD 191,192 and 193 were chosen to assess the effect of the pitch, while models KCD 129 and KCD 65 to evaluate the effect of blade number. In the meantime models, KCD 65 and KCD 7 were selected to assess the effect of the BAR. Table 6-5 presents the variation of the propeller design parameters, whilst Figure 6-22 shows the propellers ready for the tests after marking with radius lines and chord length divisions. The same figure also includes the three wake screens used.

Table 6-5 Propeller design parameters of the chosen standard series subset.

Pitch/Diameter Blade Area Ratio	0.6	0.8	1.0
0.65	KCD191 (4 Blade)	KCD192 (4 Blade)	KCD193 (4 Blade)
0.85		KCD129 (5 Blade) KCD65 (6 Blade)	
1.05		KCD74 (6 Blade)	

The systematic experimental data consisted of 576 individual tests, based on the selected 6 model propellers, conducted in uniform flow and behind the earlier described 3 systematically varied wake grids together with 3 different levels of tunnel vacuum conditions and 8 different propeller speeds. A summary of the test matrix is shown in Table 6-6.

In complementing the test matrix, Figure 6-23 is provided to summarise the complete database in terms of Advance Coefficient ( $J$ ), Resultant Cavitation Number ( $\sigma_{Resultant}$ ), Thrust and Torque coefficient ( $K_T$ ,  $10K_Q$ )



Figure 6-22 Extended subset of Meridian propellers and wake screens used for tests.

Table 6-6 Extended subset of Meridian series test matrix.

Model propeller No	P/D	BAR	Blade no	Wake flow condition	Vacuum condition	Shaft speed (rpm)	Inflow speed (m/s)
KCD 191	0.6	0.65	4	Open water, "ECT1", "ECT2", "ECT3"	Atmospheric, 150 mmHg, , 300mmHg	600, 800 1000,1200, 1400, 1500, 1750,2000	3
KCD 192	0.8	0.65	4				
KCD 193	1.0	0.65	4				
KCD 129	0.8	0.85	5				
KCD 65	0.8	0.85	6				
KCD 74	0.8	1.05	6				

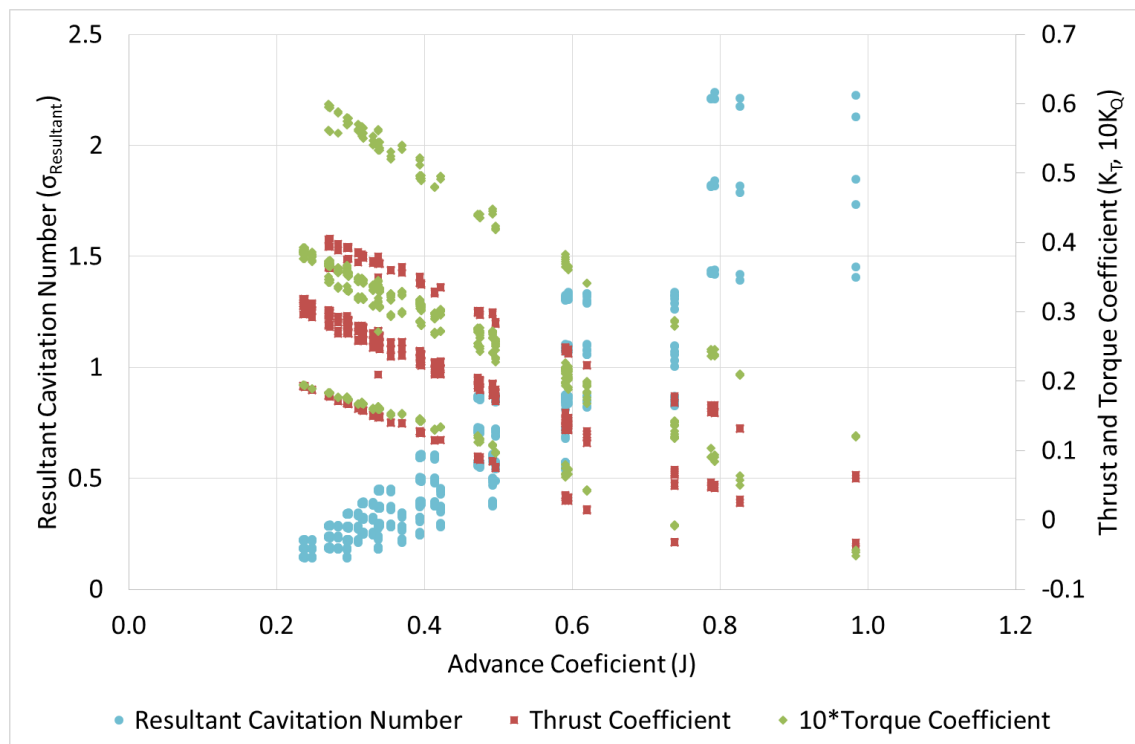


Figure 6-23 Dataset illustration as a function of Advance Coefficient ( $J$ ) in conjunction with Resultant Cavitation Number ( $\sigma_{Resultant}$ ), Thrust ( $K_T$ ) and Torque ( $10K_Q$ ) coefficients.

### **6.5.1 Presentation of results and advance analysis of cavitation induced noise data using JTFA technique**

The earlier described scope of the experimental campaign resulted in a colossal database that is unique in its nature. However, the presentation of such a large amount of data has proved to be a significant challenge. While the management of this data will be achieved using the ANN as described later in Section 6.6, in this sub-section part of the URN data collected is used to investigate the effect of major propeller design parameters (i.e. namely P/D, BAR, Z) on the URN levels.

Using hydrophones, the URN measurements are traditionally presented in the frequency domain thus enabling the comparisons of the RNL's as a measure of the relative noise performance of a propeller. However, this approach limits the interpretation of various causes for the generation of URN as well as understanding the detailed effects of these causes. In order to provide further insight into this matter, an advanced analysis tool for the cavitation induced URN is implemented in this section. The implementation of this tool has required the recordings of the pressure pulses at a strategic location above the test propellers in synchronisation with the cavitation observations using High-Speed Video (HSV) cameras during the course of the systematic tests. Both the pressure pulses and the cavitation observations were acquired at a rate of 5000 Hz to allow a fine assessment of the time signal with respect to the visual cavitation phenomena observed.

Within the framework of the above objective and approach, this section is comprised of three analysis phases. The first phase presents the analysed net noise levels in the frequency domain for the chosen sample data. Following this, the synchronized time signals and cavitation observations are put under the spotlight in the second phase. Finally, the raw pressure pulse signals are processed by using the Joint Time-Frequency Analysis (JTFA) toolkit of LabVIEW to enable the determination of the frequency band to which certain types of cavitation phenomena contribute. An overall presentation of this advance tool for the analysis of the cavitation induced URN and background is outlined in Figure 6-23

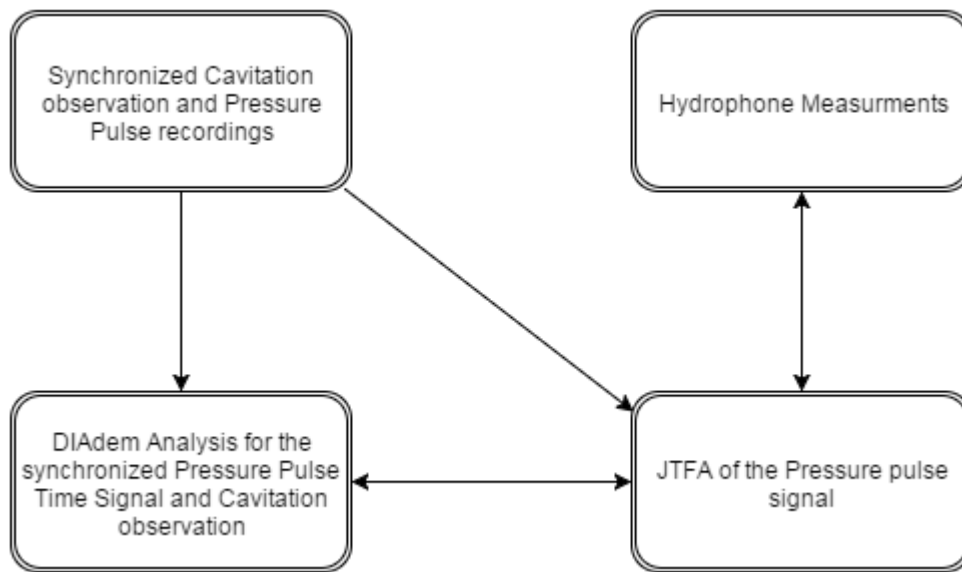
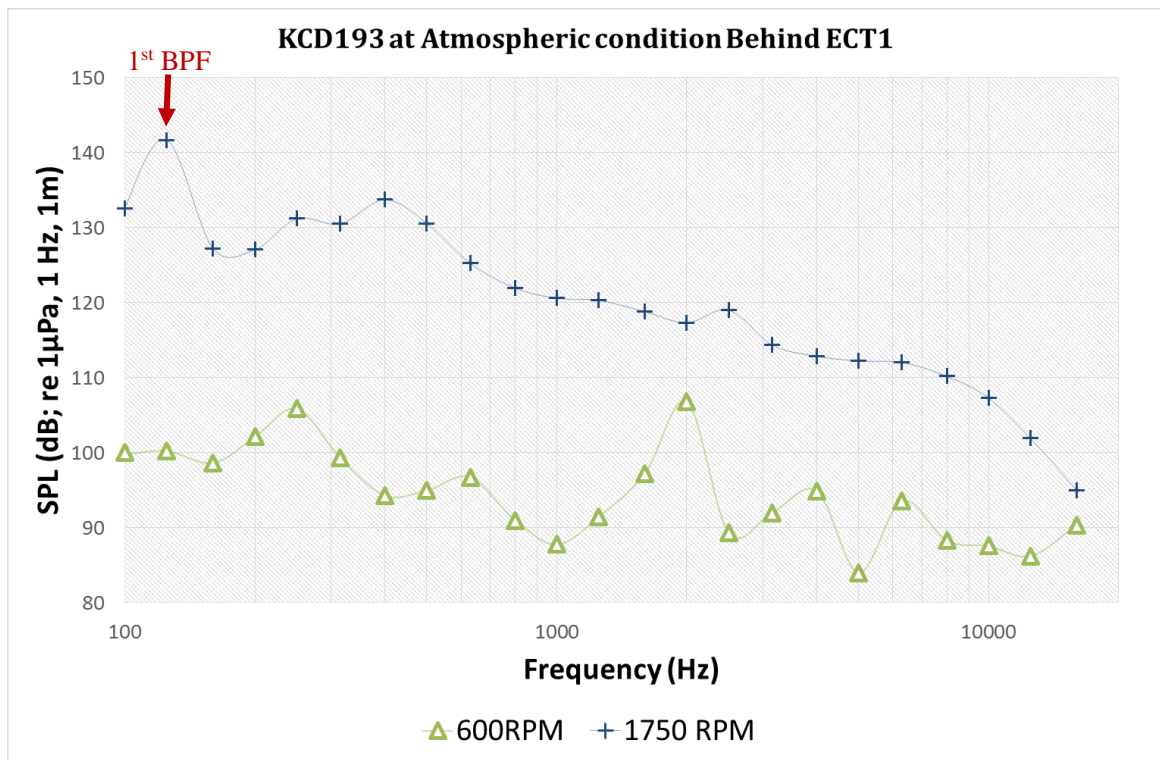


Figure 6-23 Layout of an advanced analysis tool for cavitation induced URN.

NI DIAdem and LabVIEW software tools are used to quickly locate, load, visualize, analyse, and report the measurement data collected during the data acquisition and/or generated during simulations (National Instruments, 2003, 2011). This toolkit is designed to meet the demands of today's testing environments, which require quick access, process, and report on large volumes of scattered data in multiple custom formats to make informed decisions.

### 6.5.1.1 URN data of propellers in frequency domain

Noise measurements from the cavitation tunnel tests are analysed and processed according to the procedure outlined in Chapter 3. Figure 6-24 to Figure 6-28 illustrate the influence of various propeller parameters on URN, as well as the effect of wake inflow and operating conditions. Sequentially, Figure 6-24 shows the effect of shaft speed; Figure 6-25 demonstrates the effect of the wake inflow; Figure 6-26 shows the influence of the blade number; Figure 6-27 depicts the influence of the BAR and Figure 6-28 illustrates the effect of the P/D ratio.

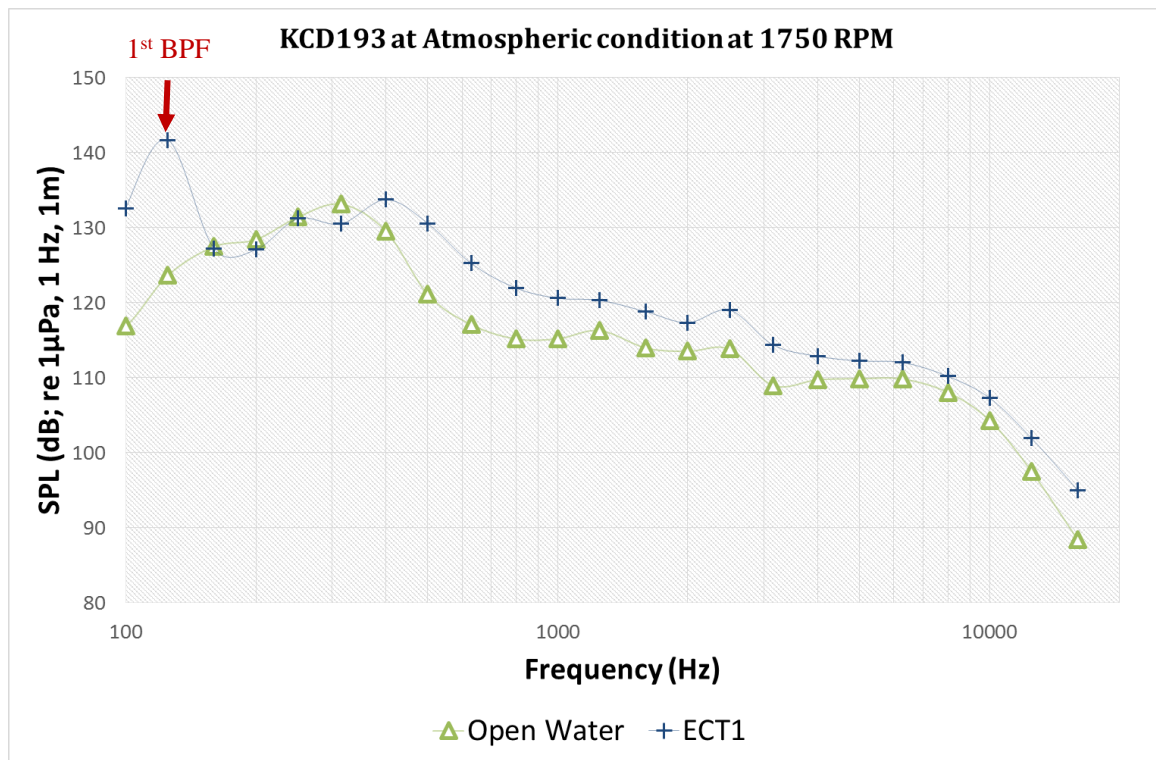


Propeller No	P/D	BAR	Blade No	Wake	J	K <sub>T</sub>	10K <sub>Q</sub>	RPM	σ <sub>v</sub>	σ <sub>n</sub>	σ <sub>Resultant</sub>
KCD193	1	0.65	4	ECT1	0.82	0.13	0.21	605	25.16	23.95	2.21
					0.28	0.40	0.59	1751		2.86	0.29

Figure 6-24 The comparison of the KCD193 propeller behind ECT 1 wake at propeller speed of 600 RPM and 1750 RPM.

Figure 6-24 presents the impact of the cavitation on the measured SPLs caused by an increase in the shaft speed and resulting change in the shaft speed based cavitation numbers and propeller performance coefficients. The figure clearly shows that the SPLs present a significant increase over the whole frequency range with amplitudes over 30 dB higher. Although such an observation is expected to be obvious, this also supports the hypothesis of the cavitation being the dominant noise source once it develops.

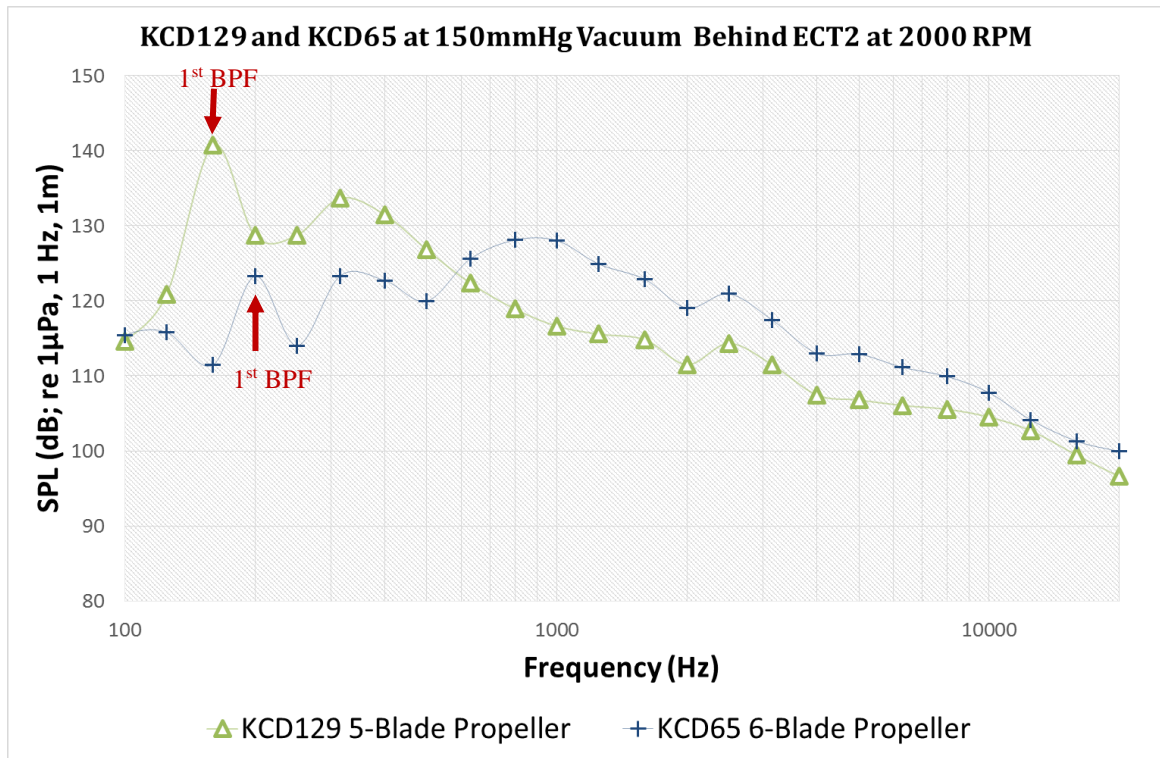




Propeller No	P/D	BAR	Blade No	Wake	J	K <sub>T</sub>	10K <sub>Q</sub>	RPM	σ <sub>v</sub>	σ <sub>n</sub>	σ <sub>Resultant</sub>
KCD193	1	0.65	4	ECT1	0.28	0.40	0.59	1751	25.16	2.86	0.29
KCD193				Uniform	0.34	0.38	0.56	1752	25.38	2.88	

Figure 6-25 Noise comparison of the KCD193 propeller behind ECT 1 and in open water condition at propeller speed of 1750 RPM.

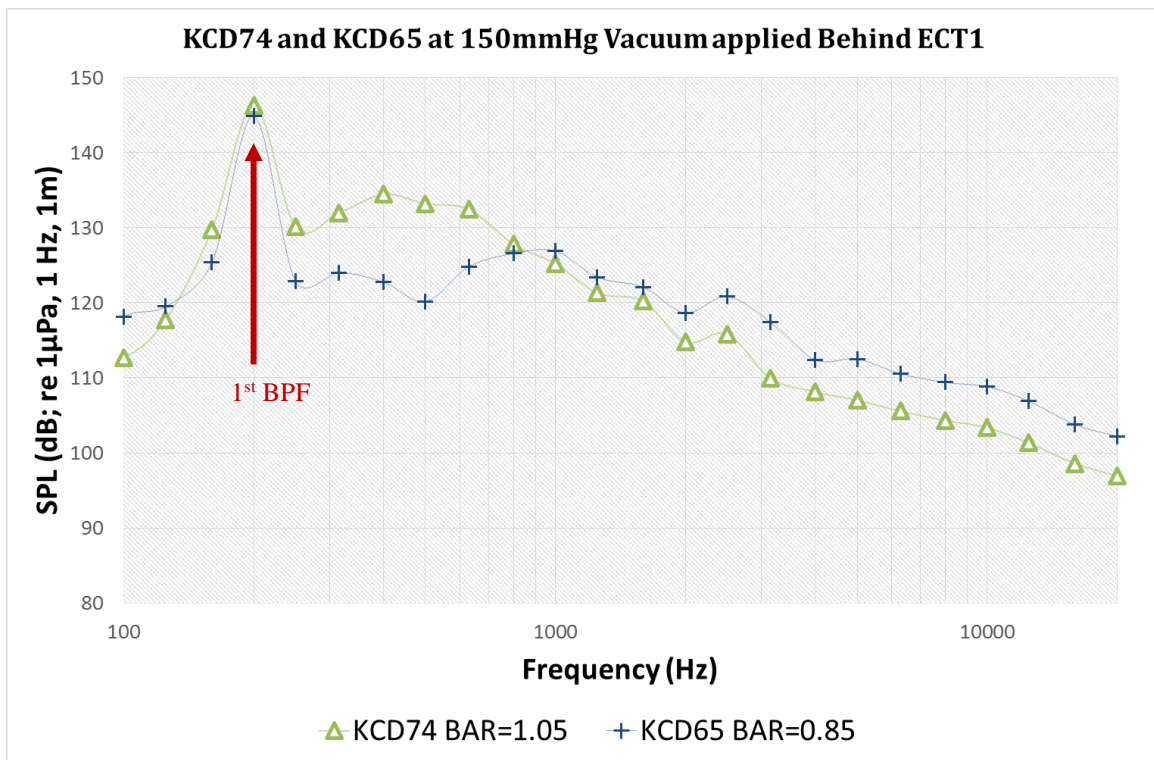
Figure 6-25 provides further evidence on the claim that the cavitation developed behind a non-uniform wake may induce higher SPLs, which can be up to 20 dB difference at the 1<sup>st</sup> blade passage frequency and no less than 5 dB difference at the broadband frequencies, compared to the SPLs measured in open water condition. This indicates that although the cavitation is the dominating factor for the RNL, the dynamics involved due to the cavitation volume acceleration emanating from the wake variation causes further elevation that may also be contributed by bursting, rebounding and collapse of the cavitation bubbles. Such cavitation dynamics give rise to the cavitation volume acceleration which is well known to be the main factor behind the hydro-acoustic cavitation noise



Propeller No	P/D	BAR	Blade No	Wake	J	$K_T$	$10K_Q$	RPM	$\sigma_v$	$\sigma_n$	$\sigma_{Resultant}$
KCD129	0.8	0.85	5	ECT2	0.24	0.32	0.39	1992	20.67	1.82	0.18
KCD 65			6			0.31		1990	20.76	1.83	

Figure 6-26 Noise comparison of KCD 129 and KCD 65 propellers behind ECT 2 wake at propeller speed of 2000 RPM.

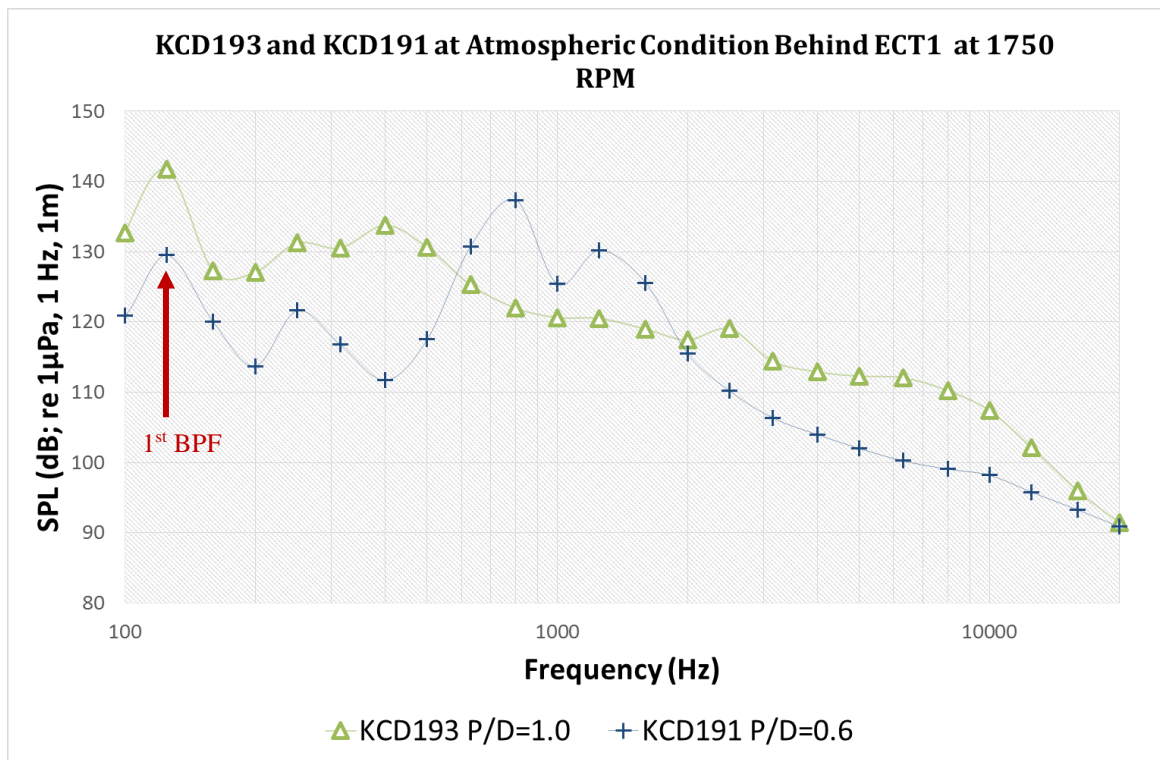
Figure 6-26 shows differences due to the number of blades on the measured SPLs from two propellers tested. Interestingly the spectral levels emitted by the two propellers cross-over a frequency around 600 Hz as such KCD 129 (5 bladed) displays higher SPLs below the cross-over frequency while KCD 65 (6 bladed) emits higher SPLs above this frequency. While this will be dominated by the nature of the cavitation experienced by each propeller over the frequency range tested, the lesser blade number of KCD 129 will induce relatively higher thrust density per blade compared to KCD65.



Propeller No	P/D	BAR	Blade No	Wake	J	$K_T$	$10K_Q$	RPM	$\sigma_v$	$\sigma_n$	$\sigma_{Resultant}$
KCD 65	0.8	0.85	6	ECT1	0.25	0.31	0.38	1988	20.99	1.85	0.19
KCD 74		1.05						1976	20.17	1.80	0.18

Figure 6-27 The comparison of the KCD 74 and KCD 65 propellers behind ECT 1 wake at propeller speed of 2000 RPM.

The comparison of the effect of the BAR is presented in Figure 6-27. The RNL are observed to be similar up to 200 Hz. However, there seems to be a hump in the spectral levels experienced by the KCD 74 from 200 Hz to 800 Hz emitting higher sound pressure levels within this frequency range. KCD 65 is observed to produce higher noise levels for the high frequency range (>800 Hz) when compared to KCD 74. This figure is intriguing as the propeller performance coefficients are exactly same and cavitation numbers are similar, but there is a significant difference in the RNL. The impact of the BAR reveals itself in terms of the thrust per blade area. Thus heavily loaded KCD 65 experiences more dynamic cavitation contributing to the high frequency region of the measured spectra.



Propeller No	P/D	BAR	Blade No	Wake	J	$K_T$	10 $K_Q$	RPM	$\sigma_v$	$\sigma_n$	$\sigma_{Resultant}$
KCD193	1	0.65	4	ECT1	0.28	0.40	0.59	1751	25.16	2.86	0.29
KCD191	0.6					0.17	0.18		25.39	2.89	

Figure 6-28 The comparison of the KCD 193 and KCD 191 propellers behind ECT 1 wake at propeller speed of 1750 RPM.

The final comparison presented by Figure 6-28 is to represent the effect of different pitch ratios on the measured SPLs. While the noise levels of KCD193, which has a higher P/D and hence thrust loading, are generally greater than those of KCD 191 over the frequency range tested, this trend changes over a frequency band between 600 Hz to 2000 Hz. Over this frequency band KCD 191, which has a lower P/D, displays two distinct humps that result in higher SPLs than for the KCD 193 SPLs. The reason behind the presence of the humps will be scrutinized further using the synchronized cavitation observation and pressure time signal method and JTFA in the following sections. As one may also note that the BPF levels also present more than 10 dB difference.

### **6.5.1.2 Synchronized fluctuating pressures and cavitation behaviour propellers in time domain**

Details of the synchronised acquisition of the pressure sensor data and high-speed video recordings of cavitation observation have been already described in Chapter 3 (Section 3.4.4 and 3.5.5). Synchronisation was achieved using a TTL signal from the motor speed encoder and a signal generator as a conditioner. The synchronized recordings and analysis of the results can enable one to make a comparison of the time signals to explore the effect of different parameters on the URN within more details. Within this framework, some of the earlier investigated parameters (in Section 6.5.2.1) has been further explored based on the analysis of the synchronized pressure signals and cavitation observations and results are discussed in the following.

Figure 6-29 to Figure 6-33 have been reproduced using the recording made during the standard series propeller tests, using Diadem software. As the size of the high-speed video recordings can occupy quite large amounts of hard disc space, they have been made for 0.1 second by totalling 500 individual images at an acquisition rate of 5000 Hz. The video recordings for the 0.1-second configuration occupying approximately 350 Gigabyte of data. Therefore, although the pressure signals are recorded for 5 seconds, they have been trimmed to match the length of the high-speed video capture to enable synchronized viewing within the software. The user interface is arranged to be divided into two, where the left-hand side of the figure belongs to the time signal of one propeller within which the upper part is the pressure time signal and bottom half is the corresponding cavitation observation. The right-hand side of the figure is likewise arranged to present the comparison that is selected. A marker traces the time signal for the corresponding cavitation observation aiding the interpretation.



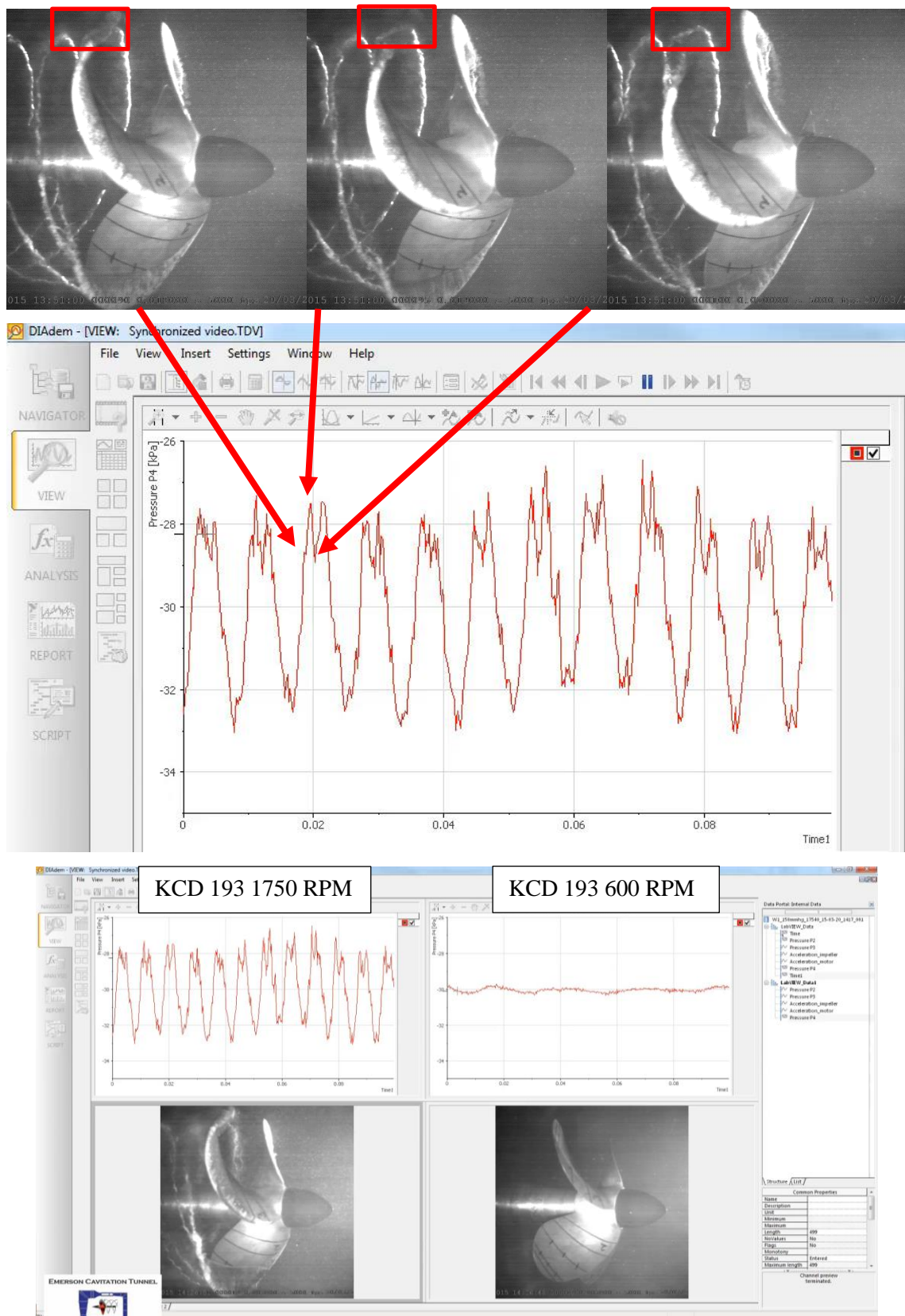


Figure 6-29 Synchronous time domain pressure signals and cavitation observations under atmospheric pressure for KCD 193 behind ECT1 for 1750 RPM (left) and 600 RPM (right).

Figure 6-29 is the reproduction of the test data used for Figure 6-24 using synchronized pressure transducer time signals and cavitation observations. The propeller is cavitating heavily for the condition with propeller speed of 1750 RPM whilst 600 RPM is a non-cavitating condition. The cavitating pressure signal shows significantly higher amplitudes with higher frequency irregularities (spikes). Such spikes are attributed to the cavitation collapse as shown within the top side of Figure 6-29 by the pressure time signal and the corresponding cavitation observations.

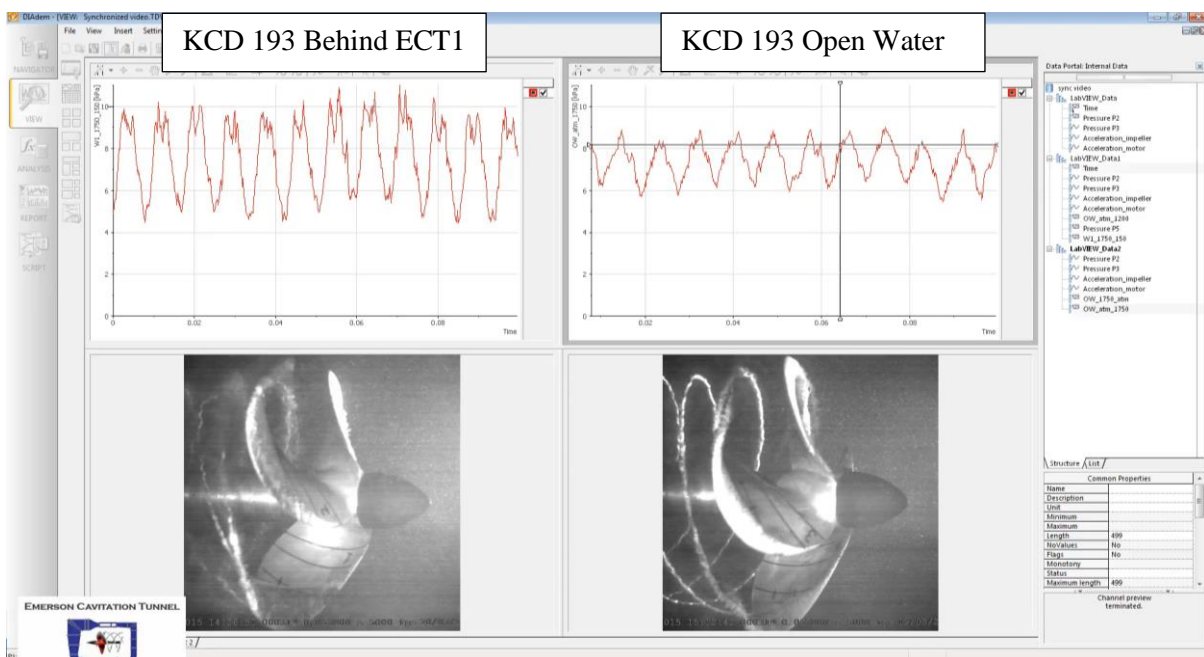


Figure 6-30 Synchronous time domain pressure signals and cavitation observations under atmospheric pressure for KCD 193 at 1750 RPM behind ECT1 (left) and open water condition (right).

Figure 6-30 shows differences only due to the wake flow; ECT1 and open water. The pressure time signals differ significantly both in terms of the amplitude and the spikes experienced by the time signal. The images also support this finding as both tip vortex and sheet cavitation for the propeller in open water condition are more stable, whilst behind ECT1, bursting of a tip vortex cavitation (TVC) is observed in the slipstream together with unstable sheet cavitation attached to the propeller blade.

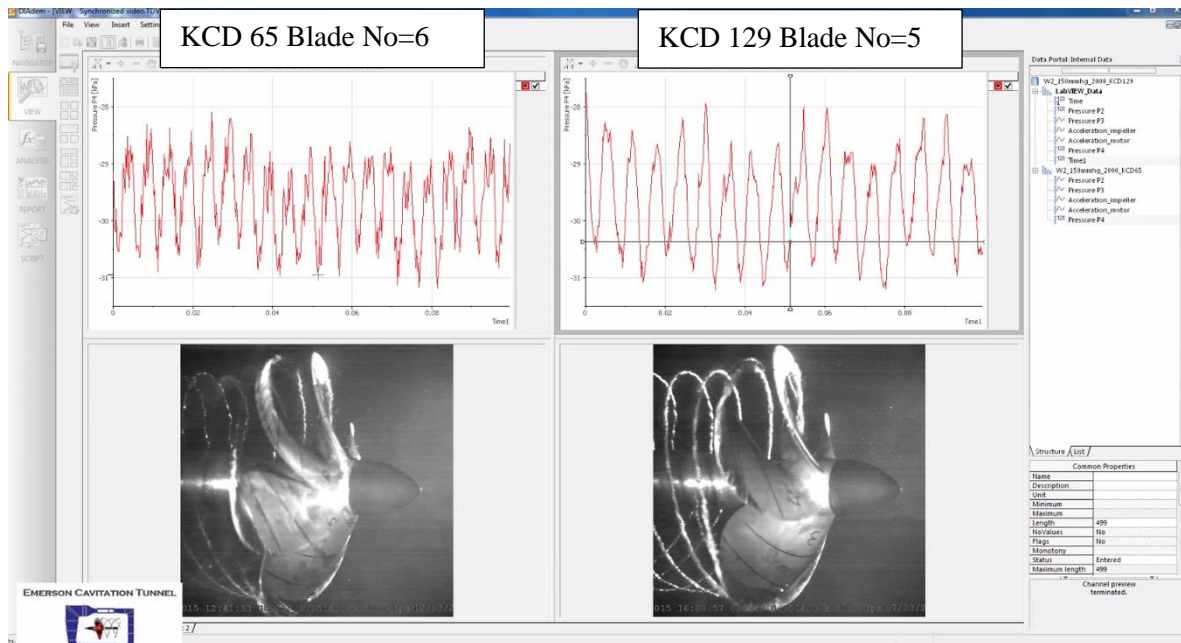


Figure 6-31 Synchronous time domain pressure signals and cavitation observations under 150 mmHg vacuum behind ECT2 at 2000 RPM for KCD 65 (left) and KCD 129 (right).

The effect of different blade numbers is shown in Figure 6-31. The thrust load is less for KCD 65 (6 blades) which has the higher number of blades. KCD 65 is experiencing rather unsteady tip vortex cavitation collapses in the propeller slipstream as shown in the images which are resulting in spikes experienced by the associated time signals. On the other hand, KCD 129 (5 blades) shows more stable cavitation and a thicker diameter of tip vortex cavitation comparatively.



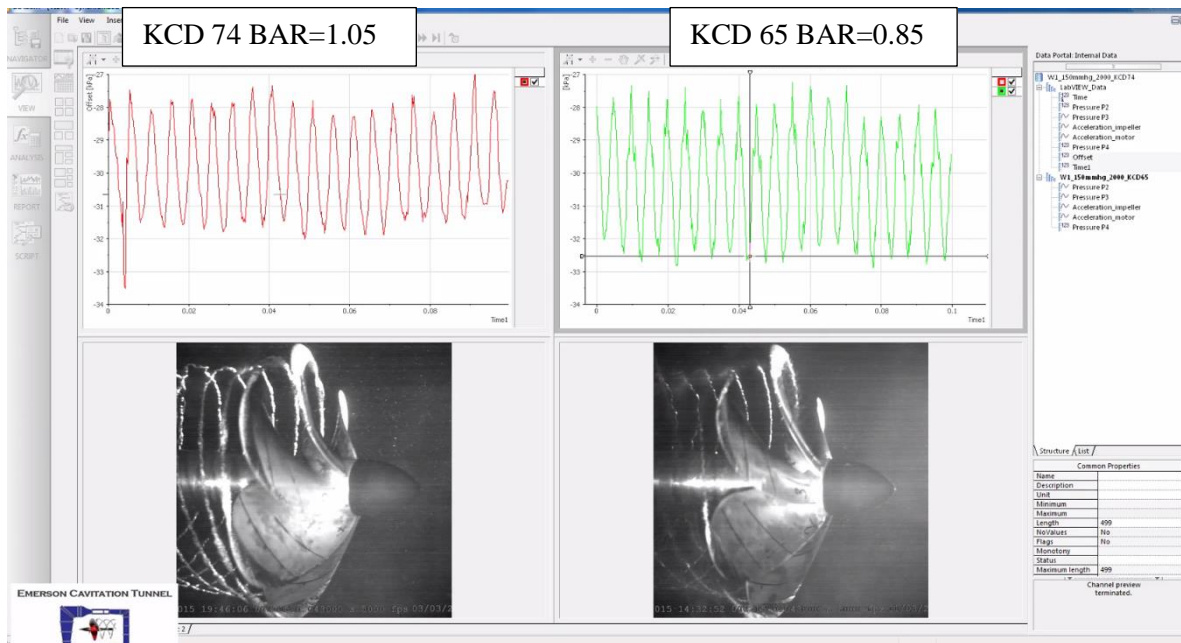


Figure 6-32 Synchronous time domain pressure signals and cavitation observations under 150 mmHg vacuum behind ECT1 at 2000 RPM for KCD 74 (left) and KCD 65 (right).

Figure 6-32 presents the effect of the BAR for two 6-bladed propellers. KCD 74 has a higher BAR, hence a smaller thrust density. This produces lesser extent and volume of sheet cavitation and hence a lower peak to peak pressure signal. The sheet cavitation produced on KCD 65, with its higher thrust loading, is relatively more unstable, showing foamy collapsing behaviour in the slipstream, whilst the tip vortex cavitation of KCD 74 is rather stable but thicker in diameter.

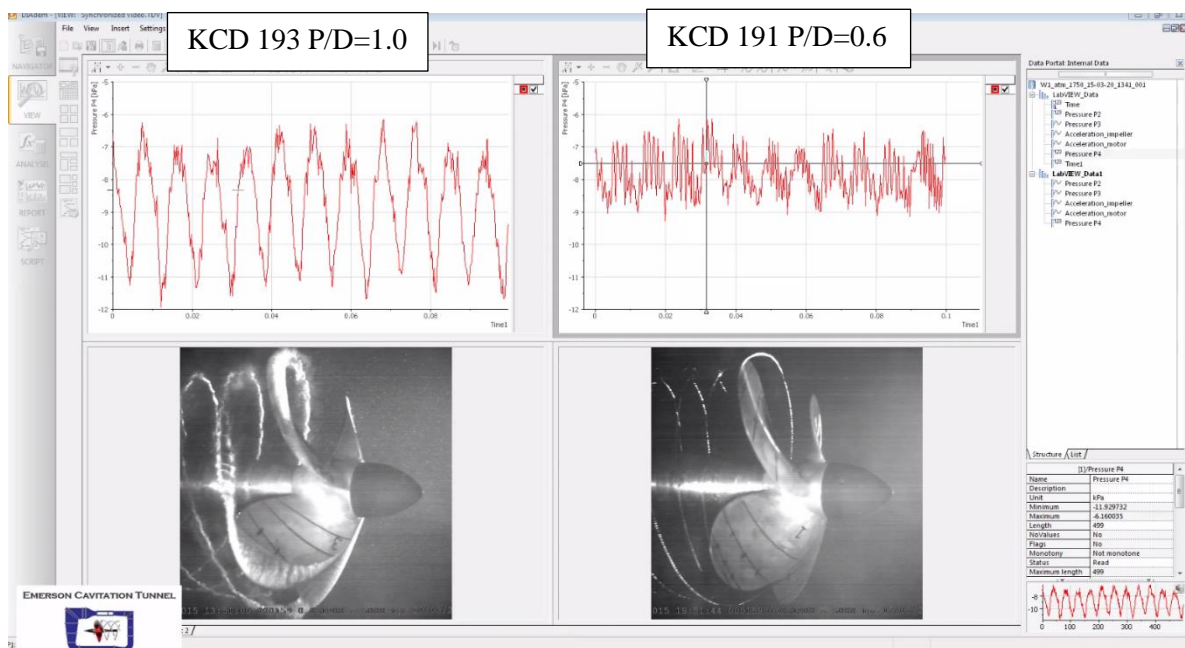


Figure 6-33 Synchronous time domain pressure signals and cavitation observations under atmospheric pressure behind ECT1 at 17500 RPM for KCD 193 (Left) and KCD 191 (Right).

Figure 6-33 shows the pressure time series and cavitation images for two different P/D ratios. At the same J-value, KCD 193 is operating at a higher loading than KCD191. Consequently, it generates a larger extent of sheet cavitation as well as unsteady tip vortices travelling into the slipstream with foamy appearance. The pressure time signal for the KCD 193 experiences a larger peak to peak amplitude, mainly due to the sheet cavitation volume and significant irregularities due to the cloudy collapse of the tip vortex cavitation. KCD 191 operates at a much lighter loading and thus produces no sheet cavitation; only intermittent tip vortex cavitation both attached to the propeller and in the slipstream. The tip vortex cavitation is bursting as it detaches from the propeller resulting in a very spiky pressure time signal.

### 6.5.1.3 Joint-time frequency analysis of fluctuating pressures and URN of propellers

The acquired pressure time signal data, described in the previous section, has then been fed into the JTFA tool in order to understand the relationship between time events of the pressure pulse signals and cavitation presence and corresponding frequency domain response. The JTFA tool does this through a spectrogram to provide an enhanced understanding of the frequency region that certain types of cavitation contributes into.

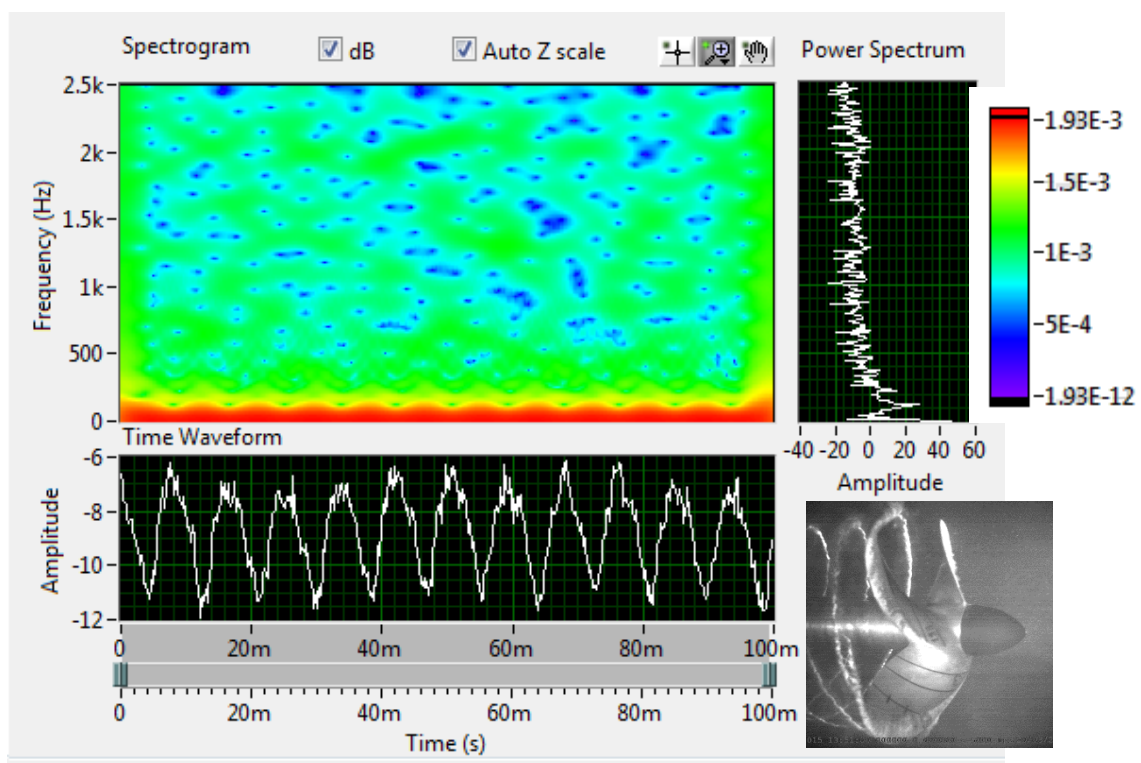


Figure 6-34 Joint-time frequency analysis of KCD 193 propeller behind ECT1 under atmospheric condition at 1750 RPM.

Figure 6-34 presents pressure recordings and analysis results of KCD 193 propeller for its most heavily cavitating condition. The spectrogram indicates that the spikes found in the time signal contribute over a broad spectral range. Although the analysis is limited to 2.5 kHz since the pressure transducer signal is sampled at 5 kHz, the noise data from the hydrophone analysis, which is shown in Figure 6-24, also indicates contributions from the cavitation dynamics at higher frequencies. Overall the spectrogram has only very small areas occupied by the blue colour referring to the lower amplitude activity while it is dominated by the greenish colour corresponding to the higher amplitude activities in the FFT at broadband range.

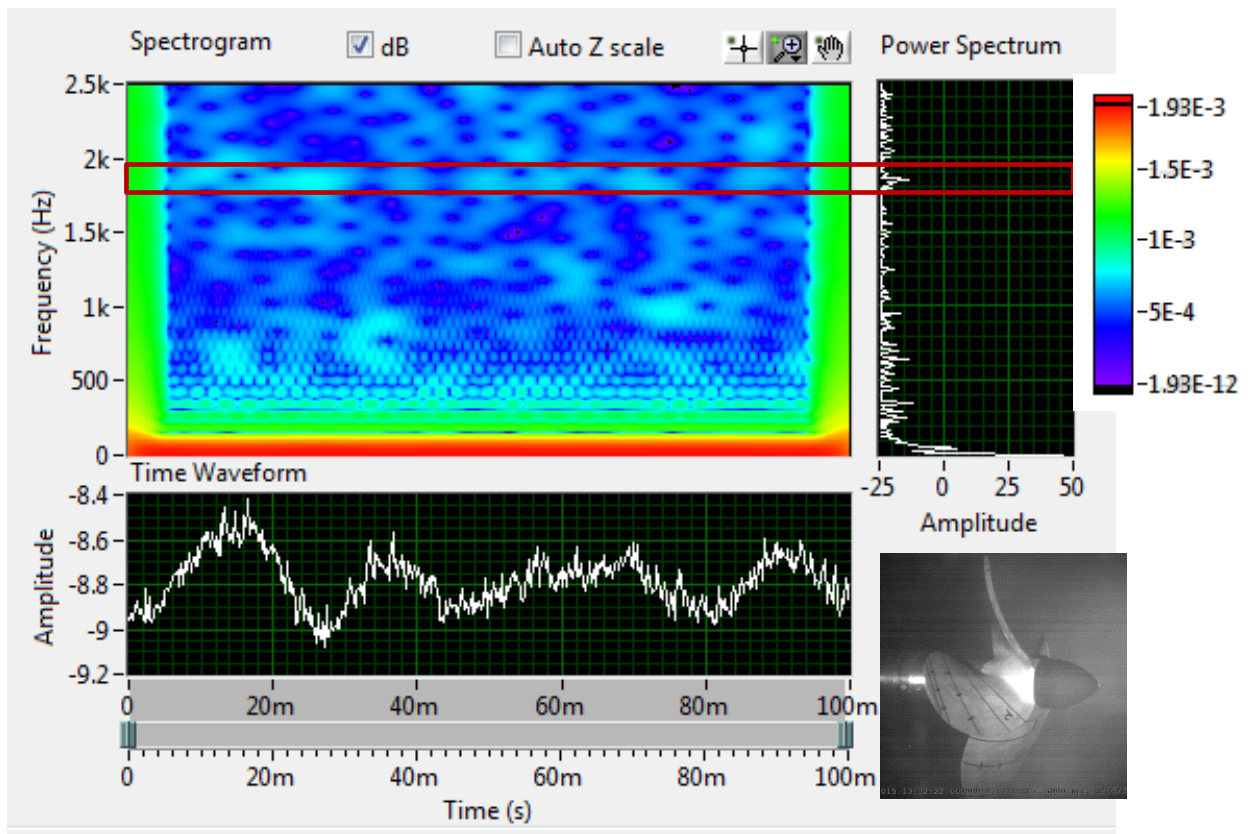


Figure 6-35 Joint-time frequency analysis of KCD 193 propeller behind ECT1 under atmospheric condition at 600 RPM.

Figure 6-35 shows the JTFA analysis of KCD 193 behind ECT1 wake at 600 RPM corresponding to a non-cavitating condition. As a consequence and shown in Figure 6-36, not only the peak to peak amplitudes have been significantly reduced but also the overall amplitude levels in the spectral domain have been considerably reduced, as indicated by the dominant blue colouring (low levels). A distinct peak is shown in the FFT results between 1.5 – 2 kHz which is also captured in Figure 6-24 by the spectral levels of the corresponding hydrophone measurements. The cause of the peak may be observed to be the light blue region present in the spectrogram potentially caused by the singing of the propeller.

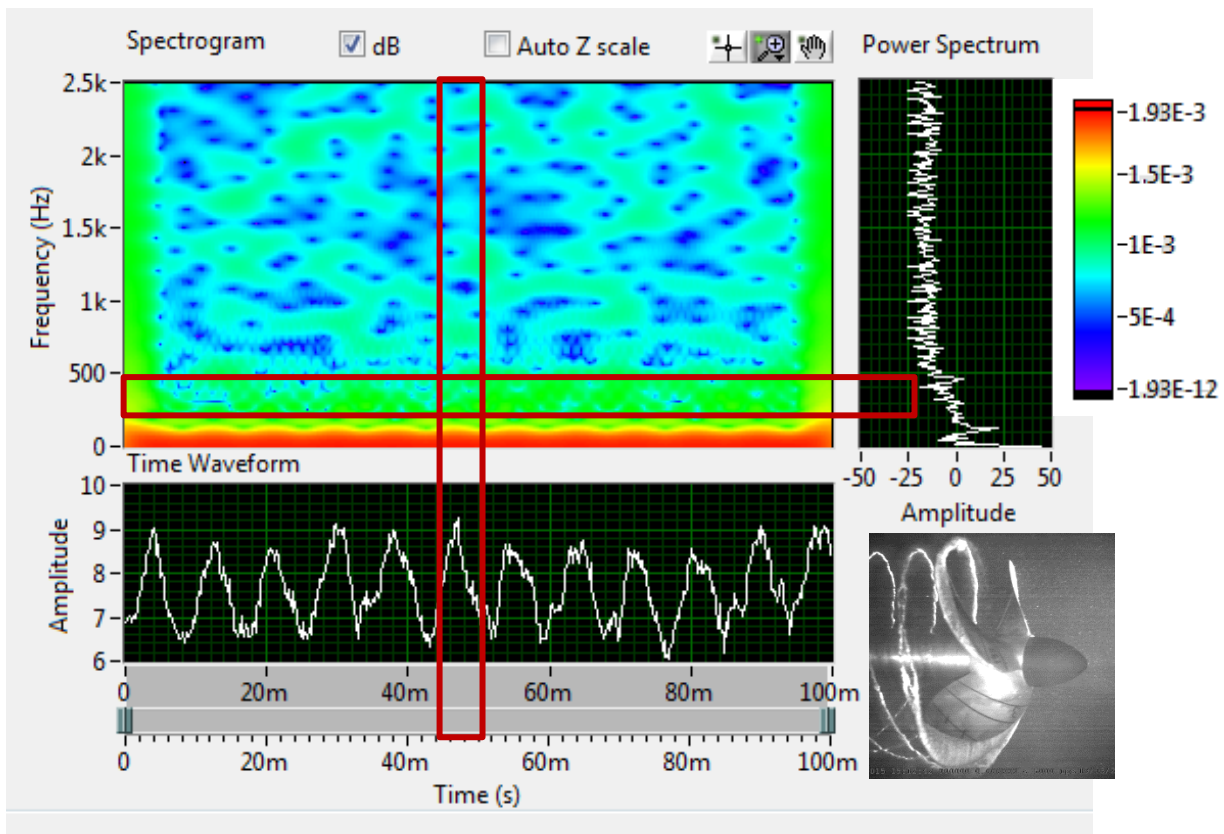


Figure 6-36 Joint-time frequency analysis of KCD 193 propeller in open water condition under atmospheric condition at 1750 RPM.

Figure 6-36 shows the pressure recording and analysis results of KCD 193 propeller at 1750 RPM but in open water condition. Overall the analysis of the results shows a reduction at the blade rate and broadband spectra in terms of the amplitudes when compared to Figure 6-34. Moreover, the previous comment is supported by the spectrogram colour map which is occupied by bluer colour footprints over the broadband range. The above findings justify the use of JTFA by further confirming the results presented in Figure 6-25. One interesting observation, which can be made from the spectrogram is the contour oscillations at the blade rate frequency. The spectrogram presents yellow colour during the peak in the time signal that coincides with the passage of a propeller blade which indicates the presence of a large cavitation volume. Following the passage of the blade, contour colour changes to green in conjunction with the trough of the time signal which is experienced by moving propeller blade. Another important aspect of Figure 6-36 is the hump in the narrow band frequency range from 160 to 400 Hz, which is again present in the noise measurements as shown in Figure 6-25. Overall the spectrogram shows a rather denser green colour in Figure 6-34 indicating the higher emanated sound pressure levels in comparison to the Figure 6-36.



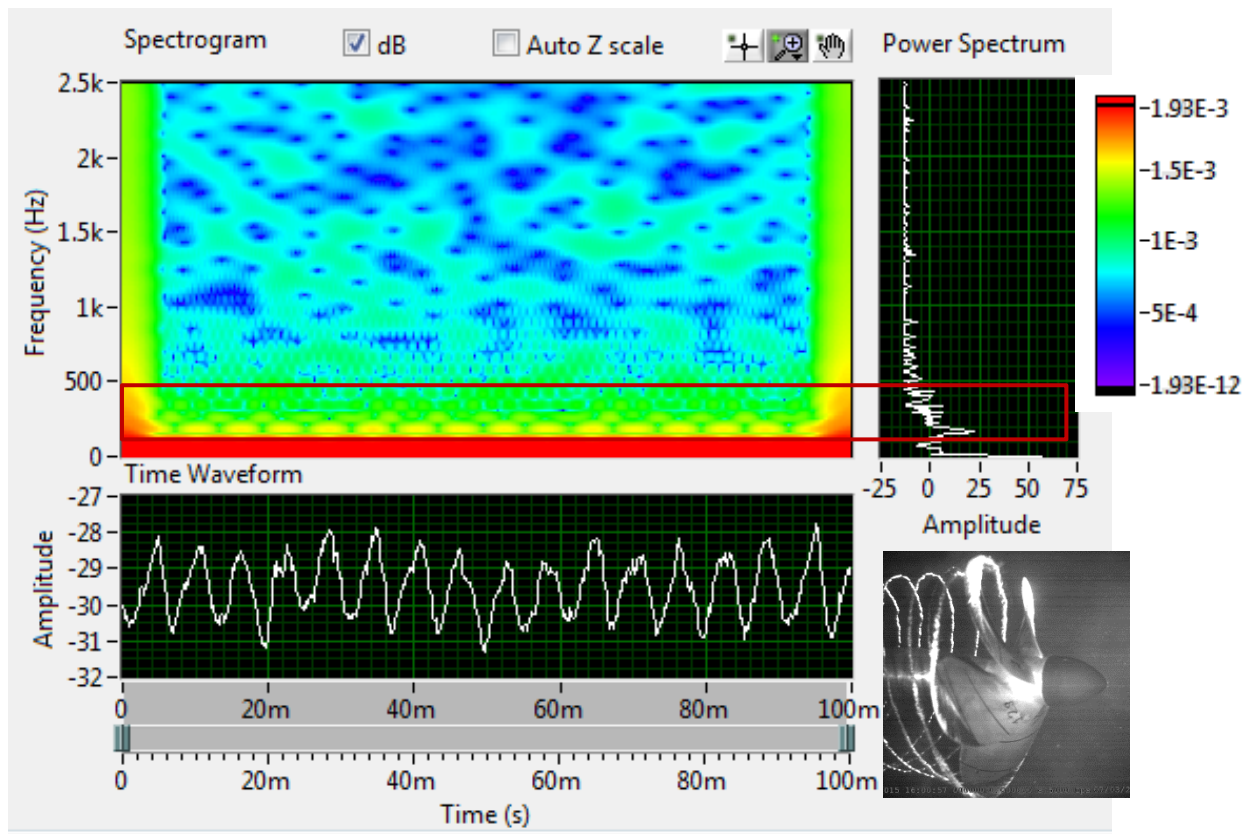


Figure 6-37 Joint-time frequency analysis of KCD 129 propeller behind ECT2 under 150 mmHg vacuum at 2000 RPM (5 blades).

Figure 6-37 represents the analysis of one of the test runs to investigate the effect of blade number. The results of the URN measurements with KCD 129 (5 blades) and KCD 65 (6 blades) for this particular test run have already shown in Figure 6-26 and Figure 6-31. In this condition, the propeller experiences stable TVC. Both the spectrogram and FFT results show elevated pressure levels in the 200 to 600 Hz frequency range as represented by the green colour. This elevation also reveals itself in the noise measurements by hydrophone as can be seen in Figure 6-26. Another interesting aspect of Figure 6-38 is the reflection of the blade rates in the spectrogram by the green and yellow pulsations present at the blade rate frequency.

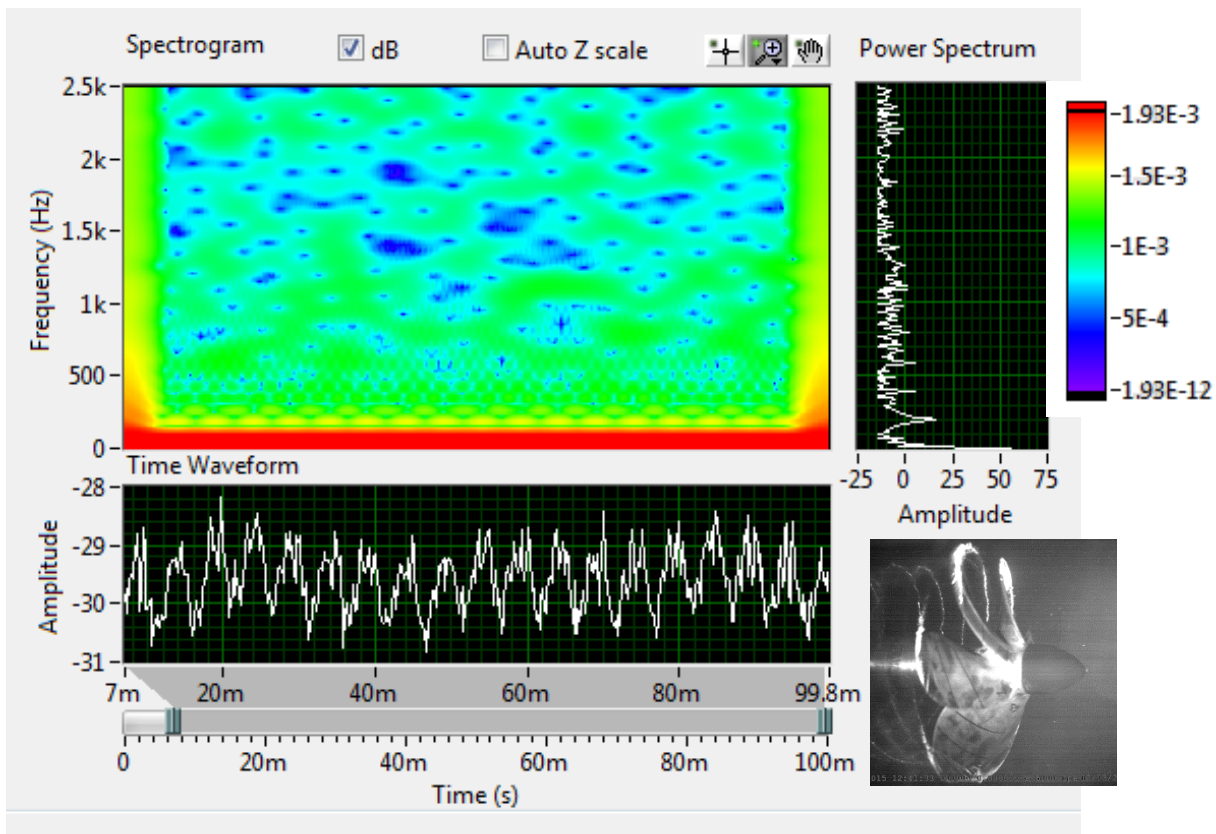


Figure 6-38 Joint-time frequency analysis of KCD 65 propeller behind ECT2 under 150 mmHg vacuum at 2000 RPM.

Figure 6-38 is the JTFA analysis results of the test run with KCD 65 propeller which is the 6 bladed counterpart of KCD 129. The comparative results of the noise measurements with both propellers (i.e. KCD 129 and KCD 65) for the same test run have been already shown in Figure 6-26 that can be combined with the JTFA results during the discussion. In this test run KCD 65 experiences a larger extent of sheet cavitation combined with a rather unstable foamy tip vortex cavitation in the slipstream. The larger volume of the sheet cavitation results in more dramatic collapse and rebounding resulting in higher cavitation volume acceleration and hence relatively spikier time signals. The comparison of Figure 6-37 and Figure 6-38 does suggest that the RNLs of KCD 129 appears to be higher up to 600 Hz compared to the results of KCD 65 since the amplitudes. The rest of the frequency range, however, indicates higher noise levels radiated by KCD 65. The above conclusion is well in agreement with the earlier presented spectral levels in Figure 6-26.

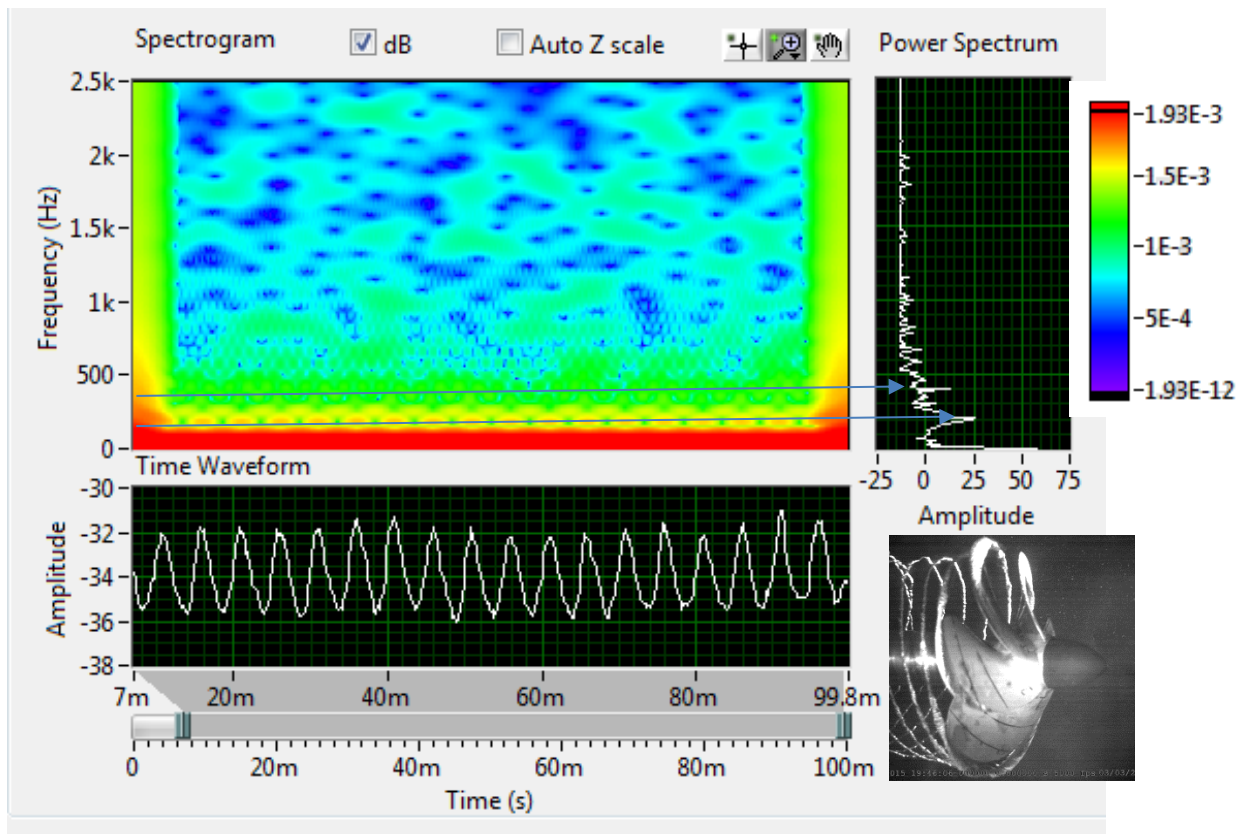


Figure 6-39 Joint-time frequency analysis of KCD 74 propeller behind ECT1 under 150 mmHg vacuum at 2000 RPM.

Figure 6-39 represents the JTFA results for KCD 74 selected to discuss the effect of the BAR on the URN levels. KCD 74 has a higher BAR compared to its counterpart propeller KCD 65. Hence, the interpretation of the results should be combined with the URN measurement results of the same propeller which have been presented in Figure 6-28 as discussed earlier. KCD 74 at this test condition does have a rather continuous green background of spectrogram results in the 200 to 600 Hz range but also has a region dominated by the blue in the high frequency. The propeller experiences a stable TVC with dynamic nature as it can be seen to experience some volume fluctuation as it travels through the slipstream. The peak at 200 Hz coincides with the 1<sup>st</sup> Blade Passage Frequency (BPF) and represented by the green and yellow fluctuation in the spectrogram. Figure 6-39 confirms the trend in the URN measurements observed in Figure 6-27 showing all dominant spectral features of the cavitating propeller.



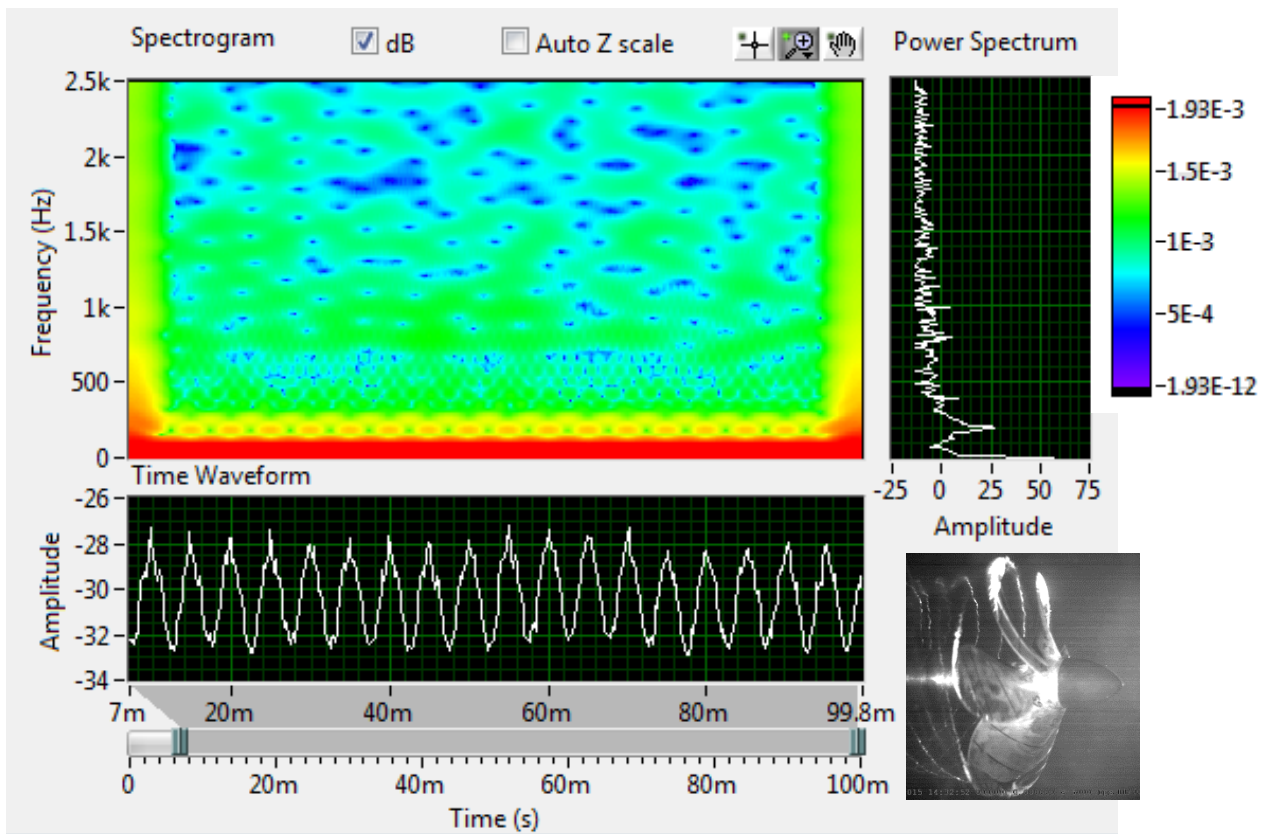


Figure 6-40 Joint-time frequency analysis of KCD 65 propeller behind ECT1 under 150 mmHg vacuum at 2000 RPM.

Figure 6-40 represents the JTFA results of KCD 65 having the lower BAR. While the background colour of the spectrogram is exactly the same up to the 1<sup>st</sup> BPF (200Hz) for both KCD 65 and KCD 74 propellers, the spectrogram shows relatively larger extent of blue colour in the 200 to 600 Hz region for the KCD 65. However, thereafter the colour code shows rather greener background which reveals itself in the FFT result as the spiky broadband components. In the light of the above comments and considering the trend in the URN spectrum as discussed in Figure 6-27, the results of the JTFA confirms the analysis results of the URN, which is further supported by the cavitation observations presented in Figure 6-32.

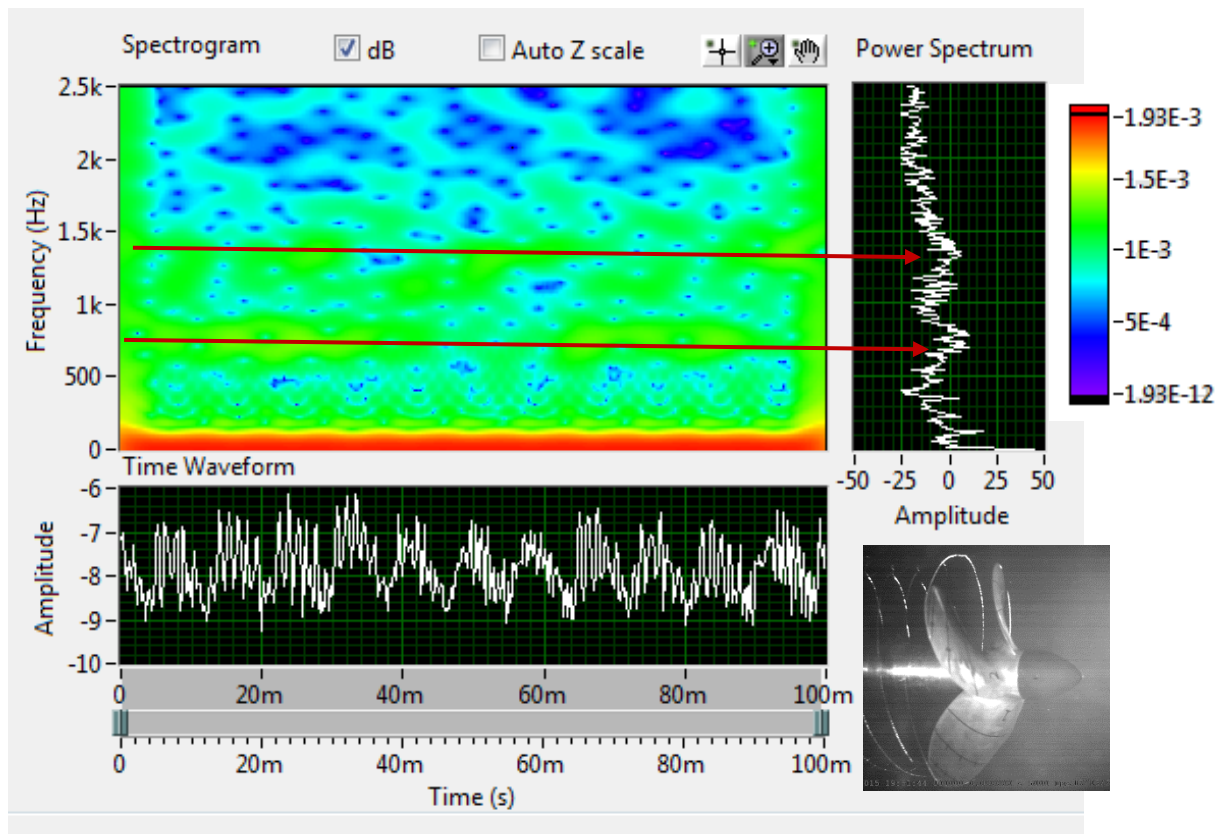


Figure 6-41 Joint-time frequency analysis of KCD 191 propeller behind ECT1 under atmospheric condition at 1750 RPM.

Figure 6-41 represents the JTFA results of KCD 191 propeller behind wake ECT1 at 1750 RPM. The propeller experiences a thin TVC cavitation that collapses in the slipstream as discussed in Figure 6-33. The spectrogram shows a rather blue region for the frequencies higher than 1.5 kHz while the rest of the frequency range between 200 to 1.5 kHz has rather green background which is also present in the power spectrum analysis part of the JTFA by the elevated levels. The impact of the TVC is displayed as large-scale spike in the pressure time signal at the exact time of the experienced collapse. These time domain spikes are reflected as continuous green coloured zones on the spectrogram at two distinct frequency ranges: one being at 400 to 1000 Hz; and other at 1000 to 2000 Hz range. The reflection of these zones is also clearly visible by two distinct humps in the RNL spectrum of KCD 191 propeller as shown in Figure 6-28. The originating cause of these humps thus can be attributed to the TVC and its dynamics with the aid of time stamped quantitative proof of the cavitation observations in conjunction with the JTFA approach implemented. As experienced in this example such a case, where there is only one type of cavitation with intermittent nature, presents a perfect example for the merits of the implemented advanced analysis approach.

#### **6.5.1.4 Further remarks on the advanced analysis tool for cavitation induced noise**

Based on the systematic data produced in this study the capability of the implemented advanced analysis tool for cavitation induced noise has been demonstrated. The main objective of this tool is to aid in understanding further details of the cavitation induced noise phenomenon. This has been achieved by making use of the synchronised fluctuating pressure signals and cavitation observations in time-domain which is combined with the JTFA technique. The implemented tool has demonstrated the further details of some of the major propeller design and operational parameters involving the URN phenomenon as well as the interpretation of some important mechanisms of the instantaneous cavitation dynamics contributing to the phenomenon.

The presented approach can be developed further by the introduction of a combined synchronized cavitation observation and JTFA. Whilst this can be still achieved with the above-presented approach, a dedicated combined software may simplify the analysis effort. Furthermore, the hardware may also be improved by use of a high-speed camera at a frame rate of 40 kHz in order to match the limit of the hydrophone frequency.

## 6.6 Development of an ANN tool for cavitation noise prediction

The database compiled from the extended systematic propeller tests has been used for the development of a cavitation noise prediction method with the aid of an ANN tool. The ANN methodology is inspired by biological neural networks, replicating the interconnection of the neurons in a nervous system of the human brain and other organisms (Rojas, 1994). Whilst the main component for both biological neural networks and artificial neural networks are Neurons, ANN tools adopt a rather non-linear processing method that suits a wide range of applications being trained on sample data. With the appropriate training an ANN based software tests and validates its predictions using the input database to evaluate the predictions of the network and to improve the estimates by means of pattern recognition. A representative sketch for an ANN is given in Figure 6-42. The codes developed for the engineering of a Neural Network for cavitation noise prediction are provided in Appendix D.

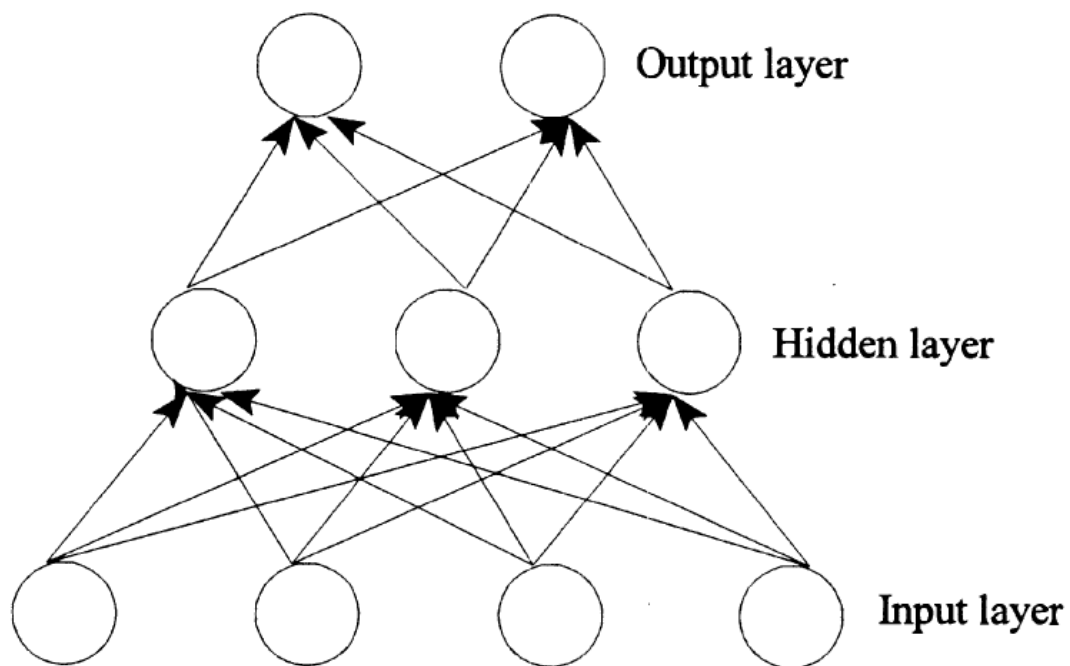


Figure 6-42 Representative sketch of a three layer feedforward ANN (reproduced from (Basheer & Hajmeer, 2000)).

The review of the applications of ANN in the marine field revealed the capabilities and reliability of this tool in terms of the prediction accuracy and data management. Thus, originating from the developed confidence, the data produced within the framework of the systematic experiments with the extended subset of Meridian propellers are compiled into a database which is function of a large number of parameters recorded during the course of the experiments. This database and associated parameters, which are represented by suitable non-dimensional parameters, have formed the basis for the development of the noise prediction tool described in the following.

The proposed approach for the development of an ANN based URN prediction of a propeller has indicated that the traditional way of presentation of the net noise levels by extraction of the background noise levels may not be applicable. This is due to the fact that the method requires elimination of the noise data for which the difference between the measured total noise levels and the background noise levels is less than 3 dB. This consequently results in empty cells to appear in the dataset which will adversely affect the accuracy of the database and hence the predictions. In order to avoid any error accumulation, which may be introduced by this approach, the total noise and background noise level measurements are compiled into two separate databases which are trained separately by the ANN. The net noise level of any member propeller is then predicted by subtracting the total noise data from the background noise with the aid of ANN.

The implementation of the above approach required the determination of different parameters both for the background noise data set and the total noise dataset. Since some of the variants, such as the propeller performance and propeller design parameters, are not applicable to the background noise levels, the input matrices are modified to include appropriate parameters.

The total noise level data for the 31 third octave centre frequencies ranging from 20 Hz to 20 kHz is predicted using 12 non-dimensional input parameters in 4 categories. These categories are specified as “propeller design parameters”, “wake parameters”, “propeller performance parameters” and “cavitation number parameters” as outlined in Figure 6-43.



Figure 6-43 Defined model scale total noise prediction parameters for the ANN.

In the same vein, the background noise level data is also trained for the prediction of 31 third octave centre frequencies. However, due to the lack of relevance of the some parameters related to the propeller, the input parameters for this prediction were achieved by only 5 parameters regarding the wake, tunnel inflow (advance coefficient) and applied vacuum level (cavitation number).

Once the structure of the prediction method for the model scale measurements are accomplished, ANN training is started. The training of the ANN is achieved through using Neural Network Fitting Tool provided by MATLAB (Beale et al., 2015). This choice was made due to the patterns recognition capability of this training technique. The MATLAB toolbox initiates a feed-forward network with hidden sigmoid neurons and linear output neurons. This option is capable of fitting multi-dimensional mapping problems arbitrarily well, given consistent data and enough neurons in its hidden layer. The network is trained with Levenberg-Marquardt backpropagation algorithm neural network. The input data is split into three categories, namely training, test and validation. 70% of the data has been used for training whilst the rest is equally divided into 15% for testing and 15% for validation. The data division is made randomly. The training is made up to 1000 iterations (epochs) if validation checks are not satisfied for the given minimum error criteria.

After determining the various setting for the ANN, the optimum number of hidden layers and number of neurons in each hidden layer needs to be set. ANN's are sensitive to the number of neurons in their hidden layers. The utilization of too few neurons can lead to under-fitting whilst too many neurons can contribute to overfitting, in which all training points are well fitted, but the fitting curve oscillates wildly between these points. In order to achieve a prediction with the

best accuracy, a MATLAB code has been used to train the ANN for a range of hidden layer numbers and neurons within them. The code was initially set to train 1 hidden layer ANN for 1 to 101 hidden neurons with 5 neuron intervals making up 21 combinations. Following this, a 2 hidden layer ANN was trained by the software for a combination of 1 to 101 neurons in each hidden layer with again 5 neuron intervals totalling  $21 \times 21$  options being tested. This code is called the “sweep function” and aided the determination if the optimum number of hidden layers and neuron numbers within and presented in Appendix D.3. For both options the mean squared error (MSE) of the predictions are plotted in order to achieve a global optimum number of hidden layers and number neurons to be used for the prediction. Within this context, MSE is a normalized performance function for the assessment of the prediction accuracies that is calculated using the normalized deviation of the estimations. The iterations of the ANN ensure the minimization of the MSE for a certain case through the back-propagation of the error value.

The above approach has been repeated for both total noise levels and background noise levels in order to enable calculation of the Net Cavitation noise levels using Equation 22 as recommended by the ITTC and ANSI (ANSI, 2009; ITTC, 1987). Once the net noise levels are calculated the three additional parameters, namely; full-scale propeller diameter, propeller speed, and mean wake are used as input by the developed code in order to perform the extrapolation of the model test based data to the full scale using Equation 25 and Equation 26. The flow chart, which provides basis for the ANN based noise prediction tool, is given in Figure 6-44.

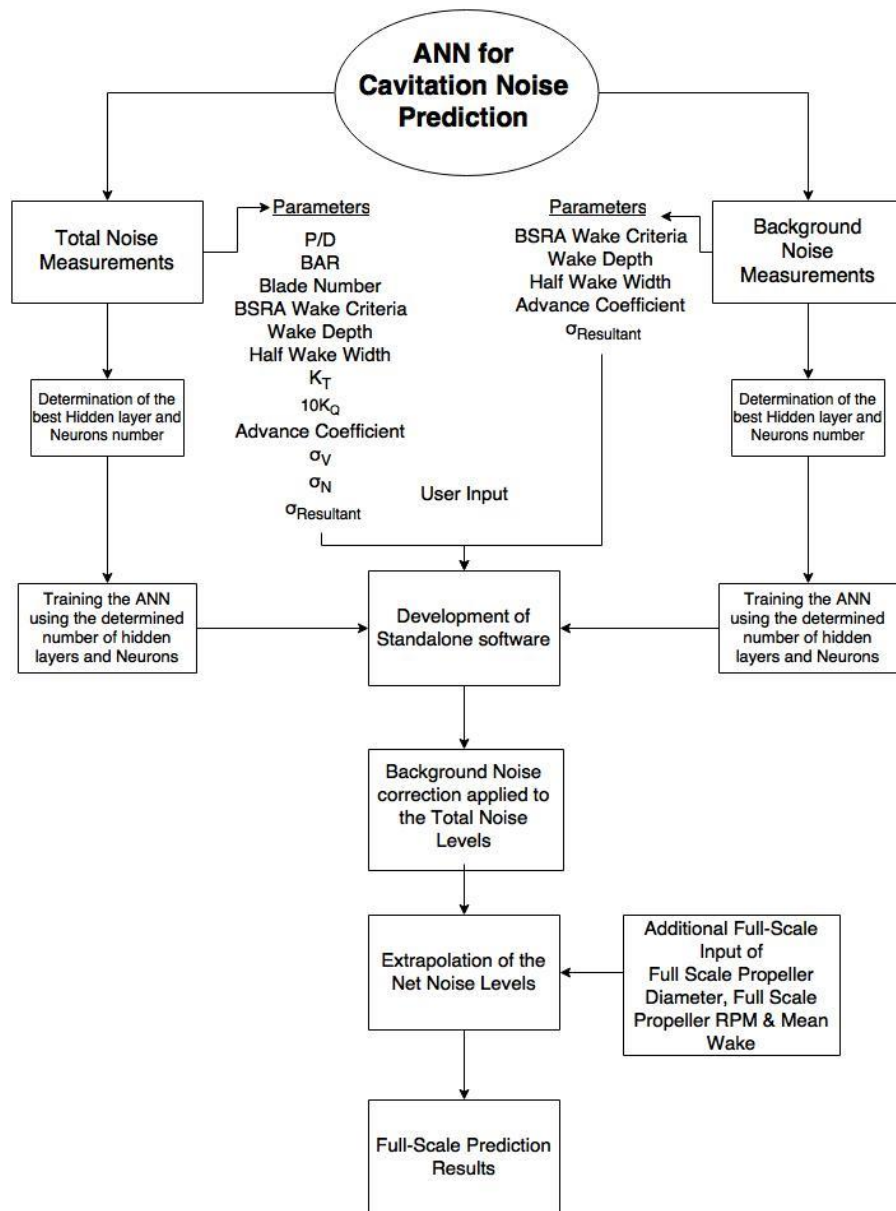


Figure 6-44 Flow chart of the prediction tool using ANN.

### 6.6.1 ANN for total noise level prediction

The above section explained the “sweep function” that used for loops to try every possible permutation for the one hidden layer and 2 hidden layer options containing up to 101 neurons, and this has initially applied to the total noise measurements to determine the global optimum prediction. Figure 6-45 and Figure 6-46 present the MSE results of the software for the two hidden layer and one hidden layer combinations.



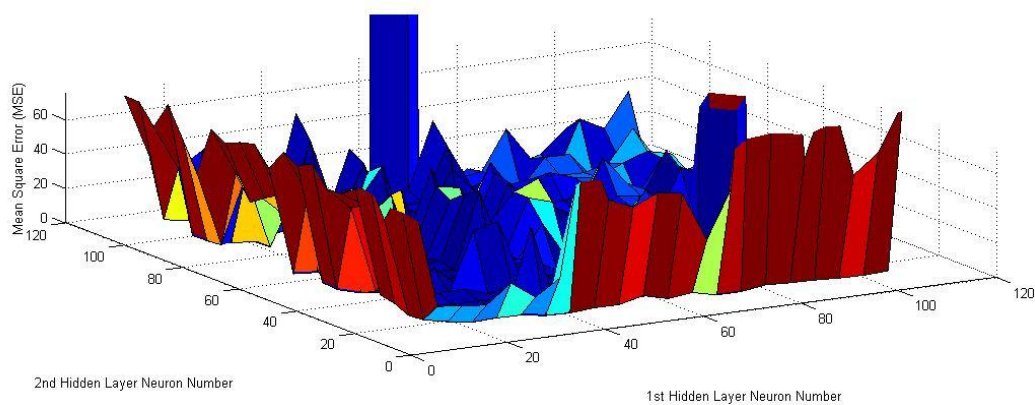


Figure 6-45 The MSE surface plot of the two hidden layer ANN for total noise levels.

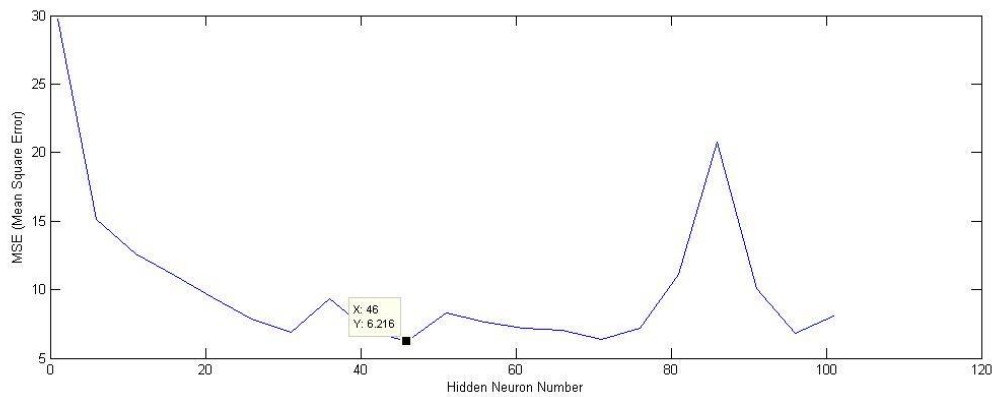


Figure 6-46 MSE plot of the one hidden layer ANN for total noise levels.

The above figures have shown that no significant improvement in terms of the prediction accuracy can be achieved in terms of the trained ANN with the use of the two hidden layers. Therefore, another sweep function has been run, training one hidden layer option with one neuron intervals from 30 to 80 neurons in order to determine the exact number of neurons that will conduct the prediction with best statistical precision. The results of the MSE of the refined sweep has shown that the best number of neurons to be used for the one hidden layer option is 46 neurons confirming the finding in Figure 6-46.

A MATLAB toolbox is then utilized to train the ANN using one hidden layer with 46 neurons inside as presented in Figure 6-47. The toolbox enables the user to retrain the network since the random initialization of the network may result in some randomness of the final trained network. The retraining has been repeated several times in order to ensure the repeatability of the statistical accuracy.

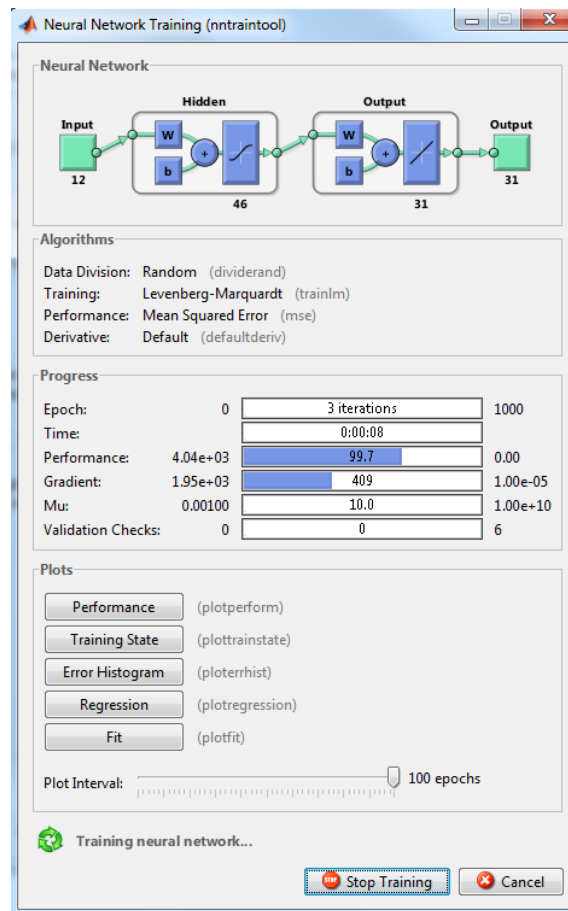


Figure 6-47. Artificial Neural Network training window of the MATLAB toolbox - Neural Network fitting with 46 hidden layer neurons for noise prediction.

Subsequent to the completion of the training various plot options are available within the MATLAB toolbox. Figure 6-48 contains plots created for the error histogram, training state, regression and performance of the trained network for the total noise level predictions. The statistical analysis of the trained networks has shown satisfactory levels of accuracy. This is clearly demonstrated by the error histogram (top left Figure 6-48) and regression analysis (bottom left Figure 6-48). Furthermore, the continuation of the iterations has not led to enhancement of the predictions as shown by performance figures as demonstrated by the figures on the right-hand side of Figure 6-48.

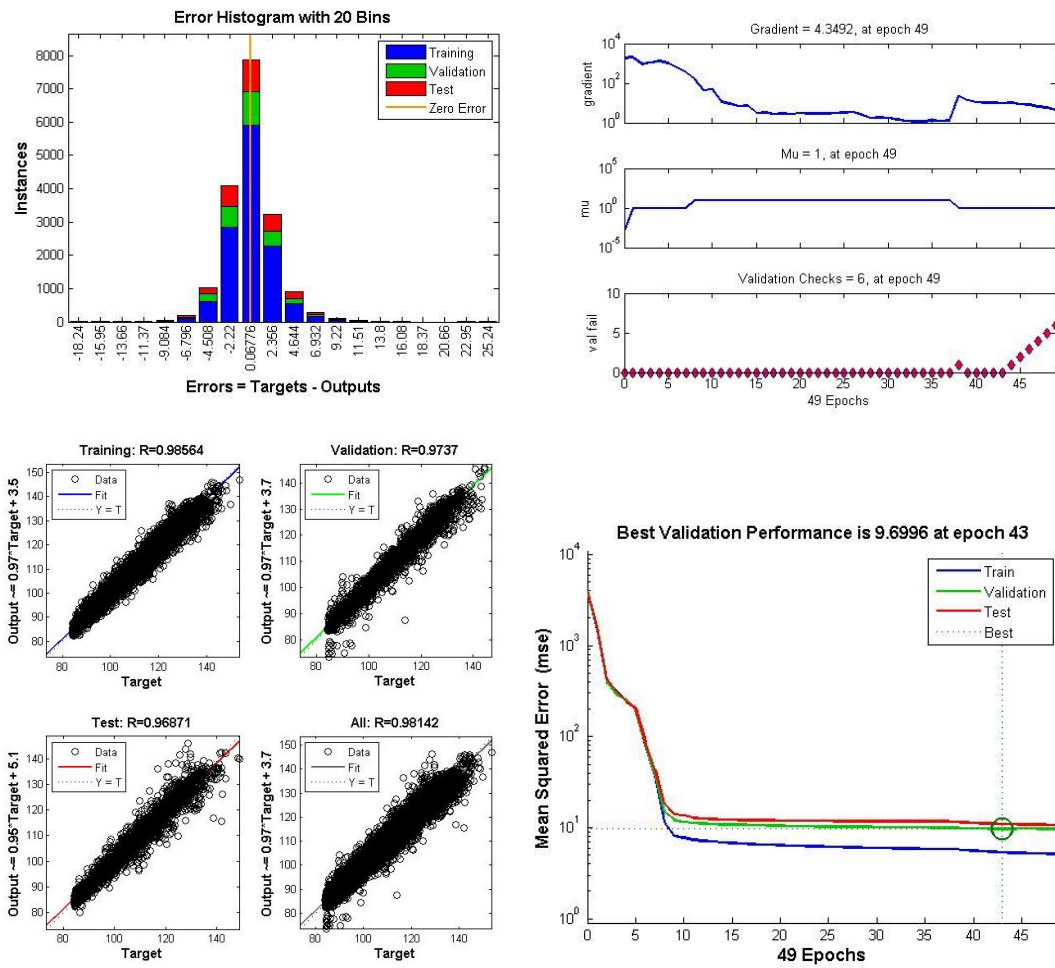


Figure 6-48 The statistical justification of the trained ANN for the prediction of total noise levels.

The trained network is then saved to be used for the prediction of the total noise levels as given by the flow chart in Figure 6-44. Thus using 12 input parameters, 31 third octave centre frequency total noise level measurements are predicted by the ANN with one hidden layer containing 46 neurons showing satisfactory statistical accuracy.

### 6.6.2 ANN for background noise level prediction

The same approach adopted for the total noise levels was repeated for the background noise levels. As stated earlier, the vital difference between the two sets of data was that not all of the 12 parameters utilized for the total noise levels were applicable to the background noise level

prediction, thus instead, 5 parameters were used as input to the ANN development for the background noise prediction. In addition to this, the level variation for the background noise was not as significant as the total noise levels and this has resulted in higher accuracy of predictions due to their easier nature for the neural network to recognize their pattern.

Following the configuration of the inputs for the background noise levels, a sweep function similar to the one used for the total noise levels was again run. Figure 6-49 and Figure 6-50 present the surface plot of the MSE for the two hidden layer and one hidden layer configuration for all possible configurations up to 101 neurons with 5 neuron intervals.

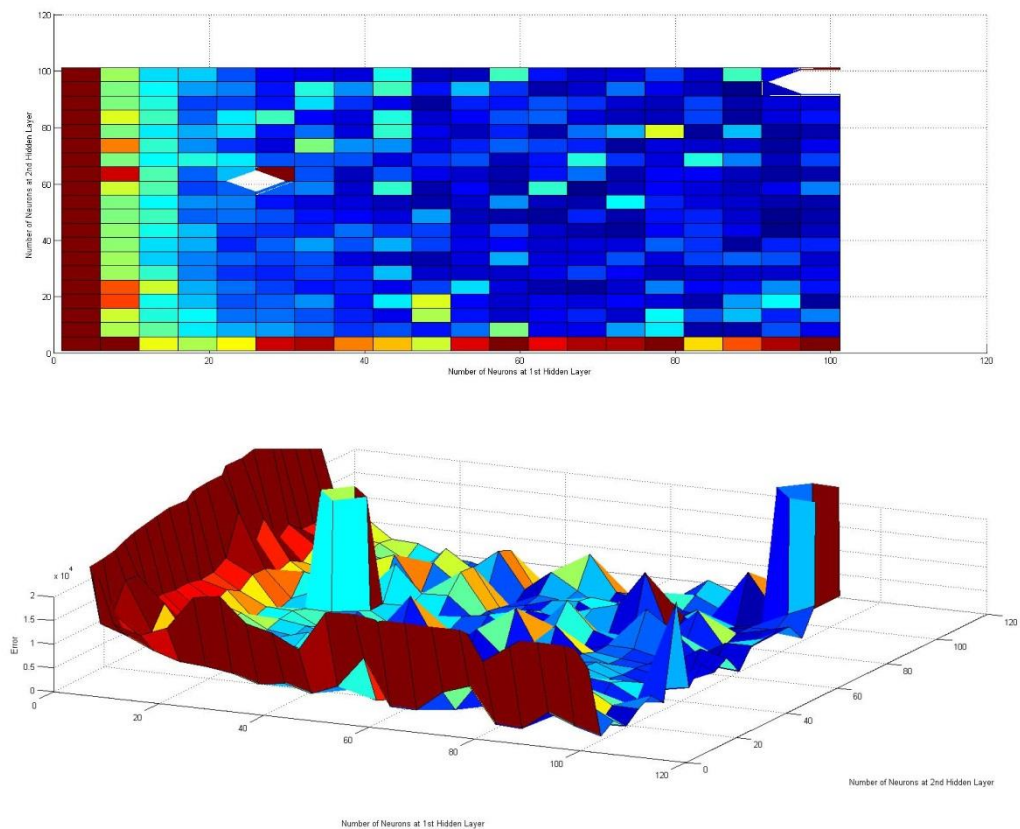


Figure 6-49 The MSE surface plot of the two hidden layer ANN for background noise levels.

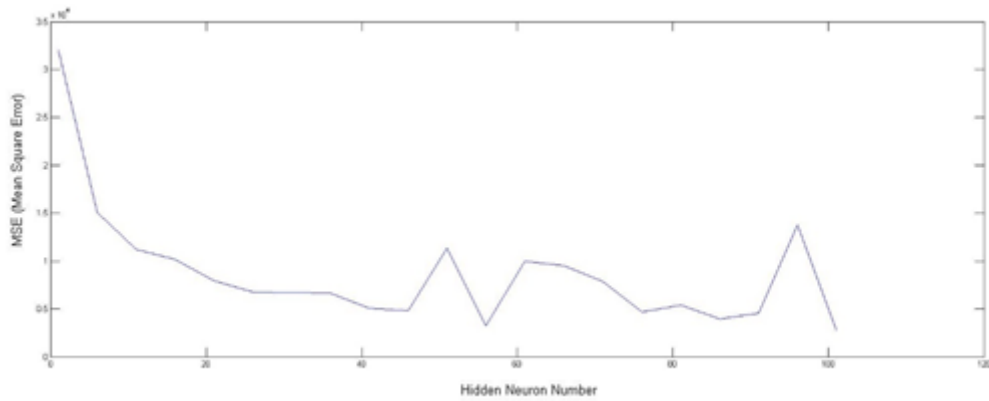


Figure 6-50 MSE plot of the one hidden layer ANN for background noise levels.

The outcome of the sweep function has again proved the two hidden layer network to be unnecessary considering the gain achieved in the prediction accuracy against the added complexity.

In light of the above conclusion, a refined sweep function has been executed for one hidden layer with 20 to 90 neurons in one neuron intervals in order to determine the exact number of neurons with the optimum accuracy. The similar approach has been followed for the background noise levels as outlined for the total noise levels prediction which resulted in the following statistical results as presented in Figure 6-51. The plots have shown good agreement with the expectations of higher statistical prediction accuracy due to the less complex nature of the target values.

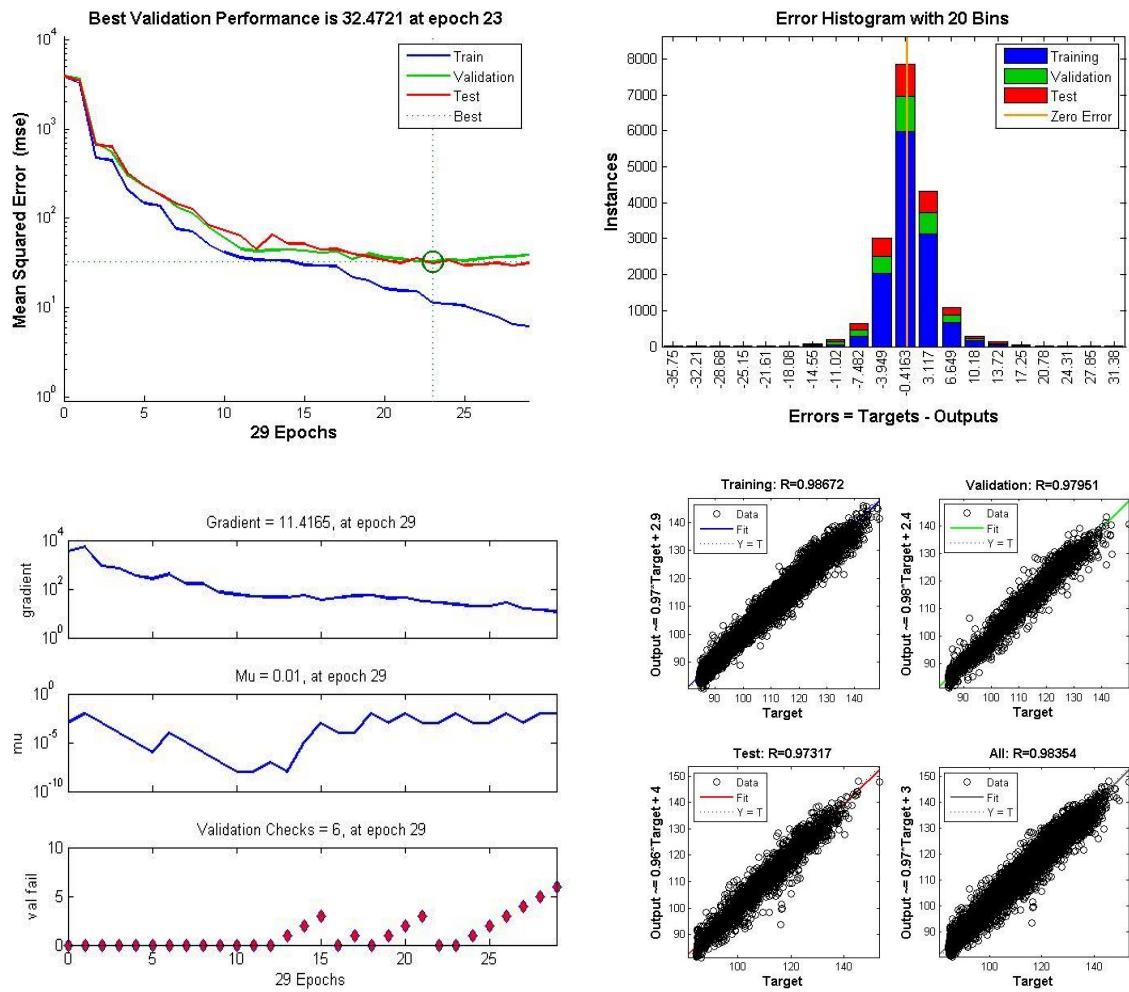


Figure 6-51 The statistical justification of the trained ANN for background noise level prediction.

Following the achievement of a satisfactory accuracy in the predictions using ANN for the background noise prediction the trained network has been saved for the development of a stand-alone executable cavitation noise prediction tool, which is described in the next section, by using the 35 neurons as they have given the best performance.

### 6.6.3 Standalone executable tool development

The trained networks for the determined optimum number of hidden layer and neurons are saved into a folder together with the graphical user interface (GUI) for the input registry. The GUI is developed again using MATLAB and prompts 15 parameters to be filled in by the user. The values are sorted to be used as input to the total noise prediction, background noise prediction and the independent values containing the full-scale propeller diameter, shaft speed, mean wake and output name as shown in Figure 6-52.

The screenshot shows a software window titled "ECT\_CAV\_NOISE" with a standard Windows title bar (minimize, maximize, close buttons). The window contains a vertical stack of input fields, each with a label and a value, and a small up/down arrow icon to the right of the value. The inputs are as follows:

Parameter	Value
P/D (Pitch to Diameter Ratio)	0.8
BAR (Blade Area Ratio)	0.65
Blade No	4
Wake Nonuniformity (BSRA Wake Criteria)	0.81
Wake depth	0.64
Wake width	95
KT (Thrust Coefficient)	0.28
10KQ (Torque Coefficient)	0.3424
J (Advance Coefficient)	0.25808
SigmaV (Free stream Cavitation Number)	38.91
SigmaN (Rotational Cavitation Number)	2.835
SigmaR (Resultant Cavitation Number)	0.285
Full Scale propeller Diameter	0.3048
Full Scale Propeller rps	29.16
Mean Wake	0.20
Output File Name	ECT_CAV_Noise Prediction.xls

At the bottom of the window are two buttons: "OK" and "Cancel".

Figure 6-52 Propeller cavitation noise prediction method user interface.



The code is then compiled using the dedicated command from the MATLAB library with the addition of the trained network files. Figure 6-53 presents the properties of the standalone executable file generated.

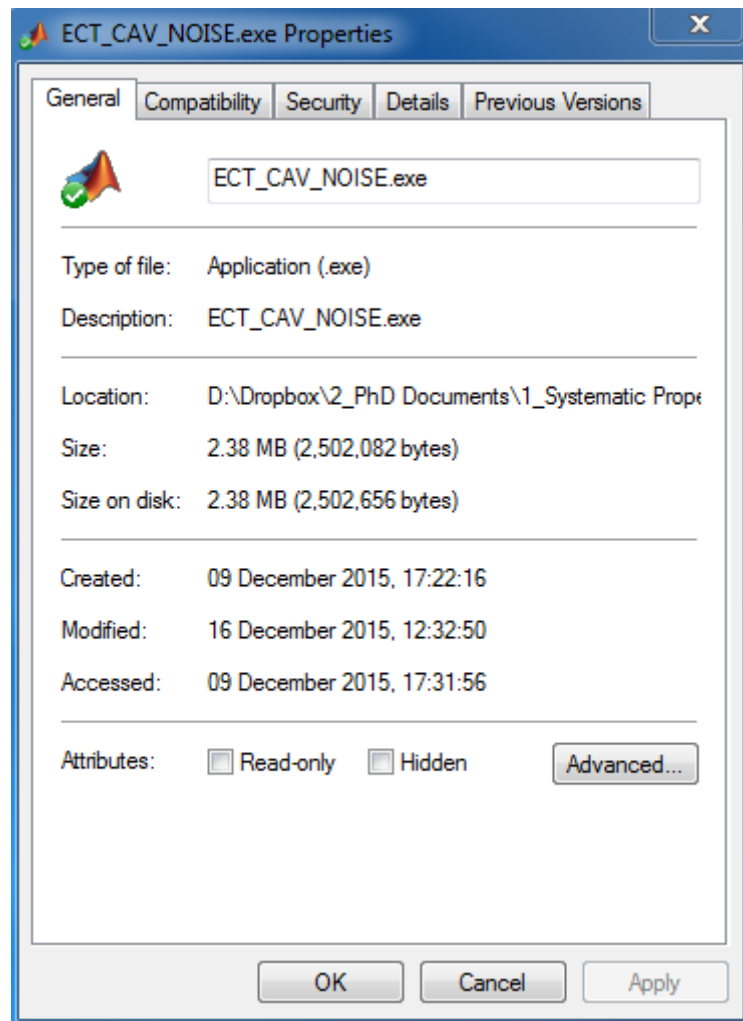


Figure 6-53 Executable cavitation noise prediction tool properties.



The resulting stand-alone cavitation noise prediction tool enables to predict the full-scale RNL of a ship using 12 non-dimensional parameters together with the full-scale propeller diameter, rotational speed and mean wake as the main input. Figure 6-55 shows a typical RNL spectrum of a ship as the main output of the cavitation noise prediction tool.

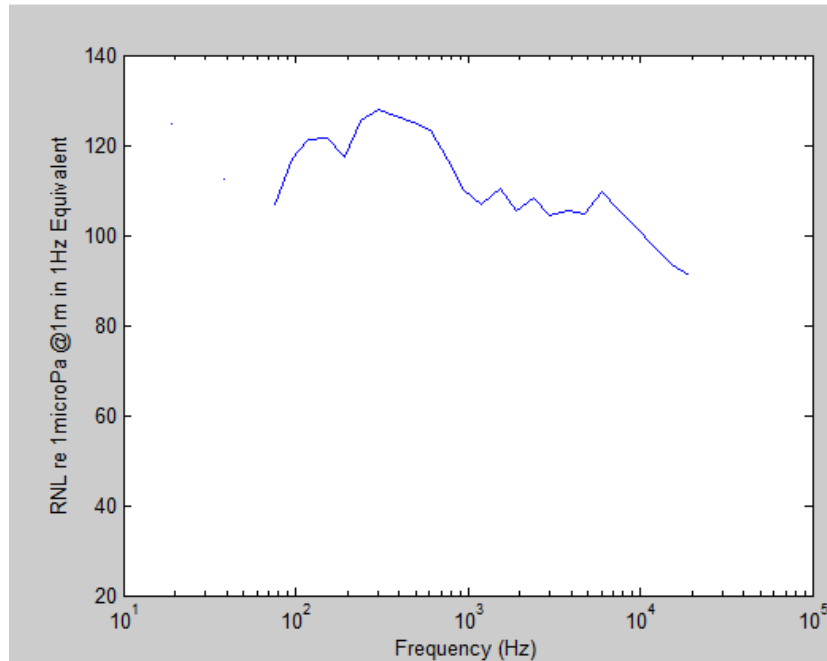


Figure 6-54 The noise prediction based on the given input data.

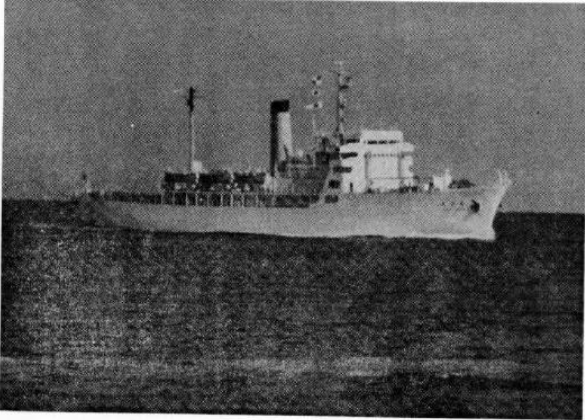
## 6.7 Validation of the developed RNL prediction method

Subsequent to the development of the RNL prediction method, it was a necessity to test and validate the end product. However, a detailed study of the publicly available literature has shown that even the benchmark cases proposed by ITTC are lacking in terms of the necessary data for the validation of the simplest noise prediction methods. Therefore, by private communications, two validation cases have been made available with satisfactory input details including the operating conditions, wake data, propeller design parameters, cavitation observations and the cavitation numbers. By all means these two test cases may not be the perfect cases due to the obvious reasons of: (i) Lack of availability of URN data; (ii) Lack of further details of the available URN data; (iii) Suitability of the available URN data in terms of the limitation of the present database. Bearing in mind these limitations the following case studies are presented.

### 6.7.1 Case Study 1: Training Ship “Sein-Maru”

The first case study involves the full-scale URN data belongs to the Japanese training ship “Sein-Maru”. The ship has been extensively tested by the Japanese research institutes and the URN data involving the full-scale trial results as well the model tests are reported in (造船研究協会, 1983). In this report, it was indicated that the initial trials conducted with “Sein-Maru’s” original conventional propeller (indicated by CP) were repeated later by the replacement of a highly skewed propeller (indicated by HSP11) to reduce the emitted noise levels. This provides the opportunity to test the prediction technique presented here on two different propellers one of which is a highly skewed. In order to run the cavitation noise prediction tool, the required input were determined by extracting and digitizing the relevant data in this report. Initially, the runs to be used for the validation cases were chosen depending on the availability of the full-scale data. The main particulars of “Sein-Maru” are given in Table 6-7.

Table 6-7 Main particulars and an image of “Sein-Maru”.

Principal Characteristics of “Sein-Maru”		
Length BP	105.00 m	
Breadth	16.00 m	
Depth	8.00 m	
Displacement	5,781.3tonnes	
$C_B$	0.576	

The axial wake data is digitized and reproduced in order to calculate various parameters necessary for the cavitation noise prediction tool as illustrated in Figure 6-55. The digitized data is then used to calculate the wake width, mean wake and wake depth.

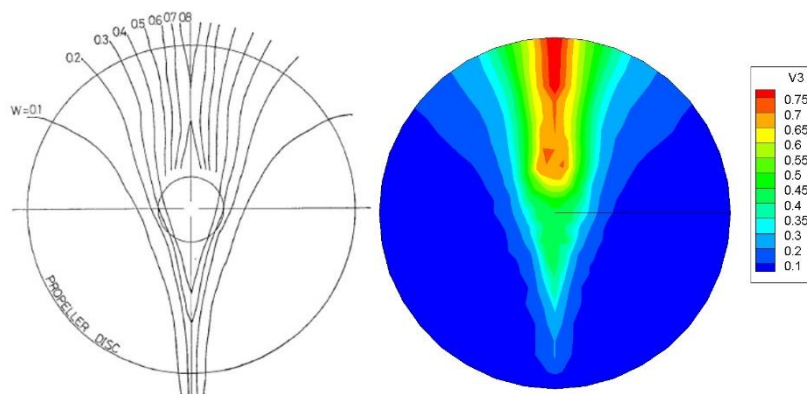
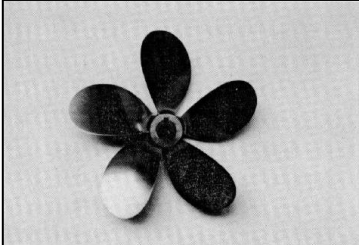
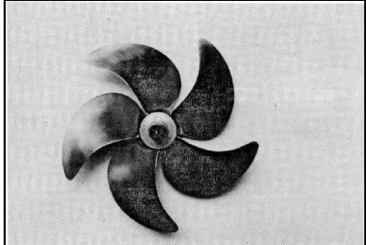


Figure 6-55 Original (left) and digitised (right) axial wake data of “Sein-Maru”.

The details of the two propellers (CP and HSPII) are then compiled as shown in Table 6-8. As it is noted in this table the highly skewed propeller has also tip off-loading feature to improve its noise emission characteristics. Whilst both propellers had a diameter of 3.6 meters the latter design has a smaller pitch to diameter ratio and higher blade area ratio than the original propeller. Finally, the blade sections of the new design are also different to the old design.

In total, more than 160 full-scale experiments were conducted during the “Sein-Maru” noise trials. Amongst these experiments the conditions that produced the URN with significant cavitation development were chosen for the validation case studies. The selected shaft speed condition was 163 RPM for both propellers. Using the experimental spreadsheet, the necessary input required by the cavitation noise prediction tool are calculated as presented in Table 6-9.

Table 6-8 Main particulars of Sein-Maru’s conventional and highly skewed propeller.

	<b>“Sein-Maru” Propeller Details</b>	
Type of the propeller	Conventional Propeller	Highly Skewed Propeller
Propeller Code	CP	HSPII (Tip offloaded)
Propeller diameter	3.6m	
Pitch to diameter ratio	0.95	0.92
Expanded blade area ratio	0.65	0.7
Number of blades	5	
Rake angle	6°	(-)3°
Skew angle (back)	10.5°	45°
Hub dia. to propeller dia. ratio	0.1972	
Blade Section	MAU	Modified SRI-B
Material	Ni-Al-Br	
Model Propeller Image		

The decision on the chosen full-scale condition was based on the requirement to detect an appreciable difference in the URN levels that may be present between the two propellers of “Sein-Maru”. Thus, the original measurement of the URN data provided in Figure 6-56 has been found satisfactory with respect to the SPL differences between the measurements with the two propellers over a discrete frequency band region of 10-100 Hz. Of course the ideal scenario would be to detect the noise difference also in the broadband frequency region, but unfortunately, such scenario was not possible to be located.

Table 6-9 The input table for ECT\_CAV\_NOISE cavitation noise prediction tool for “Sein-Marū”.

ECT_CAV_NOISE Input Table		
	Highly Skewed Propeller	Conventional Propeller
	Exp. 158	Exp. 7
P/D	0.92	0.95
BAR	0.7	0.65
Blade Number	5	
BSRA wake non-uniformity	0.805	
wake depth	0.670	
wake width	75	
$K_T$	0.205	0.259
$10K_Q$	0.315	0.353
J	0.700	0.678
$\sigma_V$	5.81	6.19
$\sigma_N$	2.847	2.847
$\sigma_R$	0.227	0.227
Full-Scale Diameter (m)	3.6	
Full Scale (rps)	2.72	2.72
Full Scale (RPM)	163	163
Mean Wake	0.24	
Brake Horse Power (BHP)	3300	3700
Power (W)	2460810	2759090
Thrust (tonnes)	26.5	33.5
Thrust (N)	259876	328523
Torque (Nm)	144166	161640
Ship Speed (Kn)	16	15.5
Ship Speed (m/s)	8.23	7.97

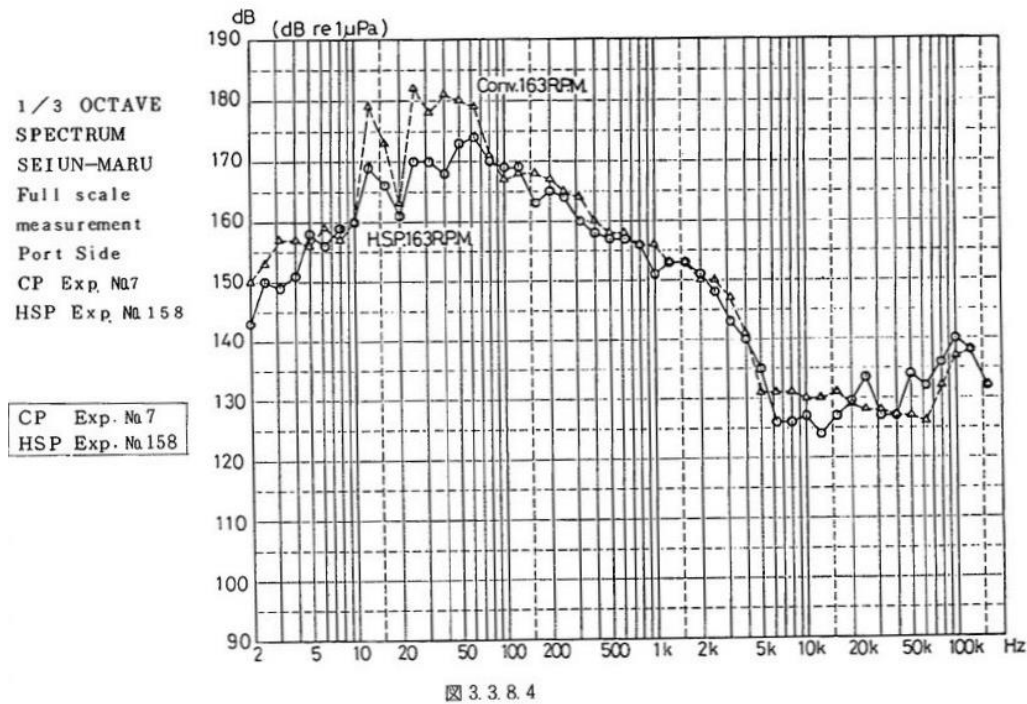


Figure 6-56 Full-scale measurements of the “Sein-Maru” HSPII and CP propeller at 163 RPM.

The full-scale URN data of “Sein-Maru”, which is shown in Figure 6-56, has been digitized to be used for the comparison purposes in order to validate the cavitation noise prediction tool, “ECT\_CAV\_NOISE”, developed in this study. The comparative data of Figure 6-57 indicates that the highly skewed propeller (HSPII) emits lower levels of noise over a discrete frequency range of 10 to 100 Hz in comparison to the conventional propeller (CP). The reasons for this difference can only be interpreted in a structured way supported by the cavitation observations. The full-scale noise measurements, therefore, were accompanied by the cavitation observations made through the hull of the “Sein-Maru”. Figure 6-57 presents the cavitation sketches drawn based on the cavitation observation recordings to provide further insight into the cavitation dynamics and to help the interpretation of the URN measurements to support the predictions.

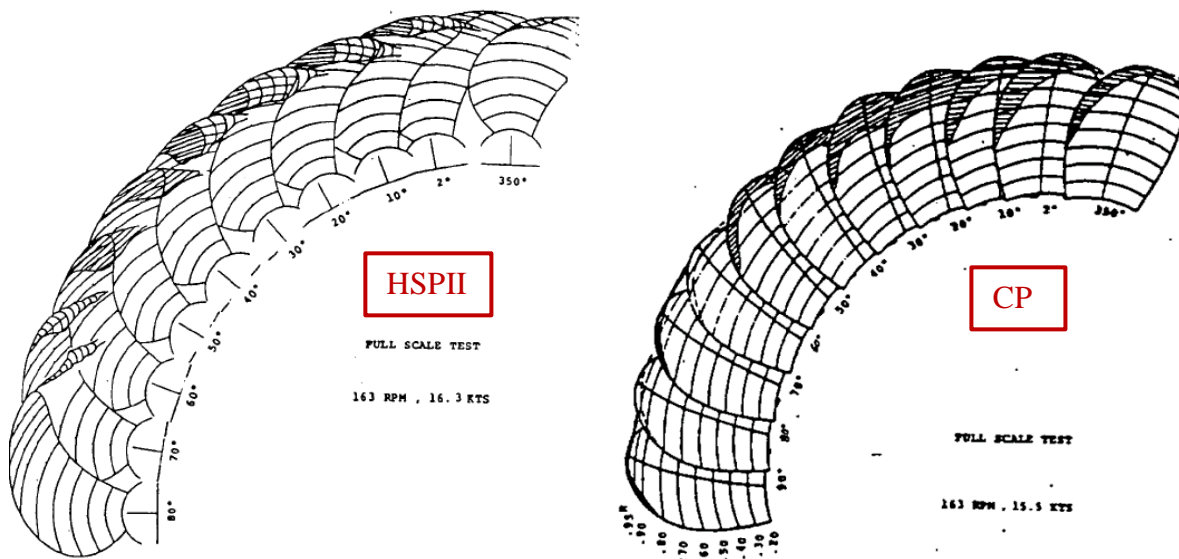


Figure 6-57 Full-scale cavitation sketches of the “Sein-Maru” HSPII and CP propeller at 163 RPM.

Figure 6-57 provides the comparison of the cavitation observations for each propeller over the top dead centre (TDC) of the propeller’s rotation plane. The sketches are provided from 350°, which is just before the TDC, up to 90° by every 10° interval. The importance of such sketches is to demonstrate the cavitation extent variation over the wake shadow where most severe cavitation volume variations are experienced. The cavitation volume variations are utmost importance as they are the main parameter used for the calculation of cavitation volume acceleration that is defined to be the dominant parameter for the cavitation induced noise. Figure 6-57, in this respect, presents the HSPII on the left-hand side of the figure showing leading edge sheet cavitation before the TDC, which then curls into a tip vortex. As the propeller continues to its rotation, the extent of the sheet cavitation increases. This consequently also results in an increase in the TVC diameter. The cavitation volume reaches its maximum at 30° after which it starts to be reduced. As shown on the right of Figure 6-58, the CP propeller, on the other hand, presents a rather large area of sheet cavitation starting from 0.5 r/R at 350°. With the rotation of the propeller, the sheet cavitation extent significantly increases and starts to cover the complete area in the tip region higher than 0.9 r/R at 30°. After this point, the propeller experiences a swift reduction in the cavitation volume with only a very weak tip vortex presence at 90°. The relatively more rapid reduction of a rather large extent of sheet cavitation of the CP propeller does reveal itself to be the reason behind the relatively high level of RNLs experienced by this propeller in comparison to the HSPII.

In the light of the above information on the full-scale cavitation observations and URN measurements, the ECT\_CAV\_NOISE predictions are compared with the full-scale URN data for the chosen condition for both HSPII and CP propeller and results are shown in Figure 6-59 and 6-58, respectively.

At a first glance, the comparison of the predicted RNLs with the full-scale measurements displays encouraging signs for the capabilities of the developed cavitation noise prediction tool. The magnitudes of the predicted RNLs of both propellers seem to be around the similar ballpark with those of the measured RNLs over the range of frequencies predicted. There are reasonably clear correlations for the prediction of the 1<sup>st</sup> blade rate effects for both propellers. Furthermore, although the developed prediction method does not include any input parameter directly related to neither skew nor the blade section details, the indirect relation and hence reflection of these parameters on the user input, such as the P/D ratio and BAR, and the propeller performance coefficient has been observed to be represented in the comparative RNLs. For example, the predicted RNL for the CP and HSPII does show reduced URN levels for the HSPII compared to the CP as expected and measured in the full-scale measurements.

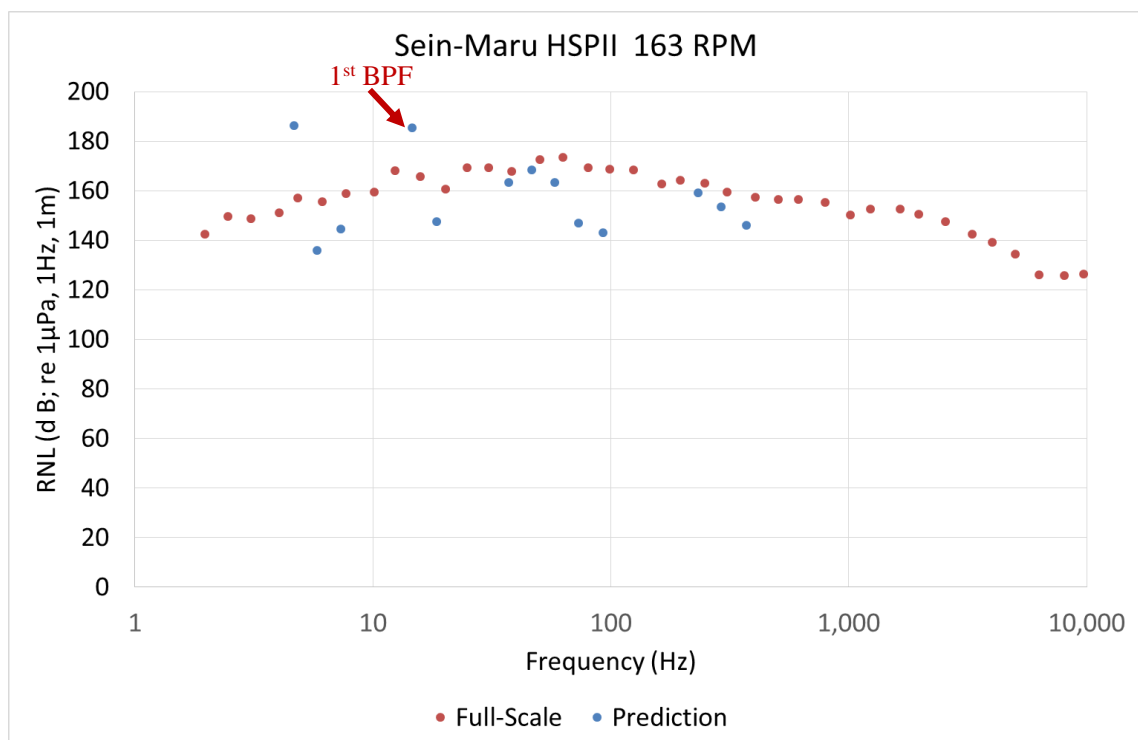


Figure 6-58 Comparison of the Full-scale and ECT\_CAV\_NOISE predictions of the “Sein-Maru” HSPII at 163 RPM.



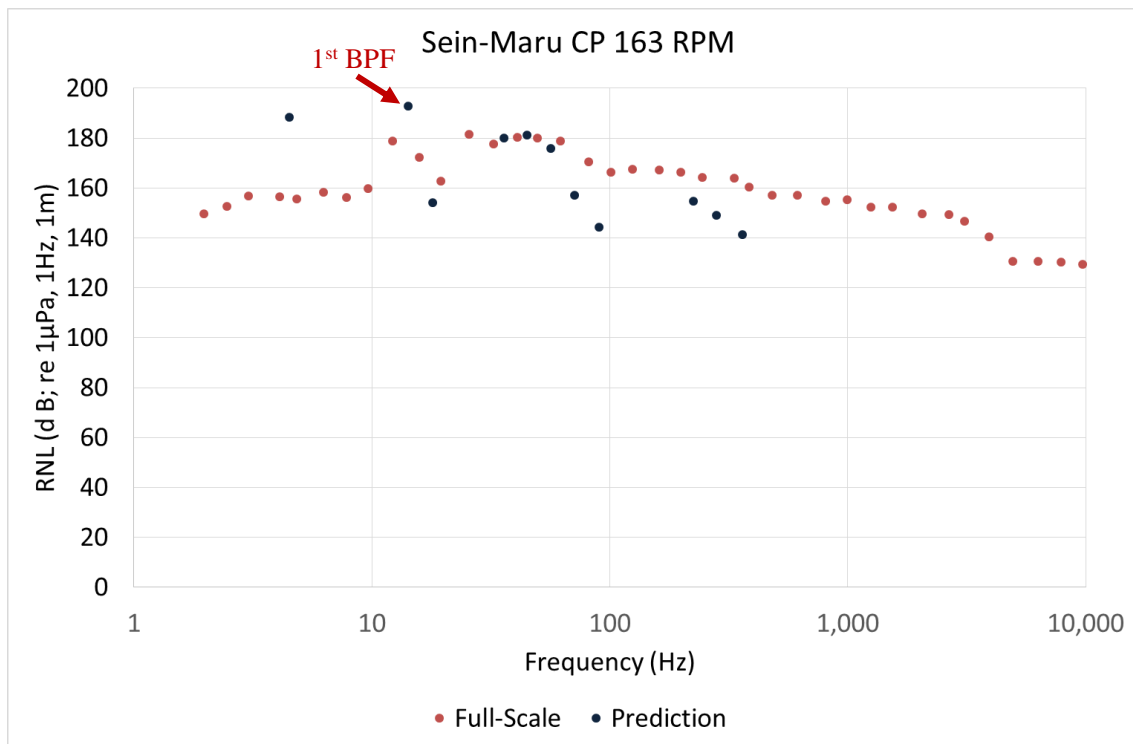



Figure 6-59 Comparison of the Full-scale and ECT\_CAV\_NOISE predictions of the “Sein-Maruru” CP propeller at 163 RPM.

### 6.7.2 Case Study 2: “Merchant Tanker (M/T) Olympus”

The second validation case study has been conducted for Merchant Tanker “M/T Olympus” which is an oil and chemical tanker constructed in 2006. The vessel has formed basis to provide benchmark URN data for the R&D activities of the collaborative EU-FP7 project AQUO (Achieving Quieter Oceans) through the full-scale trials and extensive model testing focusing on the cavitation noise (AQUO, 2012)(Tani et al., 2016). “M/T Olympus” is a 116 m long and 18 m wide vessel with a deadweight of 1989 tonnes. The main particulars of this ship are listed in Table 6-10.

Table 6-10 Main particulars and an image of “M/T Olympus”.

Principal Characteristics of “M/T Olympus”		
Length BP	116.90 m	
Breadth	18.00 m	
Depth	8.12m	
Deadweight	1989 tonnes	
$C_B$	0.7565	

The wake data is digitized and reproduced in order to be able to calculate various parameters necessary for the cavitation noise prediction tool as illustrated in Figure 6-60. The acquired wake data is then used to calculate the wake width, wake depth and mean wake.

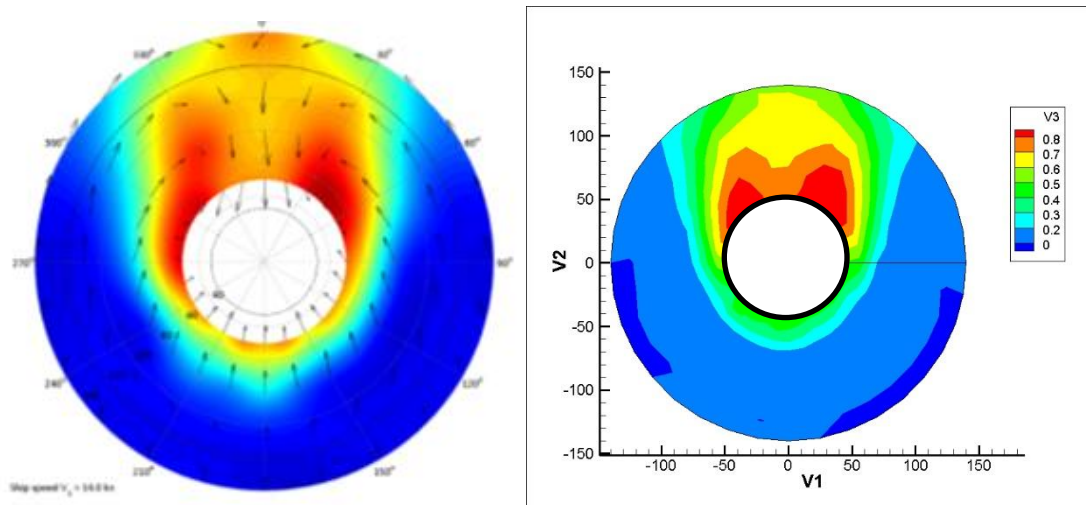


Figure 6-60 Original and digitized wake data of “M/T Olympus”.

The vessel is propelled by a four-bladed and 4.8 m diameter Controllable Pitch Propeller (CPP) with an expanded BAR of 0.45 and design pitch of 0.87 at 0.7 radii. As a result of being a CPP, the hub to diameter ratio of this propeller is relatively large being 0.287. The main particulars of the propeller are listed in Table 6-11.

Table 6-11 “M/T Olympus” Propeller details.

	<b>“M/T Olympus” Propeller Details</b>
Type of the propeller	Controllable Pitch Propeller
Propeller Code	P2772
Propeller diameter	4.8 m
Design P/D ratio at 0.7 r/R	0.87
Expanded blade area ratio	0.45
Number of blades	4
Hub dia. To propeller dia. Ratio	0.287

The full-scale noise trial data sheets and model scale test results of “M/T Olympus” are utilized to establish the input matrix of the cavitation noise prediction tool. Two full-scale trial runs, which corresponded to two different P/D ratios and coded as LC1 and LC5, are used for the validation case studies as specified in Table 6-12. As one may note while the LC1 condition is very close to the design pitch setting of the propeller LC5 condition is an off-design pitch setting which is interesting to explore.

Table 6-12 Input table for ECT\_CAV\_NOISE for “M/T Olympus”.

ECT_CAV_NOISE Input Table		
	LC1	LC5
P/D	0.857	0.56
BAR	0.45	0.45
Blade Number	4	
BSRA wake non-uniformity	1.05	
wake depth	0.73	
wake width	105	
$K_T$	0.204	0.259
$10K_Q$	0.300	0.353
J	0.543	0.678
$\sigma_V$	11.91	6.19
$\sigma_N$	3.52	2.847
$\sigma_R$	0.33	0.227
Full-Scale Diameter (m)	4.8	
Full Scale (rps)	1.952	2.72
Mean Wake	0.299	
Ship Speed (Kn)	14.13	11

The cavitation tunnel tests of the two full-scale conditions were reproduced and cavitation observations were made as part of the AQUO project activities. In these observations, as shown in Figure 6-61, condition LC1 presents a combination of a sheet cavitation and TVC through the wake shadow. The cavitation volume diminishes as the propeller gradually moves out of the wake shadow area. In LC5 condition TVC appears to be the dominant feature as it is commonly observed at the off-design pitch setting of many CPP's.

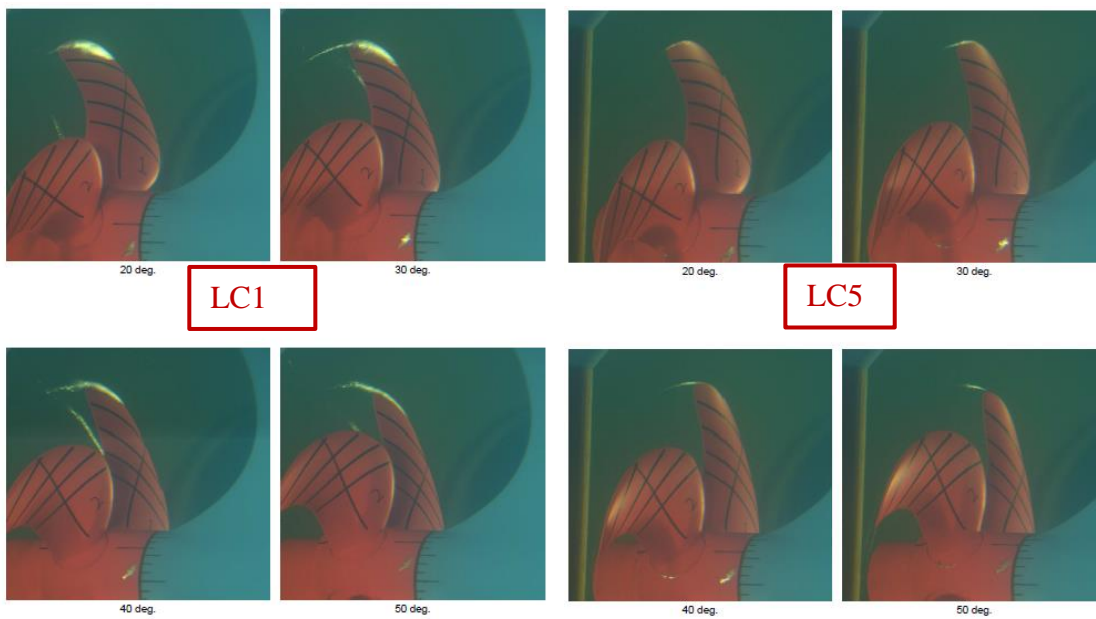


Figure 6-61 Full-scale cavitation observations from model test of the “M/T Olympus” for trial condition LC1 and LC5.

Based on the above-described two operating conditions the RNL predictions for “M/T Olympus” are made and results are compared with the full-scale RNL data as shown in Figure 6-62 and Figure 6-63 for operating condition of LC1 and LC5, respectively.

As stated earlier, there are considerable numbers of design feature differences between the propeller of “M/T Olympus” and those of the members of the Meridian series which formed the basis for the prediction methodology. Perhaps the most importantly the target propeller is a CPP while the prediction basis is a fixed pitch one. On this basis, it will be too plausible to expect any respectable correlation between the predictions and measured RNLs. Having said that the similar range of P/D, BAR, number of blades and operational conditions over which the predictions are made, should reveal some correlations although there is no guarantee on the similarity of the cavitation features and in particular its dynamics. However, as it is gathered from the cavitation observations of the “M/T Olympus” propeller and members of the series propellers the most dominant cavitation pattern are the back sheet and tip vortex cavitation for both propellers although their dynamics can be vastly different. Based on these facts, as shown in Figure 6-62 and Figure 6-63, there seems to be some correlation for the RNLs at a level of order

without any meaningful trend for the BPFs, etc. This correlation is even poorer for the off-design pitch setting (LC5). The performance deterioration for this off-design condition may be attributed to the considerably different functioning of the propeller with pressure side cavitation presence, which is not observed during any of the Meridian standard series propeller tests. Perhaps one would hope to capture the tonal (BPF) effects of the noise spectra that seem to be not so clear in the full-scale measurements, possibly due to the propagation losses, while the predictions indicate strong BPF effects. It is appreciated that the nature of the URN spectra for CPPs can be significantly different to the fixed pitch propellers' as claimed by many investigators (e.g. Berghault (2000)).

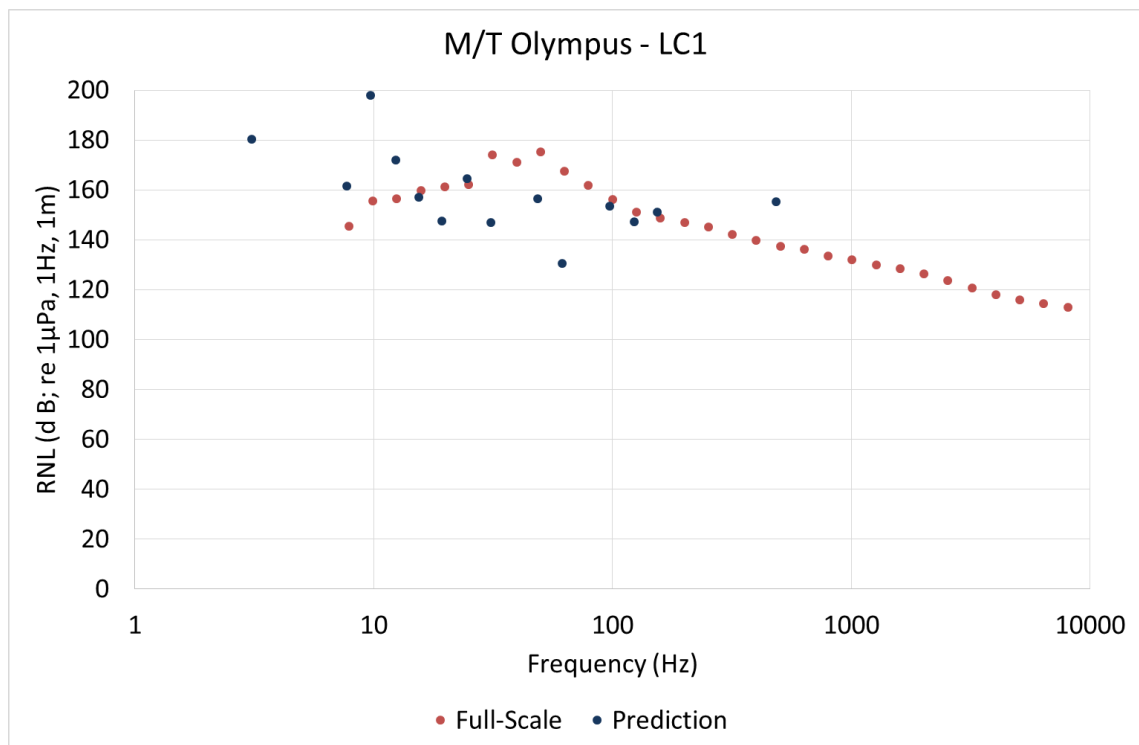


Figure 6-62 Comparison of full-scale RNLs with the predictions from ECT\_CAV\_NOISE cavitation noise prediction tool for “M/T Olympus” for trial condition LC1 (design pitch setting).

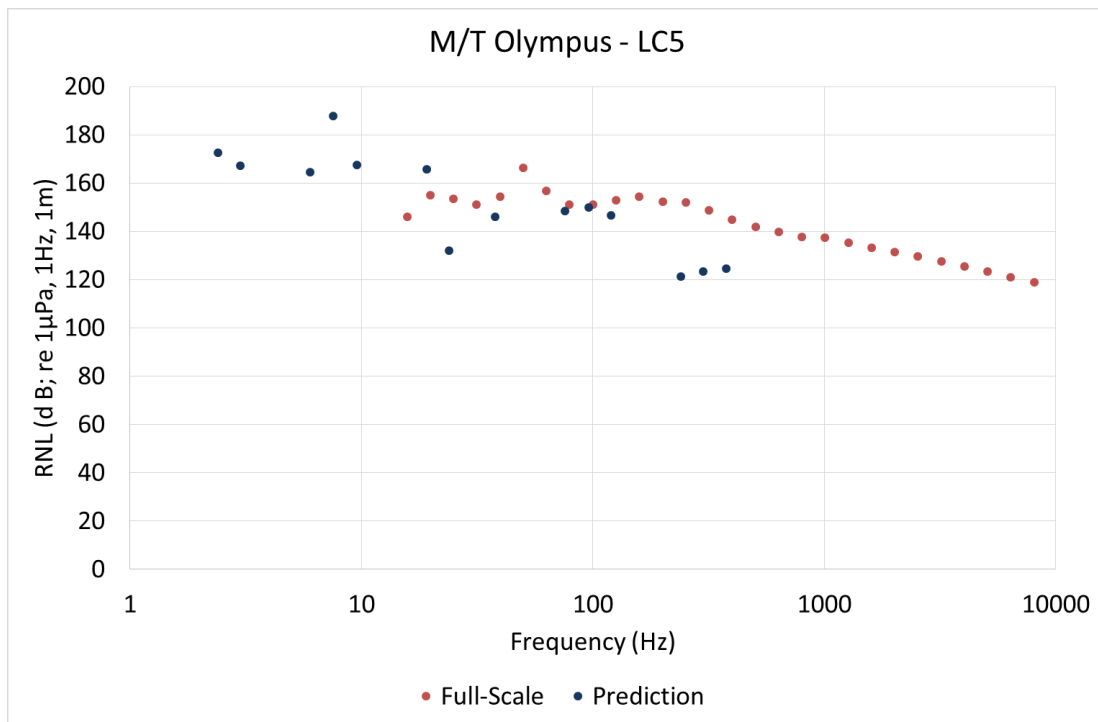


Figure 6-63 Comparison of full-scale RNLs with the predictions from ECT\_CAV\_NOISE cavitation noise prediction tool for “M/T Olympus” for trial condition LC5 (off-design pitch setting).

### 6.7.3 Further remarks on validation case studies

Overall, a first-time validation case has been set up to test the capabilities of the proposed methodology based on the systematic propeller series approach and associated cavitation noise prediction tool. In order to establish an effective validation campaign, publicly available full-scale URN data are tried to be located for typical commercial vessels. As it is highlighted in the literature review chapter and other parts of the thesis, there is still no comprehensive full-scale URN data that is representative of today’s oceangoing vessels although there is URN data from fisheries research vessels with reasonable input details.

In the absence of relevant data for the proposed approach, two validation case studies have been conducted even though they were not the ideal cases for the proposed cavitation noise prediction method. Based on the 1<sup>st</sup> validation case study with the conventional propeller (CP) of the “Sein-Marū” data has presented reasonable confidence in the predictions, the differences in the trend of the RNLs for the highly skewed propeller (HSPII) can be attributed to the skew and tip-loading features of the latter propeller. In addition relatively low block coefficient of the vessel and hence favourable wake characteristics may be another contributing factor. Such low block coefficients may be observed at some container ship designs. But, they travel at much higher speed, displaying more severe cavitation which could have been ideal to test the proposed method as the main strength of the procedure is to predict the cavitation induced noise for commercial vessel propellers.

The second validation case study, on the other hand, involved a relatively new built commercial tanker but employing a CPP, which can have inherently different noise spectra characteristics compared to a conventional fixed pitch propeller as reported e.g. by Berghault, (2000). Moreover, the predictions at the off-design conditions are even harder due to the effect of pitch on the propeller performance coefficients. Moreover, the pitch setting at this exact condition (LC5) corresponds to a value ( $P/D=0.56$ ) that is out of the region of the main experimental database (min  $P/D$  tested 0.6).

Nevertheless, besides the imperfections of the validation cases, the predictions achieved showed extremely encouraging resemblance to the full-scale noise spectra. A comparable ballpark prediction of the spectral levels for all cases are obtained by using only 15 input data and without all the cumbersome preparations for a cavitation tunnel test. The deviations in the low-frequency range were observed due to the capability of the proposed approach to predict the blade rate contributions while such tonal contributions are not present due to the propagation losses and third-octave filtering. The predicted results around the 100 Hz region have shown encouraging similarity for all cases while the predictions beyond this threshold frequency region have underestimated the measured levels in general which may be attributed to the acoustics transfer function of the tunnel.



## 6.8 Conclusions

Chapter 6 presented an experimental approach to the cavitation noise predictions of commercial vessels in full-scale by using a subset of a standard propeller series and adopting a systematic testing method. The proposed approach has been validated using full-scale case studies and results are discussed. The systematic test data for the URN, fluctuating pressures and cavitation observations have been analysed jointly for further understanding of the URN phenomenon in terms of the cavitation dynamics as well as exploring the effects of some of the important design parameters and operating conditions on URN.

Within the above framework, a small subset of the Meridian standard propeller series was chosen for the adopted approach. Three systematically varied axial-wake inflow configurations were developed based on the BSRA wake criteria and initial experiments were conducted with 3-propellers of commercially representative small subset of the Meridian series. The experimental RNLs were extrapolated to the full-scale using real oceangoing powering data for representative vessels. This was to compare the extrapolated RNLs with publicly available average shipping RNLs to justify the feasibility of the proposed approach.

With the confidence gained from the small subset of the database, an extended 6-propeller subset of the same propeller series was tested in a systematic manner including 576 unique operating points simulated in the Emerson Cavitation Tunnel using the same wake set-up. The produced systematic data was then compiled into a database to be fed into an ANN tool in terms of the total and background URN to extract then the net propeller URN. The ANN predictions of the net propeller noise levels were then extrapolated to the full scale using the full-scale propeller diameter, shaft speed and mean wake by the ANN based cavitation noise prediction tool implemented. The developed tool was then validated against two full-scale test cases.

The two test cases, which involved a 105m training ship “Sein-Marū” and 117m oil tanker “M/T Olympus”, were not the ideal cases for the validation of the proposed method but were the best due to the lack of publically available full-scale URN data. The validation studies indicated that the proposed approach can provide ball-park correlations with the RNLs of the full-scale data for the training ship in particular with its conventional propeller compared to the RNLs with her highly skewed propeller. The predictions over the tonal frequency range were particularly encouraging picking up the BRF effects as well as differentiating the favourable effect of the skew and tip-unloading of the latter propeller. The correlations for the tanker data was relatively less due to the CPP of this vessel although the RNLs were still at similar levels.

In this chapter also an advanced post-processing tool has been implemented in order to demonstrate the influences of a number of major design parameters on the RNLs as well as exploring the effect of cavitation dynamics on URN. The implementation of this tool involved the combined analysis of the hydrophone based frequency domain RNLs, synchronized time-domain pressure measurements and high-speed cavitation observations using a JTFA software in order to reveal the frequency ranges to which certain cavitation phenomenon contribute into.

The post-processing tool clearly indicated that cavitation is the dominating noise source following its inception. The wake non-uniformity is the vital parameter to consider for the standard series propeller noise tests since the cavitation dynamics experienced due to the flow irregularity is one of the main sources of the emanated noise levels. Moreover, the cavitation type experienced by any propeller is highly influential over the emanated noise levels as well as the frequency region for which particular type of cavitation contributes into. These effects can be analysed effectively by the implemented tool.

## Chapter 7 Conclusions and Recommendations

### 7.1 Introduction

*Key findings of the thesis and recommendations for further work are provided in this chapter together with an overall summary of the research conducted in this research study. A philosophical review of the research is presented in conjunction with a brief overview of the conducted study. The main conclusions drawn from this research are stated and an evaluation of the accomplished objectives leading to the achievement of the set aim is revisited. Contributions to the state of the art are highlighted together with novelties within the conducted research. Finally, recommendations are given for future research.*

### 7.2 Philosophical review of the thesis

The motivation of the study conducted in this thesis is originated from the Author's passion for undertaking on-board and laboratory-based experimental hydrodynamics. A further incentive to pursue underwater radiated noise as a subject was due to the increased global concern on the URN pollution and timely opportunity of EU-FP7 SONIC project. SONIC was a European collaborative project formed by a consortium of the major European testing facilities and maritime technology companies. The project was initiated to address the calls made by the IMO and MEPC (IMO, 2013, 2011) regarding the impacts of anthropologic activities on current levels of ambient underwater noise. The research conducted for this thesis took place in conjunction with SONIC project activities and used Newcastle University facilities such as their research vessel "The Princess Royal" and the Emerson Cavitation Tunnel. The ample amount of resources and capabilities provided the perfect environment to undertake an experimental approach utilizing both full scale and model test capabilities. Furthermore, the expertise and know-how on the subject from the members of the Emerson Cavitation Tunnel in combination with the strong heritage on the subject was another incentive to take on this challenge.

This thesis builds on more than a half-century of accumulated knowledge on the propeller design. The Emerson Cavitation Tunnel (ECT) has served the maritime industry especially in the development of standard propeller series data. Thus, research made for this thesis has exploited the available standard propeller model series existing within the facility. The experimental approach that is adopted by this study has brought the series up to date by introducing high-speed video, pressure pulse and noise measurement to the existing series performance data. Moreover, the experiments were not only conducted in the traditional open water condition, but also behind systematically varied wake inflow conditions. Such tests constitute the unique novelty of this research. However, the necessary experience to conduct and analyse the tests was achieved through several other experimental campaigns.

The experiments were designed to provide a holistic approach to experimental cavitation noise prediction. Within this framework, a series of tests with a propeller model in oblique inflow conditions provided a simple propeller noise scenario where the emitted noise levels changed due to the systematically varied inclination angles in uniform flow. In the absence of the wake inflow, the influence of shaft inclination was implemented and varied systematically, providing invaluable and comprehensive data. Following this, full-scale trials conditions for “The Princess Royal”, conducted under the SONIC project, were replicated in the ECT with the use of a ‘dummy model’. This provided an opportunity to observe the nature of unstable cavitation experienced by the model propeller, operating in a 3-dimensional, non-uniform inflow due to the presence of the model hull in front.

Within the above framework, this thesis set out to develop a propeller noise prediction tool for use in an early design stage, based on unique enhanced experimental tests with a standard propeller series tests. The tests demonstrate a novel approach to propeller noise prediction based on the standard propeller series. Furthermore, attention has been given to advance analysis methodology for the cavitation noise and in-depth understanding of the influence of propeller design parameters. Moreover, during the course of the research, the experiments provided a public body of scarce URN data which may freely be used in the development and validation of more advanced computational tools.

Thus, the main goal of the present research is to enhance the understanding of the propeller cavitation noise by conducting detailed systematic cavitation tunnel tests in order to investigate the main propeller design parameters and operating conditions and to scrutinize their impact on propeller Radiated Noise Levels (RNL). The resulting experimental data are also utilized to compile a database that enables engineering noise prediction methods to be developed and used at a preliminary design stage, together with a standard series approach.

The above stated main goal of the research was achieved by the accomplishment of a number of set objectives. Each chapter of the thesis serves to justify and contribute to at least one objective. The objectives determined in the introduction chapter are restated briefly for the reference.

1. To perform a critical review of the literature on propeller cavitation noise.
2. To design and conduct systematic cavitation tunnel tests with a particular focus on the effect of shaft inclination non-uniformity on the RNL of a model propeller.
3. To perform full-scale trials on-board a research vessel to enhance understanding of the noise source phenomena by making cavitation observations URN measurements and propeller-induced pressure pulse measurements
4. To provide dedicated propeller cavitation noise data in model and full-scale to be able to evaluate experimental methods to predict full-scale noise data using medium-size cavitation tunnels.
5. To execute preliminary tests using a commercially representative small subset of the standard propeller series cavitation tests using different grades of wakes and with loading conditions based on real oceangoing commercial vessel sea trial data.
6. To conduct systematic cavitation tunnel tests with a larger subset of standard series to establish the standard series approach and associated tool to predict the cavitation induced URN and to validate the capability of the developed tool.
7. To implement an advanced data analysis tool by making use of the synchronized pressure pulses, cavitation images and URN data. Using this tool and the systematic data produced with the series members investigate the effects of some major propeller design and operational parameters on the URN as well as the effect of cavitation dynamics.

Following the restatement of the objectives, review of the chapters of this thesis are provided together with the objective they serve:

Chapter 2, performed a critical review of the literature on propeller cavitation noise. The state of the art revealed that whilst the propeller noise prediction by using computational methods carries great potential, the current status is not satisfactory. In addition to that, it has been identified that the open literature is lacking in the details of experimental data from both full-scale and model scale experiments. Thus, while complementing the 1<sup>st</sup> objective, the identified data gaps provide justification of the adopted approach for this research.

Chapter 3 presents a detailed review of the experimental facilities, equipment and data analysis. This chapter serves as the backbone of this research contributing to all objectives since the experimental nature of the adopted approach necessitates the use of facilities, equipment and data analysis. Thus, this chapter serves objectives 2-7.

Chapter 4 considers the influence of shaft inclination on RNL. The systematic experiments conducted not only serve both practice and training purposes for subsequent cavitation tunnel testing, but also provide comprehensive data - including cavitation observation and inception, performance and noise data for variations of the inclination angle. The results and outcomes of the chapter were published as a journal article (Aktas, Atlar, Turkmen et al., 2015) and serves the 2<sup>nd</sup> objective.

Chapter 5 presents results from full-scale noise trials with “The Princess Royal” and their scaled simulation in the ECT. Detailed measurements are made at both full-scale and model tests including cavitation observation, pressure pulses, powering & performance information and RNLs. Comparisons of the conducted research were compiled as a manuscript and published in a peer-reviewed journal (Aktas et al., 2016). This chapter thus satisfies the 3<sup>rd</sup> and 4<sup>th</sup> objective.

Chapter 6 is composed of three interrelated main sub-sections. The initial part is devoted to testing a 3 model propeller subset of the Meridian standard propeller series behind three simulated axial wake variations at tunnel conditions determined with the help of powering data of ocean-going commercial vessels. These tests were conducted to check on the degree to which the commercially representative tests were presented as a conference paper (Aktas, Atlar, Fitzsimmons et al., 2015) and satisfy the 5<sup>th</sup> objective. The subsequent part of Chapter 6 presents results and analysis of the systematic cavitation and wake tests with six Meridian standard propeller series members to produce a database for the development of a tool for noise prediction and to demonstrate the use of an advanced dynamic cavitation analysis tool methodology, thereby serving to the 6<sup>th</sup> and 7<sup>th</sup> objective of the thesis.

The experiments were prepared, set-up, conducted, recorded, analysed and presented mainly by the Author, leading to his demonstration and training in a variety of engineering skills as well as a better appreciation of the experimental research. Self-involvement throughout the experimental process not only provided a deeper insight into the nature of the data but also helped meticulous interpretation of the results.

Analysis of results from the executed experiments were initially assembled into ECT reports. These reports are filed and stored for the reference of future researchers and academics. The results were then compiled into scientific articles and conference manuscripts which have been published in peer-reviewed journals and reputable international symposia (Aktas et al., 2014; Aktas, Fitzsimmons et al., 2015). The feedback received during the symposia and from journal reviewers has improved the clarity of the content and enhanced the quality of this thesis.

## 7.3 Main conclusions

The research conducted for this thesis extends the state of the art with several noteworthy contributions to the subject of URN created by propeller cavitation. Overall, the conclusions drawn in this thesis have shed contemporary light on the contentious issue of propeller cavitation noise. Amongst the major contributions of this thesis are: providing the literature with a public body of scarce if not non-existent comprehensive and detailed underwater radiated noise data carries utmost importance. Moreover, providing a novel practical noise prediction method which is based on a unique propeller-series approach, adopted to introduce the influence of the wake variation, is the first of its kind and can be considered a major contribution. Within this framework, some crucial conclusions have been derived as outlined in the following.

1. The conducted comprehensive literature review concluded that the state of the art is missing detailed information that can be produced by means of extensive experimental campaigns to enable the prediction of propeller cavitation noise. In addition to that, there is no plausible way that can provide a quick insight to the RNL of a vessel at an early design stage due to the complexity of the phenomena. This knowledge gap present in the publicly available literature justifies an experimental approach to be adopted to produce a data set of valuable and detailed full-scale and model scale propeller underwater radiated noise accessible by the public as well as a practical method for use in early design stage noise prediction.
2. The flow-unsteadiness caused by systematic variation of shaft inclination is investigated with particular emphasis on its impact on URN. Important conclusions have been drawn out of the conducted study regarding the influence of the oblique flow on the inception of cavitation and the impact of the cavitation type on the RNL as follows:
  - a. Shaft inclination has been observed to result in earlier tip vortex cavitation inception. This consequently results in higher noise levels emanating at the advance coefficients that are in the region of the inception advance coefficients.



- b. The propeller model tested in oblique flow conditions has shown two distinct types of well-developed cavitation patterns; tip vortex and sheet cavitation, which have been detected to dominate the RNL. Moreover, the signature of each type has been found contribute to the different parts of the spectral domain.
  - c. Presented systematic cavitation tunnel test data of a propeller on an inclined shaft, particularly for URN is non-existent in this detail and size. These experiments provide an invaluable benchmark data for a well-known, relatively simple, unsteady flow phenomenon contributing to the state-of-the-art.
- 3. The full-scale noise trials of the Newcastle University's catamaran research vessel "The Princess Royal" were conducted in order to allow testing of the cavitation tunnel capabilities for full-scale noise prediction. During the full-scale trials, the research vessel was heavily instrumented and recordings are made for the off board RNL, propeller induced pressure pulses, high-resolution cavitation observations and powering performance data. Such a detailed and comprehensive data enabled the reproduction of the full-scale trial conditions during cavitation tunnel tests. The conducted experiments enabled comparisons of the qualitative cavitation observation information and quantitative pressure pulse and RNL predictions. Whilst providing the literature with scarce URN data with comprehensive model scale and full-scale details also the following conclusions are obtained:
  - a. The extrapolated test results of the cavitation tunnel tests, when compared with the URN spectra acquired during the full-scale trials, have shown reasonable agreement over the low and medium frequency ranges rather than over the higher frequency range.
  - b. Applications of ITTC procedures and guidelines to the cavitation tunnel test results for underwater RNL and cavitation observations for the research vessel have shown reasonable agreement for the prediction of the full-scale trial measurements; the experimental data being obtained from a truncated dummy-hull

model with properly scaled bow and stern sections, combined with the wake screens strategically fitted at the stern.

- c. The provided full-scale data complemented with corresponding model scale cavitation tunnel test data, in particular for URN with publically available details of the vessel, makes an invaluable contribution to the state-of-the-art URN research.
4. A small but commercially representative subset of the Meridian standard propeller series was selected and tested behind the three systematically varied grades of wakes in order to validate and develop confidence on the adopted standard propeller series approach. Thus, 3 model propellers were chosen to represent the main design variants such as P/D ratio, BAR and blade number. The real ocean-going vessel powering and performance data was then utilized to determine the cavitation tunnel testing conditions. The experimental results were then extrapolated using the vessel operating conditions and following conclusions are reached at:
- a. Comparisons of the measured noise levels behind the wake and in open water condition demonstrate the importance, and hence necessity, of introducing the effect of wake in the noise investigations of propellers. While previous testing of the standard propeller series did not incorporate non-uniform inflow, due to different focus, it can be concluded that for tests focussing on propeller noise, a representation of the wake severity is of prime importance.
  - b. The extrapolated results of the cavitation tunnel tests shown good agreement in terms of the RNL and trend over the frequency range of comparison in comparison with the published average commercial shipping noise data from Wales and Heitmeyer, (2002). This provided the necessary confidence and encouragement to conduct tests with a larger subset using the same methodology but using a systematic variation of the operating conditions.

5. The qualitative justification of the adopted approach with the commercially representative small subset led to an experimental campaign with six Meridian standard propeller series members using a systematic approach. The test matrix was chosen to have a large scope of parameters in order to ensure accurate predictions. The data recorded during the experiments thus resulted in a colossal amount of recordings. In order to use the recorded data, both as raw data or to make propeller noise predictions, the recordings were compiled into a database. The compiled database is then processed through an ANN toolbox to train a neural network to recognize the patterns inherently present within the database. The trained network was then compiled to make propeller cavitation noise predictions using 12 non-dimensional and 3 full-scale parameter inputs as provided by the user. The developed cavitation noise prediction software is then put into test with two full-scale case studies in order to validate the developed approach and following conclusions are obtained:

- a. The first validation case study involved the comparisons of the URN predictions for a 105-meter training ship for which the full-scale noise measurements were available with two different propellers fitted to the ship. The original propeller was a conventional propeller with a very low skew which then replaced with a highly skewed and tip-offloaded one to improve the noise signature of the vessel. The predictions have shown that, even though the developed method does not incorporate features like the skew and tip off-loading, the effect of these features can be captured due to their inherent impact on the propeller performance parameters. For example, at same RPM, highly skewed propeller achieves higher speed, which is one of the dominating parameters for radiated noise level, while the predictions show lower RNLs in comparison to the RNLs of the conventional propeller. This trend of the predictions is in good agreement with the full-scale measurements.
- b. The second validation case study involved the comparisons of the RNL predictions for an 117-meter oil tanker driven by a single CPP. Two conditions from the full-scale trials, which were available for the design pitch and off-design pitch, were used for the comparisons of the predictions. Although CPP noise

signatures are considerably different to conventional propellers, with only 15 user inputs, a reasonable approximation to the URN levels of the vessel is achieved using the developed database and associated tool.

6. By taking advantage of the experimental nature of this research and systematic cavitation tunnel test data generated in the study, an advanced tool for the analysis of cavitation dynamics on URN was introduced and effectiveness of the tool was demonstrated to explore the influence of some major propeller design parameters on URN as well as further understanding of the effect of cavitation dynamics on URN. The developed methodology makes use of the analysis of the fluctuating pressure pulses and cavitation observations recorded simultaneously in time-domain together with the analysed URN data in the frequency domain. In this advanced analysis the Joint Time-Frequency Analysis toolbox, which provides a spectrogram and corresponding frequency domain response graphics, plays an important role together with the high-speed cavitation video images to determine the character of an instantaneous cavitation event in the frequency domain. Based on the experience of using the implemented tool it can be further confirmed that:

- a. Cavitation is the dominating source for URN of a propeller over the whole spectral frequency range following its inception. Wake non-uniformity is utmost important on the level and nature of URN experienced from a ship propeller due its consequent impact on the cavitation dynamics. The type of cavitation and dynamics experienced by the propeller is of prime importance for cavitation induced URN as it is not only influential over the radiated noise levels but also in the frequency region where it contributes into.

## **7.4 Recommendation for future work**

It is the Author's belief that his thesis has provided insight into the further understanding of cavitation induced URN providing not only publicly scarce if not non-existent URN data from both model scale tests and full-scale platforms but also led to the development of an early design stage noise prediction method. However, the scope of the studies was enormous in terms of the

data collected and the possibilities for other investigations to be carried out. The research conducted was limited and demonstrative in nature due to the available resources and time constraint. Thus, a number of further research on the subject is proposed as recommendations for future work listed below:

- **Further validation case studies for the developed URN prediction method:** The scarcity of the comprehensive full-scale noise data that is publicly available is one of the reasons that this thesis stems from. During the validation study of the prediction methodology, various sources of full-scale noise data were investigated, but no suitable source of full-scale noise data has been found that provides adequate information for a validation case. Thus, further validation case studies with suitable full-scale data on conventional commercial vessels are the most important future study that needs to be carried out.
- **Further extension of the database with strategically selected series members:** Since the current study was limited to a subset of the Meridian standard propeller series members, strategically selected additional members of the Meridian series can be tested to expand the URN database. Of course, the ideal scenario is to test the complete Meridian series to improve the range of the database for better coverage and prediction. However, this is very expensive and time-consuming. Instead, one can exploit the power of ANN with minimum viable model test data generated by the minimum necessary and strategically selected members of the series. The gap of the missing experimental data for the unselected members can be filled with the ANN predictions using the available data.

Furthermore, additional enhancements can be also implemented by the introduction of more contemporary propeller design parameters which are important from the URN mitigation point of view; such as the skew, tip unloading, new blade sections (Korkut et al., 2013), etc. Newly designed propeller models incorporating such parameters can be selectively manufactured and tested in conjunction with the further cavitation tunnel testing of the Meridian standard propeller series to modernise and enhance the database further.

- **Development of a propeller induced pressure pulse prediction method:** Since the pressure pulse data are available as an additional and invaluable by-product of the systematic database, the pressure pulse prediction can also be included in the prediction software using a separately trained ANN database.
- **Development of a systematic numerical approach to URN prediction:** One of the most attractive features of the systematic approach to the URN prediction of a ship propeller is the quick prediction time (basically an ANN based interpolation) once the database is generated. In the current study, the database is experimental and limited. The same database can be established by using numerical methods (e.g. potential flow based lifting surface or panel methods) which are validated and eventually calibrated by using the available systematic data on pressure pulses, cavitation observations and URN. This will pave way for the development of a wider base, modern and most practical prediction tool that can be used in early design stage.
- **Combining JTFA and cavitation observations:** The usefulness of the JTFA in combination with the synchronized pressure pulse time signal and cavitation observations are introduced in Chapter 6 of this thesis. This advanced analysis tool has proven to provide further insight into the effect of cavitation dynamics on URN. However, further development of software programming using NI LabView is required for the integration of the pressure pulse signals and cavitation observation images in time-domain to enhance the understanding and ease of interpretation of both pressure pulse and cavitation phenomenon. The ultimate aim is to develop a graphical user interface that enables the input of time domain pressure signal in synchronization with the cavitation observation that processes the time domain signal with JTFA to show third octave and narrow band frequency response with spectrogram in between. Such a combined post processing tool would significantly aid the interpretation of the noise measurements.
- **Implementation of cavitation noise control in the propeller design spiral:** A natural progression of this work is to engineer a methodology, where the mitigation or optimisation of the cavitation induced of a propeller, is introduced into the propeller design spiral. Potential regulatory standards based on existing silent vessel notations and further R&D work may be developed in a near future to determine an acceptable propeller

from URN point of view. Although there is no regulation in place yet to force the use of a propeller with lower RNLs, it is important to ensure that no loss in efficiency of the propeller is experienced when such implementation in the design spiral takes place.

- **Investigation of various unconventional noise mitigation methods:** The current study has focussed on the development an URN prediction method for conventional propellers and the method developed can be considered as a conventional mitigation tool for URN. However there are other means of mitigation using rather unconventional methods e.g. contracted tip loaded (CLT) propellers (Gonzalez-Adalid and Gennaro, 2011), Kappel propellers (Anderson & Andersen, 2000), pressure relief holes introduced to the tip of the propeller (Sharma et al., 1990) and coating application to a propulsor (Korkut & Atlar, 2012a), etc. Thus further studies with these interesting solutions based on the systematic approach presented in this study may be worthwhile to undertake for future research.

## References

- Abbott, I.H. & Doenhoff, A.E. Von (1959) *Theory of Wing Sections, Including a Summary of Airfoil Data*. Courier Corporation.
- Abrahamsen, K.A. (2005) 'Noise Control for Noise Sensitive Vessels', in *Proceedings of the 1st International Ship Noise and Vibration Conference*. London, United Kingdom, 20–21 June, p. 15.
- Abrahamsen, K.A. (2012) 'The ship as an underwater noise source', in *ECUA 2012 11th European Conference on Underwater Acoustics*. Edinburgh, Scotland, 2-6 July, p. 10.
- Ainslie, M. a. (2010) *Principles Of Sonar Performance Modeling*. Springer Berlin Heidelberg.
- Aktas, B., Atlar, M., Fitzsimmons, P., Shi, W., Turkmen, S. & Sasaki, N. (2015) 'Systematic cavitation tunnel tests for cavitation noise prediction of commercial ships using a standard series approach', in *The 4th International Conference on Advanced Model Measurement Technologies for the Maritime Industry*. Istanbul, Turkey, 28-30 September, p. 21.
- Aktas, B., Atlar, M., Turkmen, S., Korkut, E. & Fitzsimmons, P. (2015) Systematic cavitation tunnel tests of a Propeller in uniform and inclined flow conditions as part of a round robin test campaign. *Ocean Engineering*. 120, 136–151.
- Aktas, B., Atlar, M., Turkmen, S., Shi, W., Sampson, R., Korkut, E. & Fitzsimmons, P. (2016) Propeller cavitation noise investigations of a research vessel using medium size cavitation tunnel tests and full-scale trials. *Ocean Engineering*. 120, 122–135.
- Aktas, B., Fitzsimmons, P. & Atlar, M. (2015) 'Evaluation of a Semi-Empirical Method for the Propeller Noise Spectrum of a Fisheries Research Vessel', in *International Conference on Noise & Vibration, ICSV22*. p. 8.
- Aktas, B., Turkmen, S. & Atlar, M. (2014) The Princess Royal Full-Scale Data & Operating Conditions. *UNEW Memorandum to Task 1.3 Partners*, 3 February.
- Alkan, A.D., Gulez, K. & Yilmaz, H. (2004) Design of a robust neural network structure for determining initial stability particulars of fishing vessels. *Ocean Engineering*. 31 (5-6), 761–777.
- Anderson, P. & Andersen, S. V. (2000) 'Cavitation considerations in the design of Kappel propellers', in *Proceedings of the NCT' 50, International Conference on Propeller Cavitation*. Newcastle, United Kingdom, 3-5 April, p. 21.
- Angelopoulos, A., Fitzsimmons, P.A. & Odabasi, A.Y. (1988) 'A Semi-Empirical Method for



- Propeller Broad-Band Noise*', in Report No: W1906, British Maritime Technology Limited, p. 14.
- ANSI (2009) Quantities and Procedures for Description and Measurement of Underwater Sound from Ships – Part 1: General Requirements. American National Standard ANSI/ASAS.
- Arndt, R.E.A. (2002) Cavitation in Vortical Flows. *Annual Review of Fluid Mechanics*. 34:143–175.
- Arndt, R.E.A., Ellis, C.R. & Paul, S. (1995) Preliminary Investigation of the Use of Air Injection to Mitigate Cavitation Erosion. *Journal of Fluids Engineering*. 117 (3), 498–504.
- Arveson, P.T. & Vendittis, D.J. (2000) Radiated noise characteristics of a modern cargo ship. *The Journal of the Acoustical Society of America*. 107 (1), 118–129.
- Atlar, M. (2000) 'A History of The Emerson Cavitation Tunnel', in *International Conference on Propeller Cavitation, (NCT'50)*. Newcastle, UK. 3-5 April, pp. 3–34.
- Atlar, M. (2011) 'Recent upgrading of marine testing facilities at Newcastle University', in *The 2nd international Conference on Advanced Model Measurement Technology for the EU Maritime Industry*. Newcastle upon Tyne, UK, 4-6 April, pp. 1–32.
- Atlar, M. & Patience, G. (1998) An investigation into effective boss cap designs to eliminate propeller hub vortex cavitation. *Proceedings of practical design of ship and mobile units Elsevier Science BV*. 757–769.
- Atlar, M., Takinaci, A.C., Korkut, E., Aono, T. & Sasaki, N. (2001) 'Cavitation tunnel tests for propeller noise of a FRV and comparisons with full-scale measurements', in *International Symposium on Cavitation, CAV2001:sessionB8.007*. California Institute of Technology, Pasadena, CA USA, p. 13.
- Baiter, H.J. (1974) 'Aspects of cavitation noise', in *Cavitation, Noise and Erosion*. Fraunhofer-Gesellschaft, Forschungsgruppe Hydroakustik Ottobrunn, Germany, p. 39.
- Bark, G. (1986) 'Development of Violent Collapses in Propeller Cavitation', in *International Symposium on Cavitation and Multiphase Flow Noise, Proceedings of the ASME Symposium*. Anaheim, CA, USA, pp. 65–75.
- Bark, G. (1988) 'On the mechanisms of propeller cavitation noise', in *Ph.D. thesis, Chalmers University of Technology*. Göteborg, Sweden.
- Bark, G. (1985) Prediction of Propeller Cavitation Noise From Model Tests and Its Comparison With Full Scale Data. *Transactions of the ASME*. 107 (1), 112–119.

- Bark, G. (2000) Selected problems about scaling of cavitation noise at low and medium high frequencies. 34th WEGEMT School
- Bark, G. & Berlekomp, W.B. van (1978) 'Experimental Investigations of Cavitation Dynamics and Cavitation Noise', in *12th ONR Naval Hydrodynamics Symposium*. Washington, DC, USA, pp. 470–493.
- Basheer, I.A. & Hajmeer, M. (2000) Artificial neural networks: Fundamentals, computing, design, and application. *Journal of Microbiological Methods*. 43 (1), 3–31.
- Beale, M., Hagan, M. & Demuth, H. (2015) Neural network toolbox for use with MATLAB. *User's Guide, MathWorks*.
- Bell, J. (2008) Modelling of High Frequency Sonar Systems. *Proceedings of the Institute of Acoustics*. 30:1 – 10.
- Bensow, R.E. & Bark, G. (2010) Implicit LES Predictions of the Cavitating Flow on a Propeller. *Journal of Fluids Engineering*. 132 (4), 041302.
- Bensow, R.E. & Bark, G. (2010) 'Simulating Cavitating Flows With Les in OpenFOAM', in *5th European Conference on Computational Fluid Dynamics, ECCOMAS CFD*. Lisbon, Portugal, 14-17 June, p. 18.
- Berghault, L. (2000) 'Propeller Induced Tip Vortex Noise as Function of Blade Area and Blade Tip Loading', in *Intl. Conference on Propeller Cavitation (NCT'50)*. University of Newcastle, UK, pp. 121–135.
- Bertschneider, H., Bosschers, J., Choi, G.H., Ciappi, E., Farabee, T., Kawakita, C. & Tang, D. (2014) 'Specialist Committee on Hydrodynamic Noise', in *Final Report and Recommendations to the 27th ITTC*. Copenhagen, Sweden, p. 45.
- Bjørnø, L. & Bjørnø, I. (1999) 'Underwater Acoustics and its Applications. A Historical Review', in *Proceedings of the 2nd EAA International Symposium on Hydroacoustics*. Gdańsk-Jurata, POLAND, pp. 3–8.
- Blake, W.K. (1984) 'Aero-hydroacoustics for Ships, Volume I-II', in *David W. Taylor Naval Ship Research and Development Center, Naval Sea Systems Command*. Washington, DC, USA, p. 627.
- Blake, W.K. (1986) Propeller Cavitation Noise, The Problems of Scaling and Prediction. ASME Proceedings of International Symposium on Cavitation and Multiphase Flow Noise p.89–99.
- BMT-Cortec (1992) 'Propeller Noise Spectrum Program (PRO-SPEC) System and User

- Manual', in *British Maritime Technology - Cortec Limited*. Wallsend Research Station Newcastle, UK, p. 72.
- Bosschers, J. (2010) On the influence of viscous effects on 2-D cavitating vortices. *Journal of Hydrodynamics*. 22 (5 SUPPL. 1), 763–770.
- Brennen, C.E. (1995) *Cavitation and Bubble Dynamics*. California Institute of Technology Pasadena, California: Oxford University Press.
- Brennen, C.E. (2007) The amazing world of bubbles. *Engineering and Science*. 70 (1), 30–41.
- Brennen, C.E. & Ceccio, S.L. (1989) 'Recent observations on cavitation and cavitation noise', in *Proceedings of Third International Symposium On Cavitation Noise and Erosion in Fluid Systems*. San Francisco CA, USA, pp. 67–78.
- Breslin, J.P. & Andersen, P. (1996) *Hydrodynamics of Ship Propellers*. Cambridge University Press.
- Brooker, A. & Humphrey, V. (2014) 'Measurement of Radiated Underwater Noise from a Small Research Vessel in Shallow Water', in *A. Yücel Odabaşı Colloquium Series 1 st International Meeting - Propeller Noise & Vibration*. Istanbul, Turkey.
- Brown, N.A. (1976) Cavitation Noise Problems and Solutions. *International Symposium on Shipboard Acoustics*.
- De Bruijn, A. & Ten Wolde, T. (1974) 'Measurement and Prediction of Sound Inboard and Outboard of Ships as Generated by Cavitating Propellers', in *NSMB Symposium*. Wageningen, Netherland.
- Burrill, L.C. (1944) Calculation of marine propeller performance characteristics. *Transactions of NECIES*. 60:269–294.
- Burrill, L.C. (1963) Sir Charles Parsons and cavitation. *The Institute of Marine Engineers, Transactions*. LXIII (8), 149–167.
- Burrill, L.C. & Emerson, A. (1962) Propeller Cavitation-Further Tests on 16in Propeller Models in the King's College Cavitation Tunnel. *Transactions of the North East Coast Institution of Engineers*. 79:295–320.
- Calcagni, D., Salvatore, F., Bernardini, G. & Miozzi, M. (2010) 'Automated Marine Propeller Optimal Design Combining Hydrodynamics Models and Neural Networks', in *First International Symposium on Fishing Vessel Energy Efficiency- E-Fishing*. Vigo, Spain, p. 10.
- Carlton, J. (2012) *Marine Propellers and Propulsion*. Vol. 23. Butterworth-Heinemann.

- Cato, D.H. (2008) Ocean ambient noise: its measurement and its significance to marine animals. *Proceedings of the Institute of Acoustics*. 30 (5), 1–9.
- Ceccio, S.L. & Brennen, C.E. (1995) Observation and Scaling of Travelling Bubble Cavitation. *Journal of Fluid Mechanics*. 233 (1991), 633–660.
- Cepowski, T. (2007) Approximation of the index for assessing ship sea-keeping performance on the basis of ship design parameters. *Polish Maritime Research*. 14 (3), 21–26.
- Chahine, G.L. (2004) 'Nuclei effects on cavitation inception and noise', in *25th Symposium on Naval Hydrodynamics*. St. John's, Newfoundland and Labrador, CANADA, 8-13 August, p. 14.
- Chapman, N.R. & Price, A. (2011) Low frequency deep ocean ambient noise trend in the Northeast Pacific Ocean. *The Journal of the Acoustical Society of America*. 129 (5), EL161–EL165.
- Chekab, M., Ghadimi, P., Reza Djeddi, S. & Soroushan, M. (2013) Investigation of Different Methods of Noise Reduction for Submerged Marine Propellers and Their Classification. *American Journal of Mechanical Engineering*. 1 (2), 34–42.
- Choi, J. & Ceccio, S.L. (2007) Dynamics and noise emission of vortex cavitation bubbles. *Journal of Fluid Mechanics*. 575:1–26.
- Clarke, M.A. (1987) Noise Project, Newcastle University. Report of Stone Vickers Ltd Technical Department, Report No: H93, UK
- Clausen, H.B., Lützen, M., Friis-Hansen, A. & Bjørneboe, N. (2001) Bayesian and Neural Networks For Preliminary Ship Design. *Practical Design of Ships and Other Floating Structures*. 38 (4), 349–356.
- Cochard, N. & Arzelies, P. (1998) 'Noise source calibration in test tank', in *OCEANS'98 Conference Proceedings, IEEE*. pp. 134–137.
- Coleman, H.W. & Steele, W.G. (2009) *Experimentation, validation, and uncertainty analysis for engineers*. John Wiley & Sons.
- Couser, P., Mason, A., Mason, G., Smith, C. & Konsky, Br. (2004) Artificial Neural network for hull resistance prediction. *Computer applications and information technology in the maritime industries (COMPIT)*. 391–402.
- Denny, S.B., T., P.L., Hubble, E.N., Smith, S.K. & Najarian, R.F. (1989) A new usable propeller series. *Marine technology*. 26 (3), 173–191.
- Dimoulas, V. & Nightingale, C. (1996) 'Neural networks in condition monitoring and fault

- diagnosis of marine diesel engines. Solving engineering problems with neural networks. *Proceedings of the International Conference on Engineering Applications of Neural Networks (EANN'96)*. 2 (2), 653–656.
- Ekinci, S., Celik, F. & Guner, M. (2010) A practical noise prediction method for cavitating marine propellers. *Brodogradnja*. 61:359–366.
- Emerson, A. & Sinclair, L. (1978) Propeller Design and Model Experiments. *Trans. North East Coast Institution of Engineers and Shipbuilders*. 94:199–234.
- Eppler, R. & Shen, Y.T. (1979) Wing Sections for Hydrofoils — Part 1 : Symmetrical Profiles. *Journal of Ship Research*. 23 (3), 209–217.
- Euler, A. (1754) Histoire de l'Académie royale des sciences et des belles lettres de Berlin. *Classe de Philosophie expérimentale*. 10 (81), 105–121.
- Filcek, P. (2006) 'Ship Vibration and Noise', in *Lloyd's Register Guidance Notes Revision 2.1*.
- Firenze, E. & Valdenazzi, F. (2015) 'A Method to Predict Underwater Noise from Cavitating Propellers', in *MTS/IEEE OCEANS Conference*. Genova, ITALY: . p. 6.
- Fischer, R. (2008) Singing Propellers—Solutions and Case Histories. *Marine Technology*. 45:221–227.
- Fischer, R.W. & Brown, N.A. (2005) 'Factors Affecting the Underwater Noise of Commercial Vessels Operating in Environmentally Sensitive Areas', in *Proceedings of OCEANS 2005 MTS/IEEE*. p. 7.
- Fisher, F. & Simmons, V. (1977) Sound absorption in sea water. *The Journal of the Acoustical Society of America*. 62:558–564.
- Fitzpatrick, H.M. & Strasberg, M. (1956) 'Hydrodynamic sources of sound', in *Proceedings of First Office of Naval Research Symposium on Naval Hydrodynamics*. Washington, DC, USA, September, pp. 241–280.
- Fitzsimmons, P. (2014) 'Keynote Speech', in *A. Yücel Odabaşı Colloquium Series 1 st International Meeting - Propeller Noise & Vibration*. Istanbul, Turkey.
- Fitzsimmons, P.A. (2009) 'Cavitation developments on propellers and rudders', in *13th Congress of International Maritime Association of Mediterranean (IMAM 2009)*, İstanbul, Turkey, 12-15 October.
- Fitzsimmons, P.A. (1988) *Guidelines for the reduction of excitation forces due to cavitating propellers*. British Maritime Technology Order No. 21015 (Task CAV.11), Report No. W1761.

- Fitzsimmons, P.A. & Boorsma, A. (2007) 'Cavitation Development on Propulsors', in *SNV 2007 Conference, London, UK*. Lloyds Register.
- Fitzsimmons, P.A. & Odabasi, A.Y. (1977) *Propeller-Excited Vibration: Hydrodynamics. A Summary of Model Work and Calculations On Hull Form and Propeller*. British Ship Research Association Report NS 469; Research Item No. D35 (RB), Wallsend, Tyne and Wear, UK.
- Francois, R.E. & Garrison, G.R. (1982) Sound absorption based on ocean measurements. Part II: Boric acid contribution and equation for total absorption. *The Journal of the Acoustical Society of America*. 72 (6), 1879–1890.
- Frisk, G. V. (2012) Noiseconomics: The relationship between ambient noise levels in the sea and global economic trends. *Scientific Reports*. 2 (1), 2–5.
- Gawn, R.W.L. & Burrill, L.C. (1957) Effect of Cavitation on the Performance of a Series of 16 in. Model Propellers. *Institution of Naval Architects -- Transactions*. 99:690–718.
- Geurst, A. (1961) *Linearized theory of two-dimensional cavity flows*. Technische Hogeschool Delft, Doctoral Thesis.
- Gomez, G.P. & Gonzalez-Adalid, J. (1998) *Detailed Design of Ship Propellers*. Madrid: Fondo Editorial de Ingeniería Naval del Colegio Oficial de Ingenieros Navales y Oceánicos.
- Gonzalez- Adalid, J. & Gennaro, G. (2011) 'Latest experiences with Contracted and Loaded Tip (CLT) propellers', in *Sustainable Maritime Transportation and Exploitation of Sea Resources*. p. 47.
- Gotz, T., Hastie, G., Hatch, L.T., Raustein, O., Southall, B.L., Tasker, M., Götz, T., Hastie, G., Hatch, L. T., Raustein, O., Southall, B., Tasker, M., & Thomsen, F., Thomsen, F., Campbell, J. & Fredheim, B. (2009) Overview of the impacts of anthropogenic underwater sound in the marine environment Biodiversity Series. *OSPAR Biodiversity Series*, 441: p. 134.
- Gougoulidis, G. (2008) The utilization of artificial neural networks in marine applications: An overview. *Naval Engineers Journal*. 120 (3), 19–26.
- Van der Graaf, A.J., Ainslie, M.A., André, M., Brensing, K., Dalen, J., Dekeling, R.P.A., Robinson, S., Tasker, M.L., Thomsen, F. & Werner, S. (2012) *European Marine Strategy Framework Directive- Good Environmental Status (MSFD GES)*.
- Gutsche, F. (1964) Untersuchung von Schiffsschrauben in Schräger Anströmung. *Schiffbauforschung*, 3.

- Hadler, J.B. (1966) The Prediction of Power Performance on Planing Craft. *Transactions of the Society of Naval Architects and Marine Engineers*. 74:563–610.
- Hallander, J., Li, D.-Q., Allenstrom, B., Valdenazzi, F. & Barras, C. (2012) Predicting Underwater Radiated Noise Due to a Cavitating Propeller in a Ship Wake. *Proceedings of the 8th International Symposium on Cavitation - CAV2012*. (151), 1–7.
- Hansen, H. (2011) 'Model and Full Scale Evaluation of a 'Propeller Boss Cap Fins' Device Fitted to an Aframax Tanker', in *Second International Symposium on Marine Propulsors, SMP'11*. Hamburg, Germany.
- Harvald (1981) Wake Distributions and Wake Measurements. *Transactions of the Royal Institution of Naval Architects*. 123:265–286.
- Hildebrand, J. A. (2009) Anthropogenic and natural sources of ambient noise in the ocean. *Marine Ecology Progress Series*. 395 (5), 5–20.
- Hildebrand, J.A. (2005) 'Impacts of Anthropogenic Sound', in *Marine Mammal Research: Conservation beyond Crisis*. The Johns Hopkins University Press, Baltimore, Maryland. pp. 101–124.
- Holden, K. (1981) 'Effect of propeller design parameters on noise induced by cavitation', in A C Nilsson & N P Tyvand (eds.) *Noise Sources in Ships I: Propellers*. Nordforsk, Miljovardsserien, Sweden.
- Hsiao, C. & Chahine, G. (2008) 'Scaling of tip vortex cavitation inception for a marine open propeller', in *27th Symposium on Naval Hydrodynamics*. Seoul, KOREA 5-10 October.
- HTF (2011) 'AMT'11', in *International Conference on Advanced Model Measurement Technologies for the Maritime Industry*. Newcastle Upon Tyne, UK.
- HTF (2013) 'AMT'13', in *International Conference on Advanced Model Measurement Technologies for the Maritime Industry*. Gdansk, POLAND.
- Huse, E. (1974) 'Effect of Afterbody Forms and Afterbody Fins on the Wake Distribution of Single-Screw Ships', in NSFI Report No. R31-74: p. 35.
- IMO (2012) Adoption of the Code on Noise Levels on Board Ships. MSC 91/22/Add.1 Annex 1 337 (November).
- IMO (2013) Noise from commercial shipping and its adverse impacts on marine life. Marine Environment Protection Committee, International Maritime Organization, 66th Session, Agenda item 17
- IMO (2011) Noise From Commerical Shipping and Its Adverse Impact on Marine Life-

- Development of an international standard for measurement of underwater noise radiated from merchant ships. MEPC 62nd session Agenda item 19
- IMO (2007) 'Shipping noise and marine mammals', in *Marine Environment Protection Committee 57th Session, Agenda item 20*. p. 9.
- ISO (2012) 'Acoustics — Quantities and Procedures for Description and Measurement of Underwater Sound From Ships', in *Part 1: General requirements for Measurements In Deep Water, BSI Standards Publication*.
- ISO (2009) 'ISO/IEC Guide 98-1:2009 - Uncertainty of measurement - Part 1: Introduction to the expression of uncertainty in measurement', in p. 71.
- ISO (2015) 'Underwater acoustics — Terminology', in *ISO/DIS 18405*. p. 50.
- ITTC (1987) Cavitation committee report. 18th International Towing Tank Conference
- ITTC (2011a) 'Cavitation Induced Pressure Fluctuations Model Scale Experiments', in *ITTC – Recommended Procedures and Guidelines, 7.5 – 02-03-03.3*. p. 16.
- ITTC (2011b) 'ITTC – Recommended Procedures and Guidelines - Experimental wake scaling methods', in *7.5-02-03-02.5*. p. 7.
- ITTC (2011c) 'Model – Scale Cavitation Test', in *ITTC – Recommended Procedures and Guidelines, 7.5-02-03-03.1*. 26th ITTC Specialist Committee on Scaling of Wake Fields: p. 9.
- ITTC (2014) *Proceedings of the 27th Conference of the ITTC*. Copenhagen, Sweden.
- ITTC (2002a) 'Recommended Procedures testing and Extrapolation Methods Propulsion; Cavitation. Description of Cavitation Appearances', in *ITTC – Recommended Procedures, 7.5-02-03-03.2 , Propulsion Committee of 23rd ITTC*. p. 7.
- ITTC (2002b) Propulsion, Propulsor Uncertainty Analysis, Example for Open Water Test, in *ITTC – Recommended Procedures, 7.5-02-03-02.2 , Propulsion Committee of 23rd ITTC*. p. 9.
- Jong, C. a F. De (2009) 'Characterization of ships as sources of underwater noise Surface ship underwater noise', in *NAG/DAGA International Conference on Acoustics*. Rotterdam, Netherlands: p. 4.
- Karpathy, A. (2016) *Convolutional Neural Networks for Visual Recognition*. Available from: <http://cs231n.github.io/neural-networks-1/> (Accessed 22 February 2016).
- Knapp, R.T. (1970) *Cavitation*. New York, McGraw- Hill Book Company.
- Konno, A., Wakabayashi, K., Yamaguchi, H., Maeda, M., Ishii, N., Soejima, S., Kimura, K.,



- Yamguchi, H., Maeda, M., Ishii, N., Soejima, S. & Kimura, K. (2002) On the Mechanism of the Bursting Phenomena of Propeller Tip Vortex Cavitation. *Journal of Marine Science and Technology*. 6 (4), 181–192.
- Korkut, E. (1999) *An Investigation Into The Scale Effects on Cavitation Inception and Noise in Marine Propellers*. School of Marine Science and Technology, Newcastle University, Philosophy of Doctorate Thesis.
- Korkut, E. & Atlar, M. (2012a) An experimental investigation of the effect of foul release coating application on performance, noise and cavitation characteristics of marine propellers. *Ocean Engineering*. 41 (782), 1–12.
- Korkut, E. & Atlar, M. (2012b) 'Background Noise Measurements of The Emerson Cavitation Tunnel Following The Upgrading in 2008', in *International Conference on Hydrodynamics, ICHD-2012*. St. Petersburg, Russia, 1-4 October.
- Korkut, E., Atlar, M. & Wang, D. (2013) An experimental investigation into cavitation behaviour and pressure characteristics of alternative blade sections for propellers. *International Journal of Naval Architecture and Ocean Engineering*. 5 (1), 81–100.
- Korkut, E. & Takinaci, A.C. (2013) '18M Research Vessel Wake Measurements', in Istanbul Technical University Faculty Of Naval Architecture And Ocean Engineering, İstanbul/Turkey: p. 6.
- Kowalczyk, S. & Felicjancik, J. (2016) Numerical and experimental propeller noise investigations. *Ocean Engineering*. (In Press), 8.
- Kozhukharov, P.G. & Sadovnikov, M.Y. (1983) 'Investigation on Cavitating Screw Propellers Operating in Oblique Flow', in *Second International Conference on Cavitation*. Edinburgh, Scotland, 6-8 September.
- Kuiper, G. (1998) Cavitation research and ship propeller design. *Applied scientific research*. (58), 33–50.
- Kuiper, G. (2010) New developments and propeller design. *Journal of Hydrodynamics, Ser. B*. 22 (5), 7–16.
- Kuiper, G. (2001) 'New developments around sheet and tip vortex cavitation on ship's propeller', in *4th International symposium on Cavitation*. California Institute of Technology, Pasadena, CA, USA: p. 20.
- Kuiper, G. (2012) 'Vortex cavitation', in *Cavitation in Ship Propulsion*. pp. 65–83.
- Lange, D. De & Bruin, G. De (1998) Sheet cavitation and cloud cavitation, re-entrant jet and

- three-dimensionality. *In Fascination of Fluid Dynamics*. 58:91–114.
- Latorre, R. (1982) TVC noise envelope-an approach to tip vortex cavitation noise scaling. *Journal of Ship Research*. 26 (1), 65–75.
- Leaper, R., Renilson, M., Frank, V. & Papastravrou, V. (2009) *Possible steps towards reducing impacts of shipping noise*. SC/61/E19:5.
- Lee, C.-S. (1979) Prediction of steady and unsteady performance of marine propellers with or without cavitation by numerical lifting-surface theory. *Publication of: Society of Naval Architects and Marine Engineers*. 1–30.
- Lidtkke, A.K., Humphrey, V.F. & Turnock, S.R. (2015) Feasibility study into a computational approach for marine propeller noise and cavitation modelling. *Ocean Engineering*. (In Press), 8.
- Lloyd's Register (2010) 'Propeller Design Aspects with Respect to Noise', in *Marine Consultancy Services Technical Investigations, CRS Secretariat*. p. 16.
- Lloyd's Register (2014) Rules and Regulations for the Classification of Ships. *Notice No. 9*. 28.
- Lovett, J.R. (1978) Merged Seawater Sound-Speed Equations. *The Journal of the Acoustical Society of America*. 63 (6), 1713–1718.
- MAN (2014) Propulsion Trends in Bulk Carriers, Two Stroke Engines. *MAN Diesel and Turbo*. 26.
- MAN (2009) 'Propulsion Trends in Container Vessels', in *MAN Diesel & Turbo*. p. 28.
- Matusiak, J. (1992) *Pressure and noise induced by a cavitating marine screw propeller*. Doctor of Philosophy thesis, VTT Publications 87: Ph.D. Thesis - Helsinki Univ. of Technology Technical Research Centre of Finland, Espoo. Ship Lab. publication 87.
- McCormick, B.W. (1962) On Cavitation Produced by a Vortex Trailing from a Lifting Surface. *Journal of Basic Engineering*. 84 (3), 369–378.
- McDonald, M.A., Hildebrand, J.A., Wiggins, S.M. & Ross, D. (2008) A 50 year comparison of ambient ocean noise near San Clemente Island: a bathymetrically complex coastal region off Southern California. *The Journal of the Acoustical Society of America*. 124 (4), 1985–1992.
- McKenna, M.F., Ross, D., Wiggins, S.M. & Hildebrand, J. a. (2012) Underwater radiated noise from modern commercial ships. *The Journal of the Acoustical Society of America*. 131 (1), 92–103.

- McKenna, M.F., Wiggins, S.M. & Hildebrand, J.A. (2013) Relationship between container ship underwater noise levels and ship design, operational and oceanographic conditions. *Scientific Reports*. 3 (1760), 10.
- MCR (2011) 'Cruise report for research projects conducted from R/V Song of the Whale in French and UK waters of the English Channel', in *Marine Conservation Research International, Research conducted from R/V Song of the Whale in French and UK waters of the English Channel, May – June 2011*. Essex, UK: p. 18.
- Mitson, R.B. (1995) Underwater noise of research vessels: Review and recommendation. *Cooperative Research Report, ACOUSTEC*. 209:65.
- Mueller-Blenke, C., McGregor, P.K., Gill, A.B., Andresson, M.H., Metcalfe, J., Bendall, V., Sigray, P., Wood, D.T. & Thomsen, F. (2010) 'Effects of pile-driving noise on the behaviour of marine fish', in *COWRIE Ref: Fish 06-08 / Cefas Ref: C3371 Technical Report*.
- National Geographic Magazine (2011) *The Big Idea: Noisy Ocean*. Available from: <http://ngm.nationalgeographic.com/2011/01/big-idea/noisy-ocean> (Accessed 10 November 2015).
- National Instruments (2014) DIAdem. *Edition July 2014, Part Number 370858L-01*.
- National Instruments (2011) DIAdem, Data Mining, Analysis, and Report Generation. *User Manual*. 373082J-01122.
- National Instruments (2003) *National Instruments, LabView*.
- Neocleous, C.C. & Schizas, C.N. (1995) Artificial Neural Networks in Marine Propeller Design. *Proceedings of the International Conference on Neural Networks ICNN'95 of the IEEE*. 1098–1102.
- Neocleous, C.C. & Schizas, C.N. (1999) 'Marine propeller design using artificial neural networks', in *IJCNN'99. International Joint Conference on Neural Networks. Proceedings (Cat. No.99CH36339)*. IEEE. pp. 3958–3961.
- Neocleous, C.C. & Schizas, C.N. (2003) Neural Networks in Comparing USN and Wageningen B-Series Marine Propellers. *Proceedings of the International Joint Conference on Neural Networks*. 1:648–653.
- Nilsson, A.C. & Tyvand, N.P. (1981) *Noise Sources in Ships: Propellers. I*. Nordforsk.
- Norwood, C. (2002) An introduction to ship radiated noise. *Acoustics Australia*. 30 (1), 21–25.
- Odabasi, A. & Fitzsimmons, P. (1978) Alternative methods for wake quality assessment.

- International Shipbuilding Progress*. 25 (282), February 1978.
- Okamura, N. & Asano, T. (1988) Prediction of Propeller Cavitation Noise and Its Comparison with Full-Scale Measurements. *Journal of the Society of Naval Architects of Japan*. 164:19–32.
- Oossanen, P. van (1971) A Method for Minimizing the Occurrence of Cavitation on Propellers in a Wake. *International Ship Building Progress*. 18 (205), 321–333.
- Oosterveld, M.W.C. & Van Oossanen, P. (1975) Further computer-analyzed data of the Wageningen B-screw series. *International Shipbuilding Progress*. 22 (479), 13.
- Oshima, A. (1994) Scaling of Tip Vortex Cavitation Noise of Propeller. *Mitsubishi Heavy Industries, Ltd. Technical Review*. 31 No:3.
- Park, C., Seol, H., Kim, K. & Seong, W. (2009) A study on propeller noise source localization in a cavitation tunnel. *Ocean Engineering*. 36:754–762.
- Pennings, P., Westerweel, J. & van Terwisga, T. (2015) Sound signature of propeller tip vortex cavitation. *Journal of Physics: Conference Series*. 656:5.
- Pennings, P.C., Bosschers, J., Westerweel, J. & van Terwisga, T.J.C. (2015) Dynamics of isolated vortex cavitation. *Journal of Fluid Mechanics*. 778:288–313.
- Plesset, M.S. (1949) The dynamics of cavitation bubbles. *Journal of Applied Mechanics*. 16 (3), 277–282.
- Plesset, M.S. & Prosperetti, a (1977) Bubble Dynamics and Cavitation. *Annual Review of Fluid Mechanics*. 9 (1), 145–185.
- Plunt, J. (1980) *Part I: Noise Level Prediction Methods for Ships, Based on Empirical Data. Experiences From Empirical and Sea Calculation methods. Methods For Predicting Noise Levels In Ships*. Report 80-. Gothenburg, SWEDEN: Chalmers University of Technology.
- Pylkkanen, J. V. (2002) 'Review of propeller hydrodynamics for Liikkuteho', in *VTT*. Espoo. p. 33.
- Raestad, A. (1996) Tip Vortex Index-an Engineering Approach to Propeller Noise Prediction. *The Naval Architect, July/August*. July/Augus11–16.
- Renilson (2009) Reducing underwater noise pollution from large commercial vessels. Renilson Marine Consulting Pty Ltd, The International Fund for Animal Welfare (March).
- Richards, S.D., Harland, E.J. & Jones, S. a. S. (2007) Underwater Noise Study Supporting Scottish Executive Strategic Environmental Assessment for Marine Renewables. *QinetiQ Ltd. , QINETIQ/06/02215/2*. 82.

- Richardson, W.J., Greene, C.R., Jr., Malme, C.I. & Thomson, D.H. (2013) *Marine Mammals and Noise*. Elsevier Science.
- Rojas, R. (1994) *Neural networks A Systematic Introduction*. Springer.
- Ross, D. (1976) *Mechanics of Underwater Noise*. California, USA: Peninsula Publishing.
- Ross, D. (2005) Ship sources of ambient noise. *IEEE J. Oceanic Eng.* 30 (2), 257–261.
- Seo, K.-C., Atlar, M. & Sampson, R. (2011) 'Development of high performance standard propeller series - New 3-Bladed members for The Meridian Series', in *Targeted Advanced Research for Global Efficiency of Transportation Shipping (TARGETS) Deliverable D3.1 for Task 3.1*.
- Sharma, S.D., Mani, K. & Arakeri, V.H. (1990) Cavitation noise studies on marine propellers. *Journal of Sound and Vibration*. 138 (2), 255–283.
- Shen, Y.T. & Eppler, R. (1981) Wing Sections for Hydrofoils — Part 2 : Nonsymmetrical Profiles. *Journal of Ship Research*. 25 (3), 191–200.
- Shen, Y.T. & Strasberg, M. (2003) 'The effect of scale on propeller tip-vortex cavitation noise', in *Hydromechanics Directorate Technical Report*. Naval Surface Warfare Center Carderock Division, West Bethesda, MD, USA: p. 12.
- Simmonds, M., Dolman, S. & Weilgart, L. (1997) 'Oceans of noise: a WDCS Science Report', in *Whale and Dolphin Conservation Society*. p. 168.
- SMP (2016) *Stone Marine Propulsion, MERIDIAN design methodology*. Available from: <http://www.smp propulsion.com/Design/Design.html> (Accessed 15 February 2016).
- SONIC (2012) 'Suppression Of underwater Noise Induced by Cavitation', in *European Union Framework programme 7. FP7-SST-2012-RTD-1- SST.2012.1.1-1. - Assessment and mitigation of noise impacts of the maritime transport on the marine environment (coordinated topic within the framework of the ‘Ocean of Tomorrow’)*, FP7, Grant agreement no: 314394.
- Sontvedt, T. & Frivold, H. (1976) Low frequency variation of the surface of tip region cavitation on marine propeller blades and corresponding disturbances on nearby solid boundaries. *Norwegian Maritime Research*. 4 (2).
- Starsberg, M. (1977) Propeller Cavitation Noise After 35 Years of Study. *ASME Symposium on Noise in Fluids Engineering*.
- Tani, G., Viviani, M., Armelloni, E. & Nataletti, M. (2015) Cavitation tunnel acoustic characterisation and application to model propeller radiated noise measurements at

- different functioning conditions. *Proceedings of the Institution of Mechanical Engineers, Part M: Journal of Engineering for the Maritime Environment*. 17.
- Tani, G., Viviani, M., Gaggero, T., Hallander, J. & Johansson, T. (2015) 'Evaluation Of Methods To Measure Acoustic Transfer Functions In Cavitation Tunnels', in *The 4th International Conference on Advanced Model Measurement Technologies for the Maritime Industry, AMT'15*. Istanbul, Turkey.
- Tani, G., Viviani, M., Hallander, J., Johansson, T. & Rizzuto, E. (2016) Propeller underwater radiated noise: A comparison between model scale measurements in two different facilities and full scale measurements. *Applied Ocean Research*. 56:48–66.
- Taniguchi, K., Tanibayashi, H. & Chiba, N. (1969) Investigation into the Propeller Flow Cavitation in Oblique. *Mitsubishi Technical Bulletin No. 45, March*.
- Thornycroft, J.I. & Barnaby, S.W. (1895) Torpedo-Boat Destroyers. *Minutes of the Proceedings*. 122 (1895), 51–69.
- Troost, L. (1938) 'Open water Test Series with Modern Propeller Forms', in *Transactions of North East Coast Institute of Engineers and Shipbuilders*. p. 321.
- Urick, R.J. (1983) *Principles of underwater sound*. McGraw-Hill Book Company.
- Wales, S.C. & Heitmeyer, R.M. (2002) An ensemble source spectra model for merchant ship-radiated noise. *The Journal of the Acoustical Society of America*. 111 (3), 1211–1231.
- Wang, Y.-C. & Brennen, C.E. (1995) Shock Waves and Noise in the Collapse of a Cloud of Cavitation Bubbles. *20th International Symposium on Shock Waves, Pasadena, California, USA*. (1995), 1213–1218.
- Weilgart, L. (2005) *Underwater Noise: Death Knell of our Oceans?* (MacKenzie 2004), 1–5.
- Weilgart, L.S. (2008) The Impact of Ocean Noise Pollution on Marine Biodiversity. *International Ocean Noise Coalition*.
- Wenz, G.G.M. (1972) Review of Underwater Acoustics Research: Noise. *The Journal of the Acoustical Society of America*. 51 (3), 1010–1024.
- Wenz, G.M. (1962) Acoustic Ambient Noise in the Ocean: Spectra and Sources. *The Journal of the Acoustical Society of America*. 34 (12), 1936.
- White, P. & Pace, F. (2010) The Impact of Underwater Ship Noise on Marine Mammals. *1st IMarEST Ship Noise and Vibration Conference*.
- van Wijngaarden, E. (2011) *Prediction of Propeller-Induced Hull-Pressure Fluctuations*. 25 November, Ph.D., TU Delft.

- van Wijngaarden, E. (2005) Recent developments in predicting propeller-induced hull pressure pulses. *Proceedings of the 1st International Ship Noise and Vibration Conference*. 1–8.
- van Wijngaarden, E. (2000) 'Training Course on Propulsion Hydrodynamics- Ship Acoustics', in MARIN.
- Wijngaarden, E. Van, Bosschers, J. & Kuiper, G. (2005) Aspects of The Cavitating Propeller Tip Vortex As a Source of Inboard Noise and Vibration. *2005 ASME Fluids Engineering Division Summer Meeting and Exhibition*. 1–6.
- Williams, J.E.F. & Hawkings, D.L. (1969) Sound Generation by Turbulence and Surfaces in Arbitrary Motion. *Philosophical Transactions of the Royal Society A: Mathematical, Physical and Engineering Sciences*. 264 (1151), 321–342.
- Wittekind, D. (2009) The increasing noise level in the sea – a challenge for ship technology? *104th Congress of the German Society for Maritime Technology*.
- Wittekind, D.K. (2014) A simple model for the underwater noise source level of ships. *Journal of Ship Production and Design*. 30 (1), 7–14.
- Young, Y.L. & Kinnas, S.A. (2001) A BEM for the Prediction of Unsteady Midchord Face and/or Back Propeller Cavitation. *Journal of Fluids Engineering*. 123 (2), 311.
- 造船研究協会 (1983) '「SR183 研究部会 船尾振動・騒音の軽減を目的としたプロペラおよび船尾形状の研究」', in 船舶振興財団.

# Appendix A – “The Princess Royal” Propeller and Hull Wake Details

## A.1 Introduction

*The main objective of this appendix is to provide the full-scale propeller geometry details of Newcastle University’s research vessel “The Princess Royal” and its nominal wake details based on the model wake survey conducted in a towing tank.*

## A.2 Detailed propeller and wake data

The vessel has a 0.75m diameter 5 bladed conventional fixed pitch propeller was designed for the 15 knots service speed as shown in Figure A-1. The optimum values of pitch to diameter ratio and blade/area ratio were determined as  $P/D = 0.8475$  and  $BAR = 1.057$ , respectively. These initial particulars were derived from the basic design of the propeller based on the Wageningen B-Series data (Oosterveld & Van Oossanen, 1975). Tip clearance was selected to be 15% of the diameter at the top while a 10% clearance above the extension of the skeg plating was allowed. The clearance of the boss centre from the rudder stock was 0.5 % of the diameter.



Figure- A-1 “The Princess Royal” propellers as fitted on the vessel.

The following parts include a propeller drawing from the facility that conducted open water tests (Figure- A-2), main propeller particulars (Table- A-1), the propeller offset table (Table- A-2) and axial wake measurement results (Table- A-3) in the given order.



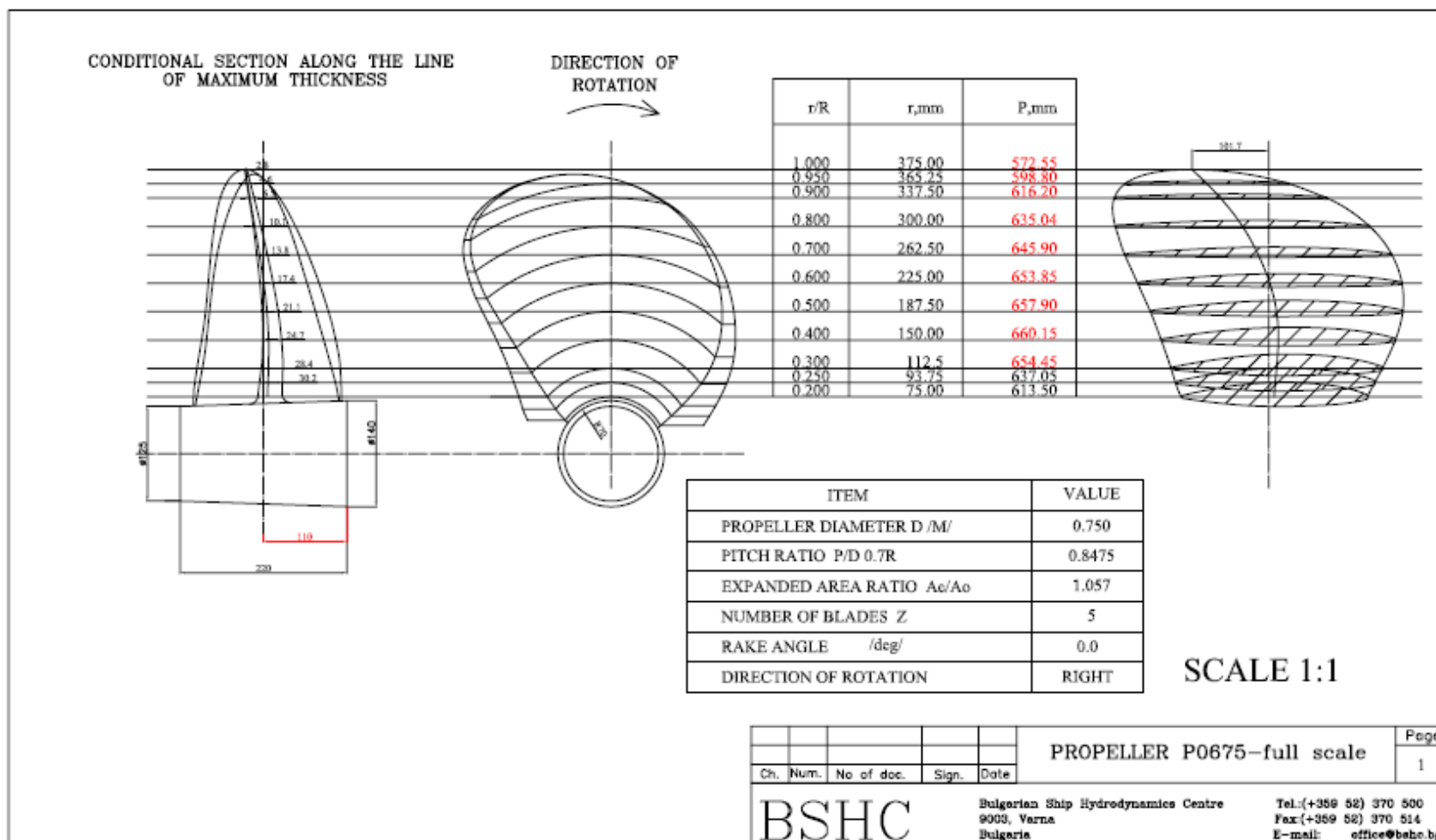


Figure- A-2 “The Princess Royal” propeller drawing.

Table- A-1 “The Princess Royal” Propeller Main Particulars.

x	Radius mm	P/D nose-tail	Pitch n-t mm	Chord mm	Skew mm	Thickness mm
0.2	75	0.8180	613.50	245.6	-6.9	32.0
0.25	93.75	0.8494	637.05	263.0	-8.1	30.2
0.3	112.5	0.8726	654.45	278.5	-10.2	28.4
0.4	150	0.8802	660.15	308.7	-12.3	24.7
0.5	187.5	0.8772	657.90	332.8	-10.0	21.1
0.6	225	0.8718	653.85	348.6	-1.1	17.4
0.7	262.5	0.8612	645.90	352.4	14.0	13.8
0.8	300	0.8467	635.03	335.5	34.9	10.1
0.9	337.5	0.8216	616.20	280.2	64.0	6.5
0.95	356.25	0.7984	598.80	216.4	81.7	4.6
1	375	0.7634	572.55	0	101.7	2.8

Table- A-2 Blade section offset table.

x = 0.20					x = 0.25				
%C from LE	x mm	Back Ord	Thickness	Face Ord	%C from LE	x mm	Back Ord	Thickness	Face Ord
0	0.00	2.82	5.64	-2.82	0	0.00	2.58	5.15	-2.58
2.5	6.14	5.29	9.79	-4.50	2.5	6.58	5.12	9.24	-4.12
5	12.28	7.47	13.41	-5.94	5	13.15	7.29	12.65	-5.35
10	24.56	10.78	18.69	-7.91	10	26.30	10.62	17.63	-7.00
20	49.12	15.27	25.61	-10.35	20	52.61	15.18	24.16	-8.97
30	73.68	17.91	29.68	-11.76	30	78.91	17.88	27.99	-10.11
40	98.24	19.13	31.69	-12.57	40	105.21	19.09	29.89	-10.80
50	122.81	19.07	31.76	-12.69	50	131.52	19.00	29.95	-10.95
60	147.37	17.81	29.78	-11.97	60	157.82	17.72	28.09	-10.36
70	171.93	15.37	25.82	-10.45	70	184.12	15.28	24.36	-9.07
80	196.49	11.77	19.90	-8.13	80	210.42	11.69	18.77	-7.09
90	221.05	7.01	12.01	-5.00	90	236.73	6.93	11.33	-4.40
95	233.33	4.18	7.32	-3.13	95	249.88	4.16	7.00	-2.84
100	245.61	1.25	2.50	-1.25	100	263.03	1.25	2.50	-1.25

x = 0.30						x = 0.40				
%C from LE	x mm	Back Ord	Thickness	Face Ord		%C from LE	x mm	Back Ord	Thickness	Face Ord
0	0.00	2.50	5.00	-2.50		0	0.00	2.17	4.34	-2.17
2.5	6.96	4.91	8.68	-3.76		2.5	7.72	4.35	7.56	-3.21
5	13.93	7.05	11.88	-4.83		5	15.44	6.28	10.35	-4.07
10	27.85	10.35	16.56	-6.20		10	30.87	9.28	14.42	-5.15
20	55.70	14.90	22.69	-7.79		20	61.74	13.43	19.77	-6.34
30	83.55	17.59	26.29	-8.70		30	92.62	15.88	22.91	-7.02
40	111.40	18.78	28.08	-9.30		40	123.49	16.96	24.46	-7.51
50	139.26	18.68	28.13	-9.46		50	154.36	16.85	24.51	-7.66
60	167.11	17.41	26.38	-8.98		60	185.23	15.69	22.99	-7.29
70	194.96	14.99	22.88	-7.88		70	216.10	13.51	19.93	-6.42
80	222.81	11.45	17.63	-6.18		80	246.98	10.31	15.36	-5.06
90	250.66	6.77	10.64	-3.87		90	277.85	6.08	9.27	-3.19
95	264.58	4.11	6.70	-2.59		95	293.28	3.67	5.84	-2.17
100	278.51	1.25	2.50	-1.25		100	308.72	1.25	2.50	-1.25

x = 0.50						x = 0.60				
%C from LE	x mm	Back Ord	Thickness	Face Ord		%C from LE	x mm	Back Ord	Thickness	Face Ord
0	0.00	1.85	3.70	-1.85		0	0.00	1.50	3.00	-1.50
2.5	8.32	3.75	6.44	-2.70		2.5	8.72	3.14	5.32	-2.19
5	16.64	5.43	8.82	-3.39		5	17.43	4.57	7.29	-2.72
10	33.28	8.05	12.29	-4.25		10	34.86	6.80	10.16	-3.36
20	66.57	11.68	16.85	-5.17		20	69.72	9.92	13.93	-4.01
30	99.85	13.83	19.52	-5.69		30	104.58	11.76	16.14	-4.38
40	133.13	14.77	20.85	-6.08		40	139.44	12.55	17.23	-4.68
50	166.42	14.67	20.89	-6.22		50	174.31	12.46	17.27	-4.81
60	199.70	13.65	19.59	-5.94		60	209.17	11.59	16.19	-4.60
70	232.98	11.75	16.99	-5.24		70	244.03	9.97	14.04	-4.07
80	266.26	8.96	13.09	-4.13		80	278.89	7.60	10.82	-3.22
90	299.55	5.45	8.24	-2.79		90	313.75	4.65	6.90	-2.25
95	316.19	3.45	5.52	-2.07		95	331.18	3.00	4.75	-1.75
100	332.83	1.25	2.50	-1.25		100	348.61	1.25	2.50	-1.25

x = 0.70					x = 0.80				
%C from LE	x mm	Back Ord	Thickness	Face Ord	%C from LE	x mm	Back Ord	Thickness	Face Ord
0	0.00	1.25	2.50	-1.25	0	0.00	1.25	2.50	-1.25
2.5	8.81	2.53	4.21	-1.68	2.5	8.39	2.11	3.48	-1.37
5	17.62	3.71	5.76	-2.05	5	16.77	2.84	4.23	-1.39
10	35.24	5.56	8.03	-2.47	10	33.55	4.30	5.90	-1.60
20	70.49	8.15	11.01	-2.85	20	67.10	6.35	8.08	-1.73
30	105.73	9.69	12.75	-3.06	30	100.64	7.57	9.37	-1.80
40	140.98	10.34	13.62	-3.28	40	134.19	8.08	10.00	-1.92
50	176.22	10.26	13.65	-3.39	50	167.74	8.00	10.02	-2.02
60	211.46	9.54	12.80	-3.26	60	201.29	7.44	9.40	-1.96
70	246.71	8.20	11.10	-2.90	70	234.84	6.38	8.15	-1.77
80	281.95	6.24	8.55	-2.31	80	268.38	4.96	6.50	-1.54
90	317.20	3.85	5.55	-1.70	90	301.93	3.23	4.57	-1.34
95	334.82	2.56	4.00	-1.44	95	318.71	2.27	3.55	-1.28
100	352.44	1.25	2.50	-1.25	100	335.48	1.25	2.50	-1.25

x = 0.90						x = 0.95				
%C from LE	x mm	Back Ord	Thickness	Face Ord		%C from LE	x mm	Back Ord	Thickness	Face Ord
0	0.00	1.25	2.50	-1.25		0	0.00	1.25	2.50	-1.25
2.5	7.01	1.74	2.90	-1.16		2.5	5.41	1.56	2.69	-1.13
5	14.01	2.19	3.25	-1.06		5	10.82	1.85	2.85	-1.00
10	28.02	3.03	3.97	-0.94		10	21.64	2.38	3.20	-0.82
20	56.04	4.38	5.16	-0.79		20	43.28	3.25	3.81	-0.56
30	84.06	5.24	5.98	-0.75		30	64.93	3.83	4.29	-0.47
40	112.08	5.59	6.39	-0.80		40	86.57	4.09	4.59	-0.50
50	140.11	5.53	6.40	-0.87		50	108.21	4.04	4.59	-0.55
60	168.13	5.13	6.00	-0.87		60	129.85	3.81	4.43	-0.62
70	196.15	4.46	5.32	-0.86		70	151.49	3.40	4.10	-0.70
80	224.17	3.57	4.49	-0.92		80	173.14	2.82	3.65	-0.83
90	252.19	2.48	3.50	-1.02		90	194.78	2.10	3.11	-1.01
95	266.20	1.88	3.00	-1.12		95	205.60	1.69	2.80	-1.11
100	280.21	1.25	2.50	-1.25		100	216.42	1.25	2.50	-1.25

Table- A-3 Nominal axial velocity ratio distribution over the propeller disk in model scale.

ANGLE (degrees)	AXIAL VELOCITY RATIO – $V_x/V_s$				
0	0.417	0.631	0.691	0.674	0.622
10	0.506	0.695	0.738	0.708	0.650
20	0.586	0.748	0.780	0.745	0.687
30	0.660	0.792	0.818	0.789	0.741
40	0.724	0.829	0.854	0.838	0.808
50	0.779	0.859	0.886	0.883	0.871
60	0.823	0.884	0.911	0.918	0.917
70	0.855	0.903	0.930	0.943	0.947
80	0.876	0.918	0.946	0.962	0.968
90	0.887	0.928	0.959	0.977	0.987
100	0.890	0.935	0.968	0.989	1.000
110	0.887	0.935	0.970	0.993	1.000
120	0.880	0.929	0.963	0.984	1.000
130	0.870	0.916	0.946	0.961	0.978
140	0.858	0.899	0.921	0.925	0.932
150	0.846	0.881	0.894	0.883	0.878
160	0.835	0.867	0.870	0.846	0.827
170	0.827	0.860	0.857	0.823	0.793
180	0.824	0.862	0.857	0.820	0.786
190	0.825	0.874	0.872	0.838	0.807
200	0.832	0.892	0.898	0.874	0.853
210	0.842	0.913	0.929	0.918	0.910
220	0.855	0.932	0.957	0.961	0.965
230	0.868	0.944	0.977	0.993	1.000
240	0.876	0.947	0.986	1.000	1.000
250	0.877	0.940	0.983	1.000	1.000
260	0.870	0.927	0.971	0.997	1.000
270	0.852	0.910	0.956	0.979	0.992
280	0.825	0.891	0.939	0.959	0.968
290	0.786	0.871	0.921	0.937	0.940
300	0.730	0.845	0.897	0.907	0.900
310	0.655	0.811	0.864	0.865	0.843
320	0.56	0.766	0.822	0.814	0.777
330	0.464	0.716	0.776	0.763	0.717
340	0.397	0.672	0.737	0.723	0.678
350	0.385	0.646	0.709	0.693	0.646
360	0.417	0.631	0.691	0.674	0.622
<b>r/R</b>	<b>0.267</b>	<b>0.453</b>	<b>0.64</b>	<b>0.827</b>	<b>1.013</b>



Table- A-4 Nominal radial velocity ratio distribution over the propeller disk in model scale.

ANGLE (degrees)	RADIAL VELOCITY RATIO – Vr/Vs				
0	0.108	-0.041	-0.146	-0.195	-0.234
10	0.04	-0.093	-0.157	-0.189	-0.207
20	0.012	-0.09	-0.12	-0.127	-0.139
30	0.004	-0.072	-0.078	-0.071	-0.073
40	0.008	-0.047	-0.042	-0.031	-0.021
50	0.021	-0.017	-0.01	0	0.017
60	0.039	0.018	0.021	0.031	0.046
70	0.061	0.055	0.053	0.064	0.072
80	0.084	0.091	0.086	0.099	0.097
90	0.106	0.12	0.116	0.129	0.12
100	0.127	0.138	0.138	0.149	0.139
110	0.143	0.146	0.152	0.157	0.151
120	0.155	0.145	0.154	0.15	0.153
130	0.164	0.138	0.146	0.132	0.143
140	0.167	0.128	0.13	0.106	0.124
150	0.168	0.119	0.111	0.079	0.099
160	0.165	0.113	0.091	0.056	0.071
170	0.16	0.111	0.075	0.041	0.047
180	0.154	0.112	0.065	0.035	0.03
190	0.146	0.115	0.062	0.038	0.024
200	0.138	0.118	0.065	0.048	0.027
210	0.129	0.119	0.071	0.061	0.04
220	0.122	0.116	0.079	0.074	0.057
230	0.114	0.109	0.084	0.082	0.074
240	0.105	0.099	0.085	0.085	0.086
250	0.095	0.085	0.079	0.081	0.088
260	0.082	0.07	0.068	0.071	0.08
270	0.064	0.054	0.051	0.056	0.062
280	0.042	0.036	0.032	0.039	0.036
290	0.016	0.016	0.012	0.018	0.008
300	-0.009	-0.005	-0.007	-0.006	-0.022
310	-0.026	-0.026	-0.027	-0.038	-0.055
320	-0.025	-0.041	-0.05	-0.079	-0.096
330	0.001	-0.042	-0.079	-0.128	-0.154
340	0.054	-0.026	-0.115	-0.18	-0.227
350	0.112	-0.005	-0.147	-0.215	-0.287
360	0.108	-0.041	-0.146	-0.195	-0.234
<b>r/R</b>	<b>0.267</b>	<b>0.453</b>	<b>0.64</b>	<b>0.827</b>	<b>1.013</b>

Table- A-5 Nominal tangential velocity ratio distribution over the propeller disk in model scale.

ANGLE (degrees)	TANGENTIAL VELOCITY RATIO – $V_t/V_s$				
0	-0.147	-0.152	-0.109	-0.096	-0.077
10	-0.182	-0.169	-0.141	-0.118	-0.108
20	-0.22	-0.19	-0.185	-0.175	-0.187
30	-0.251	-0.206	-0.21	-0.209	-0.229
40	-0.271	-0.214	-0.214	-0.215	-0.229
50	-0.277	-0.215	-0.208	-0.205	-0.208
60	-0.27	-0.209	-0.197	-0.19	-0.183
70	-0.253	-0.197	-0.185	-0.175	-0.162
80	-0.227	-0.177	-0.169	-0.159	-0.146
90	-0.196	-0.151	-0.148	-0.14	-0.13
100	-0.163	-0.12	-0.121	-0.114	-0.108
110	-0.128	-0.088	-0.088	-0.083	-0.078
120	-0.095	-0.058	-0.053	-0.047	-0.044
130	-0.065	-0.032	-0.02	-0.012	-0.009
140	-0.038	-0.012	0.007	0.018	0.022
150	-0.016	0	0.024	0.039	0.043
160	0.001	0.006	0.031	0.049	0.051
170	0.014	0.008	0.028	0.048	0.048
180	0.024	0.009	0.02	0.04	0.037
190	0.031	0.011	0.011	0.029	0.023
200	0.039	0.017	0.005	0.019	0.012
210	0.048	0.029	0.008	0.016	0.011
220	0.061	0.046	0.019	0.021	0.02
230	0.078	0.067	0.04	0.035	0.04
240	0.099	0.089	0.066	0.055	0.067
250	0.124	0.109	0.095	0.079	0.097
260	0.15	0.126	0.119	0.101	0.124
270	0.174	0.138	0.137	0.119	0.146
280	0.191	0.146	0.147	0.133	0.162
290	0.198	0.151	0.149	0.144	0.173
300	0.192	0.154	0.147	0.153	0.184
310	0.174	0.156	0.146	0.162	0.194
320	0.145	0.153	0.144	0.168	0.196
330	0.108	0.136	0.136	0.158	0.177
340	0.062	0.089	0.107	0.117	0.116
350	-0.006	-0.004	0.034	0.03	0.015
360	-0.147	-0.152	-0.109	-0.096	-0.077
<b>r/R</b>	<b>0.267</b>	<b>0.453</b>	<b>0.64</b>	<b>0.827</b>	<b>1.013</b>

Wake measurements have been carried out in the Istanbul Technical University (ITU) Ata Nutku Towing Tank. Wake measurements were conducted with a computer controlled five-hole pitot-tube. The velocities across the propeller disk were measured from 0 degrees to 360 degrees. 0 degrees of wake corresponds to the Top Dead Centre – TDC, 180 degrees of the wake corresponds to the Bottom Dead Centre – BDC and 90 degrees of the wake points out the starboard side of the hull when viewed from the aft towards the bow.

# Appendix B – Drawings and Other Details of Meridian Standard Propeller Series

## B.1 Introduction

Appendix B contains the supplement material presenting the details of the Meridian Standard Propeller Series. The Meridian Sections and profile details are initially presented. Following this, the propeller drawings of the selected subset of the series members are given in order to provide necessary additional information on the propellers.

## B.2 Propeller blade sections and details

The Meridian Standard Propeller series has been manufactured by SMP where accumulated experience in propeller design has been implemented and utilized. Figure- B-2 and Figure- B-5 present the definitions of the blade sections. The definition includes the chordwise distribution of data points and the definition used for the thickness and ordinates at the data points. Following this, the zoomed detail of the blade finish at propeller tip and the leading and trailing edge radius has been given.

<u>PITCH DISTRIBUTION.</u>										
$X = r/R$	.2	.3	.4	.5	.6	.7	.8	.9	.95	1.0
% MAX. PITCH	66.8	75.2	83.6	92.0	98.8	100	100	100	100	100
(MEAN PITCH = 95.6 %)										

Figure- B-1 Meridian Standard Propeller Section Pitch Distribution.

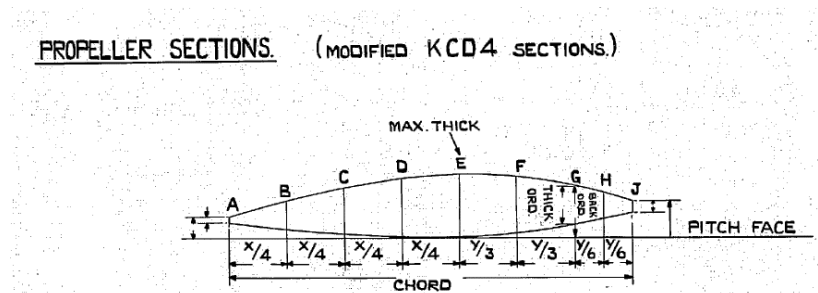


Figure- B-2 Definition of the Meridian Propeller Sections.

### THICKNESS OFFSETS

X	A	B	C	D	E	F	G	H	J
2	5.82	47.98	79.92		100%	89.12	60.30	39.44	13.90
3	6.61	48.24				91.30	63.12	41.52	12.42
4	7.59	48.53				92.0	64.22	42.00	12.29
5							64.86	42.24	12.64
6							65.16	42.58	13.32
7									14.62
8									
9									

(THICKNESS OFFSETS, NOT SHOWN HERE, SAME AS FOR BACK OFFSETS)

Figure- B-3 Thickness offset of the Meridian Standard Section.

### BACK OFFSETS (IN % OF MAX. THICKNESS (E) AT EACH RADIUS)

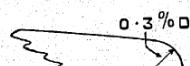
X	A	B	C	D	E	F	G	H	J
2	27.89	57.27	80.29	94.53	100%	95.40	79.36	66.46	49.65
3	20.55	52.81	78.07	94.46	100%	93.52	74.70	60.41	40.89
4	13.20	49.56	77.28	94.39	100%	92.06	70.90	54.98	32.60
5	8.89	48.84	76.92	94.43	100%	91.20	67.67	49.88	25.28
6	10.62	49.31	77.44	94.61	100%	90.98	65.59	45.40	19.40
7	12.63	50.71	78.81	94.89	100%	91.32	65.30	43.22	15.28
8	14.90	52.89	80.48	95.43	100%	91.98	65.55	43.69	17.22
9	21.45	55.31	82.13	96.42	100%	92.90	64.30	42.89	21.46

MEASUREMENTS FROM PITCH FACE

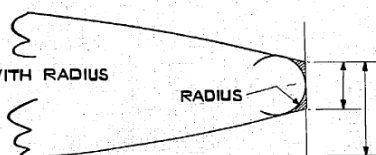
Figure- B-4 Back offsets of the Meridian Standard Section.

### BLADE FINISH

TIP THICKNESS =  $0.3\% D$



FINISH NOSE AND TAIL WITH RADIUS AS SHOWN.



ALL THICKNESSES MUST BE GIVEN TO TWO DECIMAL PLACES (IN INS.)

Figure- B-5 Detail Drawings of the Propeller Blade Finish at Tip and Nose and Tail Radius.

# STONE MANGANESE MARINE LIMITED. LONDON. ENGLAND.

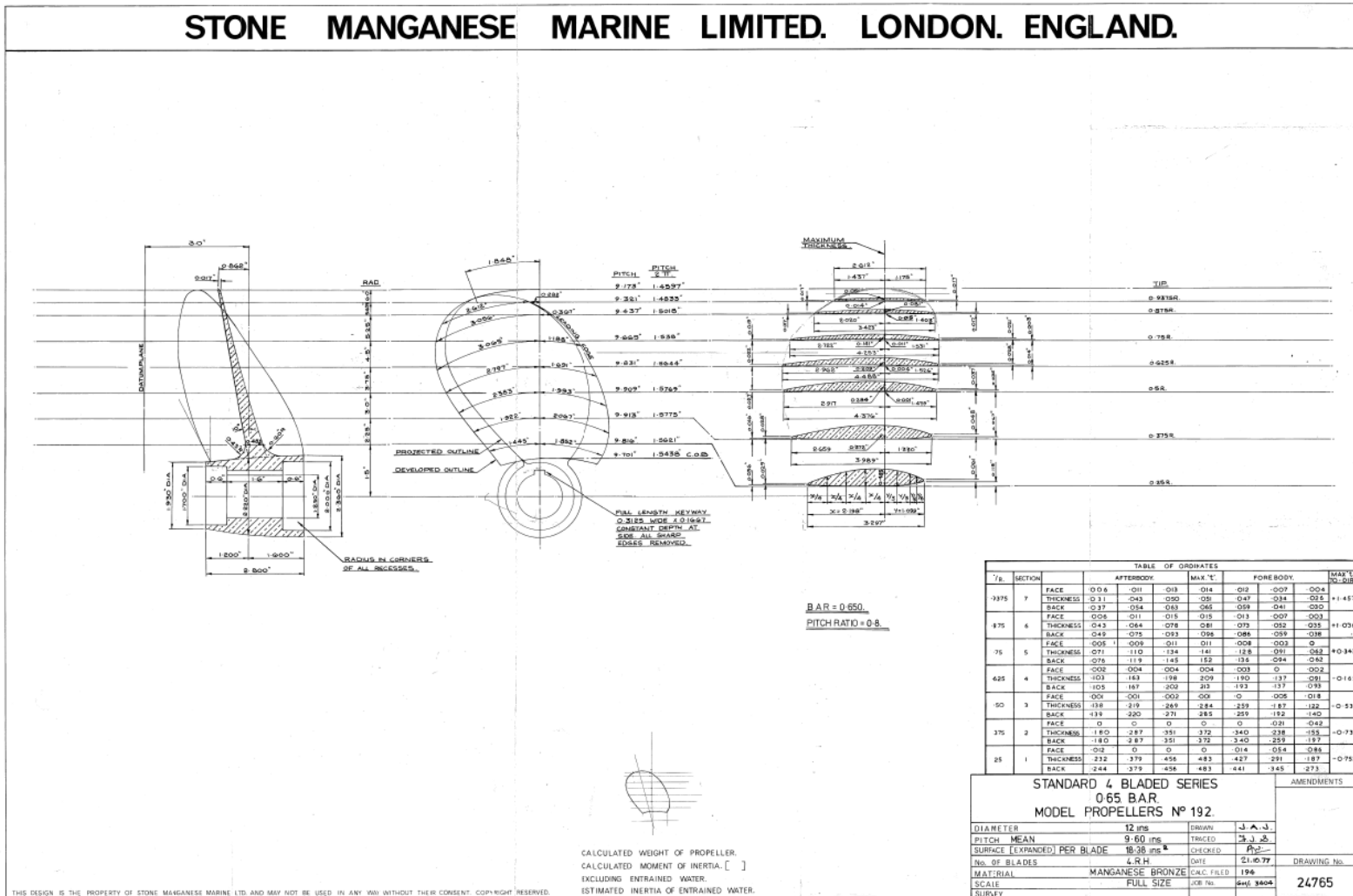


Figure- B-6 KCD 192 original propeller drawings.

# STONE MANGANESE MARINE LIMITED, LONDON, ENGLAND.

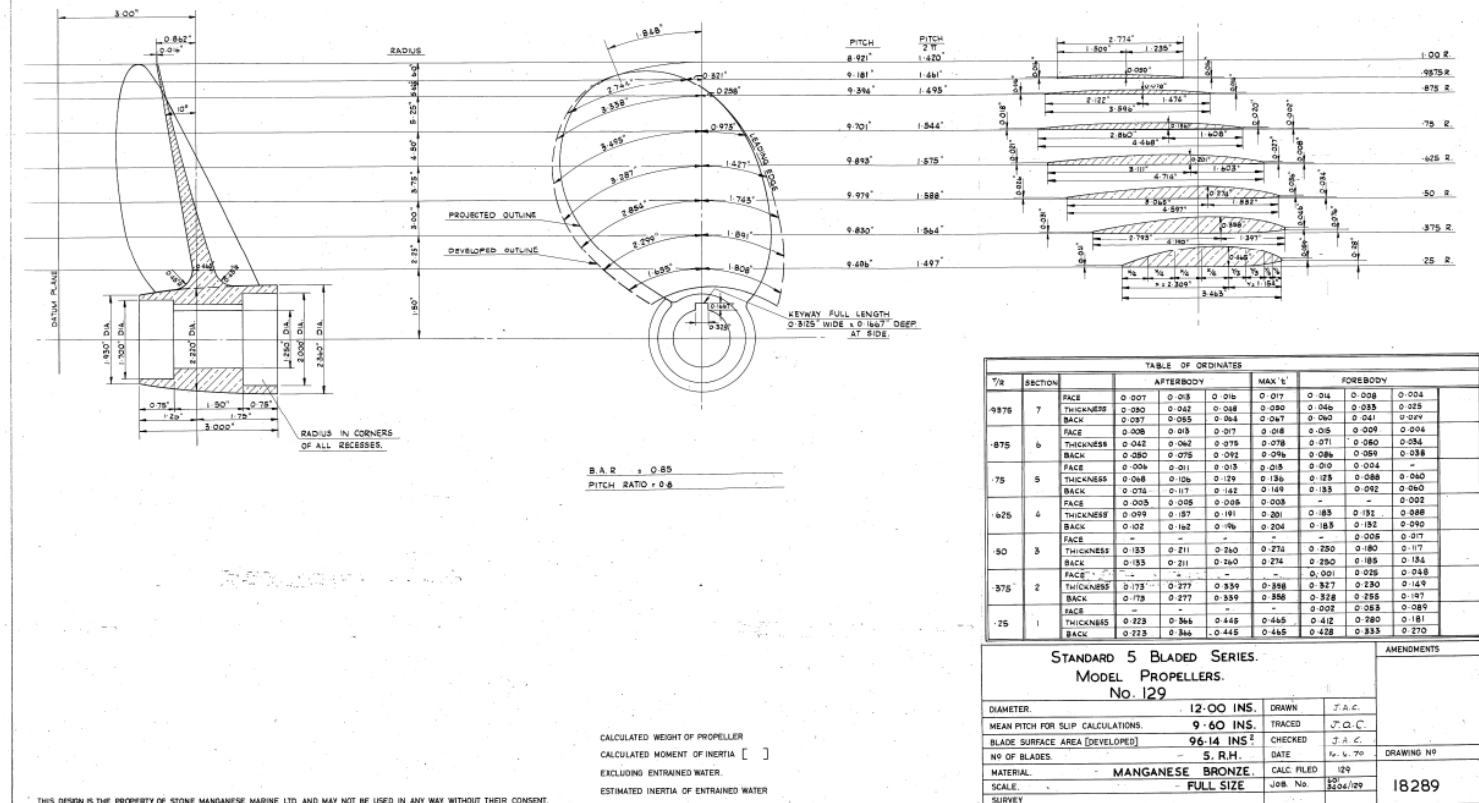


Figure- B-7 KCD 129 original propeller drawings.

# STONE MANGANESE MARINE LIMITED, LONDON, ENGLAND.

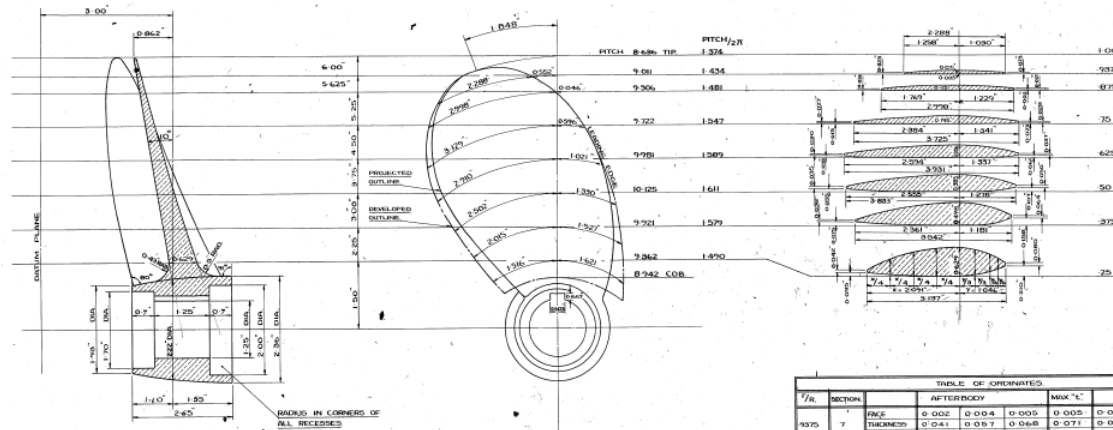


TABLE OF COORDINATES					
Y/R	SECTION	AFTERBODY	MAX "S"	FOREBODY	MAX "S"
8375	1	FACE	0.002	0.004	0.005
		THICKNESS	0.041	0.017	0.048
		BACK	0.041	0.017	0.048
8475	6	FACE	0.057	0.085	0.104
		THICKNESS	0.074	0.148	0.185
		BACK	0.102	0.150	0.185
75	5	FACE	0.019	0.005	—
		THICKNESS	0.134	0.222	0.273
		BACK	0.153	0.227	0.273
625	4	FACE	0.030	0.007	—
		THICKNESS	0.179	0.298	0.370
		BACK	0.209	0.305	0.370
375	2	FACE	0.041	0.010	—
		THICKNESS	0.230	0.381	0.476
		BACK	0.271	0.391	0.476
25	1	FACE	0.052	0.002	—
		THICKNESS	0.293	0.494	0.612
		BACK	0.345	0.506	0.612

STANDARD 6 BLADED SERIES.  
MODEL PROPELLERS.  
K.C.D. 65.

Rev. No. 239  
Date. 27.11.67

AMENDMENTS  
Rev. No. 239  
Date. 27.11.67

DIAMETER	12.00 ins.	DRAWN	K.C.
MEAN PITCH FOR SLP CALCULATIONS	9.600	TRACED	10/10/67
BLADE SURFACE AREA (DEVELOPED)	96.78 sq. ins.	CHECKED	11/11/67
NO OF BLADES	6 R.H.	DATE	20/11/67
MATERIAL	MANGANESE BRONZE OR PEWTER	CALC. FILED	K.C.D. 65.
SCALE	FULL SIZE	JOHN 165	2X 62
SURVEY			



CALCULATED WEIGHT OF PROPELLER 8.664 lbs (MANGANESE BRONZE)  
CALCULATED MOMENT OF INERTIA [ ]  
EXCLUDING ENTRAINED WATER  
ESTIMATED INERTIA OF ENTRAINED WATER

THIS DESIGN IS THE PROPERTY OF STONE MANGANESE MARINE LTD. AND MAY NOT BE USED IN ANY WAY WITHOUT THEIR CONSENT.

Figure- B-8 KCD 65 original propeller drawings.



[illegible]

		TABLE OF GRIMMATES												
T/ps	SECTION		AFTERBURY			MAG. °C			FOREBURY			PRE-GRIM		
9135 7	FACE		0.005	0.010	0.012	0.018	0.011	0.036	0.008					
	THICKNESS		0.035	0.045	0.053	0.054	0.030	0.034	0.026				1.85	
	BACK		0.038	0.055	0.065	0.067	0.061	0.040	0.031					
	FACE		0.005	0.008	0.009	0.011	0.009	0.003	0.003					
875 6	THICKNESS		0.048	0.048	0.062	0.065	0.077	0.055	0.033				1.19	
	BACK		0.050	0.076	0.073	0.064	0.086	0.059	0.037					
	FACE		—	0.001	0.001	0.001	0.001	0.001	0.001					
	THICKNESS		0.075	0.117	0.122	0.135	0.076	0.064	0.064				0.60	
625 4	FACE		0.009	—	—	—	—	0.003	0.013					
	THICKNESS		0.106	0.172	0.209	0.220	0.201	0.147	0.076				0.78	
	BACK		0.109	0.172	0.209	0.220	0.201	0.147	0.076					
	FACE		0.008	—	—	—	—	—	0.016					
510 3	THICKNESS		0.145	0.231	0.284	0.299	0.274	0.176	0.128				0.25	
	BACK		0.151	0.231	0.284	0.299	0.274	0.176	0.164					
	FACE		0.012	0.028	0.028	0.028	0.028	0.028	0.028					
	THICKNESS		0.164	0.303	0.390	0.392	0.358	0.253	0.163				0.56	
975 2	BACK		0.078	0.083	0.310	0.362	0.367	0.235	0.181					
	FACE		0.022	0.040	0.002	0.002	0.026	0.081	0.121					
	THICKNESS		0.244	0.400	0.485	0.509	0.483	0.319	0.193				0.57	
	BACK		0.008	0.008	0.008	0.008	0.017	0.037	0.037					

DIAMETER	12-00 ins.	DRAWN	S. Shattell
MEAN FITCH FOR SLIP CALCULATIONS	9-60 ins.	TRACED	EDMund
BLADE SURFACE AREA [FWELOVED]	118-76 sq ins.	CHECKED	"
NO OF BLADES	6 R.H.	DATE	10/29/60
MATERIAL	MANGANESE BRONZE	CAD FILED	NO 7-6
SCALE	FULL SIZE	JOB NO.	EX 90
SUBJECT			14647

EXCLUDING ENTRAINED WATER  
ESTIMATED INERTIA OF ENTRAINED WATER

THIS DESIGN IS THE PROPERTY OF STONE MANGANESE MARINE LTD. AND MAY NOT BE USED IN ANY WAY WITHOUT THEIR CONSENT

B-6

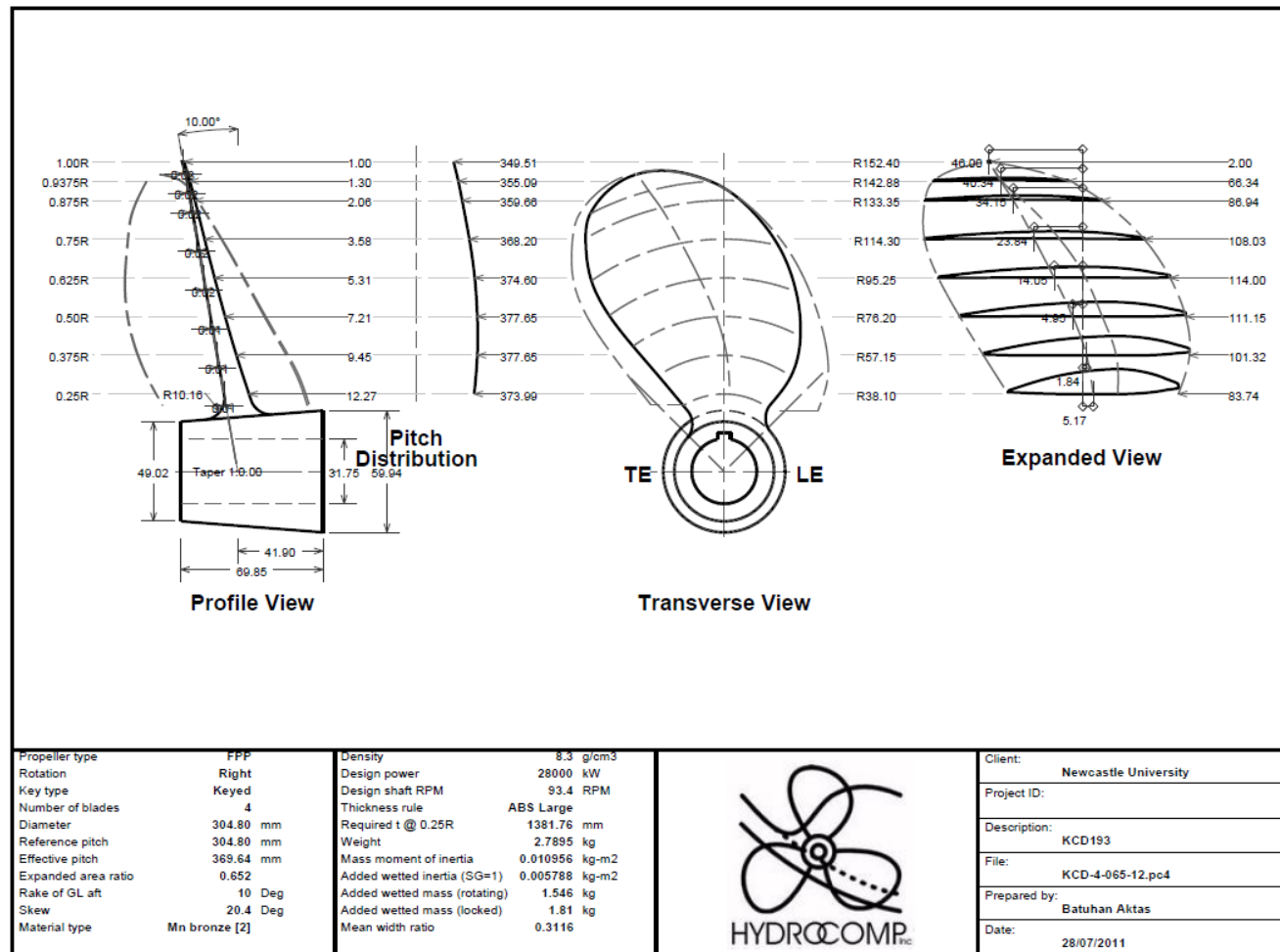


Figure- B-10 KCD 193 digitized propeller drawings in millimetre units.

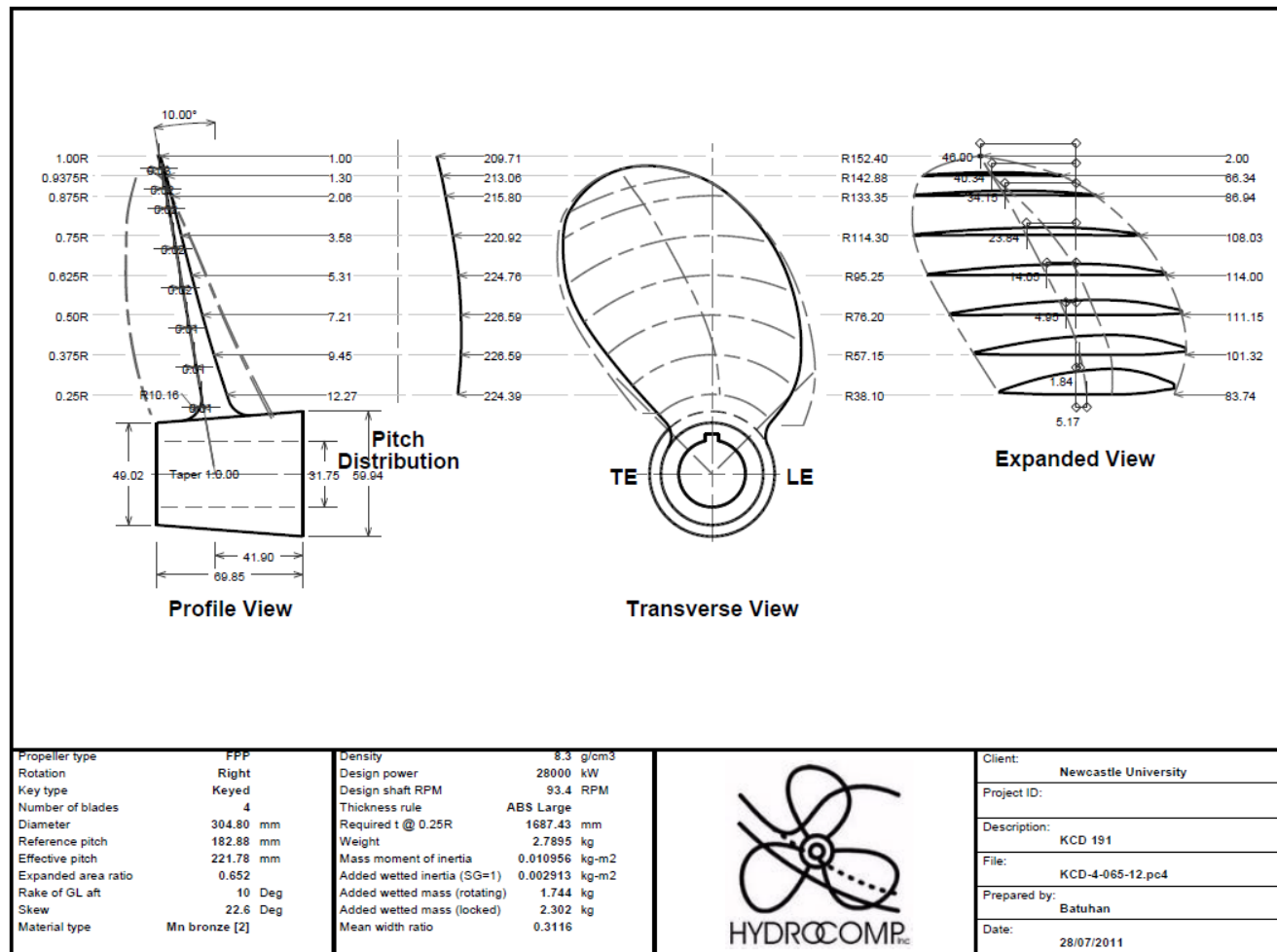


Figure- B-11 KCD 191 digitized propeller drawings in millimetre units.

# Appendix C - Background Noise Measurements for Standard Series Propeller Tests

## C.1 Introduction

*This appendix presents the summary of the background noise measurements conducted in the Emerson Cavitation Tunnel facility. The measured background noise levels of the facility are used to correct the total noise levels of the systematic test data using the Meridian standard propeller series.*

## C.2 Background noise measurements

The background noise measurements are conducted for the conditions as outlined in Table- C-1. Therefore, in addition to the exact conditions that the systematic cavitation tunnel tests using Meridian standard propeller series are conducted, the conditions for only impeller running and only dynamometer operating are also recorded and presented in this appendix. The SPL's corresponding to the test conditions listed in C-1 are presented in Figures C-1 through C-12.

Table- C-1 Background noise test matrix.

Running Condition	Tunnel water velocity V [m/s]	Dynamometer, N [RPM]	Pressure	Inflow condition
Impeller only	1, 1.5, 2, 2.5, 3, 3.5 & 4	Turned off	Atmospheric	Open Water
Dynamometer only	Turned off	600, 800, 1000, 1200, 1400, 1500, 1600, 1750 & 2000	Pressure Condition only	
Impeller & Dynamometer on	3	600, 800, 1000, 1200, 1400, 1500, 1600, 1750 & 2000	Atmospheric Pressure, 150 mmHg & 300 mmHg Vacuum applied	Open Water & Behind ECT1, ECT2, ECT3

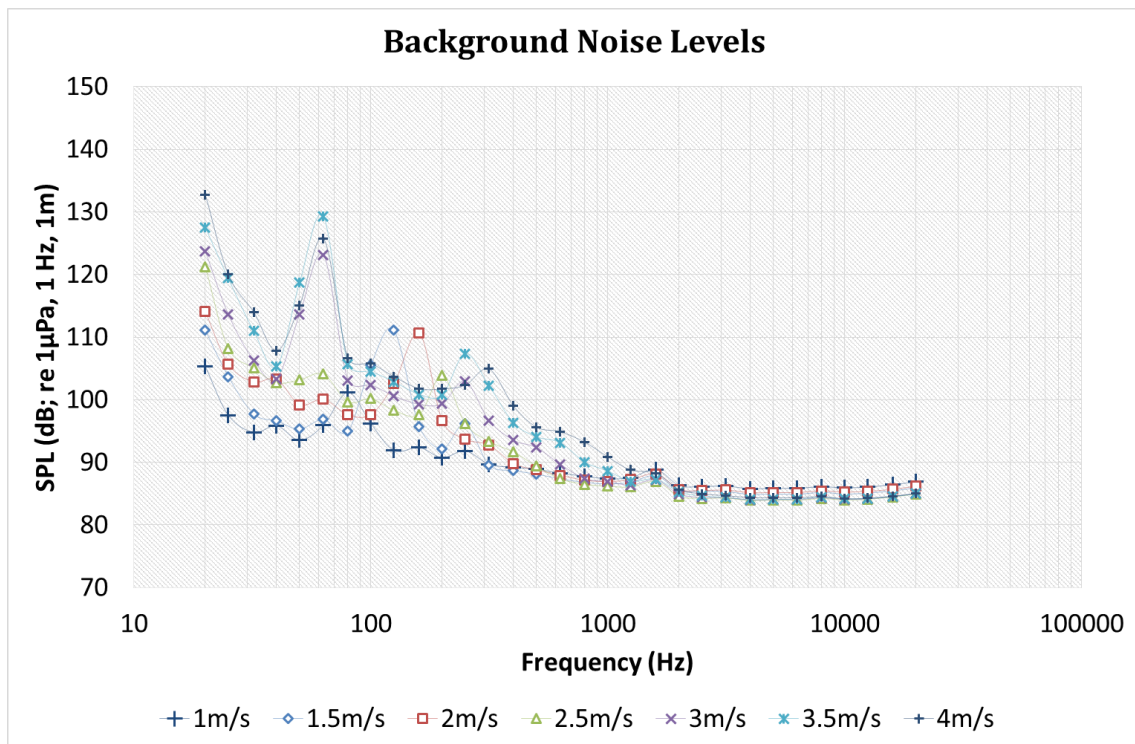


Figure- C-1 Impeller operating only background noise levels at atmospheric pressure in open water condition.

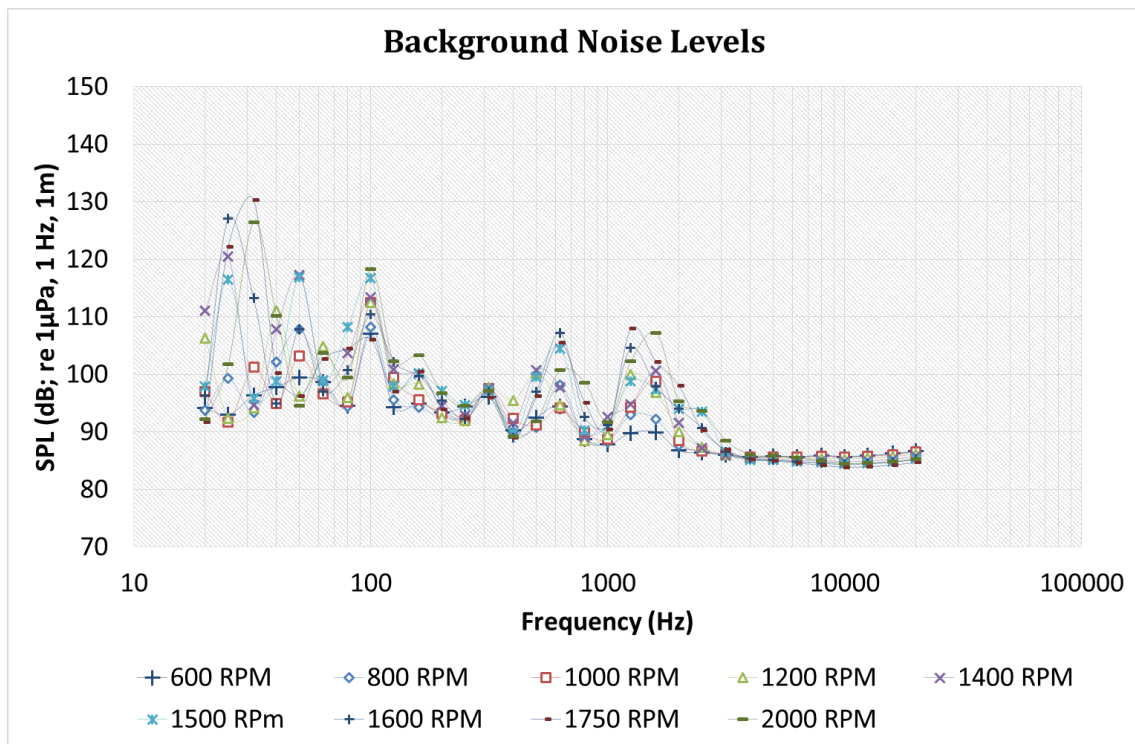


Figure- C-2 Dynamometer operating only background noise levels at atmospheric pressure in open water condition.

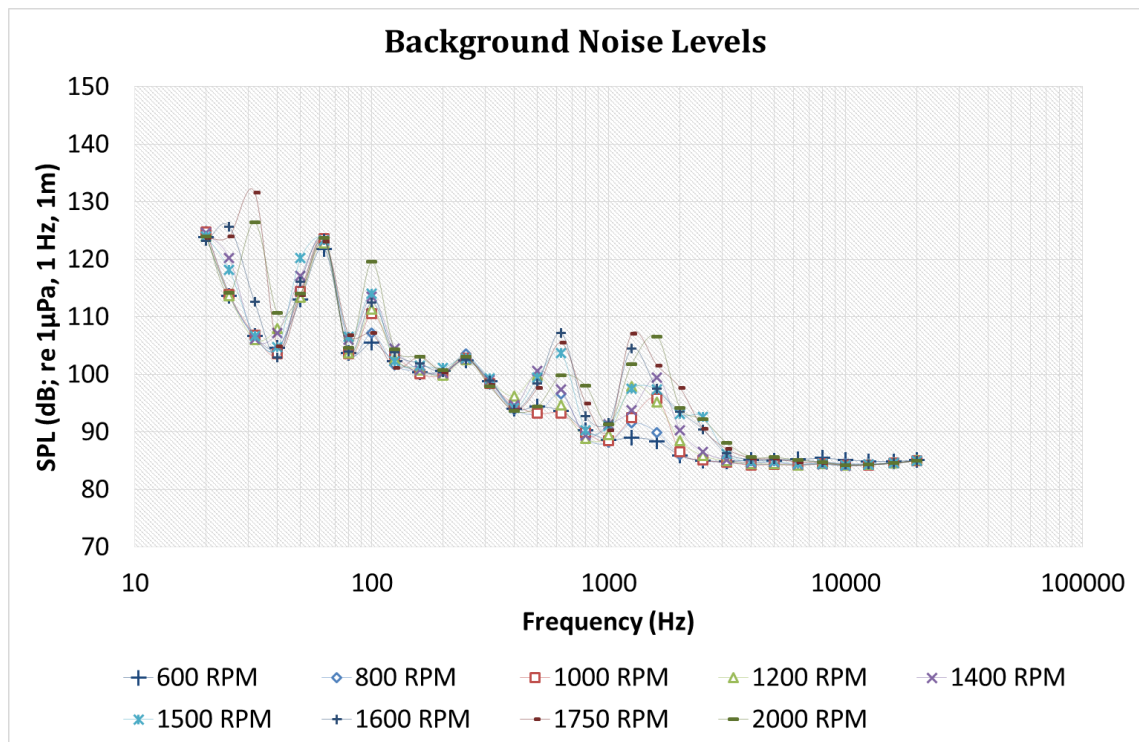


Figure- C-3 Background noise levels at 3m/s inflow speed for different dynamometer speeds at atmospheric pressure in open water condition.

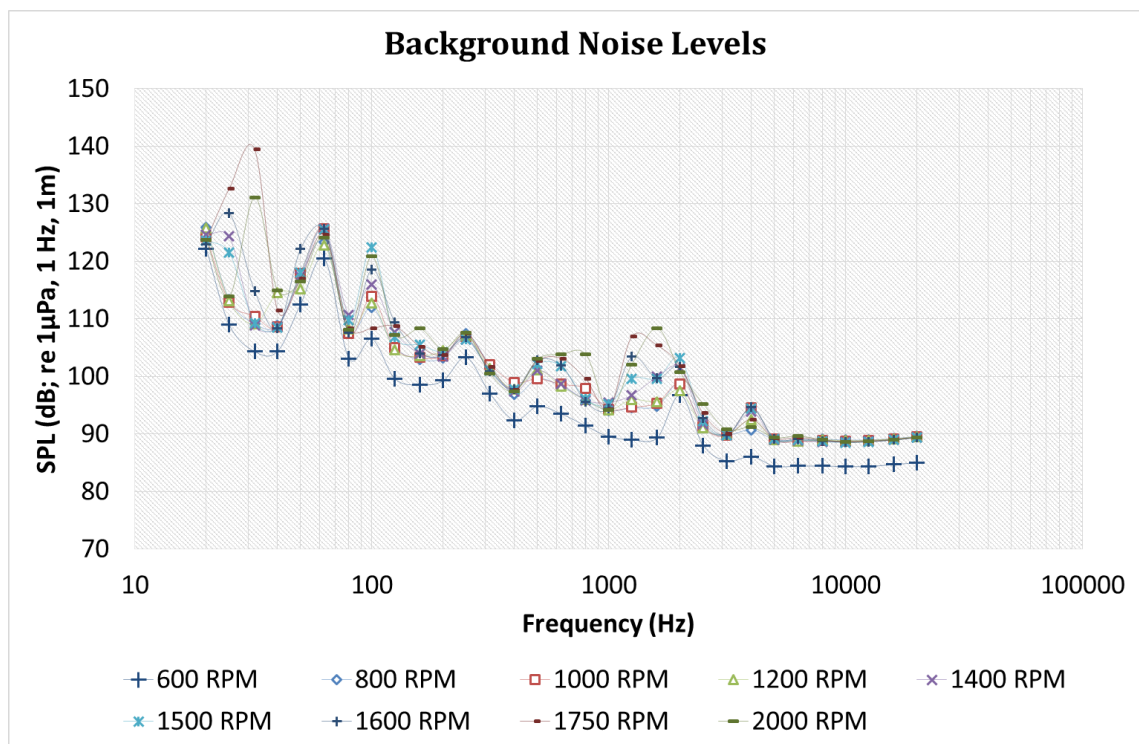


Figure- C-4 Background noise levels at 3m/s inflow speed for different dynamometer speeds at atmospheric pressure behind ECT1.



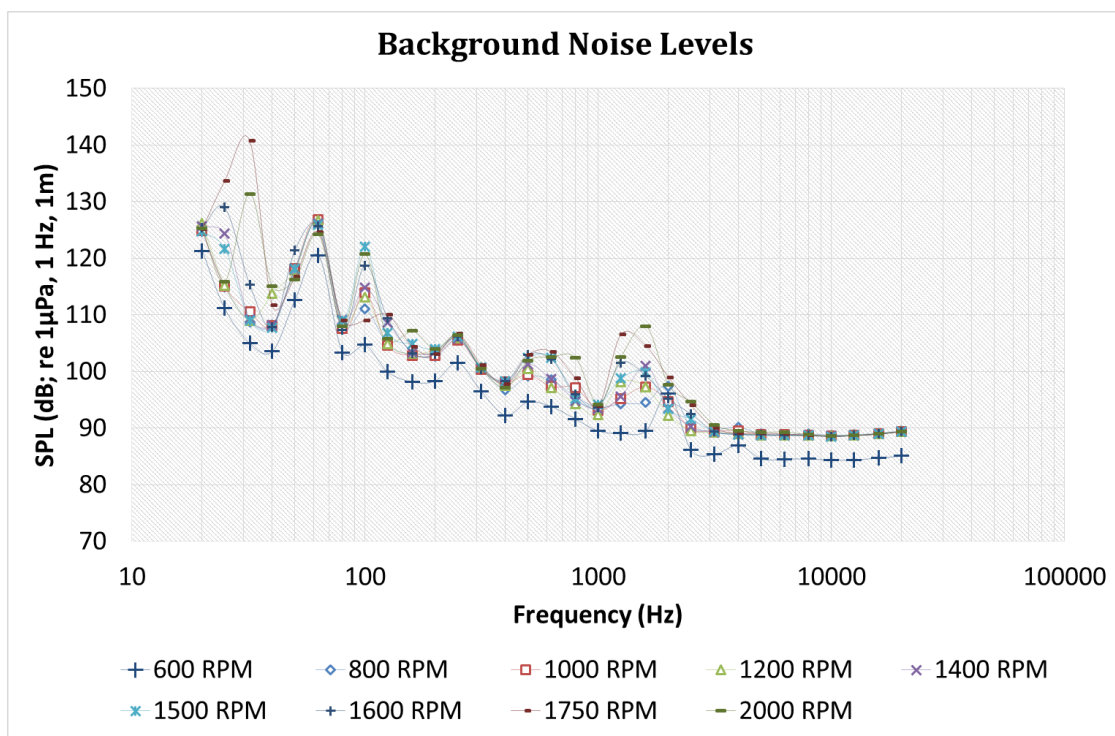


Figure- C-5 Background noise levels at 3m/s inflow speed for different dynamometer speeds at atmospheric pressure behind ECT2.

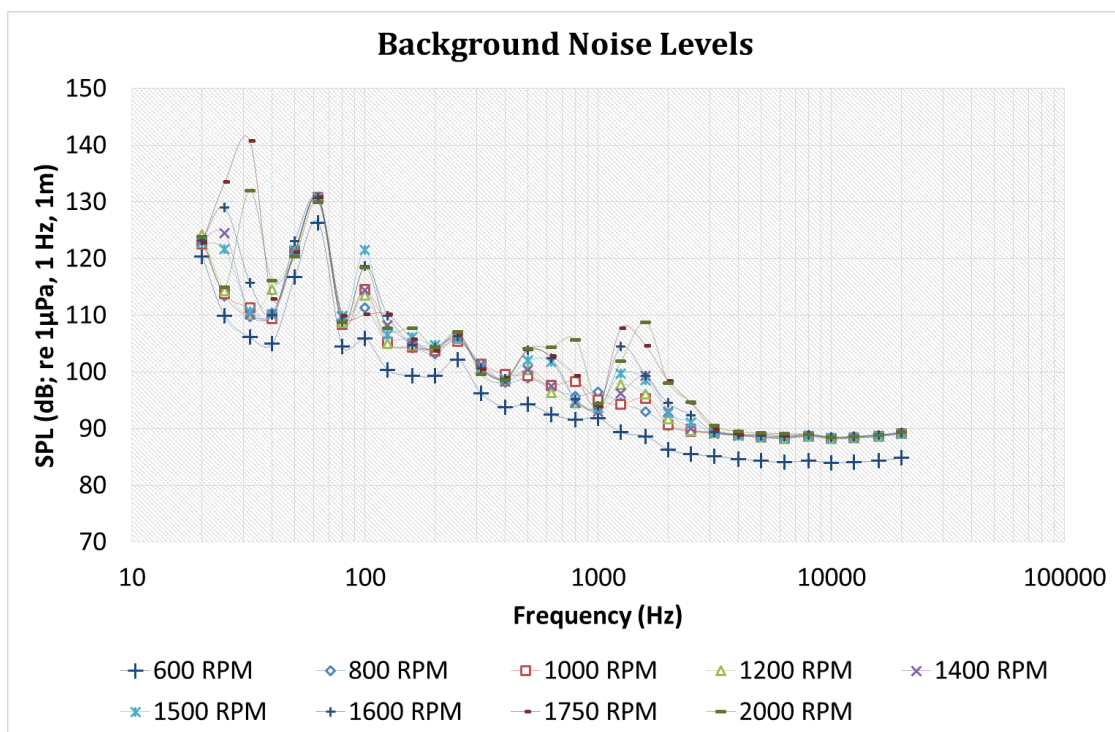


Figure- C-6 Background noise levels at 3m/s inflow speed for different dynamometer speeds at atmospheric pressure behind ECT3.

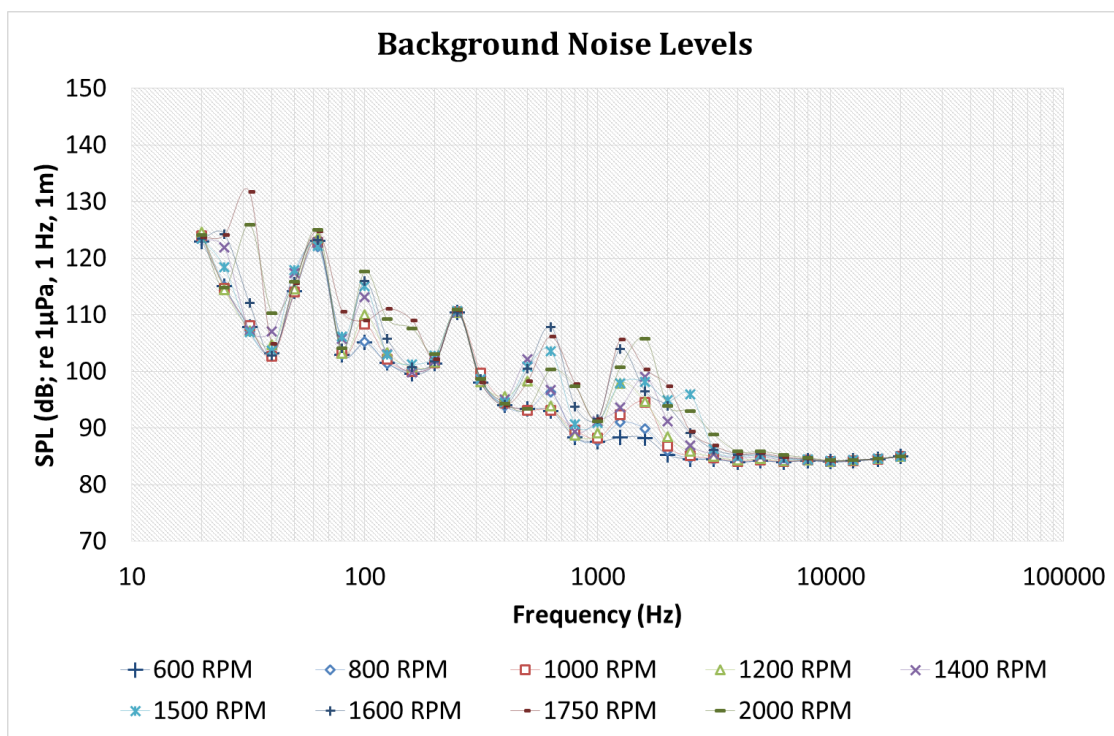


Figure- C-7 Background noise levels at 3m/s inflow speed for different dynamometer speeds at 150 mmHg vacuum applied in open water condition.

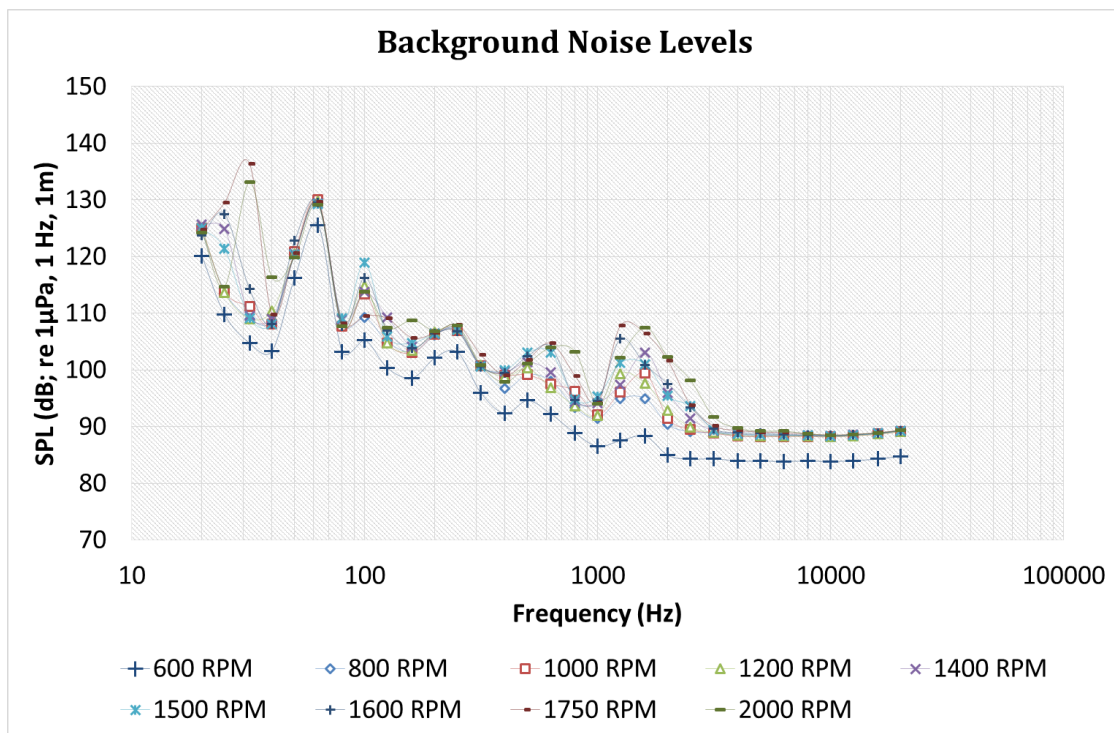


Figure- C-8 Background noise levels at 3m/s inflow speed for different dynamometer speeds at 150 mmHg vacuum applied behind ECT1.



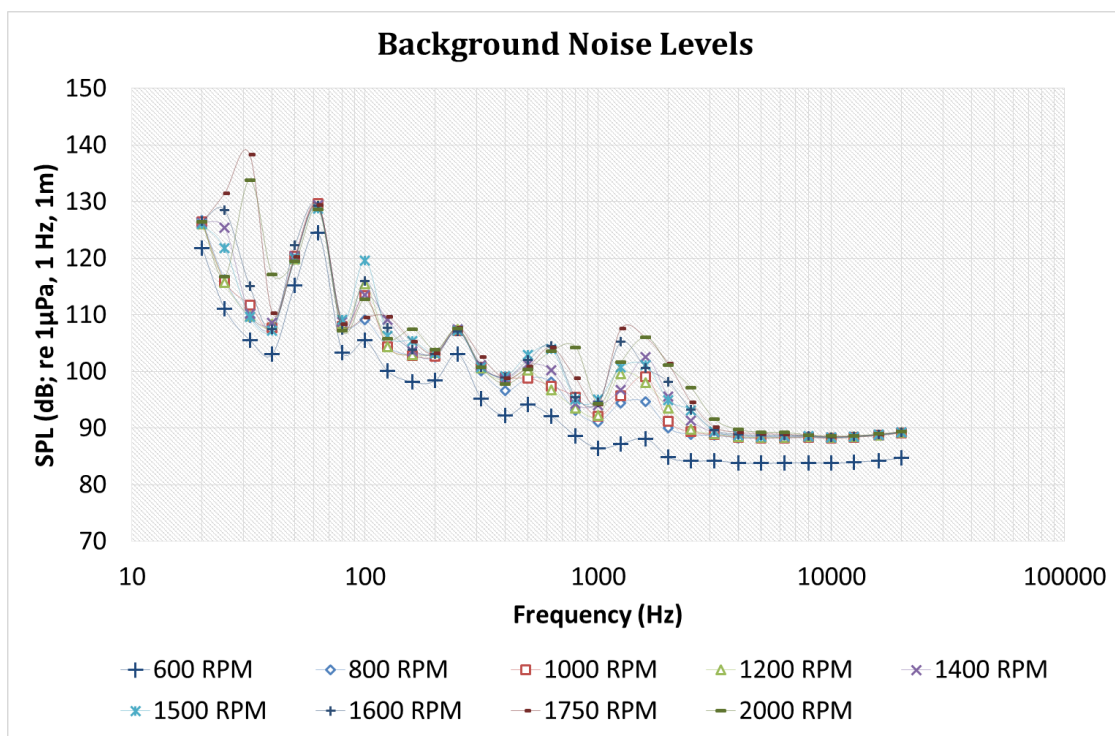


Figure- C-9 Background noise levels at 3m/s inflow speed for different dynamometer speeds at 150 mmHg vacuum applied behind ECT2.

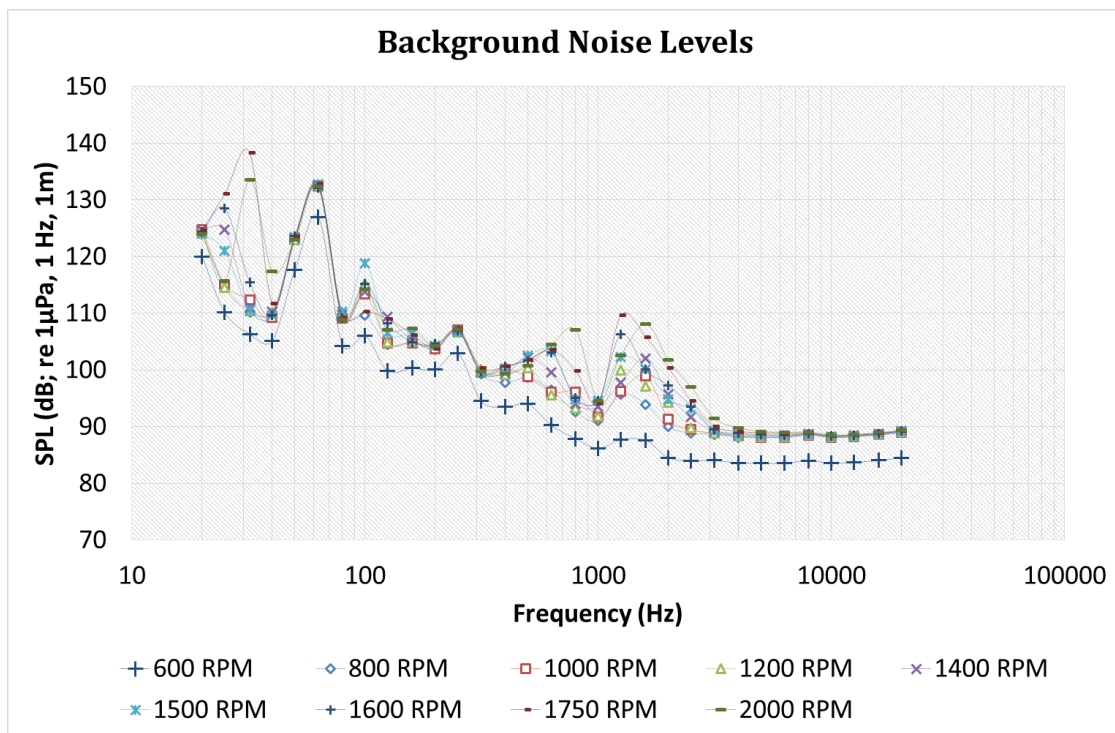


Figure- C-10 Background noise levels at 3m/s inflow speed for different dynamometer speeds at 150 mmHg vacuum applied behind ECT3.

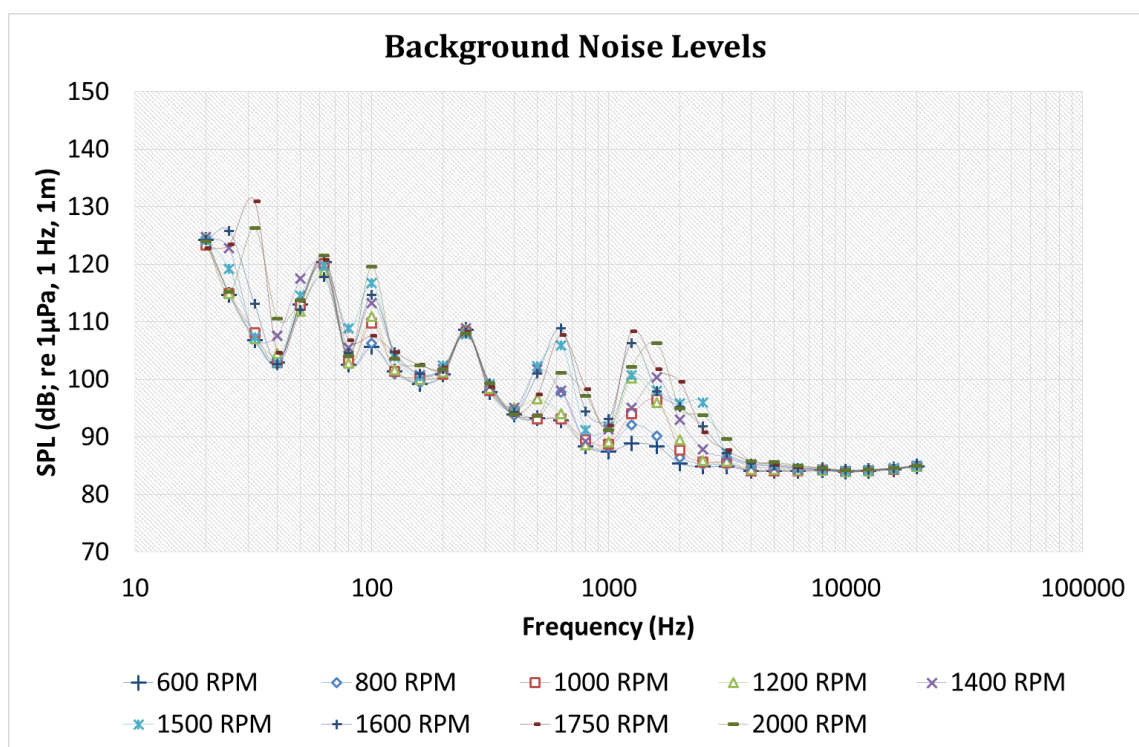


Figure- C-11 Background noise levels at 3m/s inflow speed for different dynamometer speeds at 300 mmHg vacuum applied in open water condition.

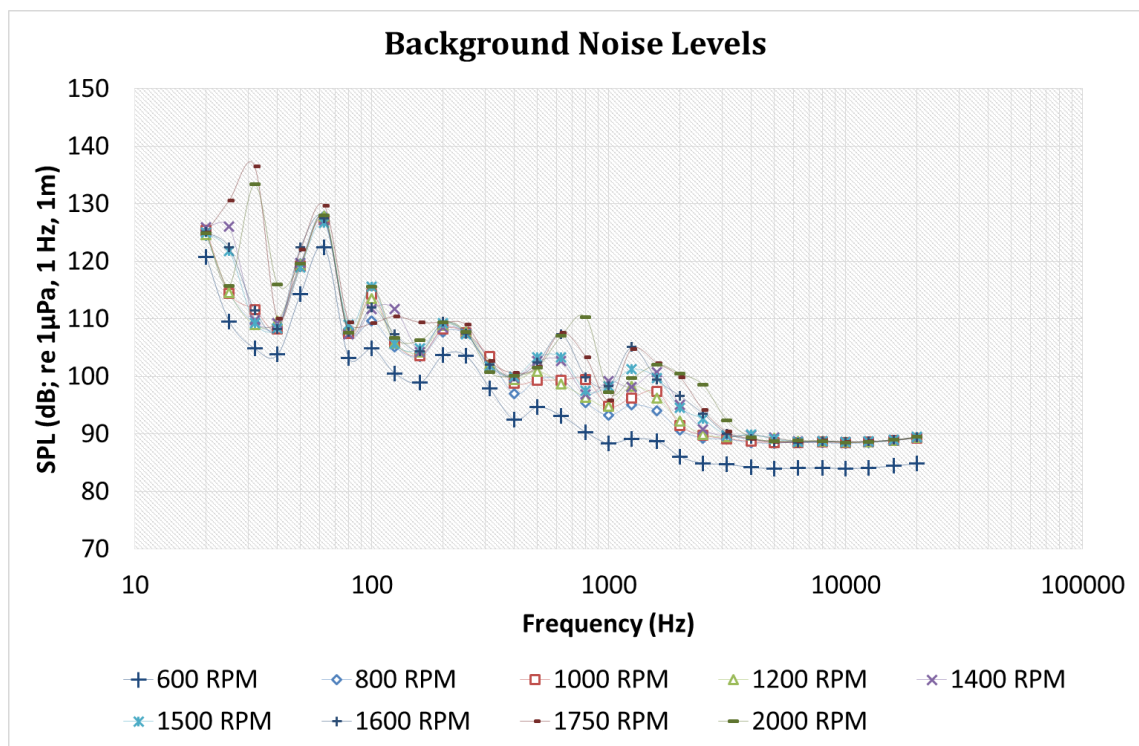


Figure- C-12 Background noise levels at 3m/s inflow speed for different dynamometer speeds at 300 mmHg vacuum applied behind ECT1.

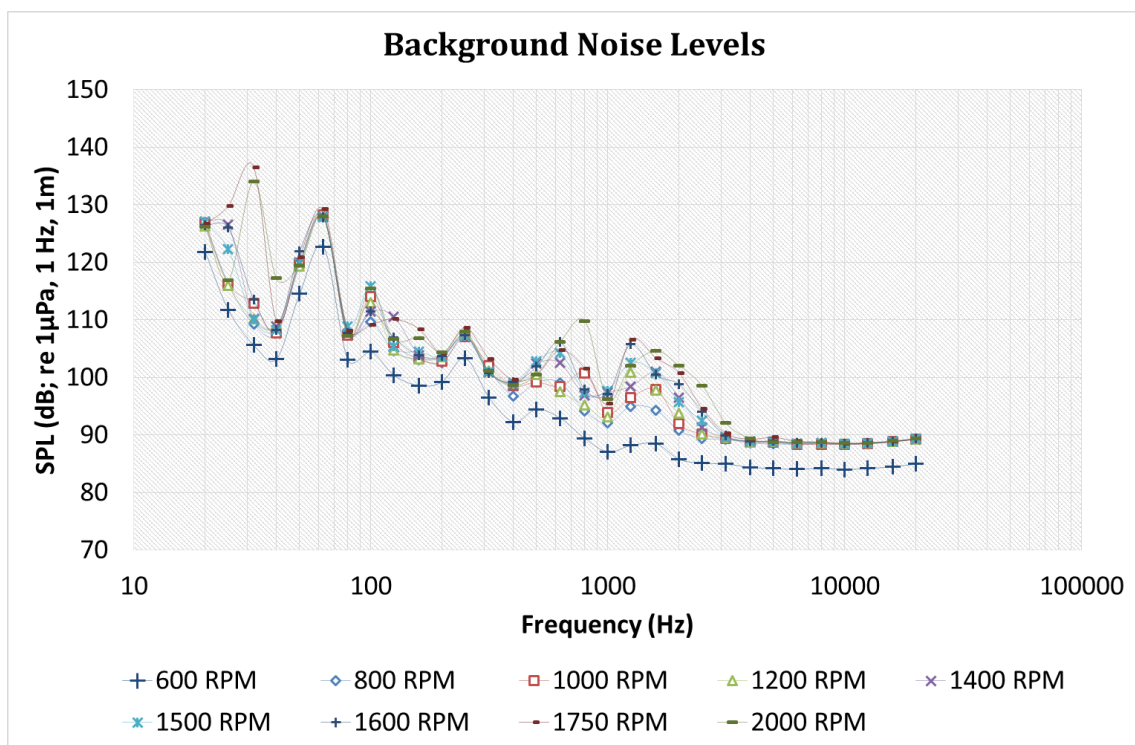


Figure- C-13 Background noise levels at 3m/s inflow speed for different dynamometer speeds at 300 mmHg vacuum applied behind ECT2.

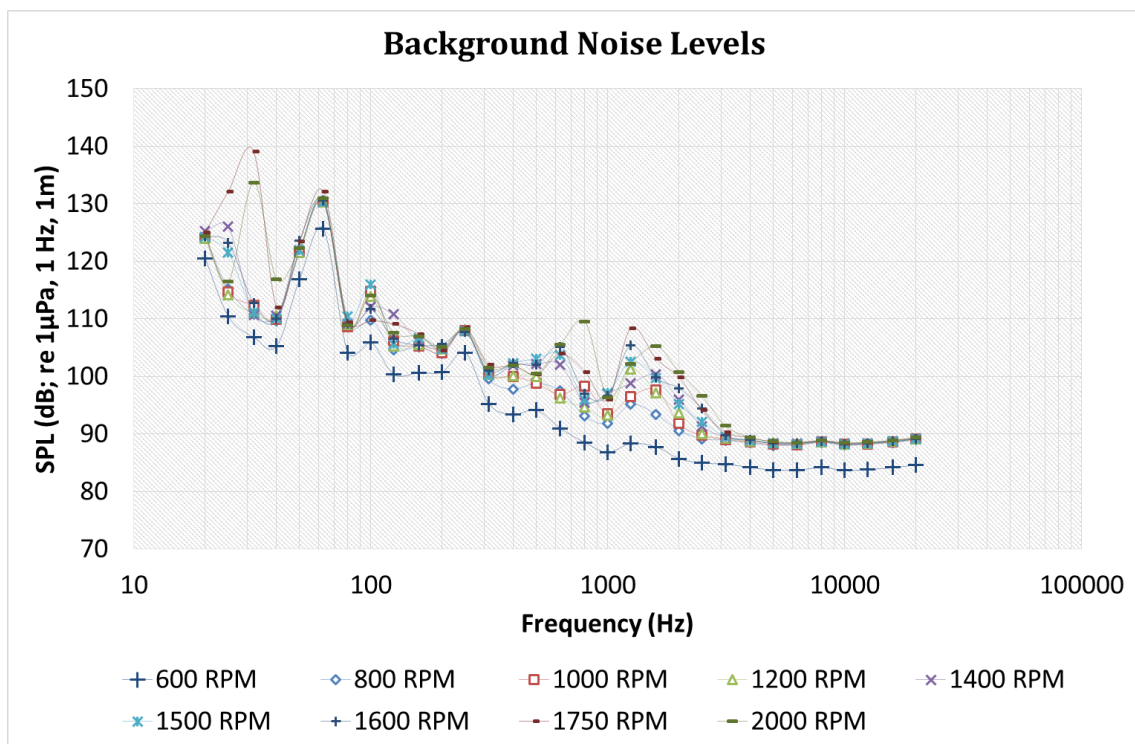


Figure- C-14 Background noise levels at 3m/s inflow speed for different dynamometer speeds at 300 mmHg vacuum applied behind ECT3.

# **Appendix D - Fundamentals of Artificial Neural Network & Associated Prediction Software**

## **D.1 Introduction**

*Appendix D provides further insight into the adopted methodology implemented for the ANN, which is used for the presentation of the propeller noise database and associated software for the noise prediction. The utilized code for the determination of the optimum number of hidden layer and neuron number is presented to enhance the understanding. Finally, the code developed for the compiled propeller noise prediction software is provided.*

## **D.2 Fundamentals of ANN**

ANN, in contrast to statistical polynomial fits, generates functional relationships between the input and the output data spaces in a multi-dimensional manner. Therefore, it is a tool that is possibly suitable for extrapolation of the data space. In order to achieve this functionality, the ANN uses neurons. Each neuron is a singular processing unit that takes several inputs originating from other neurons and produces an output that is then transmitted to other neurons.

Whilst the original ANN methodology was inspired by the human biological neuron, as sketched schematically in Figure D-1, the application of the network in the computational domain has evolved depending on the various mathematical principles.

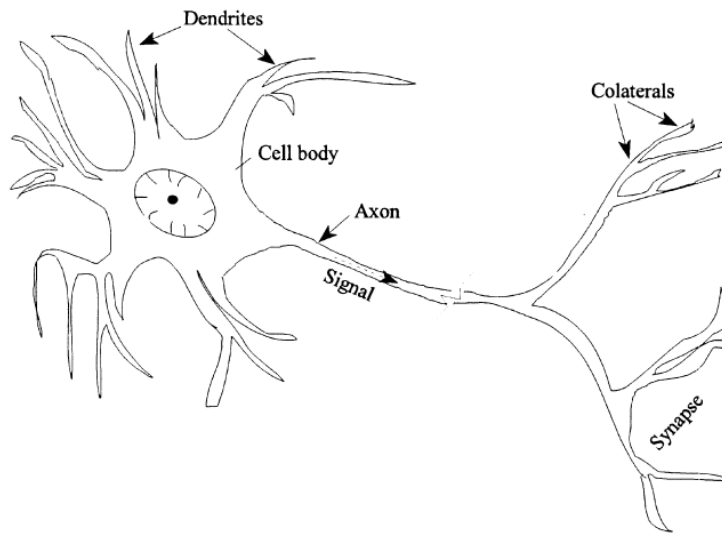


Figure- D-1 Schematic representation of a Biological Neuron (Reproduced from (Basheer & Hajmeer, 2000)).

An artificial neuron is a compilation of mathematical functions that can be conceived as a simple model of a biological neuron. Figure D-2 presents the basic single input neuron model. Based on the single input model more complex neural networks are developed as shown in Figure D-3. The set of inputs selected are summed up by the processing unit after the weight and bias values applied. Then summed up value is used as an input to a non-linear activation function that is transferred to the other neurons.

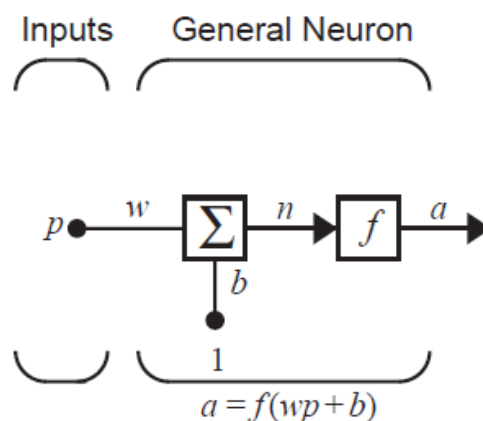


Figure- D-2 Basic single input Neuron Model (Reproduced from (Beale et al., 2015)).



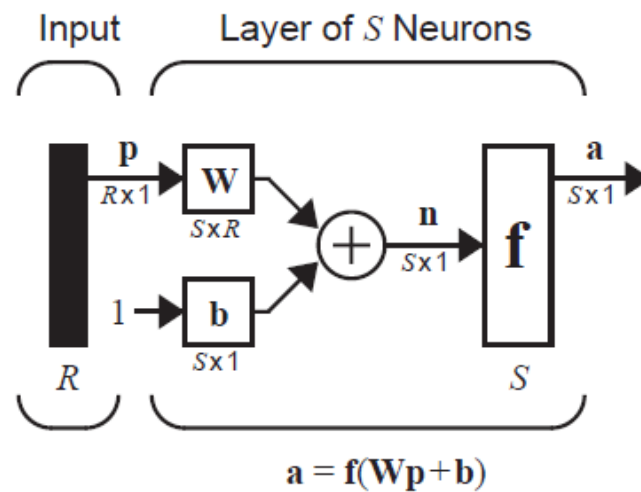


Figure- D-3 Multiple input Single Hidden layer Neural network (Reproduced from (Beale et al., 2015)).

The number of neurons is a key factor in the development of an ANN. For every application, there is an optimum number of hidden neurons that gives the best prediction. Furthermore, for more complicated applications the number of hidden layers may also need to be increased. However, while the predictions will be poor, if an unsatisfactory number of hidden neurons are used, the over usage of neurons and hidden layer will also result in a loss of the prediction performance.

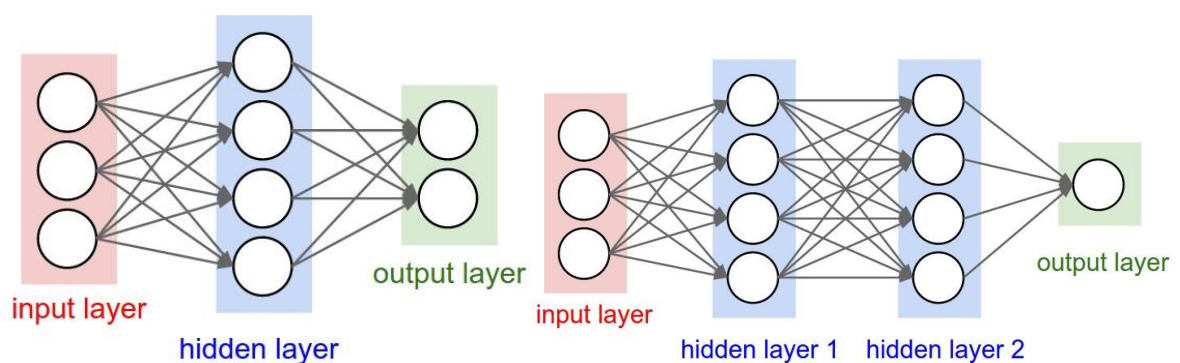


Figure- D-4 Simple representation of single hidden layer (left) and double hidden layer (right) Neural Network (Reproduced from (Karpathy, 2016)).

### D.3 MATLAB code for the determination of optimum number of hidden neurons

In order to determine the best number of hidden layer, a sweep function has been implemented by a MATLAB code. The code trains ANN for 462 alternative configurations that include two hidden layer option and one hidden layer option for neuron numbers from 1 to 101 with 5 neuron intervals. The performance of the each trained network is recorded in order to create a surface plot and a two-dimensional plot to be able to determine the best number of hidden layers and neurons with reasonable computational effort. Whilst the code given by Table- D-1 is for the time-delay neural network, other options provided by the MATLAB toolbox is also implemented to ensure the use of the best ANN method. The number of inputs are also altered in this respect to determine the optimum ANN that provides the most accurate prediction.

Table- D-1 Sweep function for determination of the optimum number of Hidden layers and Neurons.

```
% Solve an Input-Output Time-Series Problem with a Time Delay Neural Net-  
work  
  
% Script generated by NTSTOOL.  
  
% Created Wed Apr 29 12:45:11 BST 2015  
  
clear all; close all; clc;  
  
AAA=xlsread('ANN_BG_noise.xlsx');  
AAA=AAA';  
  
[x] = AAA(1:5,:);  
[t] = AAA(6:36,:);  
  
%   x - input time series.  
%   t - target time series.  
  
  
inputSeries = tonndata(x,true,false);  
targetSeries = tonndata(t,true,false);  
  
aaa = 1:5:101;  
bbb = 1:5:101;
```

```

ccc = 1:5:101;
for i = 1:21
    a = aaa(1,i);

    % Create a Time Delay Network
inputDelays = 0:1;
hiddenLayerSize = a; %a;
net = timedelaynet(inputDelays,hiddenLayerSize);

% Prepare the Data for Training and Simulation
% The function PREPARETS prepares timeseries data for a particular network,
% shifting time by the minimum amount to fill input states and layer states.
% Using PREPARETS allows you to keep your original time series data un-
% changed, while
% easily customizing it for networks with differing numbers of delays, with
% open loop or closed loop feedback modes.
[inputs,inputStates,layerStates,targets] =
preparets(net,inputSeries,targetSeries);

% Setup Division of Data for Training, Validation, Testing
net.divideParam.trainRatio = 70/100;
net.divideParam.valRatio = 15/100;
net.divideParam.testRatio = 15/100;

% Train the Network
[net,tr] = train(net,inputs,targets,inputStates,layerStates);

% Test the Network
outputs = net(inputs,inputStates,layerStates);
errors = gsubtract(targets,outputs);

```



```

performance = perform(net,targets,outputs);
error = cell2mat(errors);

e =abs(error);
es(i,:) = sum(e);
ess(i,1)=sum(es(i,:));
% if ds < best
%     best = ds
%     netb = net;
%     numbest = numHiddenNeurons
% endfor i = 1:101
end
for j=1:21
    for k=1:21
        b = bbb(1,j);
        c = ccc(1,k);
% Create a Time Delay Network
inputDelays = 0:1;
hiddenLayerSize = [b,c]; %a;
net = timedelaynet(inputDelays,hiddenLayerSize);
% Prepare the Data for Training and Simulation
% The function PREPARETS prepares timeseries data for a particular network,
% shifting time by the minimum amount to fill input states and layer states.
% Using PREPARETS allows you to keep your original time series data un-
% changed, while
% easily customizing it for networks with differing numbers of delays, with
% open loop or closed loop feedback modes.
[inputs,inputStates,layerStates,targets] = preparets(net,inputSeries,tar-
getSeries);

```

```

% Setup Division of Data for Training, Validation, Testing
net.divideParam.trainRatio = 70/100;
net.divideParam.valRatio = 15/100;
net.divideParam.testRatio = 15/100;

% Train the Network
[net,tr] = train(net,inputs,targets,inputStates,layerStates);

% Test the Network
outputs = net(inputs,inputStates,layerStates);
error_twoHL = gsubtract(targets,outputs);
performance = perform(net,targets,outputs);
error_twohls = cell2mat(error_twoHL);

d =abs(error_twohls);
ds(j,:) = sum(d);
dss(j,k)=sum(ds(j,:));

% if ds < best
%     best = ds
%     netb = net;
%     numbest = numHiddenNeurons
end
end

[C,I] = min(dss);
perfectneuron = aaa(1,I)

view(net) % View the Network

% % Uncomment these lines to enable various plots.
% %figure, plotperform(tr)
% %figure, plottrainstate(tr)
% %figure, plotresponse(targets,outputs)

```

```

figure, ploterrcorr(errors)

% %figure, plotinerrcorr(inputs,errors)

% % y(t+1) once x(t) is available, but before the actual y(t+1) occurs.

% % The network can be made to return its output a timestep early by
removing one delay

% % so that its minimal tap delay is now 0 instead of 1. The new network
returns the

% % same outputs as the original network, but outputs are shifted left one
timestep.

nets = removedelay(net);

[xs,xis,ais,ts] = preparets(nets,inputSeries,targetSeries);

ys = nets(xs,xis,ais);

earlyPredictPerformance = perform(net,tc,yc)

% wts = net.IW{1,1}

% bias = net.b{1}

```

## D.4 MATLAB code for the noise prediction tool

The plotted results of the sweep functions aided the determination of the optimum number of hidden layer and the number of neurons within. The determined numbers are repeatedly trained using the MATLAB toolbox to ensure the training performance remained similar as the ANN methodology adopts an initialization with random nature hence the trained network may result in a different performance each time.

After achieving the satisfactory ANN performance by the trained network, the finalized version is saved to be used within a user interface function written in MATLAB that prompts user input for the determined parameters that is required by the software. Finally, the user interface is compiled together with the trained networks to be converted into an executable file of the software named ECT\_CAV\_NOISE as given in Table D-2.

Table- D-2 Developed MATLAB Code for the User interface of the ECT\_CAV\_NOISE.

```
function [] = compiled_network()
%% INTERFACE for INPUTS
disp('');
disp('    Full-Scale Propeller NOISE Estimation using ANN');
disp('-----');
disp('');
%invoke interface to input values
prompt = {'P/D (Pitch to Diameter Ratio)', 'BAR (Blade Area Ratio)', 'Blade No', 'Wake Nonuniformity (BSRA Wake Criteria)', 'Wake depth', 'Wake width', 'KT (Thrust Coefficient)', '10KQ (Torque Coefficient)', 'J (Advance Coefficient)', 'SigmaV (Free stream Cavitation Number)', 'SigmaN (Rotational Cavitation Number)', 'SigmaR (Resultant Cavitation Number)', 'Full Scale propeller Diameter', 'Full Scale Propeller rps', 'Mean Wake', 'Output File Name'};
dlg_title = 'ECT_CAV_NOISE' ;
lines = 1.5;
options.Resize='on';
options.WindowStyle='normal';
def = {'0.8', '0.65', '4', '0.81', '0.64', '95', '0.28', '0.3424', '0.25808', '38.91', '2.835', '0.285', '0.3048', '29.16', '0.20', 'ECT_CAV_Noise Prediction.xls'};
answer = inputdlg(prompt,dlg_title,lines,def,options);
y = answer{1, 1};
Input1 = str2num(y);
y = answer{2, 1};
Input2 = str2num(y);
y = answer{3, 1};
Input3 = str2num(y);
y = answer{4, 1};
Input4 = str2num(y);
y = answer{5, 1};
Input5 = str2num(y);
y = answer{6, 1};
Input6 = str2num(y);
y = answer{7, 1};
Input7 = str2num(y);
y = answer{8, 1};
Input8 = str2num(y);
y = answer{9, 1};
Input9 = str2num(y);
y = answer{10, 1};
Input10 = str2num(y);
y = answer{11, 1};
Input11 = str2num(y);
y = answer{12, 1};
Input12 = str2num(y);
y = answer{13, 1};
Input13 = str2num(y);
y = answer{14, 1};
Input14 = str2num(y);
y = answer{15, 1};
Input15 = str2num(y);
y = answer{16, 1};
Input16 = (y);
%make the input array for total noise and BG Noise
Total_Noise = [Input1;Input2;Input3;Input4;Input5;Input6;Input7;Input8;Input9;Input10;Input11;Input12;];
BG_Noise = [Input4;Input5;Input6;Input7;Input12];
```

```

frequency
=[ 20;25;31.5;40;50;63;80;100;125;160;200;250;315;400;500;630;800;1000;12
50;1600;2000;2500;3150;4000;5000;6300;8000;10000;12500;16000;20000];
%% LOAD ANN model
load Total_network;
Total_prediction=sim(net,Total_Noise);
load BG_network;
BG_prediction=sim(net,BG_Noise);
for i=1:31
if Total_prediction(i)-BG_prediction(i)<3;
Net_noise(i)=0
FS_Noise(i)=0
FS_frequency(i)=0
else
Net_noise(i)=10*((log10((10^(Total_prediction(i)/10))-
(10^(BG_prediction(i)/10)))));
FS_Noise(i)=Net_noise(i)+(60*log10(Input13/0.3048)+40*log10(Input14*In-
put9*0.3048/3)+20*log10(1025/1003));
FS_frequency(i)=frequency(i)*Input14*Input9*0.3048/(3*(1-In-
put15));
end
end
disp(' ');
disp(' Full-Scale Propeller Cavitation Noise Prediction');
PROP_CAV_NOISE=[FS_frequency;FS_Noise]'
dlmwrite(Input16,PROP_CAV_NOISE,'\t');
figure
semilogx(FS_frequency,FS_Noise)
xlabel('Frequency (Hz)'); ylabel('RNL re 1microPa @1m in 1Hz Equivalent');

```